Rotary kilns with sectional internals & lifters

- Industrial process example of iron oxide pigment production -

Dissertation

zur Erlangung des akademischen Grades eines

Doktors der Naturwissenschaften

- Dr. rer. nat. -

vorgelegt von

Joscha Prießen, M.Eng.

geboren in Kempen

An der

Universität Duisburg-Essen

Fakultät Chemie

Essen 2022

DOI: 10.17185/duepublico/77182
URN: urn:nbn:de:hbz:465-20230329-115449-7

Die vorliegende Arbeit wurde im Zeitraum von Dezember 2017 bis Dezember 2020 in der Arbeitsgruppe von Prof. Dr.-Ing. Heyko Jürgen Schultz an der Hochschule Niederrhein in Krefeld sowie im der Arbeitsgruppe von Prof. Dr. Malte Behrens am Lehrstuhl für die Anorganische Chemie der Universität Duisburg-Essen durchgeführt. Die Arbeit entstand im Rahmen einer Industriepromotion in Kooperation mit der Lanxess Deutschland GmbH, Business Unit Inorganic Pigments in Krefeld-Uerdingen.

Tag der Einreichung:	08.06.2022
Tag der Disuputation:	03.11.2022
Gutachter:	Prof. Dr. Malte Behrens
	Prof. Dr.-Ing. Heyko Jürgen Schultz
Vorsitzender:	Prof. Dr. Oliver J. Schmitz

Eidesstattliche Erklärung

Ich versichere hiermit an Eides statt, dass ich die vorgelegte Dissertation mit dem Titel

„*Rotary kilns with sectional internals & lifters - Industrial process example of iron oxide pigment production* –„

selbstständig, ohne fremde Hilfe und ohne die Benutzung anderer, als die in der Arbeit angegebenen, Hilfsmittel angefertigt habe. Alle Stellen, die wörtlich oder sinngemäß aus veröffentlichten und nicht veröffentlichten Quellen entnommen wurden, sind als solche in der Arbeit kenntlich gemacht. Die vorliegende Dissertation wurde in dieser oder ähnlicher Form noch bei keiner anderen Universität eingereicht.

Wachtendonk, November 2022

Joscha Prießen

Danksagung

Besonders bedanken möchte ich mich bei Prof. Dr.-Ing. Heyko Jürgen Schultz für die drei Jahre, in denen ich in seiner Arbeitsgruppe meiner Forschungstätigkeit nachgehen durfte. Insbesondere hervorheben möchte ich dabei die Bereitschaft das Forschungsinteresse thematisch zu erweitern und die Motivation dieses „Neuland“ zu betreten. Ebenfalls hervorheben möchte ich die Anstrengungen, das Promotionsvorhaben in Form einer Industriepromotion mit den drei Partnern Hochschule Niederrhein, Universität Duisburg-Essen und der Lanxess Deutschland GmbH zu ermöglichen.

Weiterhin möchte ich mich bei Prof. Dr. Behrens bedanken für die Bereitschaft, das Promotionsprojekt zu unterstützen und die bereits dargestellten Kooperationen einzugehen. Ich habe mich über die freundliche Aufnahme und Unterstützung, den Austausch und die Motivation durch Ihn und die Arbeitsgruppe sehr gefreut.

Für die außergewöhnliche Möglichkeit das Promotionsvorhaben mit einem Industriepartner und starkem Anwendungsbezug gestalten zu können möchte ich mich in aller Form bei der Lanxess Deutschland GmbH – Business Unit Inorganic Pigments - bedanken. Hier möchte ich persönlich insbesondere Herrn Dr. Wolfgang Oehlert (Vice President Technical Operations), Dr. Roland Flindt (Betriebemanager Pasten & Klinker) sowie Thomas-Oliver Neuner (Bereichsingenieur Pasten & Klinker) hervorheben, die maßgeblich zu dieser Möglichkeit beigetragen haben. Auch den Kollegen der technischen Betriebsbetreuung, insbesondere Frank Pesch und Hartmut Wenders und Jewgenij Sajdok möchte ich für die fachlichen Diskussionen danken. Für die Unterstützung aus der Abteilung Innovation Particle Technology möchte ich namentlich und stellvertretend Christoph Munsch meinen Dank aussprechen.

Ein weiterer Dank gebührt den Kollegen und Mitarbeitern der Hochschule Niederrhein, welche mich im Verlauf meiner Arbeit begleitet und unterstützt haben. Hierbei möchte ich mich insbesondere bei Jan Vanvlodorp und Svenja Schramm für Austausch, Hilfsbereitschaft, gute Laune und konstruktives Zusammenarbeiten bedanken.

Ebenfalls möchte ich die Kollegen der technischen Chemie an der Hochschule Niederrhein und insbesondere Herrn Dr. Bartholomäus Luczak, Herrn Dr. Björn Noll (Lewandowski), Herrn Dr. Florian Wörmeyer (Filarsky) und Herrn Dr. Dennis Wunschik aus der Biotechnologie meinen Dank aussprechen. Die anregende wissenschaftliche Diskussion, gegenseitige Unterstützung als

auch freundschaftliche Motivation und Ratschläge haben diese Arbeit und mich persönlich bereichert. Auch die Aktionen abseits des thematischen Bezuges haben diese Zeit besonders gemacht.
Ein großes Dankeschön auch an die Studierenden, die ich im Laufe Ihrer Abschlussarbeiten betreuen durfte und die zur Entwicklung der Arbeit sowie zu meiner persönlichen Entwicklung beigetragen haben. Alles erdenklich Gute für den weiteren Lebensweg wünsche ich Thomas Kreutzer, Marten Mehring, Thorsten Lange, Laura Lenters, Jan Selders, Gizem Irgat, Torben Kawka, Oliver Richter, Fabienne van Stiphoudt, Jano Bremes, Jasmina Alisic und Fernando Barths.

Abschließend möchte ich mich außerordenlich bei meinen Freunden und meiner Familie bedanken. Ihr habt diese Arbeit überhaupt ermöglicht und über die gesamte Zeit für die Rahmenbedingungen gesorgt, die zum Gelingen beigetragen haben. Insbesondere ohne meine Frau Alexandra Neumann-Prießen wäre die Arbeit nicht möglich gewesen. Du hast häufig verzichtet und mich trotzdem in schwierigen Phasen motiviert und mir in vielen Dingen des täglichen Lebens die Arbeit erleichtert oder abgenommen. Ohne dich wäre die Arbeit nicht zu dem geworden, was sie ist.

Kurzfassung

Drehrohröfen sind in der thermischen Feststoffverarbeitung weit verbreitet häufig angewandt. Die vorliegende Arbeit befasst sich exemplarisch mit dem Kalzinierungsprozess im Drehrohrofen bei der Eisenoxidpigmentherstellung nach dem Laux-Verfahren. Betrachtet wird der Drehrohrofenprozess als Ganzes, jedoch wird insbesondere auf die besondere Gestaltung des Ofens/Reaktors mit verschiedenen Einbauten und deren Auswirkungen eingegangen. Im Mittelpunkt der Untersuchungen steht die Analyse des axialen und transversalen Feststofftransports in einer Drehtrommel mit Hubschaufeln und insbesondere mit Sektionaleinbauten. Die Herangehensweise der Untersuchungen beruht auf der Zerlegung des Ofenprozeses in seine Einzelphänomene (Reaktionen, Feststofftransport, Wärmetransport) und der anschließenden Zusammenführung der Erkenntnisse in einem mathematischen Modell

Bei der Analyse der "Reactions in iron oxide conversion" (Part II) wird die Reaktionskinetik experimentell untersucht. Es konnte festgestellt werden, dass die Sauerstoffkonzentration (im technisch relevanten Bereich > 10 Vol.-% O_2) und die Heizraten (bis zu 20 K/min) keinen Einfluss auf die Kinetik haben. Für Magnetite, die aus verschiedenen Eisensalzen hergestellt wurden, sowie für die industriellen Laux-Magnetite konnte ein unterschiedliches kinetisches Verhalten gezeigt werden. Ein starker Einfluss des Fe^{2+}/Fe^{3+}-Verhältnisses des Magnetitedukts, insbesondere auf die Wärmebilanz der Reaktion (Oxidationsenthalpie), wurde festgestellt.

Der Kernteil der Arbeit "Solid transport in rotary drums" (Part III) befasst sich mit den Feststofftransportprozessen in Drehrohren. Es wurde eine modulare und flexible Drehrohrapparatur aus PMMA entwickelt, um den Feststofftransport experimentell mittels optischer Methoden zu untersuchen. Hinsichtlich des axialen Feststofftransports erhöhen Sektionaleinbauten die Verweilzeit, reduzieren aber die Kapazität, während die axialen Dispersionskoeffizienten vergleichbar zum Leerrohr sind. Der Einfluss der Einbauten hängt von der Länge und Anzahl der Sektionen ab, was in einer empirischen Gleichung quantifiziert wurde. Darüber hinaus wurde das Saeman-Modell erfolgreich an die Beschreibung von Drehrohren mit Sektionaleinbauten angepasst. In transversaler Richtung konnten grundlegend andere Bewegungsmuster als beim Leerrohr beobachtet werden. Die Kinetik der Transversalvermischung ist schneller, was auf den anderen Mischmechanismus zurückgeführt werden kann. Darüber hinaus konnte ein Vorteil von Sektionaleinbauten in Bezug auf die Mischgüte, insbesondere bei inhomogenen Schüttgütern, festgestellt werden. Unterschiede in den Austauschflächen zwischen

Gas, Wand und Festbett konnten mit einer empirischen Gleichung in Abhängigkeit von der Sektionenzahl ermittelt und quantifiziert werden.

Die Analyse von axial diskontinuierlich gestalteten Hubschaufeln ergab eine Erhöhung der axialen Dispersionskoeffizienten um bis zu eine Größenordnung im Vergleich zu kontinuierlichen Hubschaufeln. Die Hold-Ups und Verweilzeiten sind bei axial segmentierten Hubschaufeln vergleichbar mit denen des Leerrohrs, bei axial durchgehenden Hubschaufeln jedoch deutlich erhöht. Folglich ist der Hold-Up bei axial segmentierten Hubschaufeln deutlich schlechter, was durch Transversalmessungen bestätigt wurde, bei denen ein eindeutiger Zusammenhang mit der axialen Länge festgestellt werden konnte. Dieses Phänomen wurde auch in Modellrechnungen bestätigt, aus denen $L_L > 5 * L_r$ (L_L=axiale Länge; L_r=radiale Ausdehnung) als sinnvolle Faustregel für die Auslegung abgeleitet wurde.

Der Wärmetransport in Drehtrommeln („Heat transport in rotary drums“, Part IV) wird mit angepassten Ansätzen aus der Literatur beschrieben. Ein mathematisches Modell, das alle überlagerten Wärmetransportmechanismen enthält, wird mit Hilfe der Netzwerkmethode aufgestellt.

In der mathematischen Modellierung („Mathematical modeling“, Part V) werden schließlich alle Ergebnisse aus den vorangegangenen Untersuchungsteilen zu einem eindimensionalen mathematischen Modell des Drehrohrofenprozesses zusammengefasst. Dabei wird die Methode der Querschnittsmodellierung angewandt und die Gleichungen mit dem Newton Verfahren gelöst. Die axialen Temperaturverläufe und Konzentrationen im Drehrohrofen wurden ermittelt und exemplarisch mit dem industriellen Referenzprozess validiert. Der Einfluss von Sektionaleinbauten wurde erstmalig in einer Sensitivitätsanalyse quantifiziert, was als Alleinstellungsmerkmal hervorzuheben ist. Durch den Einsatz von Sektionseinbauten wird die Reaktionszone im Ofen verschoben und das Temperaturniveau im Ofen durch die verbesserten Austauschflächen im Referenzprozess um ca. 200 K gesenkt.

Abstract

Rotary kilns are widespread and common in the thermal processing of solid material. This thesis deals with the exemplary calcination process in the rotary kiln during iron oxide pigment production according to the Laux process. The rotary kiln process is considered in its entirety, but particular attention is paid to the special design of the kiln/reactor with various internals and their effects. The core of the investigations is the analysis of the axial and transverse solids transport in a rotary drum with lifters and in particular with sectional internals. The overall approach is based on the decomposition of the kiln process into its individual phenomena (reactions, solid transport, heat transport) and the subsequent combination of the findings in a mathematical model.

In the investigation of the "Reactions in iron oxide conversion" (Part II) the reaction kinetics is analyzed experimentally. It could be found that the oxygen concentration (in a technically relevant range > 10 vol.% O_2) and heating rates (up to 20 K/min) do not impact the kinetics. Different kinetic behavior of magnetites prepared from different iron salts as well as for the industrial Laux magnetites could be shown. A high influence of the Fe^{2+}/Fe^{3+}-ratio of the magnetite educt, especially on the heat balance of the reaction (enthalpy of oxidation) was found.

The core part of the thesis "Solid transport in rotary drums" (Part III) focuses on the solid transport processes in rotary drums. A higly modular and flexible rotary drum apparatus construced in PMMA was developed to investigate the solid transport experimentally utilizing optical methods. Regarding the axial solid transport, sectional internals increase the residence time but reduce the drum capacity while the axial dispersion coefficients are similar to the bare drum. The influences of sectional internals depend on the length and number of sections, which was quantified in an empirical equation. Furthermore, the Saeman-model has been adapted successfully to describe rotary drums with sectional internals. In the transverse direction, fundamentally different motion patterns could be observed compared to the bare drum. The kinetics of the transverse mixing is faster, which could be attributed to the different mixing mechanism. Additionally, an advantage of sectional internals could be found in terms of mixing goodness, especially for inhomogeneous bulk materials. Differences of exchange areas between gas, wall and solid bed could be found and quantified with an empirical equation as a function of section number.

The analysis of axially discontinuous designed lifters revealed an axial dispersion increase up to one magnitude in comparison to continuous lifters. The hold-up and the residence times are comparable to the bare drum for axially segmented lifters, but are significantly increased for axially

continuous lifters. Following, the hold-up of axially segmented lifters is significantly worse, which was confirmed in transverse flow measurements, where a clear relation to the axial length could be established. This phenomenon was further confirmed in model calculations, from which $L_L>5*L_r$ (L_L=axial length; L_r=radial extent) was derived as a reasonable rule of thumb for the design.

The "Heat transport in rotary drums" (Part IV) is described with adapted approaches from literature. A mathematical model containing all superimposed heat transport mechanisms is set up using the network method.

Finally, in the "Mathematical modeling" (Part V), all results from the previous investigations parts are combined in a one dimensional mathematical model of the rotary kiln process. The method of "cross-section modeling" is applied and the equations are solved using the newton method. The axial temperature-profiles and concentrations in the rotary kiln are determined and validated exemplary with the industrial reference process. The impact of sectional internals has been quantified for the first time in a sensitivity analysis, which has to be highlighted as a unique feature. The use of sectional internals shifts the reaction zone and reduces the temperature level in the kiln by approx. 200K due to the improved exchange surfaces in the reference process.

Table of contents

Part I Introduction

1 Situation-analysis

The rotary kiln equipment under consideration in this thesis is implemented in the pigment production according to the Laux-process. The main process is described in the basic patents from 1925 [1,2] with minor extensions in 1926 and 1927 [3–5]. The Laux-Process is based on the Bechamp-Reaction from 1854, which was an old route to produce aniline from nitrobenzene via reduction with iron. In this reaction the oxidized iron was a waste product [6,7].

Laux was able to modify the process by addition of iron(II)-chloride/aluminium-chloride-solutions and sulfuric acid or phosphoric acid and gain an iron oxide from that process in very high pigment quality. Different colors and color shades can be created via the reaction conditions and additives. The main reactions are as following [6]:

$$2\,Fe + C_6H_5NO_2 + 2\,H_2O \rightarrow 2\,\alpha FeOOH + C_6H_5NH_2 \quad (0.1)$$

$$9\,Fe + 4\,C_6H_5NO_2 + 4\,H_2O \rightarrow 3\,Fe_3O_4 + 4\,C_6H_5NH_2 \quad (0.2)$$

Adding iron(II)-chloride directs to black (magnetite) products, while aluminum-chloride as additive leads to yellow (goethite) iron oxides [7]. Since scrap iron is used as precursor and all products (aniline and iron-oxides) are used afterwards, the process is very sustainable [8]. The main reaction takes place in a stirred tank reactor and the product is subsequently processed according to the flow sheet presented in Figure I - 1.1.

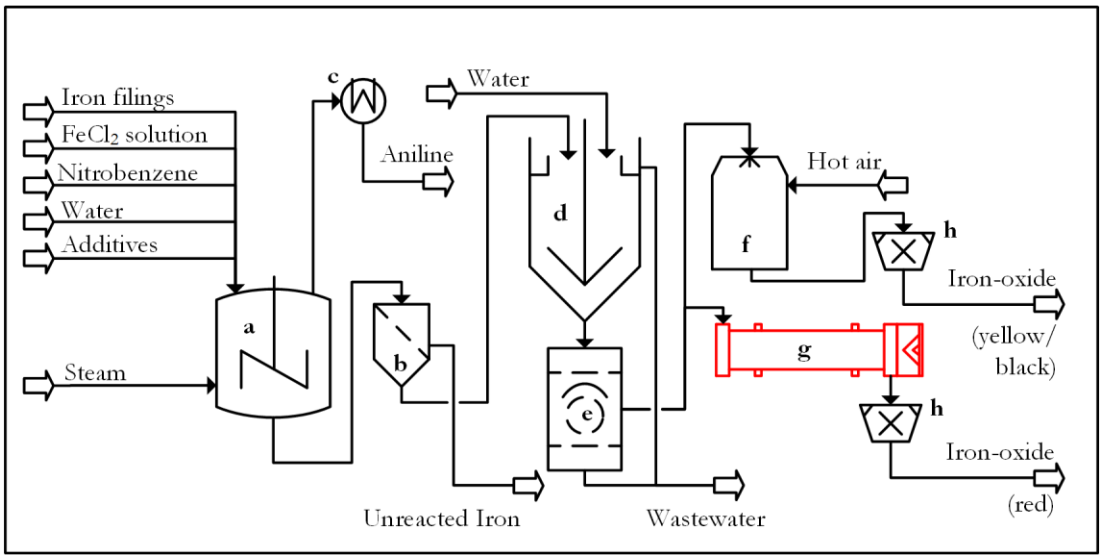

Figure I - 1.1: Flow-sheet of iron-oxide production with the Laux-process according to Buxbaum [7]: a: reactor; b: classifier; c: condenser; d: thickener; e: drum filter; f: dryer; g: rotary kiln; h: mills.

Unreacted iron is separated in classifier devices. The pigment suspension is washed in thickeners and drum filters are used for mechanical dewatering of the suspensions. Afterwards the pigments are dried to finally yield yellow or black pigments after milling. To produce a red pigment (hematite), the magnetite is calcined in rotary kilns (Figure I - 1.1, red) where magnetite is oxidized. This rotary kiln process is the main topic of the thesis. A picture from a Lanxess production site in Krefel-Uerdingen with a part of an industrial rotary kiln is presented in Figure I - 2.1 together with a silo.

Although rotary kilns have been used for a long time in history, the processes are not understood in detail since a high number of influencing and interacting variables makes the kiln process a complex system. In general, each rotary kiln is unique in its configuration and in particular several different internal configurations are used.

No similar and fully scaled down model of the equipment under consideration is available. Furthermore, literature reviews revealed a lack of scientific data regarding the different used configurations especially in the used kiln internals (lifters & sectional internals). Consequently, no universal predictions regarding the process behaviour are available and an estimation of the impact from equipment or internal modifications is not possible.

Besides the process equipment, the impact of different characteristics of magnetite precursor is not available, since Laux-magnetites have not been in focus of scientific research compared to different production routes as e.g. precipitation.

2 Description of goals

Due to the stated situation the main goals of the investigations in this thesis are:

- Gain information on the process and develop a deeper understanding of the rotary kiln process
- Investigate the impact of the used kiln internal structure and sectional internals in particular
- Develop a tool to predict the rotary kiln behavior and investigate the impact of different internal types
- Optimize the rotary kiln process if possible with the stated information

Figure I - 2.1: Rotary kiln in ironoxide pigment production, Lanxess process plant (Krefeld) [6]

3 Methodology & concept

Experiments in industrial production processes and in industrial scale are not possible, due to missing production capacity and the production of off-spec material. Based on the lack of an available fully scaled down laboratory apparatus the work is divided up into parallel working streams. The streams focus on the investigation of the basic phenomena taking place in the kiln process, which are:

- chemical reactions
- solid transport processes
- heat transport processes

Each of these topics is elaborated in separate streams and each stream aims on a mathematical description of the process. The structure of the work is adapted to this mode of working and each of the fields is documented in one main part of this thesis. In the final part (with content), the gained knowledge and derived models are merged together to create a full mathematical model and thus description of the process. The methodology is visualized in Figure I - 3.1 as flow diagram.

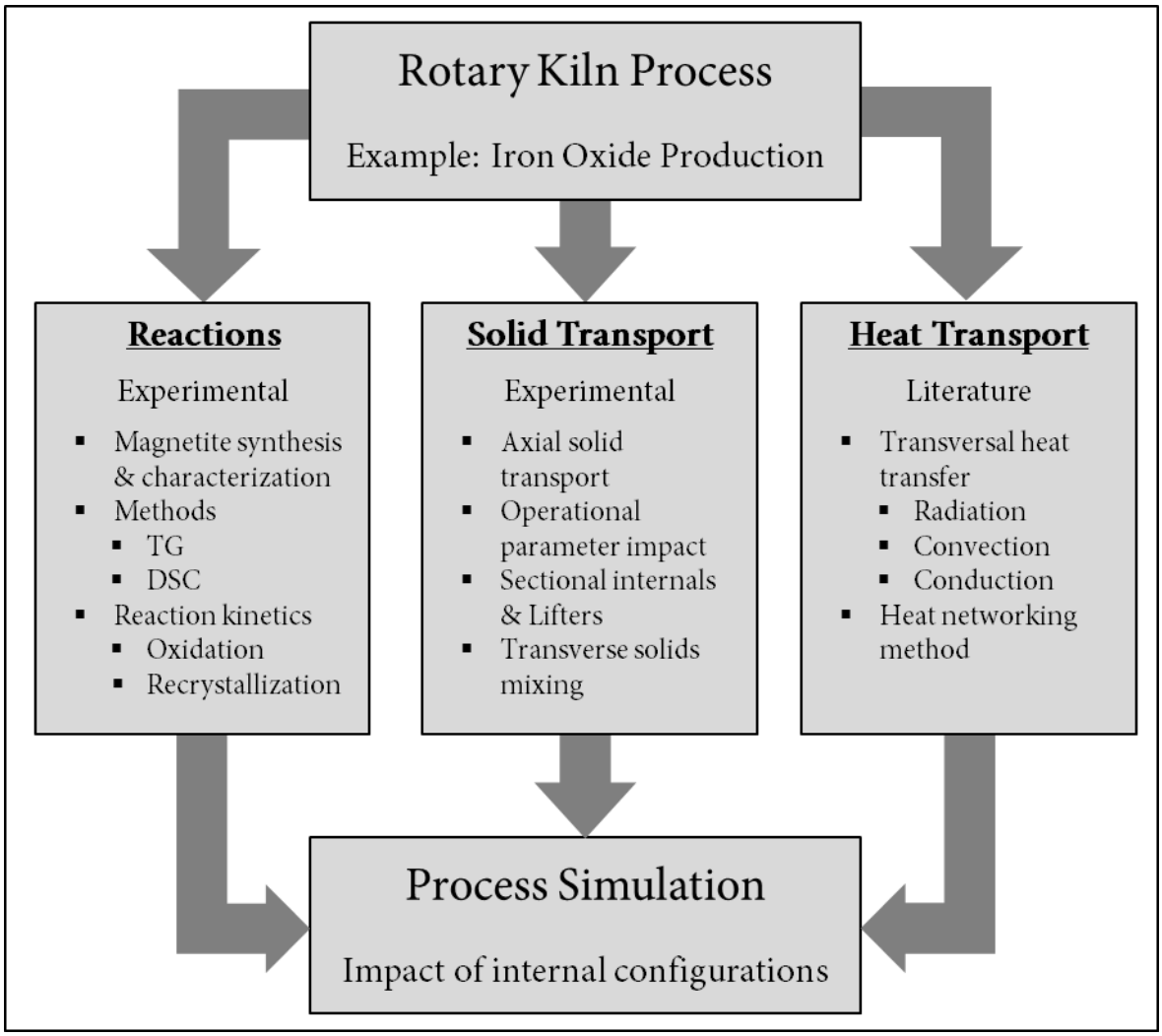

Figure I - 3.1: Schematic sketch of the basic methodology of the present work

The basic assumption of mathematical modeling in this work is the cross section modeling of rotary drums or kilns. This enables a reactor (rotary kiln) description in axial direction, if the processes taking place in one slice of the reactor are known. The modeling procedure is presented in detail in the last part of this work.

Part II Reactions in iron oxide conversion

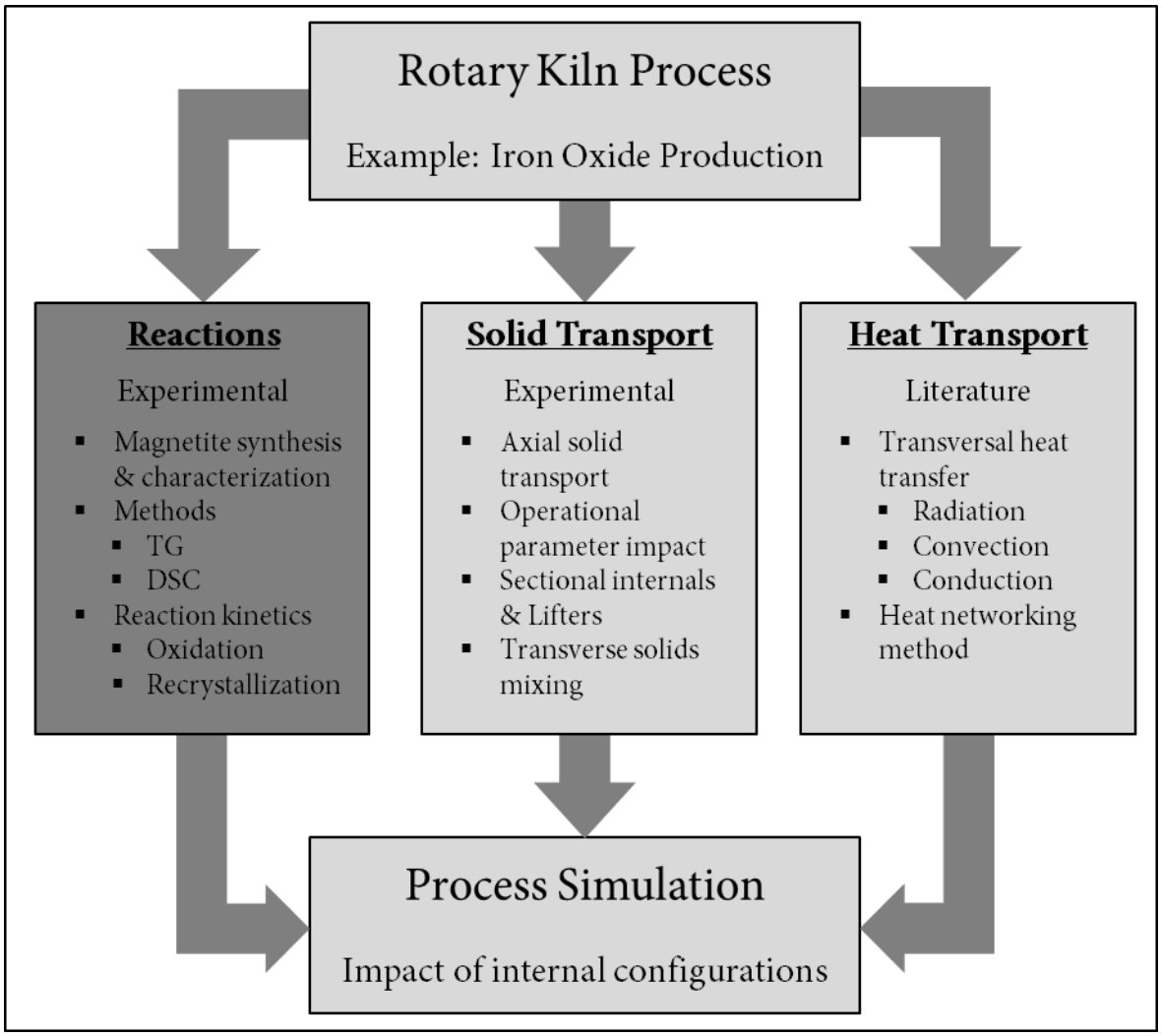

1 Introduction and Motivation

Iron oxides participate in many processes in nature or with technical background. In industrial use, they can be found from the very large to the very small scale. The following bullet points provide examplary fields in which iron oxides are involved or applied:

- Pig iron & steel production (reduction processes from iron ores) [9]
- Pigments (natural and synthetic) [7]
- Geology & geolocial processes [10]
- Nanomaterials (ferrofluids, functional materials and medical application fields) [11–14]
- Catalysts (e.g. Haber-Bosch process, ammonia synthesis) [15]
- Magnetic storage devices (compact cassettes, audio tapes etc.) [7,16]

Following, many different iron oxides are known and also widely explored and investigated. A large overview with a lot of data on iron oxides is provided by Cornell & Schwertmann [6]. The production processes of iron oxides are also manifold, ranging from solid-gas reactions and precipitation to hydrothermal synthesis [17] and sol-gel processes. Furthermore, the transformation reactions between the different iron oxides are also fundamentally known and researched.

However, the diversity of iron oxides and hydroxides is boon and bane at once, which explains the number of extensive research papers, since every tiny detail in this field matters. The behavior of many characteristics of iron oxides can be influenced and controlled by a multitude of parameters, in the best case the control is consciously. An example of this fact is the series "Investigations on magnetic sound carriers" (original: „Untersuchungen an Magnettonträgern“) [16].

Regarding the process in focus of this work (transformation reactions), knowledge on kinetic data is required in particular. There is still some need for measurements and research here, as it is known from literature, that the kinetics are also strongly dependent on further influencing variables and the exact characteristics of the magnetite educt. This is exemplary shown as an example in Figure II - 1.1, where the reaction progress with time is compared for a natural and a synthetic magnetite. As can be seen easily the different starting materials lead to completely different reaction kinetics.

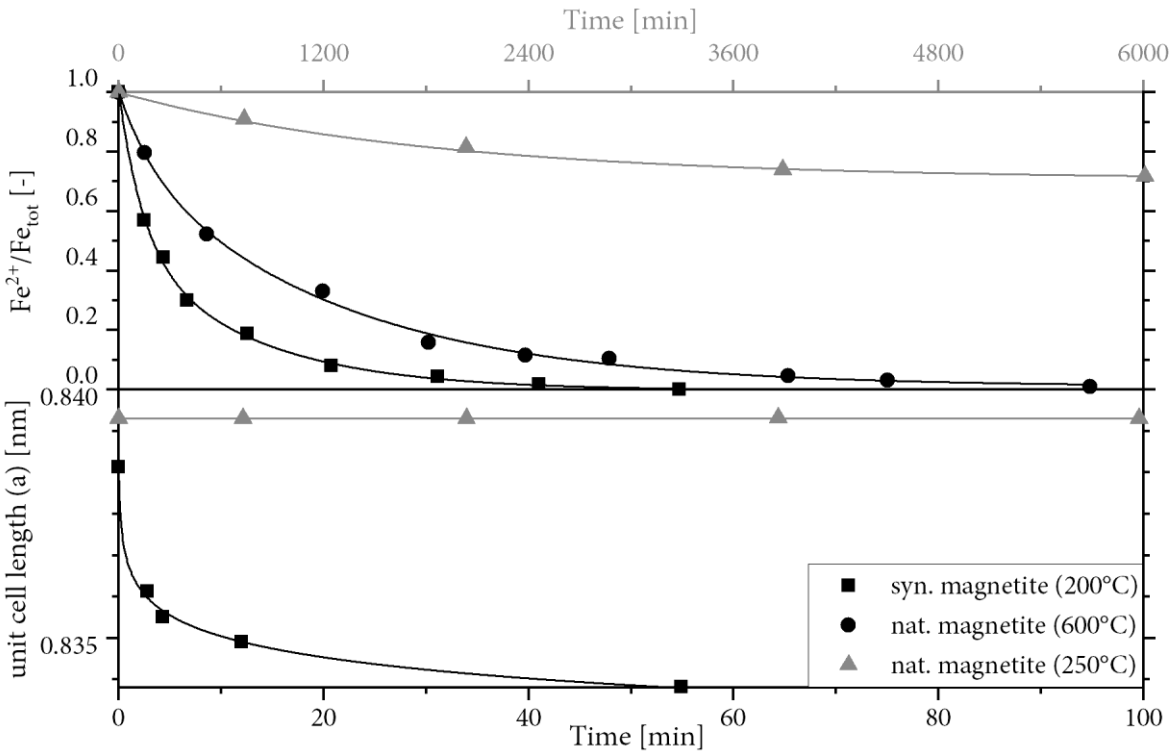

Figure II - 1.1: Exemplary diagram of reaction kinetics at oxidation of various magnetites. Top: reaction progress via Fe^{2+} content; bottom: reaction progress via unit cell length. Gray curves refer to top x-achsis (adapted from [6,18])

Following, it can be assumed, that for a correct process description, the kinetic data has to be further categorized with regard to the characteristics of the materials or magnetites used. In literature, there are also contradictory statements on the dependence of the kinetics on various variables, such as particle size. Furthermore, this fact requires at least the verification whether the technical products with impurities used in the considered process provide comparable kinetic data to those pure materials in literature investigations. Cornell & Schwertmann report, that foreign ions such as sulphate and chloride can also be incorporated in small quantities in the crystal lattice [6].

It should also be taken into account, that magnetite in the investigated industrial process is produced using the Laux process. Kinetic analyses of exactly these products are not available, since in the literature mostly natural magnetites, or magnetites produced by laboratory preparation (e.g. precipitation) are used. As described before, foreign ions are also incorporated into the oxide crystal. These ions are present in the synthesis according to the Laux process, as explained in the introduction (Part I). Concluding, the conversion reactions of iron oxides, which are carried out in technical scale in the rotary kiln, are examined in this chapter with regard to known and suspected influencing variables. The focus is on thermal analysis using thermogravimetry and differential

scanning calorimetry. Since the reactions are also exothermic, as will be explained later, a precise description of the reactions in the rotary kiln is essential since the heat tone is also suspected to be massively influenced.

2 Theoretical background and current state of research

Iron oxides are a very common chemical compound on Earth, as iron is the fourth most frequent element (4.6 ma.%) in the elemental distribution of the Earth's crust, often in the form of its oxides [9]. As described earlier iron oxides have been investigated very intensively. This chapter gives an overview on the current state of research regarding the investigated compounds and the used methodology.

2.1 Description of iron oxides

There are six different known pure iron oxides [6]. These are listed in Table II - 2.1 with their trivial names and the most important basic data.

In addition to the pure oxides of iron, there are also numerous hydroxides and mixed oxide-hydroxides [6]. The structures occurring and considered in detail in this work are magnetite (Fe_3O_4) as the starting material of the process under consideration, hematite (α-Fe_2O_3) as thermodynamically stable product and, maghemite (γ-Fe_2O_3) as a metastable intermediate (transition phase) between the former two species.

Chemically or thermodynamically, the oxides can be described with a phase diagram where oxygen content and temperature [19] are plotted against each other. But in practice the characteristics and process behavior of these iron oxides also depend on the detailed properties, such as the particle size, the structure of the crystal (differences possible) and the incorporation of water and other foreign ions into the crystal lattice. The following is a detailed explanation of the iron oxides considered in this work.

Table II - 2.1: Ironoxides and their basic data [6,9,20–23]

Formula		αFe_2O_3	Fe_3O_3	γFe_2O_3	βFe_2O_3	ϵFe_2O_3	FeO
Trivial name		Hematite	Magnetite	Maghemite	-	-	Wuestite
Color		red	black	black/ brown			black
Structure		corund	invers spinell	defect spinel		defect NaCl	defect NaCl
Density	kg/L	5.26	5.18	4.87			5.9
Magne-tism		weak ferro-magnetic	ferri-magnetic	ferri-magnetic		antiferri-magnetic	antiferri-magnetic
Heat of formation	kJ/ mol	-826.2±1.25 [24]	-1116.9 [20]	-805.8±5.7 [21]			-272.0±2.1[22]
Molecular weight	g/ mol	159.7	231.5	159.7	159.7	159.7	71.8

2.1.1 Magnetite (Fe_3O_4)

Magnetite is a substance with ferrimagnetic properties (below the Curie temperature of 850K), which is also reflected in its name. It has a black colour and a crystal density of 5.18 kg/L [6]. Magnetite is a mixed oxide containing Fe^{2+} and Fe^{3+} ions in a crystal lattice of oxygen anions, which are arranged in the cubic packing, or face-centred cubic cell (fcc) [6,9,25]. It has inverse spinel structure with a Fe^{2+}/Fe^{3+} ratio of 0.5. Thus the ideal magnetite consists of 72.4 ma.% iron and 27.6 ma.% oxygen. One half of the Fe^{3+} is located in the tetrahedral vacancies (A), the other half is located in the octahedral vacancies (B) of the oxygen lattice, together with the Fe^{2+} ions [26]. A more correct notation indicating the lattice occupation is therefore [25]:

$$(Fe^{3+})_A(Fe^{3+},Fe^{2+})_BO_4 \tag{2.1}$$

Via electron mobility due to the two oxidation states of iron in octahedral position, magnetite is electrically conductive above the Verwey temperature of 117K [27–29], although this temperature is also dependent on the exact stoichiometry [30].

One unit cell of the crystal consists of 32 O^{2-} anions or 8 formula units, respectively [6], the octahedra are edge-linked, the tetrahedra are corner-linked to the octahedra, with no connection in between [27]. The distance between the oxygen anions was determined to be 8.3963 Å [6,31].

Considerable stoichiometry deviations from the ideal composition (Fe^{2+}/Fe^{3+}-ratio = 0.5) can be found for different magnetites, especially if they are produced by precipitation from aqueous solutions [6,25,27]. Stoichiometry deviations can occur in all iron oxides, which is based on their structural relationships and similarities [9]. The stoichiometry deviation can be explained e.g. by removing Fe^{2+} from the lattice, achieving the charge balance by incorporating OH^- at oxygen sites. As a result, the magnetite may contain about 2-4% water [25,32]. According to Kampeis, this fact cannot be determined via X-ray analysis, although Nestler et al. report a correlation of crystal-disorder in X-ray fine structure analysis [33]. Fleet also reports from X-ray investigations with stable structures deviating from the ideal spinel [34].

The stoichiometry deviation (denoted with δ) is explained by Huber and Cornell et al. [6] by cation deficits, which results in the following notation of non-stoichiometric magnetite [27]:

$$Fe^{3+}_{2+2\delta}Fe^{2+}_{1-3\delta}O_4 = Fe_{3-\delta}O_4 \tag{2.2}$$

From that formula the following relation of the stoichiometry deviation (δ) and the Fe^{2+}/Fe^{3+}-ratio (R) can be established:

$$\frac{n(Fe^{2+})}{n(Fe^{3+})} = R = \frac{1-3\delta}{2+2\delta} \tag{2.3}$$

Rearranging of this relation leads to the equation to calculate δ from the experimentally measurable Fe^{2+}/Fe^{3+}-ratio:

$$\delta = \frac{1-2R}{3+2R} \tag{2.4}$$

The deviation also leads to a different molar weight of the magnetite regarding to equation (2.2), which can be calculated according to the molar weights of iron and oxygen.

In order to describe the thermodynamic behavior of magnetite, a breakdown to wuestite and maghemite is used as model in this work. Thus, the mixed oxide can be written as follows:

$$Fe_3O_4 = FeO \cdot Fe_2O_3 \tag{2.5}$$

This formula is used in this work even in the case of stoichiometry deviation.

Besides the stoichiometry deviation regarding the cations, further anions can also be incorporated into the oxygen lattice, such as chloride or sulphate [6]. Clear stoichiometry is not given in general in these cases.

2.1.2 Maghemite (γ-Fe_2O_3)

Maghemite is a ferrimagnetic substance (Curie temperature is higher than the transformation to hematite) with a brownish colour and a crystal density of 4.87 kg/L [25,27]. It is metastable and transforms to hematite (α-Fe_2O_3) by further heating. Maghemite has the same crystal lattice of oxygen anions as magnetite - face centered cubic (fcc). The spinel structure of magnetite is therefore preserved, but no Fe^{2+}-ions are present and octahedral lattice sites (B) are unoccupied [6,25,27,35]. The fact is also visualized in the following molecular formula [25]:

$$(Fe_{24}^{3+})_A\left(Fe_{40}^{3+},\square_8\right)_B O_{96} \tag{2.6}$$

In this ideal maghemite, there is a tetragonal symmetry with the lattice constants a = 8.34 Å and c=3a [25,35,36]. For magnetite, also a particle size dependent structure is suspected [36]. In addition to this ideal formation, however, a statistical distribution of the vacancies can also occur and a primitive cubic lattice with a=8.34 Å is formed [25,27]. Intercalation of water is discounted to stabilize the lattice [37]. Furthermore, a solid solution of magnetite and hematite is considered in addition to maghemite. Which behaviour occurs and which products are formed during the transformation of magnetite is dependent on the pre-treatment and the particle size of the originating magnetite [38–40].

2.1.3 Hematite (α-Fe_2O_3)

Hematite is the thermodynamically stable iron oxide with red colour (particle size dependent) and a crystal density of 5.26 kg/L [6,27]. It is slightly ferromagnetic at room temperature, paramagnetic above the Curie temperature (956K) and antiferromagnetic below the Morin temperature (260K) [6,27]. In contrast to the two previous oxides, the oxygen anion lattice now crystallizes analogously to corundum in the hexagonal closest packing (hcp), with Fe^{3+} ions occupying 2/3 of the octahedral sites. Each of the three coordination polyhedra are corner-linked and two of them are face-linked.

In addition, edge linkage occurs [6,27]. Hematite can also form defective structures and e.g. create OH^- ions with charge balance via Fe^{3+} vacancies [6].

2.1.4 Conversion Reactions

The described iron oxides can be produced via thermal treatment or chemical reaction and furthermore are convertible into each other. The reaction conditions are decisive for product is formed. This is one of the central issues, e.g. in the economically very important metallurgy, which deals with the reduction route of iron oxides to metallic iron. In this thesis, however, the focus is on oxidation reactions, in particular the reaction of magnetite (produced in the industrial Laux process) to maghemite and haematite. This chapter provides an overview for the considered reactions from literature with focus on the kinetic data.

2.1.4.1 Magnetite to Maghemite

The reaction from magnetite to maghemite generally proceeds according to the following equation:

$$4\,Fe_3O_4 + O_2 \rightarrow 6\,\gamma Fe_2O_3 \tag{2.7}$$

Using this reaction equation with its stoichometric coefficients and the molar weights of the species from Table II - 2.1 the specific mass increase Δm_{rel} can be calculated to:

$$\Delta m_{rel} = \frac{\left(6 \cdot M_{Maghemite}\right)}{4 \cdot M_{Magnetite}} = 1.0348 \tag{2.8}$$

Therefore, the mass of ideal magnetite increases due to oxidation by the uptake of oxygen from the gas phase by 3.48%. However, as explained in chapter 0, magnetite is not always present with its ideal Fe^{2+}/Fe^{3+} ratio of 0.5. In order to generalize equation (2.7), the oxidation and reduction are separately considered. Oxdiation of Fe^{2+} in a non stoichiometric magnetite (equation (2.9)) and reduction of oxygen (equation (2.10)) result in the total reaction equation (2.11) for oxidation.

$$(1-3\delta)\,Fe^{2+} \rightarrow (1-3\delta)\,Fe^{3+} + (1-3\delta)\,e^- \tag{2.9}$$

$$\frac{1}{2}O_2 + e^- \rightarrow \frac{1}{2}O_2^- \tag{2.10}$$

$$(1-3\delta)\,Fe^{2+} + \frac{1-3\delta}{2}O_2 \rightarrow (1-3\delta)\,Fe^{3+} + \frac{1-3\delta}{2}O_2^- \tag{2.11}$$

Incorporating this knowledge in the overall reaction (equation (2.7)) the stoichiometry can be generalized to:

$$4\,Fe_{3-\delta}O_4 + 2(1-3\delta)\,O_2 \;\rightarrow\; 2(3-\delta)\,Fe_2O_3 \tag{2.12}$$

Whether the reaction takes place and which conditions influence the formation of the intermediate maghemite has been investigated by several authors. It is related to the reaction conditions (velocities), the pretreatment and production of the magnetite (e.g. tempering, ball milling, etc.) and the particle size [37–39,41]. An increasing size of the magnetite particles has an adverse effect on the oxidation, leading to the fact that if the particle diameter exceeds 0.5 nm, complete oxidation to maghemite is no longer possible without the formation of hematite [42–44].

The mechanism of the reaction is based on the diffusion of iron cations to the outside, since the radii of the oxygen anions are larger and form the crystal lattice. The mobility of iron cations is provided by defects in the lattice and via free octahedral/tetrahedral vacancies [27,45]. The charge balance is guaranteed via diffusion of electrons to the outer phase interface, where they are taken up by the oxygen in its reduction [40]. Oxygen anions then enlarge the crystal from the outside, as visualized in Figure II - 2.1.

A balance for both phases provides the progress of reaction as follows. Fe^{3+} diffuses through the maghemite-phase and is added to the crystal surface with oxygen from the gas phase according to [27]:

$$Fe^{3+} + \frac{3}{4}O_2 + 3e^- \rightarrow \frac{3}{8}Fe_{8/3}\square_{1/3}O_4 \tag{2.13}$$

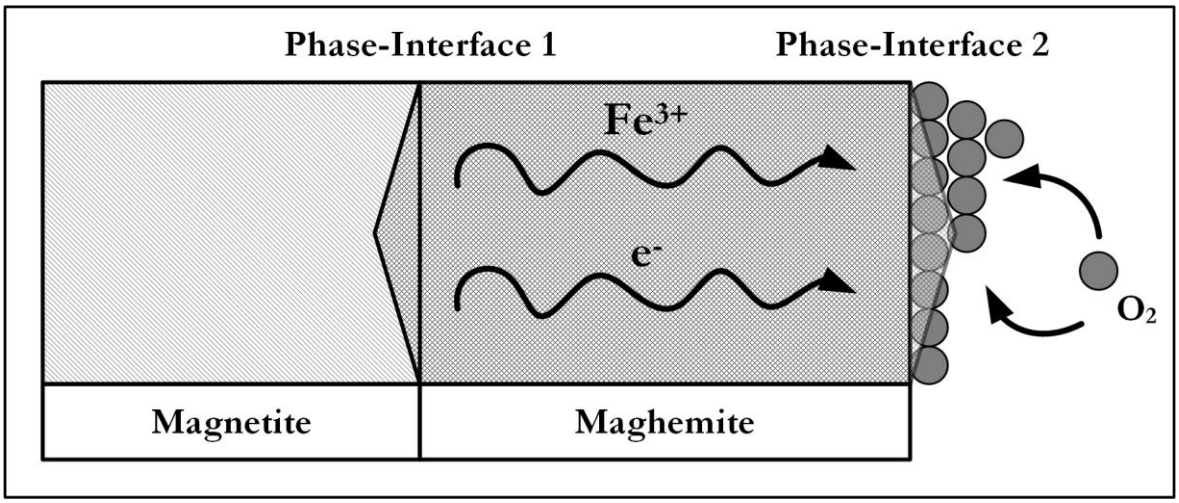

Figure II - 2.1: Sketch of the oxidation mechanism according to Huber [27]

In the magnetite phase the diffused Fe^{3+} is removed and maghemite is formed [27]:

$$3Fe_3O_4 \rightarrow 3Fe_{8/3}\square_{1/3}O_4 + Fe^{3+} + 3e^- \tag{2.14}$$

According to both equations, the diffusion of one mole of Fe^{3+} results in 27/8 moles of γ-Fe_2O_3. 1/9 of this maghemite is formed at the surface of the original magnetite-crystal, 8/9 of the maghemite phase is formed in the inner crystal [27].

Besides the mechanism, the reaction has to be considered thermodynamically. According to Hess's law [23] the reaction enthalpy $\Delta_R H$ can be calculated from the standard heats of formation ($\Delta_f H^0$) from the products and educts, which have been given in Table II - 2.1, as well as stoichometric coefficients from equation (2.7). Oxygen is delivered elementary as O_2 with a heat of formation of 0 kJ/mol, therefore the calculation gives:

$$\Delta_R H = \frac{\left[\left(6 \cdot \Delta_f H^0(Maghemite)\right) - \left(4 \cdot \Delta_f H^0(Magnetite)\right)\right]}{4} = -91.8 \frac{kJ}{mol} \tag{2.15}$$

According to the rules of thermodynamics, the oxidation reaction is decomposeable into two partial reactions, because magnetite can also be considered as $FeO \cdot Fe_2O_3$ (chapter 0). Since the crystal structure of magnetite and maghemite are equal, the following applies to the Fe^{3+} part:

$$\gamma - Fe_2O_3 \rightarrow \gamma - Fe_2O_3 \tag{2.16}$$

Thus no transition of state takes place for the Fe_2O_3 in the oxidation reaction. The second part of the mixed oxide is considered as wustite (FeO) and reacts according to:

$$4\,FeO + O_2 \rightarrow 2\,\gamma - Fe_2O_3 \tag{2.17}$$

In order to complete the understanding of the oxidation reaction, it has to be considered by means of reaction kinetics. Sidhu et al. found the conversion at 220°C to be completed in 50-60 minutes and no further changes took place afterwards. At room temperature (20°C), no reaction to maghemite took place even within one week [18]. In contrast to that, Feitknecht et al. [40] found that samples of synthetic magnetite from aqueous solution continue to oxidize even at room temperature. Sidhu found diffusion coefficients of Fe^{3+} in the reaction to maghemite of 0.8-2.1*10^{15} cm^2/s.

Huber performs oxidations on tempered wet-chemically synthesized magnetites and determines the isothermal kinetics according to the Jander equation. He determined values of: 89.87/139.47/172.3 kJ/mol for particle sizes of 100/200/350 nm and propagated a linear dependence of the activation energy on the particle size [27]. Furthermore, he found no dependence of the oxidation rate on the oxygen partial pressure for the two smaller magnetites. He further shows that the preparation route of the magnetite has massive influence on the reaction/oxidation behaviour of the material. David et al. also observed this fact and assume an influence of e.g. water that has been incorporated into the crystal [37].

Gillot et al. [46] deliver values in oxidation kinetics for various particle/crystallite sizes. They propose that the creation of y-Fe_2O_3 depends on crystallite size. Below 500 nm y-Fe_2O_3 will be created, above 1000 nm α-Fe_2O_3 is produced. In between that size range the kinetics is divided into two steps from magnetite to hematite and maghemite as intermediate. Egger et al. and Feitknecht et al. also propose the existence of a particle size dependency, but they determine the critical particle size (where y-Fe_2O_3 is not stable) to 300 nm [39,44].

Until today, kinetic data on this reaction has been obtained by many authors. The analytical techniques that have been used are:

- Thermogravimetry (TG)
- In situ X-ray diffraction (XRD)
- Differential thermal analysis (DTA)

Kinetic analyses on the oxidation were carried out by Gillot et al. [46] and Huber [27], who performed isothermal analyses and evaluated them using the Arrhenius equation. Gillot found a logarithmic dependence on particle size, Huber a linear one. Egger et al. also investigated the oxidation isothermally and determined characteristic transformation temperatures by means of DTA [44]. Sidhu analysed the oxidation kinetics by observing the Fe^{2+} content [18]. David et al. also determined transformation temperatures in the range 180-580 °C (mostly 180-300°C), but did not publish particle sizes or BET-surfaces [37]. Przepiera et al. have performed dynamic TG-experiments and provided kinetics according to the AEG-A3 model after analysis by the Coats-Redfern method [47]. All data is presented in Figure II - 2.2. Gallagher has performed isothermal experiments and gives an activation energy of 115.8 kJ/mol (1.2eV), but without determining a particle size [48].

The data clarifies that Huber, Sidhu et al. and Gillot et al. have achieved similar results, at least in the same magnitude. Egger determined transformation temperatures, whose principle progression with the particle size corresponds to those of the activation energies.

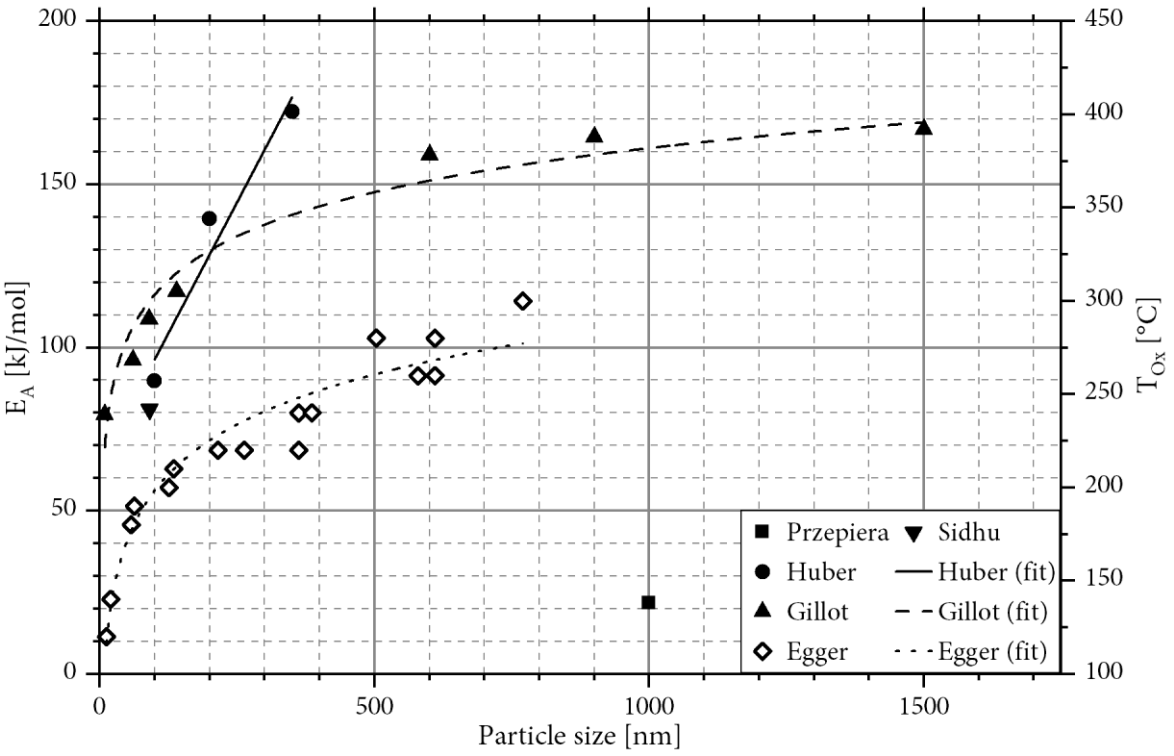

Figure II - 2.2: Kinetic data for oxidation reaction from various authors [18,27,44,46,47] in dependency of particle size. Filled signs indicate activation energies (E_A), hollow signs represent oxidation temperatures (T_{Ox})

Przepiera et al. chose a different evaluation method and published a significantly lower activation energy. Sanders et al. state that the activation energies found are massively dependent on the evaluation method [49] and have used many different evaluation methods. They used magnetite with a sieve fraction of 74 microns and published a mean activation energy of 120 kJ/mol.

Monazam et al. [50] have carried out loop-combustion experiments at high temperatures 750-900°C. They provided an activation energy of 53.6 ±3.6 kJ/mol for 200 µm sieve fraction. The sieve fraction here is most likely not comparable to the crystallite size by BET or TEM determination. The kinetics has been analyzed under non-isothermal conditions.

2.1.4.2 Maghemite to Hematite

The second reaction proceeds formally according to the following reaction equation. The equation indicates that there is no change in the mass during reaction.

$$\gamma - Fe_2O_3 \rightarrow \alpha - Fe_2O_3 \tag{2.18}$$

It is therefore no "real" chemical reaction with several reactants, but a physical transformation of the crystal lattice. This effect demonstrates that higher temperatures or activation energies are required to enable the mobility of ions in the lattice. However, it also increases complexity in the analysis of the process. The following properties have been used to observe the reaction-progress:

- X-Ray (changing lattice constants) [47,51,52]
- Mössbauer-spectroscopy [27]
- Magnetism [53]
- DTA/DSC (thermal reaction impact) [47,49]

The mechanism of the reaction is complex and Feitknecht et al. report that there is a dependency on crystallite size [39,44,54]. For small particles (BET > 4m²/g) the recrystallisation takes place in a single step after oxidation. Magnetites with a medium crystal size (BET between 4 and 2 m²/g) oxidise to a mixed phase ($Fe_{[3-n/3]}O_4$) and disproportionate to magnetite and hematite afterwards. The remaining magnetite will directly oxidise to hematite at higher temperatures. The large magnetite crystals (BET < 2 m²/g) directly oxidise to hematite and no maghemite is formed in between. Colombo stated that the mechanism is dependending on the crystal structure the existing nuclei of maghemite and hematite in the magnetite material [41].

Besides the mechanism the thermodynamics of the reaction is analyzed analogously to the oxidation reaction with Hess's law and the standard heats of formation:

$$\Delta_R H = \Delta_f H^0(Hematite) - \Delta_f H^0(Maghemite) = -20.4 \frac{kJ}{mol} \tag{2.19}$$

Thus, the recrystallisation is an exothermic process. Since from one mole of magnetite 1.5 moles of maghemite are formed considering both reaction steps the reaction enthalpy is -30.6 kJ/mol based on magnetite as starting material.

The last important point in reaction description is the kinetic investigation. In his work, Schimanke found that the transformation from metastable maghemite to hematite is kinetically determined and provides a half-life for the transformation at room temperature of 10^{16} years. Furthermore, he determined a dependence of the transformation kinetics on the crystallite size towards faster velocities with smaller crystallites [52,55]. Feitknecht et al. [42] also conclude that the kinetics becomes slower with larger crystallites, since the crystal lattice, which has to be rearranged starting from nuclei, is larger. Additionally, they state that ions from impurities as e.g. chloride have an inhibiting effect, since they found significantly higher conversion temperatures with magnetites from chloride. The stated reason is that larger ions make lattice contraction (see lattice constants) more difficult during lattice rearrangement.

Besides direct kinetic considerations, the conversion temperature (T_{con}) can be estimated from DTA-measurements. Egger et al. report that no dependency of conversion temperature from crystallite size could be found [44]. Grimm et al. stated conversion temperatures of 370-600°C in air with increasing T_{con} for increasing particle sizes and provide the hint of influencing impurities for their flame pyrolysis products [56].

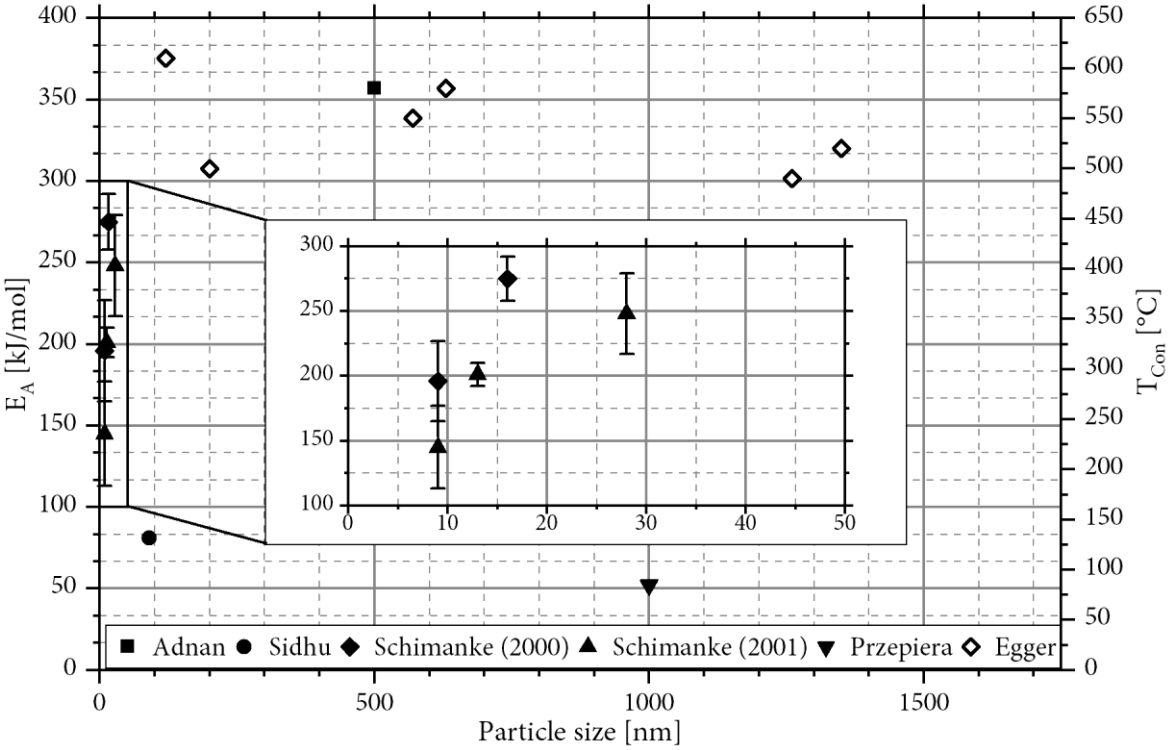

Figure II - 2.3: Kinetic data for conversion reaction from various authors [18,44,47,52,53,55] in dependency of particle size. Filled signs indicate activation energies (E_A), hollow signs represent conversion temperatures (T_{con})

Adnan et al. describe, that the transformation is thermally activated and that the energy barrier for conversion is lower at (very) high pressures (e.g. at oceanic ground) [53]. They found an activation energy of 357 kJ/mol (3,7 eV) with a particle size of 500nm for a BASF (FT26) product. The visualization of the literature data in Figure II - 2.3 clearly shows that the kinetic data on the recrystallization is not consistent. As reported earlier no dependency to particle size is observable. If there are any reasons for the fluctuation in the activation energy, they are not fully understood yet.

2.1.4.3 Macrokinetics

The information and data summarised in the previous two chapters dealt with the physicochemical properties of the material and their changes during the reactions. The focus was on the microstructures in the crystals and the crystallites. For the considered process in industrial scale, it should also be introduced, that reactions of solids can exhibit macrokinetics if the particles build aggregates which are bigger in orders of magnitude compared to the crystallites considered so far.

Iron oxides are often processed to pellets of various compositions as ores for utilisation in blast furnaces etc. with pellet diameters in the range of a few centimeters [57]. Contrary to the statements

in chapter 2.1.4.1 a functionality of the reaction rate from e.g. oxygen partial pressure can be observed and the porosity of these pellets is also decisive [58,59]. The shrinking core model (see also Levenspiel [60]) has been applied by Davis [61] in the description of that case. This model assumes a macroscopic sphere in which a growing product layer is formed by reaction from the surface to the inner material sphere, which serves as an inhibiting barrier. Davis could show that diffusion control through the formed hematite layer prevails, which results in the following description of the reaction rate [60–62]:

$$\frac{dr_c}{dt} = \frac{-4D_{eff} \cdot c_{O_2}}{\rho_c \left[r_c \left(1 - \frac{r_c}{R}\right) + \frac{D_{eff}}{k} \right]} \tag{2.20}$$

The equation describes the reaction rate as a reduction of the reactant core r_C in the particle as a function of the gas concentration c_{O2}, and the effective diffusion coefficient through the product layer D_{eff}, as well as the mass transfer coefficient from the gas to the sphere k. Pictures of such spheres with unreacted cores are shown e.g. by Tang et al. [63]. It can be observed, that sintering processes influence the diffusion control and thus the speed of the reaction, which has been investigated e.g. by Sandeep Kumar et al. [64]. In addition to the gas concentration, temperatures and heating rates can also impact on the macrokinetics. However, the entire (complex) material behaviour must be taken into account, which is in turn influenced by impurities, etc. As known from the previous chapter, these points affect the reaction rate r_C in microkinetics as well.

2.2 Thermal Analysis

Thermal analysis in general includes all measurements of physical sample-properties as a function of its temperature, or the response of a material exposed to specific temperatures and temperature changes [65–67]. There are a variety of instruments available to perform thermal analysis depending on the properties investigated. For example, in magnetite analysis, the magnetic property could also be chosen for analysis using e.g. thermomagnetometry [68].

Thermal analysis is commonly used in the field of polymeric substances and materials, but can also be used for various materials or inorganic substances such as in geology [69]. In this work, thermogravimetry (TG) and dynamic differential scanning calorimetry (DSC) are used as main instruments and techniques. Thus, these methods are presented in more detail below.

2.2.1 Thermogravimetry (TG)

In thermogravimetry, basically the mass of the sample is observed during the temperature treatment, i.e. against temperature or time [65]. Consequently, processes with an exchange of mass between the sample and the surrounding atmosphere can be analysed [27]. It is irrelevant whether the processes are based on physical (desorption, etc.) or chemical (oxidation, etc.) nature.

The following equipments are essentially required to perform the analyses and record the data [66]:

- Analytical balance with high sensitivity
- Furnace
- Temperature measuring device
- Gas purging system
- Control and data aquisition unit

Various systems from Netzsch were used in this work, a "Netzsch TG 209 F1 Libra" and a "Netzsch TG 209 cell" with a "TASC 414/3" temperature controller. Out of the generally feasible sample arrangements "side-loading" and "bottom-loading" [65] these devices use the third type, namely "top-loading". The weighing mechanism works with electromagnetic compensation. The principal measurement set-up of both TGA types is presented in Figure II - 2.4.

The sample is placed in a furnace chamber and connected to the weighing mechanism located underneath the furnace. The weighing mechanism is operated under inert gas atmosphere (N_2) during measurements. The sample chamber can be purged with two different gases in a controlled manner, with a flow direction from the bottom to the top. Different gases, each with different mass or volume flows, can be used to set the atmosphere. Furthermore, the sample chamber can be evacuated, gases can be switched on or off and changes in volume flows during the measurement are possible.

During each experiment, the time, temperature and mass are recorded as measured values. In addition, the TG209 F1 Libra device calculates a so-called ‘c-DTA’, where thermal effects and their character (exothermic or endothermic) are recorded in accordance with the DTA analysis [70]. This also includes (re-)crystallisation processes, for example. From the TG-results, the progress of the mass with the temperature is obtained. From this in turn, absolute mass losses or increases can be calculated and the progress of mass (m_t) and also conversion X with the time t can be analyzed via [65]:

$$X = \frac{m_t - m_0}{m_\infty - m_0} \tag{2.21}$$

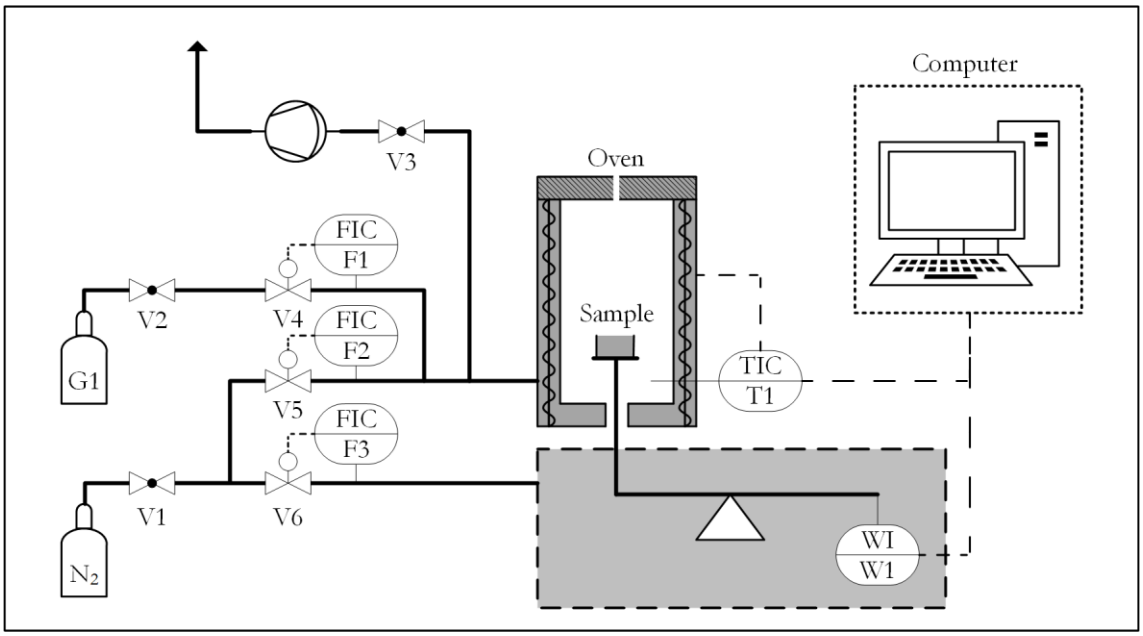

Figure II - 2.4: Sketch of the principal functionality of the used TG-apparatus according to [70,71]

2.2.2 Differential Scanning Calorimetry (DSC)

The differential scanning calorimetry (DSC) essentially measures the differences in heat flux to a sample and to a reference while both materials are subjected to a temperature program [66]. DSC is a caloric method and the most widely used thermal analysis technique nowadays [65,66], although it was developed by Perkin-Elmer only in 1963. All processes with thermal effects can be investigated, e.g. phase transitions, crystallisations, glass transitions etc. [65] but also endothermic or exothermic reactions.

With the heat flux DSC, which was developed based on the DTA, and the power compensation DSC, there are two basic methods [65]. The Netzsch device used in this work, a "DSC 204 Phoenix", works according to the heat flux DSC principle. Therefore, this method is explained in more detail. Instead of the cylinder-type and turret-type measuring arrangements [72], which are also possible, the Netzsch DSC uses a disk-type measuring arrangement. The following Figure II - 2.5 presents the schematic design of the DSC.

Reference- and sample-crucible are positioned symmetrically onto a furnace or in general a temperature controllable basement. The two crucibles are separated from the furnace via a thermoelectric disc (constantan) to this basement and temperature sensors are integrated into the basic sample positions (cromel disc) [65,72].

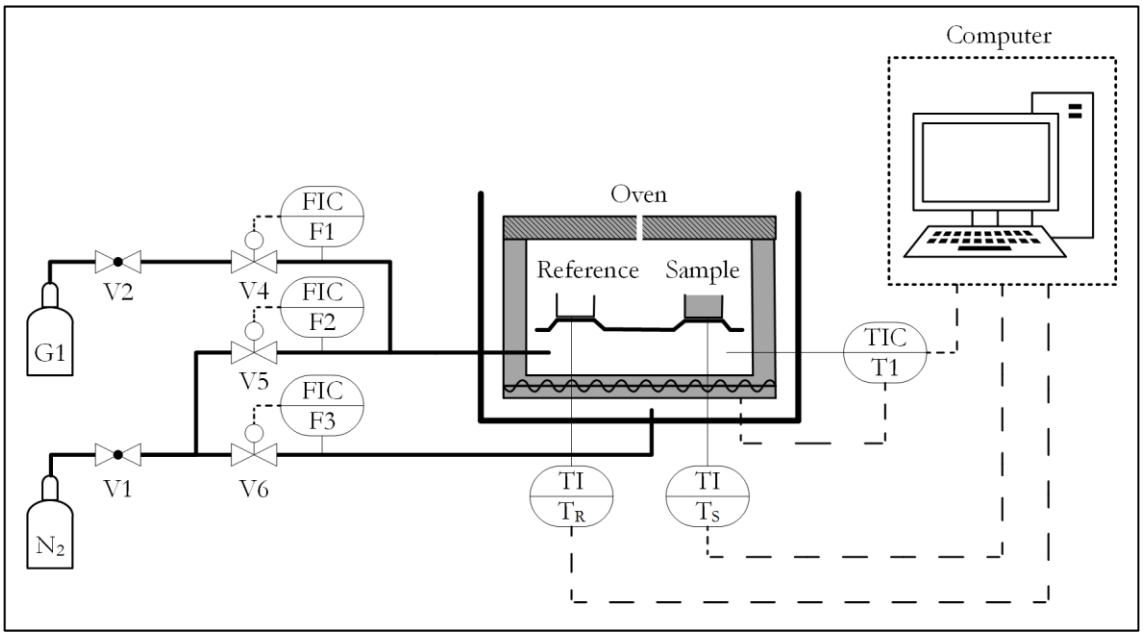

Figure II - 2.5: Sketch of the principal functionality of the used DSC-apparatus [65,73]

Since the heat flow is no directly measurable quantity, an indirect technique has to be used. In general this is a temperature difference ΔT between sample (T_S) and reference (T_R), which is proportional to the heat flux $\dot{Q}$ [74]:

$$\dot{Q} \propto \Delta T = T_S - R_R \tag{2.22}$$

The constant of that proportionality is measured in a calibration run. Different possible crucible materials can be utilized and different atmospheres can be supplied to the sample room via the gas supply [65]. The following parameters affect the DSC-measurements [75]:

- Heating/cooling rate, start and end temperature
- Sample mass
- Gas atmosphere and volume flow
- Crucible material and size

Various data can be derived from the measurements (also depending on the measuring mode). Among them are [74]: Heat capacity, glass transition temperature, heat of fusion, thermal fingerprinting of materials, but also reaction kinetics and enthalpy [76]. In order to calculate the reaction progress Figure II - 2.6 presents a typical DSC-signal.

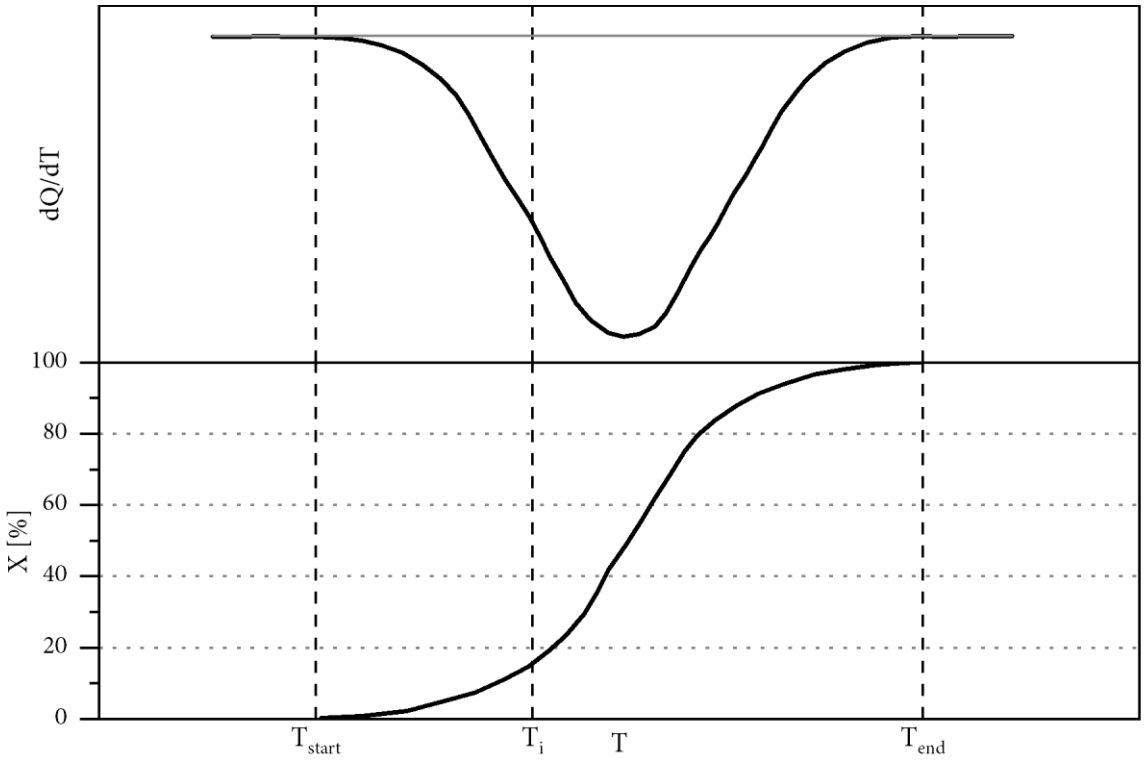

Figure II - 2.6: a: Exemplary diagram of reaction measurement with heating effect; b: calculated conversion; according to [76]

Assuming that the peak in the DSC-signal is evoked by a chemical reaction, the heat of reaction or reaction enthalpy ΔH_R can be calculated with non isothermal conditions to [76]:

$$\Delta H_R = \int_{T_{start}}^{T_{end}} H_S(T) - H_B(T)\, dT \tag{2.23}$$

H_S is defined as sample signal and H_B denotes the baseline signal. The area between baseline and measured DSC-signal therefore is a measure of the reaction enthalphy The conversion X can be calculated for non isothermal conditions by [76,77]:

$$X = \frac{\int_{T_{Start}}^{T} H_S(T) - H_B(T)\, dT}{\int_{T_{start}}^{T_{end}} H_S(T) - H_B(T)\, dT} \tag{2.24}$$

Summarizing the equation in words, the conversion is the fraction of current peak area to total peak area. The integration of the measured data is performed via numerical integration with the trapezoidal method [78]:

$$\int_a^b f(x)\,dx = \frac{1}{2}\sum_{i=a}^{b}\left[\left(f_i(x) + f_{i+1}(x)\right)\cdot(x_{i+1} - x_i)\right] \tag{2.25}$$

2.3 Reaction kinetics

Magnetite and maghemite are metastable as described in chapter 2.1 and are converted into the thermodynamically stable hematite (α-Fe_2O_3) in the presence of oxygen and at sufficiently high temperatures. In addition to the thermodynamic description of a reaction, i.e. whether it takes place, in which direction it takes place, under which conditions it takes place and which heat tone it exhibits, it is very important to have information about the speed of reactions or the reaction kinetics.

Thus, in the description of chemical reactors the reaction rate(s) of the reaction(s) and related processes taking place are of central importance. In this context, the reaction kinetics generally describes the change of substances with time due to chemical reaction, e.g. by the amount of substances (n) formed or consumed per time-unit (t). The reaction kinetics is a mathematical description of the reaction rate of a species (i). This is represented mathematically by means of a differential equation to describe the reaction rate (r), which is generally a function of the reaction conditions in the reactor [60]:

$$r_i = \left(\frac{1}{\nu_i}\right)\cdot\frac{dn_i}{dt} = \frac{dX_i}{dt} = f(conditions) \tag{2.26}$$

For standardization purposes, the stoichiometric coefficient (ν) is taken into account. X indicates the conversion of the reactants, which is defined as follows [79]:

$$X_i = \frac{n_i^0 - n_i}{n_i^0} \tag{2.27}$$

In order to describe this reaction rate as a function of the reaction conditions, a rate law is established in which the relevant conditions are included. For fluid-fluid reactions, these are usually concentrations or (partial) pressures [60]. For solid reactions, the model or mechanism is usually a function of the conversion (f(X)) itself. In addition, temperature is an important influencing factor.

Thus, a description of the rate constant k as a function of temperature (k(T)) is also considered. Following, the general rate law for solid reactions is [80,81]:

$$\frac{dX}{dt} = k(T) \cdot f(X) \tag{2.28}$$

k(T) is described with a pre-exponential factor k_0 and an activation energy E_A according to the Arrhenius-law, which then results in [80,81]:

$$\frac{dX}{dt} = k_0 \cdot e^{-\frac{E_A}{RT}} \cdot f(X) \tag{2.29}$$

This is the basis for all further calculations and analyses on kinetics. The parameters in that equation (k_0, E_A and f(X)) are called the kinetic triplet describing the reaction [81]. In the following, reaction mechanisms are introduced and afterwards the analysis of experimental data according to different methods is presented. An overview of the multitude of options in the analysis is provided by Khawam et al. [77] in the form of a flow chart. Here, the isothermal and non-isothermal (according to Coats-Redfern) model-fitting methods are utilized.

2.3.1 Reaction models/mechanisms

There are numerous descriptions of the reaction mechanisms or rate-laws (f(X), see equation (2.29)), which have been developed in the past and are known from literature. They are given either as differential or in the integrated form (g(X), explanation see chapter 2.3.2). All equations can be condensed to a composite description [80]:

$$g(X) = X^m(1-X)^n(-\ln(1-X))^p \tag{2.30}$$

The constants m, n and p are defined by the underlying models. Some of these models are based on chemical reactions in homogenous fluids, which are usually described according to reaction orders proportional to the reactant concentrations or products [80]. Furthermore, there are nucleation models assuming spontaneous nucleation with subsequent growth, which is progressing according to different models. Growth can be described e.g. by the power laws or according to the growth models proposed by Avrami and Eroveef [80]. Diffusion models are based on considerations of

diffusion in heterogeneous reaction systems, where reactants have to pass a product layer [80]. Geometric contraction models assume nucleation from the surface of the crystal to the interior, depending on the present geometry [80]. All models used in this work are listed in Table II - 2.2 in integral (g(X)) form.

Table II - 2.2: Kinetic models of rate equations [80,82]

No	Name	Integral form $g(X)$
	Reaction order models	
1	Zero order (F0)	α
2	First order (F1)	$-\ln(1-X)$
3	Second order (F2)	$(1-X)^{-1}-1$
4	Third order (F3)	$\frac{1}{2}[(1-X)^{-2}-1]$
5	One third order (F1/3)	$1-(1-X)^{\frac{2}{3}}$
6	Three quarters order (F3/4)	$1-(1-X)^{\frac{1}{4}}$
7	One and a half order (F3/2)	$(1-X)^{-\frac{1}{2}}-1$
	Nucleation models	
8	Power law 3/2	$X^{\frac{3}{2}}$
9	Power law 1/2	$X^{\frac{1}{2}}$
10	Power law 1/3	$X^{\frac{1}{3}}$
11	Power law 1/4	$X^{\frac{1}{4}}$
12	Exponential law	$\ln(X)$
	Sigmoidal rate equation	
13	Avrami-Erofeev A1	$-\ln(1-X)$
14	Avrami-Erofeev A3/2	$[-\ln(1-X)]^{\frac{2}{3}}$
15	Avrami-Erofeev A2	$[-\ln(1-X)]^{\frac{1}{2}}$
16	Avrami-Erofeev A3	$[-\ln(1-X)]^{\frac{1}{3}}$
17	Avrami-Erofeev A4	$[-\ln(1-X)]^{\frac{1}{4}}$
18	Prout-Tomkins	$\ln\left(\frac{X}{1-X}\right)$

	Geometrical contraction models	
19	Contracting area (R2)	$1-(1-X)^{\frac{1}{2}}$
20	Contracting volume (R3)	$1-(1-X)^{\frac{1}{3}}$
	Diffusion models	
21	One dimensional (D1)	X^2
22	Valensi equation (D2)	$X+(1-X)\cdot\ln(1-X)$
23	Jander-equation (D3)	$\left(\left(1-(1-X)\right)^{\frac{1}{3}}\right)^2$
24	Ginstling-Brounshtein (D4)	$1-\frac{2}{3}X-(1-X)^{\frac{2}{3}}$
25	Zhuravlev, Lesokin, Tempelman (D5)	$\left((1-X)^{-\frac{1}{3}}-1\right)^2$
26	Anti-Jander (D6)	$\left((1+X)^{\frac{1}{3}}-1\right)^2$

Besides these models in literature even more approaches are stated e.g. by Georgieva et al. [82].

2.3.2 Isothermal kinetic investigation

Based on equation (2.29), rearrangement of the differential equation for the isothermal case by separating the variables and subsequent integration delivers:

$$\int_0^X \frac{dX}{f_i(X)} = \left(k_0 e^{-\frac{E_A}{RT}}\right)_i \cdot \int_0^t dt \tag{2.31}$$

The index i describes the chosen model from the above stated equations (see chapter 2.3.1), which can now be used in equation (2.31). With the definition of the integrated rate-law of:

$$\int_0^X \frac{dX}{f_i(X)} = g_i(X) \tag{2.32}$$

the equation (2.31) can be linearized to following expression [83,84]:

$$g_i(X) = \left(k_0 e^{-\frac{E_A}{RT}}\right)_i \cdot t \tag{2.33}$$

This is a linear equation when plotting g(X) versus time with the rate constant as slope, since the temperature T is constant (isotherm). Which model is suitable has to be determined by comparing the regression coefficients of the linear fits (model fitting method) from experimental data with different tested models (i) [83,84]. However, e.g. Gomez-Villacieros et al. noted, that the regression coefficients differ only very slightly (in isothermal analyses) and therefore a selection of the correct model with this methodology is associated with difficulties [85].

Performing the analysis at different constant temperatures leads to different slopes as result from equation (2.33) (k(T)). The Arrhenius equation is linearized by taking the logarithm [83]:

$$\ln\big(k(T)\big) = \ln(k_0) - \frac{E_A}{R} \cdot \frac{1}{T} \tag{2.34}$$

By plotting ln(k(T)) against 1/T, the Arrhenius parameters k_0 (intersect) and E_A (slope) can be determined from the slopes according to equation (2.34) using linear regression. Again there is criticism on the method, as hidden assumptions are incorporated in the derivation e.g. the rate equation or the activation energy is constant over the entire reaction-progress [86]. However, since this method is widely used and the accuracy is sufficient in practice, the kinetic parameters are sufficiently determined with isothermal analysis.

2.3.3 Non-Isothermal kinetic investigation

In this work, a constant heating rate β is always used in non-isothermal analyses, which means [81]:

$$\frac{dT}{dt} = const. = \beta \tag{2.35}$$

Equation (2.29) (see chapter 2.3) can therefore be transformed into a non-isothermal rate-law [80,81]:

$$\frac{dX}{dt} \cdot \frac{dt}{dT} = \frac{dX}{dT} = \frac{k_0}{\beta} e^{-\frac{E_A}{RT}} \cdot f_i(X) \tag{2.36}$$

Analogously to the procedure in isothermal analysis, the equation can be converted by separating the variables with subsequent integration [77,81]:

$$g_i(X) = \frac{k_0}{\beta} \cdot \int_0^T e^{-\frac{E_A}{RT}} \cdot dT \tag{2.37}$$

In contrast to the isothermal investigation now the Arrhenius-expression has to be considered in the integral, since the temperature is no constant anymore. The integral can be substituted to [77,81,87]:

$$g_i(X) = \frac{k_o E_A}{\beta R} \cdot \int_x^\infty \frac{e^{-x}}{x^2} dx = \frac{k_o E_A}{\beta R} \cdot p(x) \tag{2.38}$$

Now the temperature integral (p(x)), which has no exact analytical solution, must be approximated by suitable methods. For example Doyle proposes a linear approximation via the logarithm of p(x) [88,89]. Furthermore, series approximations are proposed, e.g. by the Schlömilch series [90] or by Senum and Young with rational series approximation [91]. In addition to the integral approximation method, there is also the possibility of performing non-linear temperature programmes in the experiment, which enable analytical integration [92].

2.3.4 Coats-Redfern method

The most common method to estimate p(x) in practice is a technique named after Coats and Redfern (Cai et al. determine 100 citations from 2002-2008 only in the field of coal combustion [93]). Coats and Redfern used asymptotic series expansion for the estimation of the temperature integral and equation (2.38) becomes [94,95]:

$$g_i(X) = \frac{k_0 R T^2}{\beta E_A}\left[1 - \frac{2RT}{E_A}\right] e^{-\frac{E_A}{RT}} \tag{2.39}$$

This equation can now be linearized by rearranging and taking the logarithm. A division by T^2 and insertion of the mean temperature T_m of the investigated temperature range delivers [77]:

$$\ln\left(\frac{g_i(X)}{T^2}\right) = \ln\left(\frac{k_0 R}{E_A \beta}\left[1 - \left(\frac{(2RT_m)}{E_A}\right)\right]\right) - \frac{E_A}{R} \cdot \frac{1}{T} \tag{2.40}$$

A plot of $\ln(g(X)/T^2)$ against 1/T yields in a straight line if the rate-law g(X) is correct or appropriate. The Arrhenius parameters can be determined from the slope and the intercept of linear regression. This method is also criticized for its accuracy in the approximation of the temperature integral [93,96,97] and it is not recommended to use the method. However, its usage is wide spread, it can be applied with manageable effort and Cui et al. show, that the deviations for the activation energies in coal combustion are less than 10% [93].

3 Experimental

In the experimental part of the reaction investigation different magnetites are analyzed to investigate the impact of the magnetite characteristics on the conversion reactions. At first, different magnetites have been synthesized as samples, and characterized afterwards. Following, the conversion reactions are analyzed with thermal methods.

Additionally, three samples produced industrially with the Laux-process (LXS-A, LXS-B and LXS-C) as well as one commercial magnetite (COM-A) of unknown origin are tested parallel to the synthesized products.

3.1 Synthesis of Magnetites

The synthesis of magnetite can be performed in many different techniques and based on various precursor materials [6,98]:

- Via precipitation in aqueous solution:
    - From raw or scrap iron dissolved in acid [99]
    - From dissolved Fe^{2+} salts as precursor and following oxidation [98]
- Via solvo-thermal synthesis [100]
- Via flame pyrolysis of aqueous solutions containing iron salts
- Via reduction of maghemite/hematite with e.g. CO at high temperatures [101]

For the reasons mentioned in the introduction, the preparation in this thesis is performed via precipitation of aqueous solutions of different Fe^{2+}-salts (sulphate, chloride and a 50/50 mixture of both) in order to simulate the properties of the Laux magnetite as good as possible. The effort to perform the Laux-synthesis in laboratory scale was too high. The procedure is similar to a description given by Feitknecht et al. [42] and Huber [27], who dissolve Fe^{2+}-salts, namely iron(II)-sulfate and iron(II)-chloride. The solution is precipitated with ammonia afterwards and iron(II)-hydroxide is created [42].

$$FeCl_2 + 2\,H_2O + 2\,NH_3 \rightarrow Fe(OH)_2 + 2\,NH_4Cl \quad (2.41)$$

$$FeSO_4 + 2\,H_2O + 2\,NH_3 \rightarrow Fe(OH)_2 + (NH_4)_2SO_4 \quad (2.42)$$

2/3 of these iron(II)-hydroxides are oxidized with KNO_3-solution as oxidizing agent afterwards as this procedure ensures only the formation of magnetite as highest oxidation level [102]. Other agents as e.g. H_2O_2 prefer the formation of Maghemite [103].

$$9\,Fe(OH)_2 + 2\,KNO_3 \rightarrow 3\,(FeO \cdot Fe_2O_3) + 2\,NO + 2\,KOH + 8\,H_2O \quad (2.43)$$

The oxidation and reduction reactions can be denoted as follows:

$$9\,Fe(OH)_2 \rightarrow 3\,(FeO \cdot Fe_2O_3) + 6\,e^- + 6\,H^+ + 6\,H_2O \quad (2.44)$$

$$2\,NO_3^- + 6\,e^- + 4\,H^+ \rightarrow 2\,NO + 4\,OH^- \quad (2.45)$$

It is known from literature, that the process parameters as dosing speed, stirring speed, temperature etc. influence the crystal sizes formed [104]. Furthermore, it is known that the reaction temperature and the pH-value determine [103], whether and to what extent magnetite is formed at all. In general, no magnetite is formed below pH=9. This pH-limit is in turn temperature-dependent and temperatures >75°C should be present as determined by Simon and Emons [105].

In many papers the synthesis is conducted under strict oxygen exclusion (as e.g. in [27]). But especially in industrial scale this is difficult, as all liquids would have to be degassed. Simon and Emons [106] report, that the presence of atmospheric oxygen only leads to an oxidation of $Fe(OH)_2$ and this is converted into additional magnetite. Therefore, the impact is not considered as too high and the preparation is done with industrial focus.

The synthesis is performed in a standard stirred labscale apparatus, which consists of a 500 mL bulb equipped with a thermometer, a reflux condenser and a dropping funnel. Additionally, a stirrer (type: half-moon; height: 24mm, length: 69mm; thickness: 3mm) is used as mixing-device driven by a motor. Heating is provided via an oil bath on a heating plate with magnetic stirrer.

Two synthesis-series have been conducted in this work, which are described by procedure 1 (HS1) and procedure 2 (HS2) in the following chapters. Afterwards the characterization of the products is described. As already stated, three different industrial samples from Laux-Process (LXS-A, LXS-B,

LXS-C) and a commercial magnetite sample (COM-A) have been investigated besides the synthesized products.

3.1.1 Procedure 1 (HS1-series)

In this procedure 0.3 mol $FeSO_4$ or 0.3 mol $FeCl_2$ or a mixture of 0.15 mol $FeSO_4$ and $FeCl_2$ each are dissolved in 100 mL deionized water. Next, 150 mL ammonia-solution (25%) is added dropwise until pH>9. The dosing time was set to 10 minutes for all batches. The solution is heated afterwards and 34 mL of KNO_3 (200 g/L) solution is added as oxidant, while intensive stirring with 380 rpm is provided. The dosing time of oxidant was set to 10 minutes. Afterwards the solution is stirred for additional 20 minutes.

All variables influencing the reaction stated in the former chapter have been kept constant except the precursor material and the temperature of synthesis (T_{syn}). These have been varied in three stages each, which are presented in Table II - 3.1.

After the synthesis is completed, the batch is cooled down and the magnetite is fixed to the bottom with a magnet. The fluid is decanted and in the same manner the product is washed three times with deionized water (250 mL each). The suspension is filtered and the filtercake is washed again with deionized water until a neutral pH-value is reached.

In order to dry the product without any influence of temperature in air, the batches have been frozen and dried in a freeze drying apparatus (*Alpha 2-4 LDplus* from Christ). Afterwards the products have been dried additionally over P_2O_5 in an exsiccator for 2 days. In the end, the batches are characterized as described in chapter 3.1.3.

Table II - 3.1: Batches synthesized according to procedure 1

Batch	T_{syn} °C	Precursor
HS1-A	90	$FeSO_4$
HS1-B	82	$FeSO_4$
HS1-C	75	$FeSO_4$
HS1-D	75	$FeCl_2$
HS1-E	82	$FeCl_2$
HS1-F	90	$FeCl_2$
HS1-G	90	$FeSO_4$ / $FeCl_2$
HS1-H	82	$FeSO_4$ / $FeCl_2$
HS1-I	75	$FeSO_4$ / $FeCl_2$

3.1.2 Procedure 2 (HS2-series)

In the second procedure the same apparatus was used as described before. The procedure is based on procedure 1 in the contents of used chemicals. The rotational speed of the stirrer was set to 305 rpm here and the solution is stirred only 5 minutes after the reaction was finished. In procedure 2 not only the temperature (T_{syn}) and precursor have been varied but also the dosing time or speed (t_{dose}) of the KNO_3-solution. Additionally, each of these parameter combinations have been used for three times, and the product is washed with a different number of wash-cycles (n_{wash} = 2, 3 and 4) with 250 mL of deionized water for each cycle in the reaction device. The washing water is decanted with a pipette, while magnetite is fixed to the bottom with a magnetic stirrer, after each cycle. Finally, the product is mobilized as suspension with 100 mL deionized water and filtered without further washing of the filter cake.

Table II - 3.2: Batches with procedure 2

Batch	T_{syn} °C	Precursor	t_{dose} min	n_{wash}
HS2-A	77	$FeCl_2$	10	3
HS2-B	77	$FeCl_2$	10	2
HS2-C	77	$FeCl_2$	10	4
HS2-D	84	$FeCl_2$	15	3
HS2-E	84	$FeCl_2$	15	2
HS2-F	84	$FeCl_2$	15	4
HS2-G	90	$FeCl_2$	20	3
HS2-H	90	$FeCl_2$	20	2
HS2-I	90	$FeCl_2$	20	4
HS2-J	77	$FeSO_4$	10	3
HS2-K	77	$FeSO_4$	10	2
HS2-L	77	$FeSO_4$	10	4
HS2-M	84	$FeSO_4$	15	3
HS2-N	84	$FeSO_4$	15	2
HS2-O	84	$FeSO_4$	15	4
HS2-P	90	$FeSO_4$	20	3
HS2-Q	90	$FeSO_4$	20	2
HS2-R	90	$FeSO_4$	20	4
HS2-S	77	$FeSO_4$ / $FeCl_2$	10	3
HS2-T	77	$FeSO_4$ / $FeCl_2$	10	2
HS2-U	77	$FeSO_4$ / $FeCl_2$	10	4
HS2-V	84	$FeSO_4$ / $FeCl_2$	15	3
HS2-W	84	$FeSO_4$ / $FeCl_2$	15	2
HS2-X	84	$FeSO_4$ / $FeCl_2$	15	4
HS2-Z	90	$FeSO_4$ / $FeCl_2$	20	2
HS2-AA	90	$FeSO_4$ / $FeCl_2$	20	4

Drying is executed in the freeze dryer as already stated and afterwards for three days in an exsiccator with $CaCl_2$. The chosen parameter settings with dedicated sample-notation are presented in Table II - 3.2.

3.1.3 Magnetite sample characterization

After synthesis was completed, the samples have been characterized regarding different aspects. The main aspects of this study are the influence of particle size, and the content of (foreign) ions. It is intended to check, whether the reactions are influenced in their progress by impurities as they occur in real industrial processes. Besides the two stated charcteristics the iron-content of the magnetite and the Fe^{2+}/Fe^{3+} ratio are good measures to chemically describe the precursors for subsequent thermal investigations.

3.1.3.1 Particle Size

Particle size measurement is a wide field and results are often dependent on the chosen specific analyzing procedure. Therefore, different techniques of particle size measurement have been tested in this study.

- Laser diffraction method
- Scanning electron microscopy (SEM)
- Transmission electron microscopy (TEM)
- BET-surface measurements

Laser diffraction measurements have been performed with a Sympatec *HELOS/KR-RODOS* system. As expected, the range of values was in µm-magnitude, since magnetite agglomerates due to its magnetic characteristic. This was not consistent with the other utilized techniques and therefore the results are not presented.

The SEM pictures have been taken with a Hitachi *TM 3000* SEM-microscope with maximum magnification of 30,000X. Exemplary pictures of two synthesized products are presented in Figure II - 3.1. As is obvious, the resolution is not appropriate for particle size analysis. The application of higher resolutions delivered blurred images, which could not be analyzed. Additionally, the images delivered the proof, that values from Laser diffraction in µm-range are not plausible, since they should be analyzable with the stated SEM apparatus in this case.

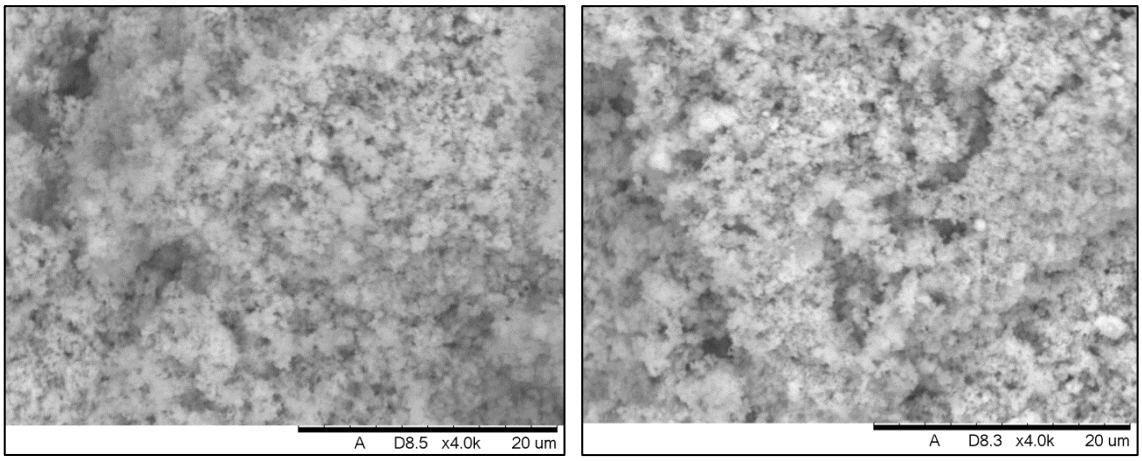

Figure II - 3.1: Exemplary SEM-pictures; left: sample HS2-E; right: sample HS2-H

Finally, the BET-technique (developed by Brunauer et al. [107]) was used to measure the surface of the products by gas-adsorption. The BET-surface determination has been done with a Micromeritics *Tristar II 3020*. The samples have been prepared by heating to 140°C in pure and dried nitrogen flux. Measurements have been conducted according to DIN66131 [108] at 77K with 90% He and 10% N_2 in a gas flux. The presented values are calculated from 3 points automatically with the analysis software delivered from the manufacturer. With the BET-Surface S the particle diameters d_P are calculated by assuming a sphere as described by Dubois et al. [109] analogous to the Sauter mean diameter [110]:

$$d_P = \frac{6}{S \cdot \rho_P} \tag{2.46}$$

The assumptions made with this approach are:

- particles are spheres
- all particles are uniform in size
- particles are not porous.

The solid density is assumed to the literature value of 5.18 (cf. Table II - 2.1). Weibel et al. [111] found a good agreement of the BET-method, and data obtained by XRD-measurements and TEM measurements in their study.

The results of the particle size determination via BET are presented summarized with further characterizing data in chapter 3.1.4. In order to plausibilize the results, TEM-images have been made from sample HS2-K as shown in Figure II - 3.2.

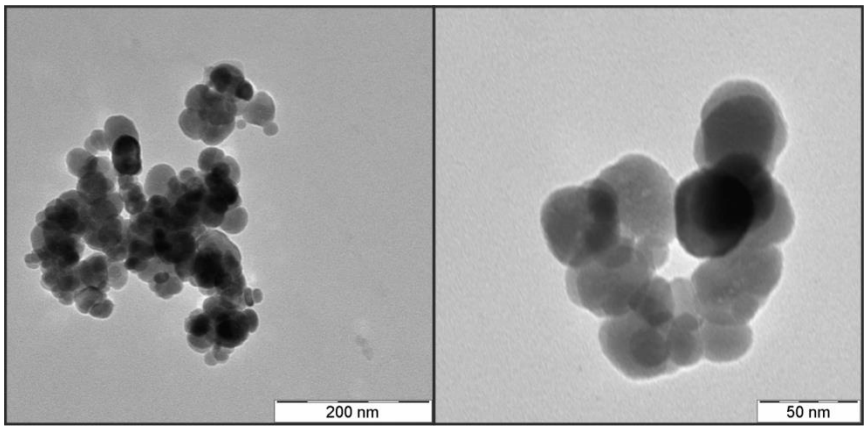

Figure II - 3.2: Exemplary TEM-images of magnetite-sample HS2-K.

The measuring device calculated particle sizes via image analysis from 195 particles, which results in a histogram given in Figure II - 3.3 (q_0, quantity probability). From that particle size distribution (PSD), the integrated PSD ($Q_0(x)$) has been calculated and is as also given in Figure II - 3.3.

The RRSB-function (Rosin, Rammler, Sperling, Bennet) has been fitted to the experimental $Q_0(x)$ via least squares method with the location parameter (x') and dispersion parameter (n) as fitting factors. The RRSB-function is based on considerations to the probability theory and is often applied graphically due to DIN 66145 [112] based on the following equation [110,113]:

$$Q_0(x) = 1 - \exp\left[-\left(\frac{x}{x'}\right)^n\right] \tag{2.47}$$

The resulting parameters from the fit are x'=33.13 nm and n=2.63. The value of the uniformity coefficient (n) indicates a very narrow distribution or high particle size uniformity (the higher n is above a value of 1, the better the uniformity is). The RRSB-distribution calculated with these parameters is also presented in Figure II - 3.3 for comparing purposes. A double logarithmic linearization with the experimental data and linear fit to the RRSB-function delivered a good regression with R^2=0.98.

Summarizing it can be stated, that particle sizes are RRSB-distributed and the calculated mean diameter from the RRSB-fit is 33.13 nm and in perfect congruence with the BET-value of 33.64 nm. This validates the values of particle diameter calculated from BET, which are used for further data evaluation in the following part of the thesis.

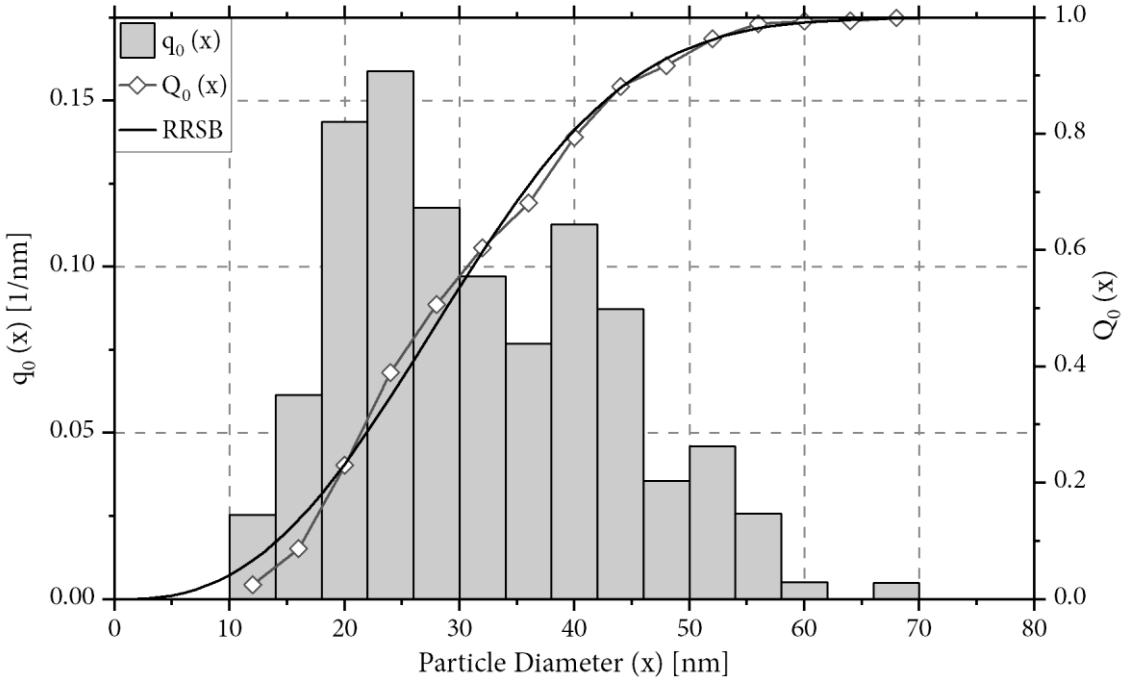

Figure II - 3.3: Particle size distribution from TEM-measurements with sample HS2-K as density distribution ($q_0(x)$, histogram) and cumulative distribution ($Q_0(x)$) Parameters for RRSB-distribution are x'=33.13 nm and n=2.63.

3.1.3.2 Fe^{2+}/Fe^{3+}-ratio

As described in chapter 0 magnetites can have a varying content of Fe^{2+}-ions. This will impact on the behavior of that magnetite, since diffusion etc. is easier due to the vacancies in the crystal lattice. Furthermore, there should be an impact on thermodynamics. Therefore, the Fe^{2+}/Fe^{3+} ratio is measured to describe the synthesized products.

This is done via Cerimetry, which is a redox-titration with a Cer(IV)-sulfate solution in a solution of sulfuric acid [114]. Due to Jander et al. [114] and Nestler et al. [33] Cerimetry is the favorite method in the determination of iron ions. Cerimetry has been used by Nestler et al. in the determination of Fe^{2+}/Fe^{3+}-ratio and thus the disorder in magnetites. They found a good correlation between cerimetry measurements and XRD-patterns in crystal analysis [33].

The solutions of Cer(IV)-sulfate are stable for a long time and can be heated without changing concentration. Additionally, the solutions are more transparent and reading the burette is easier. Cerimetry is based on the reduction of Cer^{4+} [114,115]:

$$Ce^{4+} \rightarrow Ce^{3+} + e^{-} \tag{2.48}$$

In the determination of iron the ions of Fe^{2+} are oxidized quantitatively in acidic solution according to [114]:

$$Fe^{2+} + Ce^{4+} \rightarrow Fe^{3+} + Ce^{3+} \tag{2.49}$$

As indicator Ferroin-solution (c=0.025 mol/L) is used and the titration is stopped at the color transition from red to slight blue. Adding a little amount of $NaHCO_3$ to the solutions prohibits the oxidization with oxygen from air, since CO_2 is created covering the liquid-surface.

Fe^{3+}-contents must be reduced prior to the titration. Zink is used to perform the reduction by adding Zn-powder in excess in acidic solution and separating remaining Zn via filtering. The reduction takes place according to:

$$2\,Fe^{3+} + Zn \rightarrow 2\,Fe^{2+} + Zn^{2+} \tag{2.50}$$

Afterwards the titration with Cer(IV)-sulfate was done, which results in a total iron content Fe_{tot}. The calculation of the desired ratio can be executed with:

$$\frac{Fe^{2+}}{Fe^{3+}} = \frac{m(Fe^{2+})}{m(Fe_{tot}) - m(Fe^{2+})} \tag{2.51}$$

In the experimental procedure roughly 250 mg of the magnetite sample are weighted and dissolved in 100 mL sulfuric acid. 5 mL are taken from that solution with a pipette and mixed with sulfuric acid of medium concentration. From a commercial Cer(IV)-sulfate solution (c=0.1 mol/L) for analyzing purposes, a solution with c=0.01 mol/L was produced. The titrations have been performed with a *Titrette®* (50 mL, precision: 30 µL) from Brand.

Prior to the titration the titer of Cer(IV)-sulfate is determined by titration of iron powder.

The results of total iron content in the synthesized magnetites and the Fe^{2+}/Fe^{3+}-ratio are presented in the summarized results in Table II - 3.4.

3.1.3.3 Included elements

In the preparation of magnetites different precursors have been used. In order to determine the content of different elements in the samples X-Ray-fluorescence (XRF) measurements have been performed with a *Spectro Xepos* XRF-device from Ametek. Roughly 4g of each sample are prepared by crushing and mixing the powder in a mortar and the sample is measured as powder.

The magnetite samples synthesized according to procedure 1 (chapter 3.1.1, HS1) have been checked due to plausibility of included elements. Measurements have only been performed with samples HS1-C, HS1-E and HS1-G, all synthesized from different precursors, in order to determine the contents of chlorine, sulfur and iron in the magnetite products.

The magnetite samples from procedure 2 (HS2-series) have been fully investigated with the same procedure. For a better overview, the results of all measurements are presented in the summary of results in chapter 3.1.4.

3.1.3.4 Analysis of washing water

Besides the magnetite sample characteristics stated in the former chapters the washing solution in procedure 2 has been analyzed. First, the conductivity of the liquids has been measured with a *TetraCon 325* conductivity electrode and a *LF 340 Conductivity Meter* from WTW at 25°C. The conductivity of the mobilizing water (mob.) is assumed as equal to the conductivity of the filter cake.

Besides the conductivity the content of elements (S, Cl, Fe) in the washing solutions of the last cycle is determined using the XRF-device stated in chapter 3.1.3.3 with a cuvette for liquid-analysis. Additionally, the mobilizing water is investigated in the same manner. Roughly 3g of each solution are analyzed. The results of both measuring techniques are presented in Table II - 3.3.

Table II - 3.3: Left: Results of conductivity measurements for washing water of all cycles and mobilising water (mob.) according to samples from procedure 2. Right: Results of elements quantification with XRF for last washing solution and mobilizing water.

	Conductivity [mS/cm]					Element-content [ma.-%]					
	cycle					last cycle			mob.		
	1	2	3	4	mob.	S	Cl	Fe	S	Cl	Fe
HS2-A	28	9.38	5.37		3.88	0.00205	0.1403	0.00140	0.00237	0.2057	0.00155
HS2-B	34.7	12.09			5.45	0.00045	0.5020	0.00135	0.00118	0.2110	0.00164
HS2-C	35.3	10.54	3.84	1.19	0.28	0.00350	0.0095	0.00141	0.00018	0.0002	0.00167
HS2-D	31.1	9.45	3.04		0.92	0.00105	0.1118	0.00169	0.00079	0.0002	0.00143
HS2-E	40.2	12.36			4.19	0.00019	0.6171	0.00143	0.00101	0.1703	0.00174
HS2-F	45.1	13.66	4.54	1.37	0.31	0.00054	0.0166	0.00140	0.00084	0.0002	0.00143
HS2-G	38.1	11.6	3.38		0.75	0.00203	0.1058	0.00174	0.00042	0.0002	0.00143
HS2-H	33.4	9.38			3.81	0.00036	0.4629	0.00144	0.00120	0.1546	0.00146
HS2-I	36.1	9.07	2.36	0.78	0.52	0.00115	0.0002	0.00136	0.00042	0.0002	0.00144
HS2-J	29.9	10.2	4.24		2.49	0.10570	0.0002	0.00212	0.06034	0.0002	0.00142
HS2-K	26.6	10.12			3.7	0.27770	0.0002	0.00135	0.09190	0.0002	0.00116
HS2-L	28	12.67	4.84	2.36	2.26	0.05069	0.0002	0.00168	0.05581	0.0002	0.00252
HS2-M	28.1	10.44	4.56		2.68	0.11560	0.0002	0.00160	0.06367	0.0002	0.00146
HS2-N	33.1	13.55			4.76	0.37950	0.0002	0.00143	0.11630	0.0002	0.00145
HS2-O	29.3	12.62	5.05	2	1.66	0.04625	0.0002	0.00112	0.03864	0.0002	0.00234
HS2-P	32.4	13.25	5.91		3.61	0.13390	0.0002	0.00262	0.09091	0.0002	0.00153
HS2-Q	31.7	12.91			5.24	0.33750	0.0002	0.00134	0.13130	0.0002	0.00158
HS2-R	33.5	15.12	5.64	2.57	2.13	0.05993	0.0002	0.00132	0.05091	0.0002	0.00130
HS2-S	54.7	29.6	14.73		8.48	0.21100	0.4517	0.01231	0.12440	0.2328	0.00108
HS2-T	61.2	28.4			12.01	0.44650	1.0040	0.00038	0.16990	0.3506	0.00156
HS2-U	60.5	25.5	11.66	6.08	5.23	0.08429	0.1534	0.00120	0.07386	0.1110	0.00125
HS2-V	70.1	31.4	13.97		6.17	0.20440	0.4401	0.00127	0.08812	0.1524	0.00141
HS2-W	57.5	26.2			11.43	0.40260	0.9098	0.00120	0.15540	0.3164	0.00134
HS2-X	69.8	33.2	15.88	7.9	3.22	0.11040	0.2162	0.00125	0.04239	0.0484	0.00140
HS2-Y	62.2	24.7	13.24		9.87	0.18820	0.4023	0.00114	0.14210	0.2678	0.01709
HS2-Z	59.9	27.5			18.28	0.42100	0.9586	0.00121	0.27390	0.5606	0.00115
HS2-AA	72.8	32.5	15.14	5.85	3.19	0.08846	0.1464	0.00104	0.04504	0.0429	0.00107

3.1.4 Interim summary

All results regarding the sample characterization are summarized in this chapter and first interpretations are derived from the data and its visualization.

Table II - 3.4: Summarized results of the characterization of industrial magnetite samples from Laux-process used in this study, as well as commercial magnetite sample.

	Precursor	d_P (BET) nm	Fe^{2+}/Fe^{3+}	Fe_{tot} ma.-%
LXS-A	Laux	105,1	0,76	67,1
LXS-B	Laux	44,9	0,76	67,3
LXS-C	Laux	78,42	0,82	67,7
COM-A	Unknown	150,2	0,73	66,9

The particle sizes of the Laux-magnetites in Table II - 3.4 are in the range of 44.9-105.1 nm. The commercial product exceeds this range by approx. 50% with 150.2 nm particle size. The results show, that the Laux magnetites have a significant stoichiometry deviation from the ideal Fe^{2+}/Fe^{3+} ratio of 0.5. The synthetic magnetites all contain a significant excess of Fe^{2+}. Furthermore, the total iron content is lower compared to the theoretical value of 72.4 ma.-%, so the Laux magnetites all have cation deficiencies (assuming an invariable oxygen lattice). The commercial magnetite is comparable to the Laux pigments in terms of particle size, iron content and Fe^{2+}/Fe^{3+} ratio.

The aggregated results for the synthesized products according to procedure 1 (HS1-series) are presented in Table II - 3.5.

The particle sizes of the HS1-magnetites depend on the synthesis temperature, with increasing temperature the particle size of the products decreases. This is depicted in Figure II - 3.4.

Table II - 3.5: Summarized results of the characterization of magnetite samples synthesized with procedure 1 (HS1-series)

			Cerimetry			XRF		
	Precursor	T_{syn} °C	d_P (BET) nm	Fe^{2+}/Fe^{3+}	Fe_{tot} ma.-%	S ma.-%	Cl ma.-%	Fe ma.-%
HS1-A	$FeSO_4$	90	40.43	0.79	64.4			
HS1-B	$FeSO_4$	82	45.8	0.69	67.3			
HS1-C	$FeSO_4$	75	51.8	0.74	66.8	0.1298	0.0024	68.33
HS1-D	$FeCl_2$	75	73.5	0.68	60.0			
HS1-E	$FeCl_2$	82	41.5	0.80	68.9	<LOD	0.2792	76.85
HS1-F	$FeCl_2$	90	38.2	0.78	63.4			
HS1-G	$FeSO_4/FeCl_2$	90	39.7	0.71	62.9	0.1906	0.1388	66.67
HS1-H	$FeSO_4/FeCl_2$	82	45.1	0.79	69.1			
HS1-I	$FeSO_4/FeCl_2$	75	66.5	0.72	67.5			

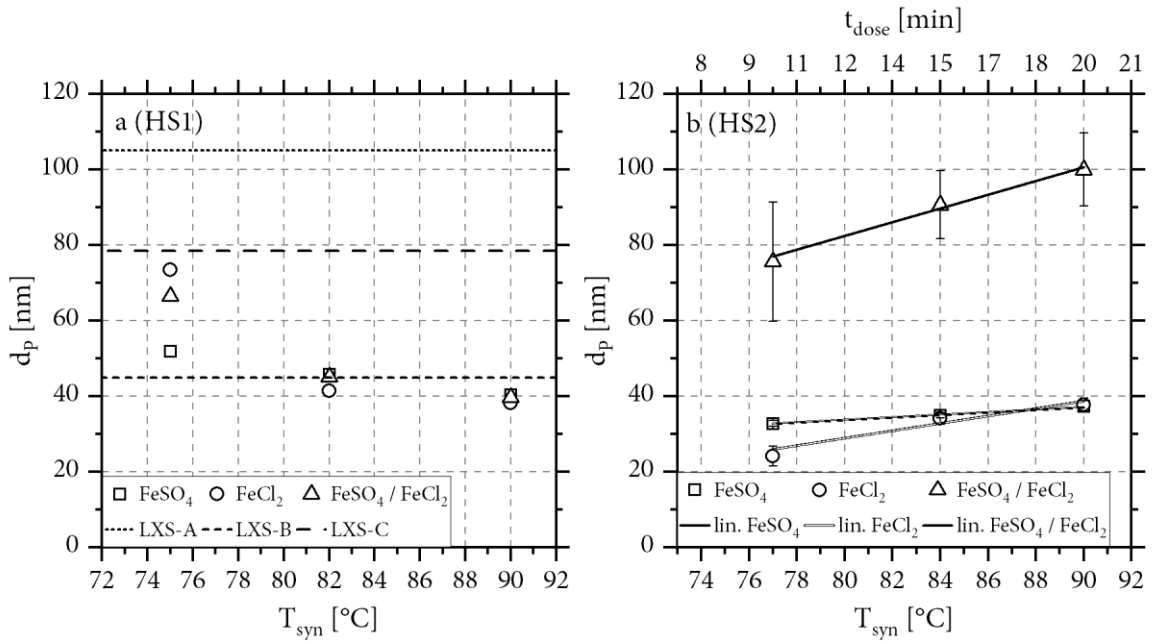

Figure II - 3.4: Diagramm of magnetite particle size versus the synthesis temperature. a: HS1-values for all used precursors and LXS-values; b: HS2-values, aggregated with linear regression depending on synthesis temperature

This dependence on temperature seems to be much less pronounced for sulphate as a precursor reactant, than for chloride or the mixture. At the highest synthesis temperature (90°C), all products have almost the same particle size (approx. 40 nm) regardless of the precursor. The influence of the precursor anion on the particle size thus decreases with increasing temperature. Regarding Fe^{2+}/Fe^{3+} ratio and total iron content, there are no correlations to the reaction temperature or to each other. The values for Fe^{2+}/Fe^{3+}-ratio and total iron content are in the range of the Laux products. The particle sizes of the Laux samples LXS-C and LXS-B are in the range of the synthesis products, while sample LXS-A has clearly larger particles.

The results of the XRF-analysis (Table II - 3.5) plausibilize the assumption, that the available anions are present in the synthesis product. HS1-C contains mainly sulphur (from sulphate), HS1-E only chlorine (from chloride), whereby sulphur is below the level of detection (LOD). For HS1-G, both anions are present in similar amounts. The iron content in HS1-E is remarkable, since it is clearly above the cerimetrically determined amount with 76.85 ma.-%. It is also higher than the theoretical Fe-content and is therefore interpreted as a mismeasurement.

The aggregated results of the synthesis products according to procedure 2 (HS2-series) are shown in Table II - 3.6.

Table II - 3.6: Summarized results of the characterization of magnetite samples synthesized with procedure 2 (HS2-series)

	Precursor	T_{syn}	t_{dose}	n_{wash}	d_P (BET)	Cerimetry		XRF		
						Fe^{2+}/Fe^{3+}	Fe_{tot}	S	Cl	Fe
		°C	min		nm		ma.-%	ma.-%	ma.-%	ma.-%
HS2-A	$FeCl_2$	77	10	3	22.11	0.21	63.0	0.00020	0.23440	66.24
HS2-B	$FeCl_2$	77	10	2	27.03	0.23	63.6	0.02213	0.26570	66.23
HS2-C	$FeCl_2$	77	10	4	23.40	0.25	56.3	0.37510	0.12700	65.03
HS2-D	$FeCl_2$	84	15	3	35.83	0.35	55.0	0.00020	0.04356	66.58
HS2-E	$FeCl_2$	84	15	2	33.56	0.48	47.1	1.75400	0.62830	42.83
HS2-F	$FeCl_2$	84	15	4	33.00	0.46	66.0	0.00020	0.04518	64.19
HS2-G	$FeCl_2$	90	20	3	37.62	0.57	61.3	0.34020	0.14340	64.63
HS2-H	$FeCl_2$	90	20	2	39.52	0.33	71.6	0.36090	0.12540	65.85
HS2-I	$FeCl_2$	90	20	4	36.10	0.46	56.7	0.00020	0.12580	65.80
HS2-J	$FeSO_4$	77	10	3	32.58	0.32	68.7	0.02035	0.04094	63.04
HS2-K	$FeSO_4$	77	10	2	33.64	0.50	60.3	0.91980	0.02254	96.58
HS2-L	$FeSO_4$	77	10	4	32.10	0.43	63.5	0.09578	0.00587	70.18
HS2-M	$FeSO_4$	84	15	3	34.57	0.50	56.1	2.22800	0.34970	32.24
HS2-N	$FeSO_4$	84	15	2	35.61	0.62	56.6	0.11940	0.00175	67.52
HS2-O	$FeSO_4$	84	15	4	34.61	0.35	60.7	2.31600	0.77820	34.65
HS2-P	$FeSO_4$	90	20	3	38.15	0.44	66.4	0.36160	0.12420	66.23
HS2-Q	$FeSO_4$	90	20	2	38.30	0.34	65.1	0.09689	0.00197	66.64
HS2-R	$FeSO_4$	90	20	4	35.71	0.36	62.4	2.40700	0.18730	35.89
HS2-S	$FeSO_4/FeCl_2$	77	10	3	61.25	0.41	60.2	0.32360	0.02116	66.92
HS2-T	$FeSO_4/FeCl_2$	77	10	2	73.17	0.46	59.0	0.09971	0.00229	69.21
HS2-U	$FeSO_4/FeCl_2$	77	10	4	92.37	0.41	62.6	2.21600	0.34810	37.32
HS2-V	$FeSO_4/FeCl_2$	84	15	3	87.88	0.45	64.0	2.13900	0.72420	36.75
HS2-W	$FeSO_4/FeCl_2$	84	15	2	100.72	0.45	69.6	0.36190	0.12900	64.84
HS2-X	$FeSO_4/FeCl_2$	84	15	4	83.33	0.43	68.2	0.16140	0.05272	67.39
HS2-Y	$FeSO_4/FeCl_2$	90	20	3	103.88	0.55	57.8	2.36900	0.18400	36.11
HS2-Z	$FeSO_4/FeCl_2$	90	20	2	107.05	0.54	59.7	0.35150	0.01900	67.00
HS2-AA	$FeSO_4/FeCl_2$	90	20	4	88.96	0.63	59.4	0.20860	0.03305	71.72

Mean values and relative standard deviations are determined from each of the three syntheses with the same settings but different washing cycles (e.g. HS2-A, HS2-B, HS2-C). The magnetites from the second series tend to have more sub-stoichiometric amounts of divalent iron compared to the ideal magnetite (ratio <0.5). This suggests increased oxidation to Fe^{3+} during the reaction. Although the incomplete washing also leads to the presence of Fe^{2+} from the reactants (liquid), the results of the Fe^{2+}/Fe^{3+} ratio for each group with different washing cycles are in good agreement.

The particle size results are shown in Figure II - 3.4. Regarding the temperature dependence, an inverse trend as in the HS1 series can be found. Since the oxidation rate was also varied at the same time, it can be concluded that it overcompensates the temperature. As the oxidation rate decreases (t_{dose} increases), the particle size increases. Huber reports a decrease in the particle size when the

dosing time is increased [27]. Therefore, the opposite case was determined in this study. Furthermore, he reports a reduction in particle size when the concentration of precursor in the reaction mixture is increased, which was not varied in this work.

For the HS2-series it can also be shown, that the influence of the selected parameter variations is low for the sulphate precursor-salt. The chloride-salt, however, does not behave as distinct at low temperatures as for the HS1-series. It is noticeworthy, that in the second procedure the presence of both reactants at once leads to significantly higher particle sizes than the products from one reactant salt. These products are also in the range of the particle size of the Laux sample LXS-A.

In summary, the following main points can be deduced from the synthesis results:

- Dependence of the crystallite size on the synthesis temperature
- Dependence of the crystallite size on the oxidation rate (comparable influence in the selected parameter range).
- On average, lower iron contents in magnetites were determined than the literature value for ideal magnetite indicates (Fe^{2+}/Fe^{3+}=0.5).

3.2 Thermal Analysis

All synthesized products stated in the former part have been investigated via thermal analysis. The used procedures are explained in this chapter.

3.2.1 Preliminary Experiments

In preliminary experiments, appropriate parameters for the investigation of all samples are determined in first steps. Furthermore, the sensitivity of results regarding different analyzing parameters is checked as well as the robustness of the methods themselves. Since dynamic measurements are used, these parameters are especially the heating rate and for the oxidation reaction the oxygen content in the gas atmosphere.

3.2.1.1 Thermogravimetry

First, the impact of different gas-atmospheres or oxygen contents has been tested using the sample LXS-C. The *Netzsch TG 209 F1 Libra* is equipped with MFC-controllers that allow the mass or volume flow to be adjusted. Oxygen and nitrogen were connected via the two available purge gas connectors. Using different ratios of the volume flows, oxygen contents of 10, 20, 50 and 100 vol.-%

were set by volumetric mixing as atmosphere in the furnace. The absolute volume flow of purge gas is 50 mL/min for all measurements.

The heating rate was set to 20 K/min in the temperature range from room temperature (approx. 30°C) to 1000°C. As sample mass 25-35 mg were weighted. The results of the measurements are presented in Figure II - 3.5.

It can already be clearly observed at this point, that in the temperature range of 200-400°C, in which the sample oxidizes (mass increase), the curve progression is almost identical. In the industrial scale, oxygen contents in the gas of >10 vol.-% are expected. A dependence on the oxygen partial pressure can therefore be excluded. Thus, it can be concluded at this point, that the reaction or the reactor can be influenced by increasing the oxygen content (except for the considerations in section 2.1.4.3).

In a further step, the dependence of TG-measurements from the heating rate have been tested. In this purpose, samples LXS-A, LXS-B and LXS-C were measured with the *Netzsch TG 209 F1 Libra* using heating rates of 5, 10 and 20 K/min. Further parameters during the measurement were an atmosphere of 100% O_2 and approximately 20-30 mg of sample was weighted in. The results are presented in Figure II - 3.6.

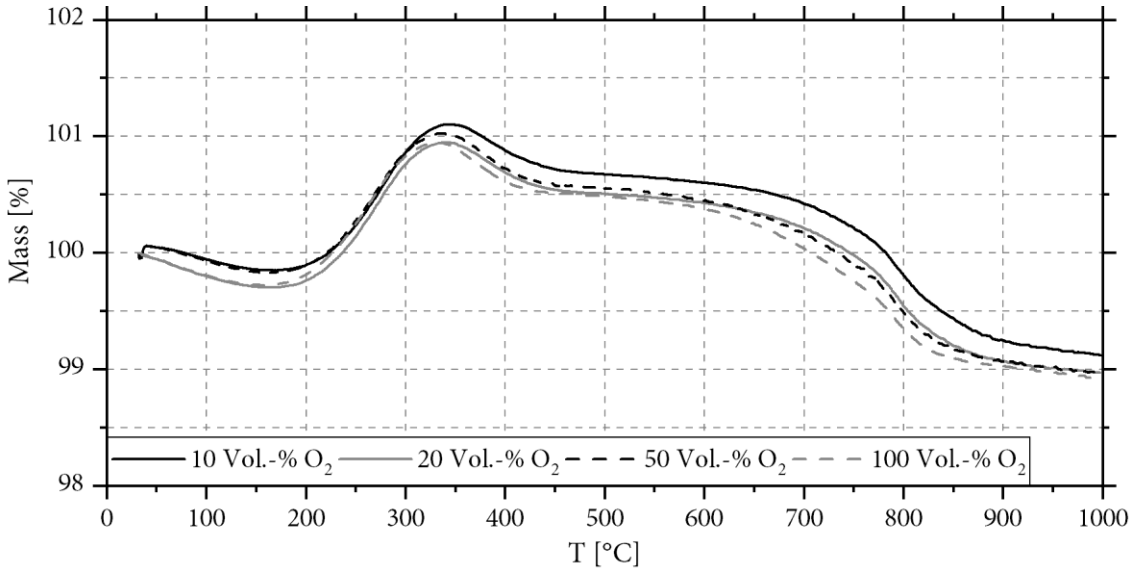

Figure II - 3.5: TG-analysis of magnetite sample LXS-C with various atmospheres of different oxygen content (N_2/O_2-mixture)

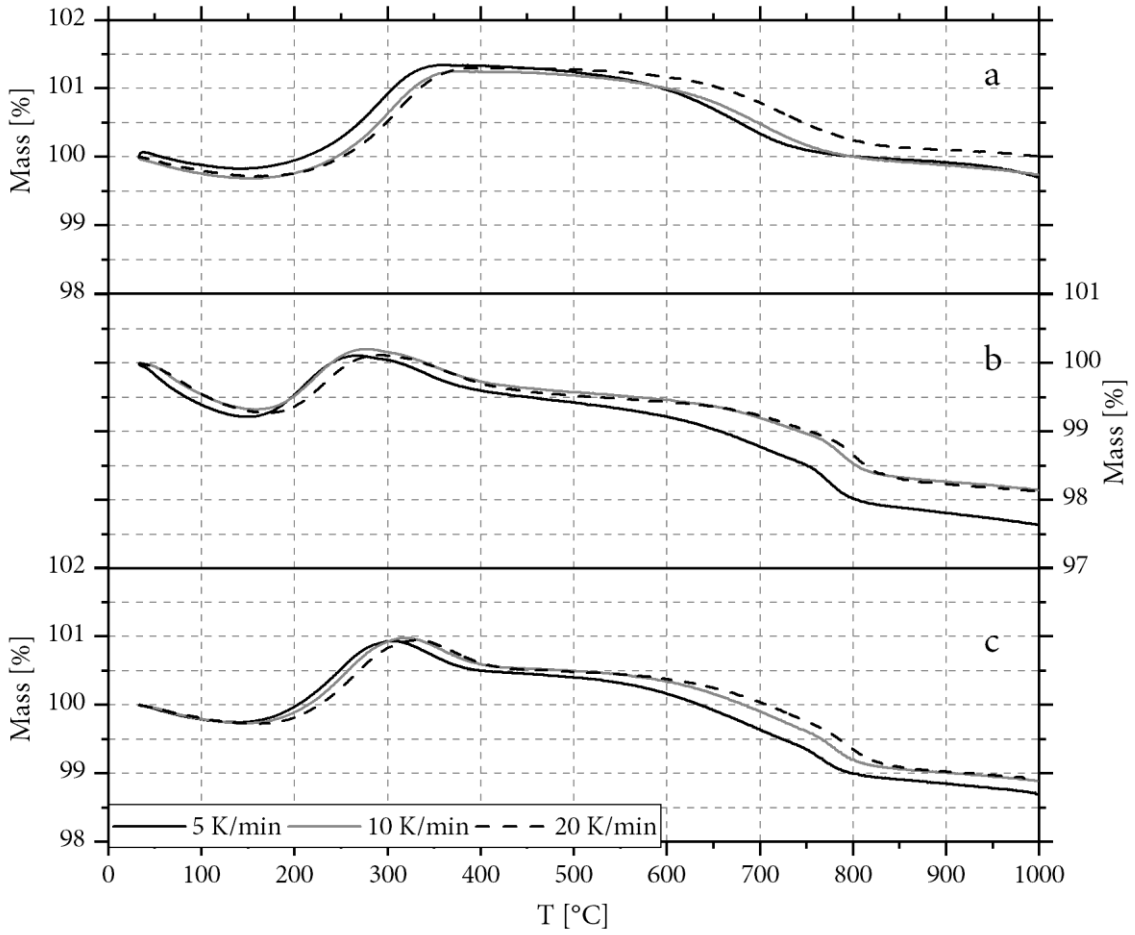

Figure II - 3.6: Comparing diagram of TG-analysis of magnetite samples LXS-A (a), LXS-B (b) and LXS-C (c) with different heating rates.

It can be observed, that there is a shift on the temperature axis in the range of mass gain (oxidation) at approx. 200-400°C depending on the sample material (cf. Figure II - 3.6 a,b,c). Comparing each of the three measurements for the same sample, the oxidation-onset is always ascending from 5 to 20 K/min. This shift is plausible because, assuming approximately equal reaction rates, the sample reaches higher temperatures at faster heating rates until the reaction is complete.

However, the shift is classified as minimal compared to the further characteristic curve progression. The characteristic shapes of all curves of each sample are also the same, regardless of the heating rate. Fundamental information is therefore not lost by using a specific heating rate. Thus, the heating rate of 20 K/min is selected for all further analyses to minimize the experimental time and effort.

Regarding the series of measurements of HS2-samples the specific sample HS2-C has been investigated with different sample-masses. The Al_2O_3-crucible was filled to different levels and heated in the *Netzsch TG 209 cell* with 20 K/min to 1000°C with 12.5 mL/min of synthetic air passing the furnace. The results are presented inFigure II - 3.7.

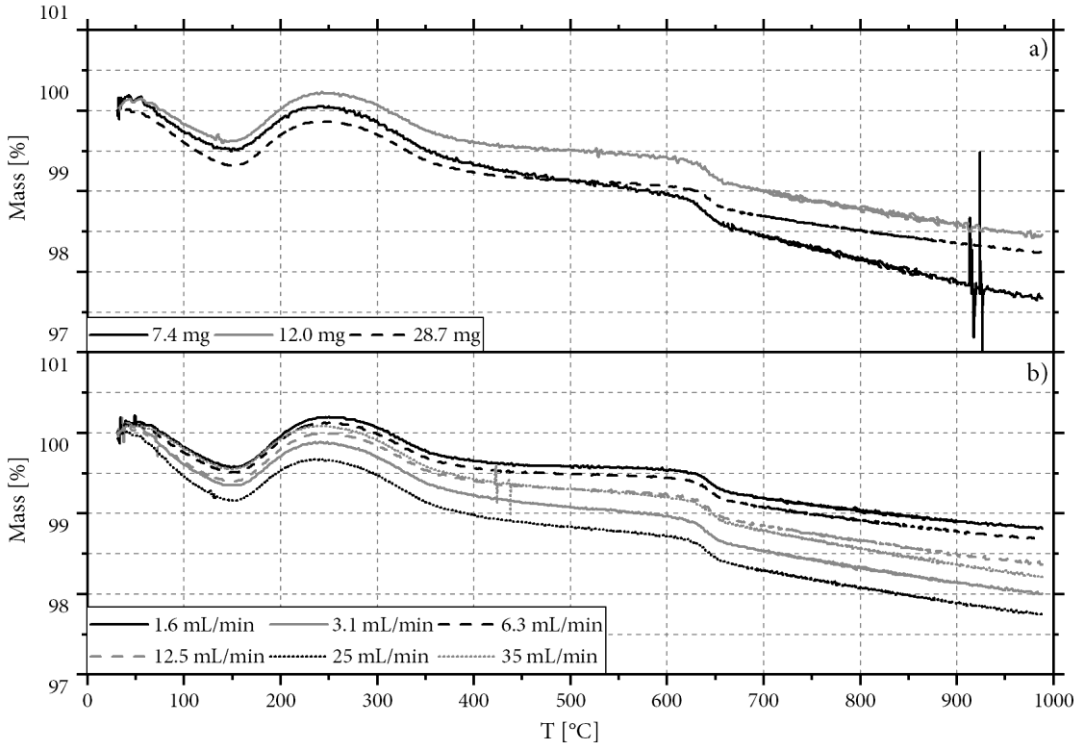

Figure II - 3.7: Diagrams of TG measurements with sample HS2-C; a: with different masses in the crucible; b: under variation of gas flow (synthetic air).

Furthermore, sample HS2-C was investigated with different flows of synthetic air (1.6/3.1/6.3/12.5/25/35 mL/min). The heating rate again was set to 20 K/min to ensure consistency over all measurements. The results are additionally presented in Figure II - 3.7. The artifacts in both parts of Figure II - 3.7 (top at ca. 925°C; bottom at ca. 425°C) are evoked by shocks due to closing doors and can be neglected.

3.2.1.2 Differential Scanning Calorimetry

The dependence of the measurements on the volume flow of the purge gas has also been tested with the DSC (*Netzsch DSC204 cell*) apparatus. For this purpose, the sample HS2-C was analyzed at different volume flows of synthetic air through the furnace at a heating rate of 20 K/min. Al_2O_3-crucibles were used, the DSC reference-sample is an empty crucible of the same composition. The possible temperature-range of the DSC is fully utilized with an interval from room temperature to 700°C. The results are presented in Figure II - 3.8.

It is obvious, that all DSC-curves have the same characteristic progress and all peaks occur at the same temperatures. However, a shift of the curves is visible regarding the DSC-axis, which is equivalent to a shift of the baseline.

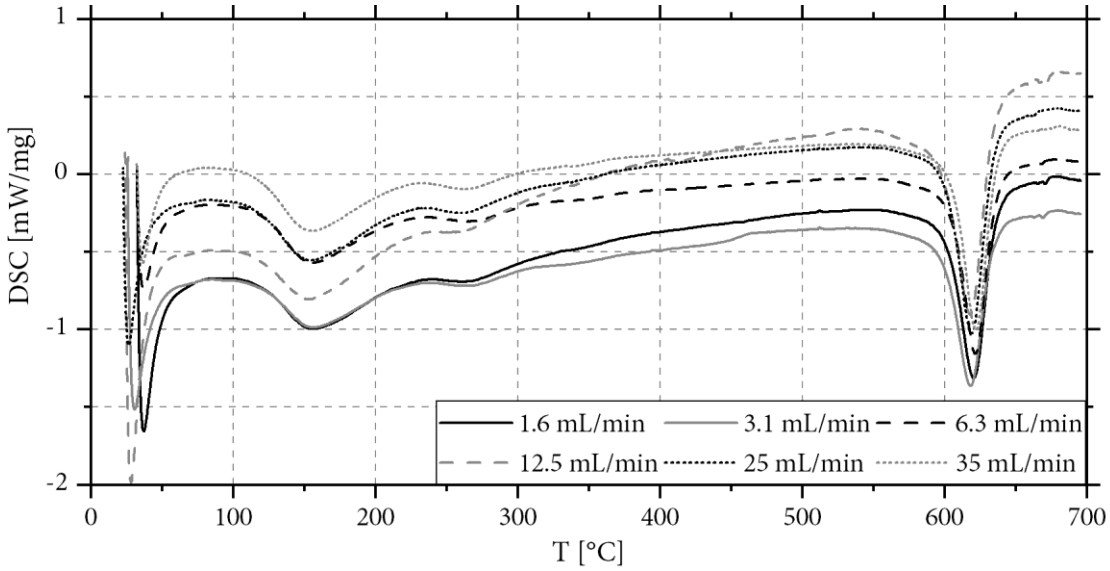

Figure II - 3.8: DSC-analysis of sample HS2-C for different volume flows of synthetic air as purge gas, heating rate: 20 K/min.

An exception in the characteristic curve-progression can be found for 6.3 mL/min, where the curve is somewhat flatter after the first peak between about 100-200°C. With higher volume flows, the DSC-curves increase in absolute terms, but this may be due to the calibration. Since the baseline is adapted to each curve in every single evaluation, this effect is not significant for the evaluation. The volume flow therefore has no influence on the DSC-analysis, which was to be expected after the results found in the TG earlier.

Furthermore, the sample HS2-C was analyzed regarding the weighed-in sample mass. For this purpose, three measurements were carried out with different crucible fillings. Again, the crucible was heated with 20 K/min in the range from room temperature to 700°C and purged with 12.5 mL/min synthetic air. The results are presented in Figure II - 3.9. Analogously to the results from the purge-gas variation, the characteristic curve progress is the same. Here, the baseline is not shifted in height, but in its slope. The higher the sample masses, the flatter the baseline curves. Consequently, the effects are negligible here as well, since they have no influence on the subsequent evaluation (baseline-fitting).

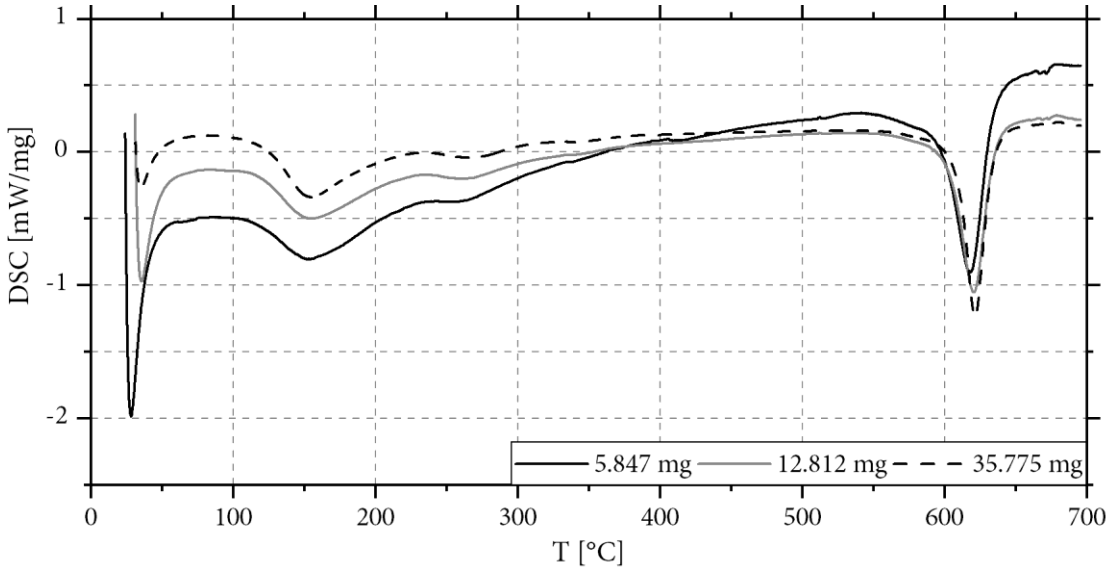

Figure II - 3.9: DSC-analysis of sample HS2-C for different crucible filling degrees/sample masses, heating rate 20 K/min, synthetic air flow 12.5 mL/min.

3.2.2 Thermogravimetry

After checking the basic robustness of the analyzing techniques, all stated samples (chapter 3.1) have been analyzed using TG and DSC. In the following chapter the applied procedures for TG measurements are presented.

3.2.2.1 Isothermal measurements

Since dynamic measurements and isothermal measurements have a competitive character (see chapters 2.3.2 / 2.3.3), isothermal measurements were carried out for the sample COM-A with TG in order to enable a comparison with the results of the dynamic measurements with regard to the kinetics analysis. For this purpose, the sample was first heated at 50 K/min to five different temperatures (200/220/240/250/265°C) and then kept at these constant temperatures. During the heating process, the furnace was purged with 50 mL/min N_2. After reaching the respective target temperature, a constant atmosphere of 100% O_2 at a flow rate of 50 mL/min was applied with a shift in purge-gas. The analyses were performed in a platinum crucible. Results are presented in Figure II - 3.10.

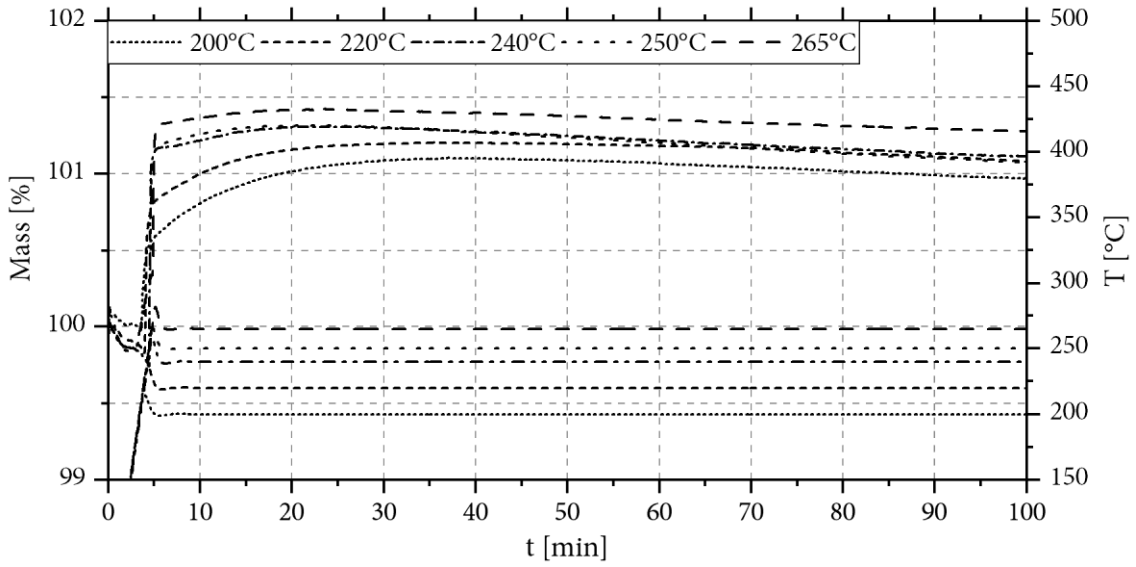

Figure II - 3.10: Isotherm TG-analysis of magnetite sample COM-A.

It is striking that the oxidation reaction already starts during the heating process despite the nitrogen atmosphere. This can only be caused by atmospheric oxygen, which was initially left in the powder bed of sample material in the crucible. Furthermore, it is noticeable that the maximum mass increase is directly dependent on the selected final temperature. The mass for 200°C is clearly below the mass for 265°C with a correlation of temperature and mass.

3.2.2.2 Dynamic measurements

The Laux-samples, the commercial sample as well as the HS1-series have been analyzed using a *TG 209 F1 Libra*. Atmospheres of 20 vol.-% O_2 and 80 vol.-% N_2 have been created via volumetric mixing using the mass flow controllers (cf. Figure II - 2.4). The total gas flowrate was set to 50 mL/min. According to the results from the preliminary experiments the heating rate was set to 20 K/min. Besides the mass, c-DTA signals have been measured and stored.

The samples of the HS2-series have been analyzed using a *TG 209 cell*. Synthetic air (21 vol.-% O_2) has been used and no additional N_2 was introduced for further mixing etc. The heating rate was set to 20 K/min and the volume flow of synthetic air was fixed to 12.5 mL/min. Each sample of the HS2-series was measured three times in order to gain statistical information.

Since in the preliminary experiments of sample HS2-C (cf. Figure II - 2.4) the overall mass after the thermal treatment was lower than at the beginning, each HS2-sample was additionally measured in a pure N_2 atmosphere with the same settings (20 K/min; 12.5 mL/min). Before each experiment, the furnace was evacuated with the vacuum pump (cf. Figure II - 2.4) and filled up with nitrogen to

ambient pressure afterwards. Analyzing a “difference-curve” from original and an "inert" experiment or the reheating of the sample as baseline correction is suggested for small mass changes during the analysis in the literature as well [65,116].

3.2.3 Differential Scanning Calorimetry

DSC measurements have only been performed with the HS2-sample series using a *Netzsch DSC 204 cell* and a *Netzsch TASC 414/3A* temperature-controller. All measurements have been performed using Al_2O_3 crucibles. The samples of the HS2-series have been measured from room temperature to 700°C (maximum temperature) with 20 K/min heating rate. The synthetic air volume flow was set to 20 mL/min in all measurements. In order to estimate errors, a sample of each precursor material was tested in multiple runs. These were samples HS2-A, HS2-J and HS2-S.

4 Results & Discussion

In this chapter the analysis of the experimental data of the thermal investigations is presented. The evaluation procedure already introduced theoretically in chapter 2.3 is applied and the results are related to the sample characteristics. Characterization results have been presented in the interim summary in chapter 3.1.4.

4.1 Thermogravimetry

The evaluation of the thermogravimetric measurements is carried out separated for both reactions (oxidation/recrystallization) and the two different sample series (HS1/HS2) with the related methods described in chapter 3.2.2.2.

4.1.1 Oxidation reaction (HS1 & LXS samples)

In the following, the kinetic evaluation is presented exemplary for sample LXS-A. The evaluated kinetic data of all measurements are delivered afterwards.

A diagram of mass vs. temperature is presented in Figure II - 4.1. At the beginning of the heating process, the mass initially decreases. This can be explained by adsorbed water, and was found in all TG-measurements. This is followed by a section with an increase in mass caused by oxidation. Later, the mass decreases again due to currently unexplained reasons. For the kinetics analysis of the oxidation, only the part of the mass increase is evaluated, as marked in grey in Figure II - 4.1.

The mass increase range is determined by searching the minimum and maximum of the curve and the mass increase is converted into the conversion X:

$$X(T) = \frac{m(T) - m_{start}}{m_{end} - m_{start}} \tag{2.52}$$

The conversion is set to 0.000001 at the start for numerical reasons and the final conversion is defined as 0.999999. This ensures that the calculations of the logarithms in the rate-laws do not generate any errors.

Utilizing this experimental (mass-based) conversion, the functions of conversion are calculated on the basis of the various kinetics models in the integrated form (cf. Table II - 2.2). These are plotted against 1/T analogously to the Coats-Redfern method (cf. chapter 2.3.4), as shown in Figure II - 4.2. It can be seen clearly, that the models deliver linearizations of varying quality. This is checked by means of linear regression using the regression coefficient and determining the slope and the intercept. Exemplarily this is shown in Figure II - 4.2 (f) using the AEG-A1 model, as this model provides the best regression coefficient for sample LXS-A. Finally, the activation energy is calculated from the slope of the linear regression. As an example, the activation energies and regression coefficients for all kinetic models for sample LXS-A are listed in Table II - 4.1.

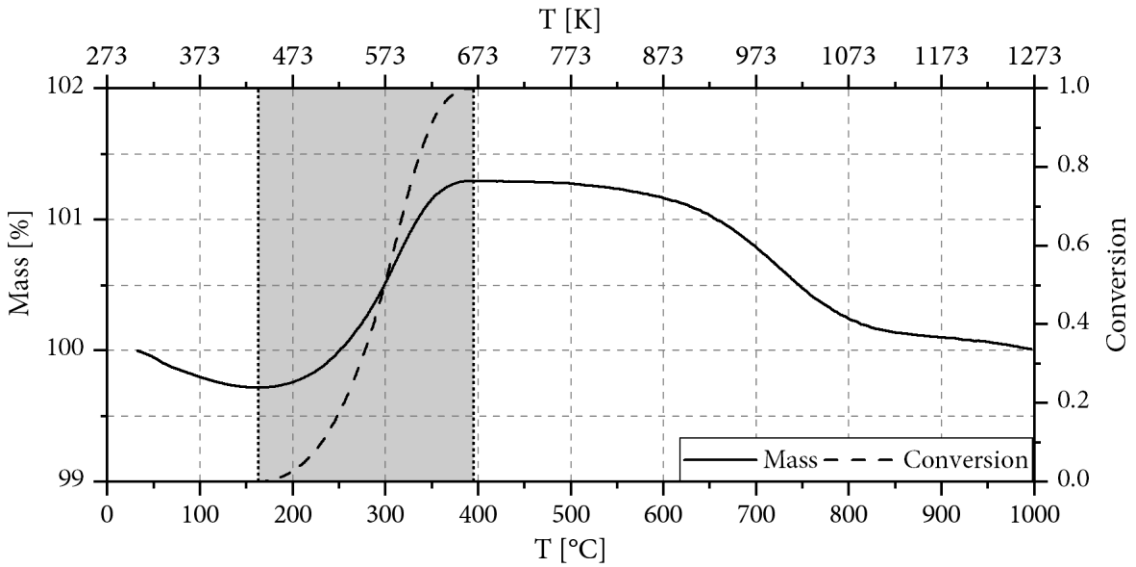

Figure II - 4.1: Example of Oxidation conversion calculation for sample LXS-A.

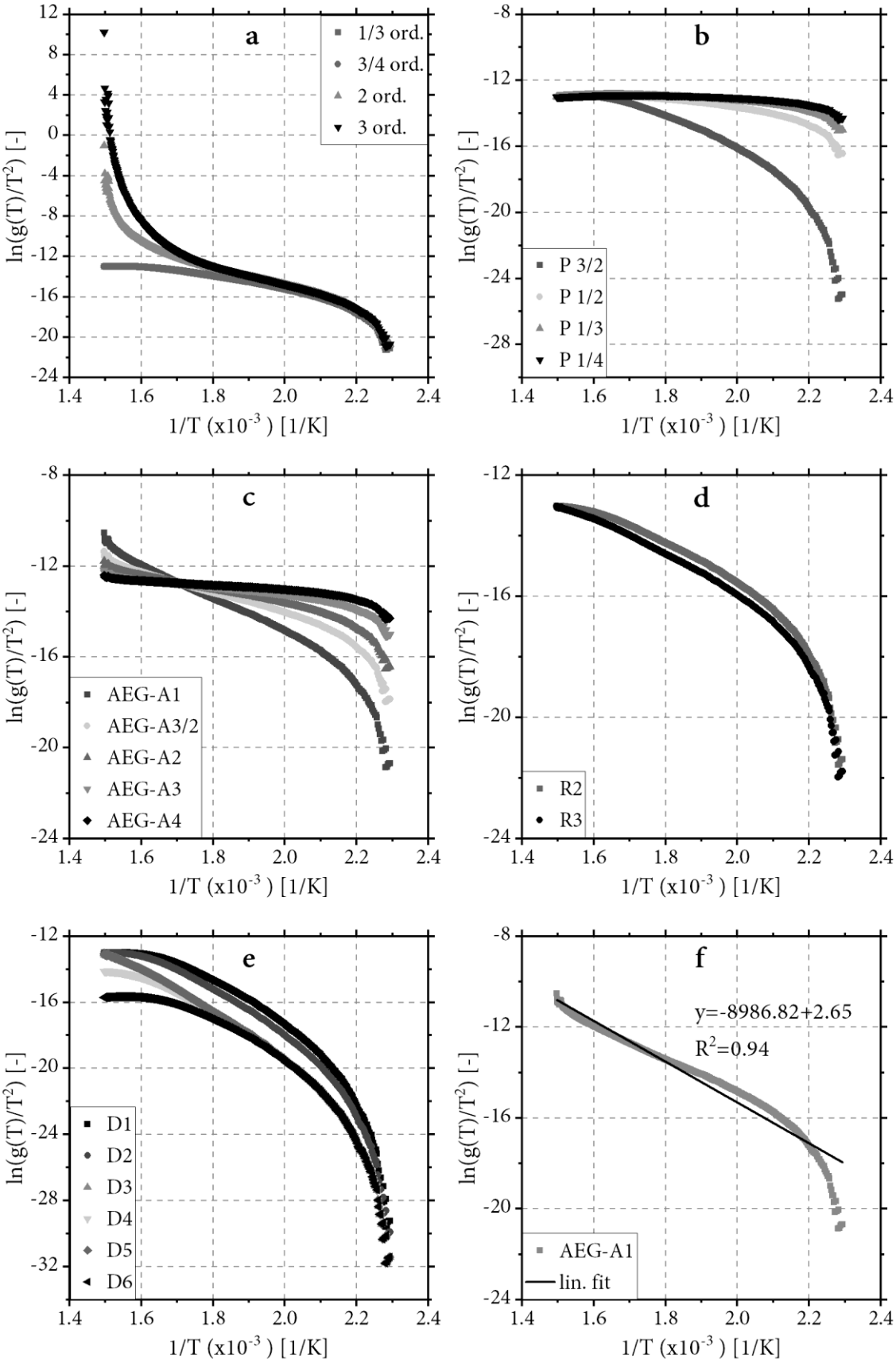

Figure II - 4.2: Diagrams from Coats-Redfern method in kinetic analysis of sample LXS-A. a: reaction orders; b: nucleation models (power laws); c: Avrami-Eroveef models; d: contraction-models; e: diffusion models; f: AEG-A1 model with related linear regression fit.

Table II - 4.1: Regression coefficients and activation energies for all tested models on oxidation kinetics of sample LXS-A

Reaction order			Nucleation			Avrami-Eroveef			Contraction			Diffusion		
	E_A	R^2		E_A	R^2		E_A	R^2		E_A	R^2		E_A	R^2
	kJ/mol			kJ/mol			kJ/mol			kJ/mol			kJ/mol	
F1/3	61.4	0.87	P3/2	90.1	0.85	A1	74.7	0.94	R2	64.0	0.89	D1	123.1	0.86
F3/4	60.2	0.86	P1/2	24.0	0.78	A3/2	46.8	0.94	R3	67.0	0.91	D2	130.9	0.89
F2	110.4	0.89	P1/3	13.0	0.69	A2	32.9	0.93				D3	143.1	0.92
F3	155.1	0.78	P1/4	7.5	0.56	A3	18.9	0.90				D4	134.7	0.90
						A4	12.0	0.86				D5	143.1	0.92
												D6	116.5	0.84

As can be seen clearly in Table II - 4.1, some models (e.g. P1) deliver no suitable description of the kinetic data. Furthermore, it is obvious that the activation energy is strongly dependent on the chosen model. The parameter 'activation energy' can therefore only be used combined with the related model.

For the samples of the HS1-series as well as for the Laux samples and for the commercial sample, the models of the 2nd-order reaction kinetics and the Avrami-Eroveef A1 model provide the highest regression coefficients on average considering all samples. The results are listed in Table II - 4.2, including the mean regression coefficients of all samples.

Table II - 4.2: Results of activation energies (E_A) and regression coefficients (R^2) of HS1-series and LXS-samples.

		2nd Order		Avrami-Eroveef A1	
Sample	d_P [nm]	R^2	E_A [kJ/mol]	R^2	E_A [kJ/mol]
LXS-A	105.11	0.89	110.4	0.94	74.7
LXS-B	44.93	0.93	173.8	0.92	114.1
LXS-C	78.42	0.92	122.0	0.94	85.4
COM-A	150.23	0.94	119.1	0.87	80.6
HS1-A	40.43	0.92	147.4	0.80	98.2
HS1-B	45.8	0.94	139.4	0.86	90.4
HS1-C	51.78	0.95	168.7	0.93	111.7
HS1-D	73.45	-	-	-	-
HS1-E	41.49	0.93	139.3	0.87	83.3
HS1-F	38.18	0.91	141.9	0.81	89.1
HS1-G	39.68	0.94	155.0	0.87	101.4
HS1-H	45.14	0.93	151.4	0.85	98.8
HS1-I	66.49	0.95	107.7	0.90	70.5
Mean		0.93		0.88	

Sample HS1-D cannot be evaluated due to a constant mass decrease while measurement. Here, incomplete drying is assumed to be the reason. Although the Avrami-Eroveef model and other models are based on theoretical derivations, the second order reaction describes the kinetics best considering the overall data in Table II - 4.1.

A diagram of the activation energies as a function of the particle size and the different precursors (and thus anions) is presented in Figure II - 4.3. Based on this plot a decreasing trend can be derived for the activation energy with particle size in the analyzed range. Furthermore, it can be seen that, exept for one sample of sulphate, the Laux samples have the highest activation energies.

4.1.2 Oxidation reaction (HS2-samples)

The samples of the HS2-series were analyzed with the *TG 209 cell*. In addition to oxidation using synthetic air (three runs), all samples were also measured in a nitrogen atmosphere. As an example, the measured TG-curves for sample HS2-A are shown in Figure II - 4.4. It is easy to see, that the measurements in synthetic air are very similar, especially in the oxidation range (mass increase in the range of approx. 150-250°C).

Furthermore, the measurement with nitrogen atmosphere results in a steady mass decrease. The mass decrease stagnates for a short time in the range of oxidation with synthetic air. In addition, there is another mass decrease in the range of approx. 600-650°C, which occurs both under oxidative conditions and under N_2-atmosphere.

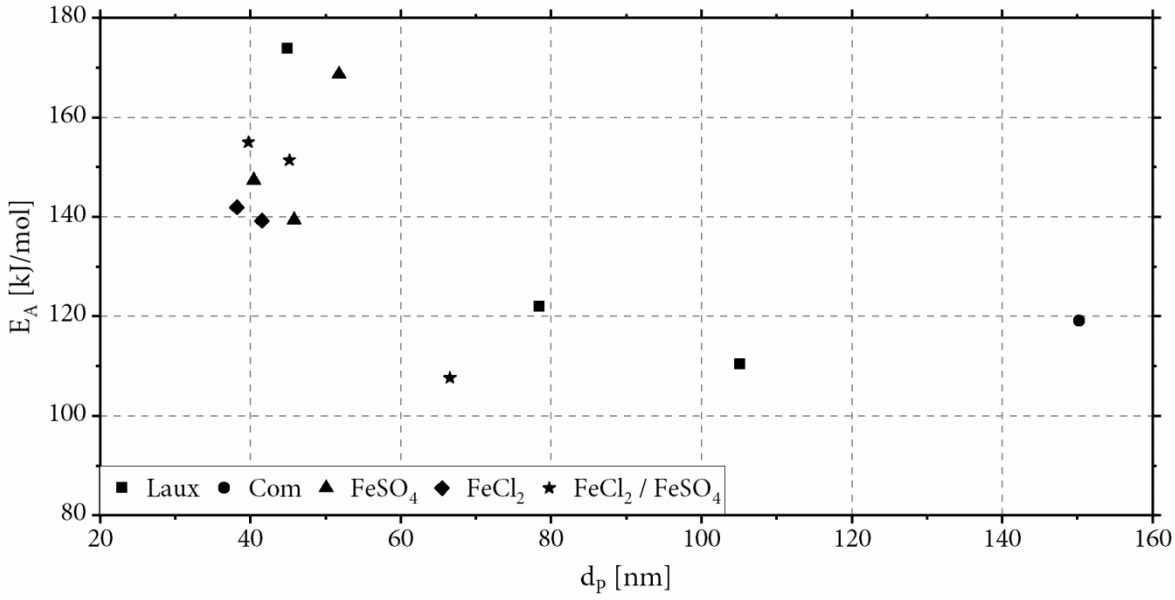

Figure II - 4.3: Diagram of activation energies (based on 2nd order kinetics) in dependency of particle size (BET) for various samples of different precursor origin (LXS, COM, HS1-series).

Welch et al. also found a mass decrease for precipitated magnetites while tempering at higher temperatures of 700°C. The mass decrease was found to be ca. 2.5% due to the loss of water [37]. This is a plausible explanation for the mass decrease after oxidation or as simultaneous process to oxidation. From the curves using oxidative conditions and under nitrogen atmosphere, a difference curve m_Δ (with the unit %) can be calculated by:

$$m_\Delta[\%] = m_{air} - m_{N_2} + 100 \tag{2.53}$$

This curve theoretically describes pure oxidation without the mass decreases due to the volatile components. These are assumed as water, in the first stage as adsorbed water, later as crystalline water, but evidence cannot be provided with the methods in this work. In Figure II - 4.4, this difference curve is also presented and it can be seen, that the curve describes almost exclusively a mass increase. However, after the already described mass decrease in the range of 600-650°C, the mass of the difference-curve also decreases to almost the initial mass (value 100%).

Consequently, two evaluations can be derived of the HS2-series. One regarding the original oxidation curves and one with regards to the difference curves. Comparable to the already described evaluations of the HS1-series, the range of mass increase is selected for the analysis of the oxidation reaction and a conversion calculation is carried out. Subsequently, the kinetic model descriptions mentioned in chapter 2.3.1 are tested and a selection is made on the basis of the regression coefficients.

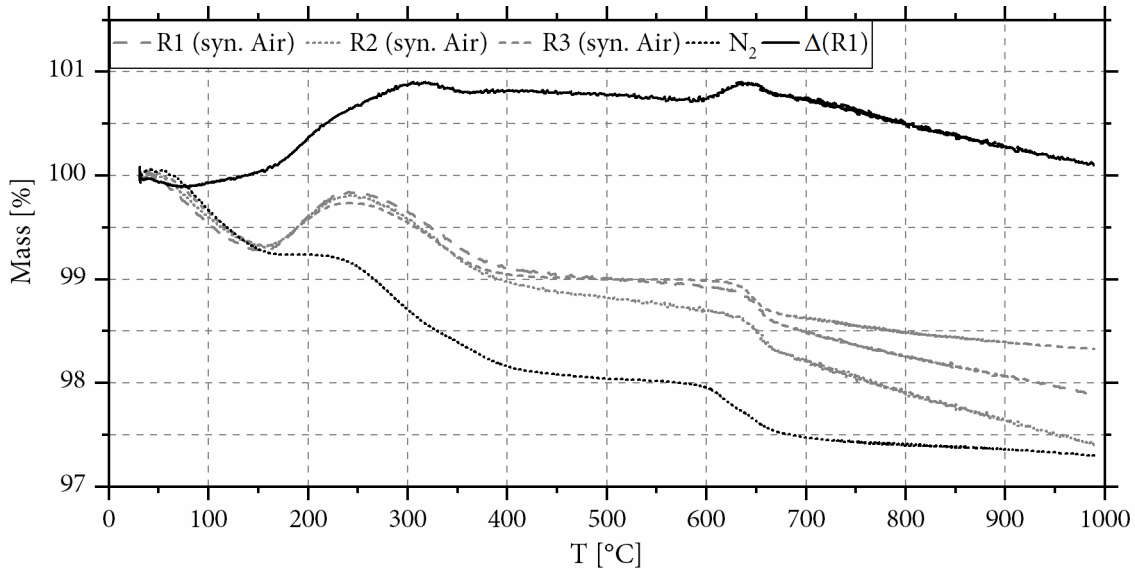

Figure II - 4.4: Exemplary TG-results from sample HS2-A measured three times with synthetic air (R1/2/3) and in N_2-atmosphere as well as resulting difference (Δ) of R1 in synthetic air and nitrogen.

On average, the Avrami-Eroveef A1 model is best suited for the description of oxidation curves (mean R^2=0.94), for the difference curves the description according to the 2nd-order reaction (mean R^2= 0.95) is superior. The results of all measurements are presented in Table II - 4.3.

In Figure II - 4.5, the dependence of the activation energy (calculated with the Avrami-Eroveef A1 model) on the oxidation curves is plotted against both the particle size and the conductivity and thus the ion content of the magnetite samples investigated. No direct correlation or dependence can be derived from this plot. Therefore, it can be stated that in the investigated parameter regime no strict dependencies are observable.

Table II - 4.3: Activation energies of oxidation curves (analyzed with Avrami-Eroveef A1-model) and Δ-curves (analyzed with 2nd order reaction model) for all runs in the investigation of HS2-series.

	Oxidation (Avrami-Eroveef A1)					Δ (2nd Order)				
	E_A [kJ/mol]				Std [%]	E_A [kJ/mol]				Std [%]
	R1	R2	R3	Mean		R1	R2	R3	Mean	
HS2-A	108.0	100.5	124.4	110.9	11.0	52.2	52.0	55.2	53.1	3.4
HS2-B	104.4	107.8	111.7	108.0	3.4	83.8	76.6	95.5	85.3	11.2
HS2-C	106.7	101.1	107.0	104.9	3.1	57.9	71.4	86.6	72.0	20.0
HS2-D	85.8	87.6	89.0	87.5	1.8	79.0	78.6	86.2	81.3	5.3
HS2-E	95.7	99.2	99.6	98.2	2.2	85.4	86.8	78.3	83.5	5.4
HS2-F	91.3	81.0	96.3	89.6	8.7	71.5	79.1	88.6	79.7	10.7
HS2-G	90.3	92.0	93.2	91.9	1.6	67.1	65.2	85.9	72.7	15.7
HS2-H	90.3	90.1	92.0	90.8	1.1	74.9	72.5	82.2	76.6	6.6
HS2-I	95.1	89.7	92.1	92.3	2.9	80.2	74.8	86.9	80.6	7.5
HS2-J	101.8	105.6	97.3	101.5	4.1	76.9	91.6	95.8	88.1	11.3
HS2-K	96.3	95.5	100.6	97.5	2.8	87.6	86.8	95.7	90.0	5.5
HS2-L	96.2	99.2	98.3	97.9	1.6	67.1	83.5	98.1	82.9	18.7
HS2-M	98.6	98.1	97.0	97.9	0.9	90.7	92.6	88.8	90.7	2.1
HS2-N	91.0	96.9	96.2	94.7	3.4	90.8	95.5	94.6	93.6	2.7
HS2-O	90.1	105.4	96.0	97.1	8.0	81.5	98.5	94.9	91.6	9.7
HS2-P	91.1	95.4	97.0	94.5	3.3	83.7	93.1	95.1	90.6	6.7
HS2-Q	92.0	92.5	92.5	92.4	0.4	88.2	92.7	94.5	91.8	3.5
HS2-R	91.0	91.6	97.1	93.3	3.6	134.3	132.4	138.8	135.2	2.5
HS2-S	88.8	86.1	90.0	88.3	2.2	78.3	50.6	84.7	71.2	25.5
HS2-T	88.5	90.4	87.0	88.6	1.9	75.6	78.3	72.1	75.3	4.2
HS2-U	75.7	77.7	76.6	76.7	1.3	58.4	66.3	68.1	64.3	8.0
HS2-V	88.4	81.7	83.1	84.4	4.2	67.9	72.7	63.2	68.0	7.0
HS2-W	52.1	86.5	84.2	74.2	25.9	60.6	76.4	75.8	70.9	12.7
HS2-X	82.4	81.3	81.0	81.6	0.9	78.1	73.9	75.6	75.9	2.8
HS2-Y	98.1	84.7	89.9	90.9	7.4	64.0	60.9	85.9	70.3	19.4
HS2-Z	118.6	104.7	100.1	107.8	8.9	90.3	71.8	76.0	79.4	12.2
HS2-AA	83.6	90.3	83.9	85.9	4.4	87.6	87.6	84.9	86.7	1.8

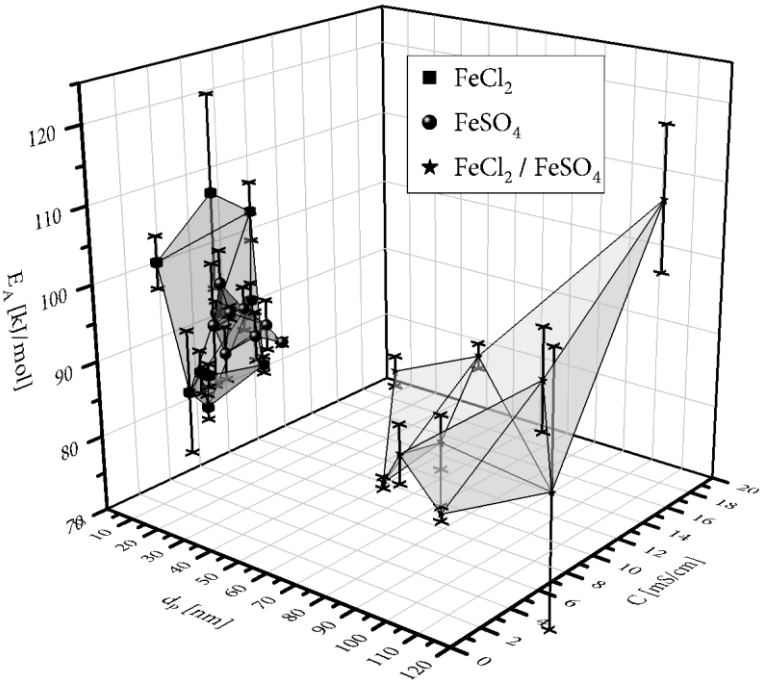

Figure II - 4.5: Plot of activation energies (A1-model, from TG-data) of oxidation curves from HS2-series in dependency of particle size d_P and conductivity C of the samples.

Figure II - 4.6 delivers the projections of conductivity and particle size from Figure II - 4.5 to enable a dedicated analysis. Again, there is no directly observable dependence on conductivity or particle size. However, the tendency towards lower activation energies with increasing particle size in the investigated area is also confirmed here.

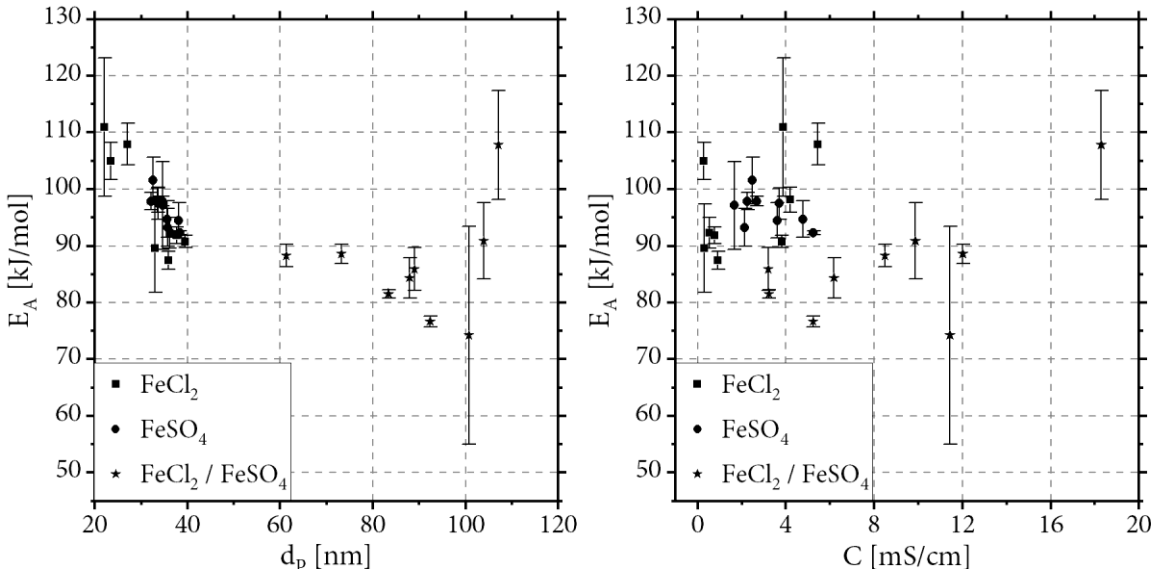

Figure II - 4.6: Plots of activation energies E_A (A1-model, TG-data) of oxidation from HS2-series; Left: E_A vs. particle size d_P; Right: E_A vs. and conductivity C of the samples.

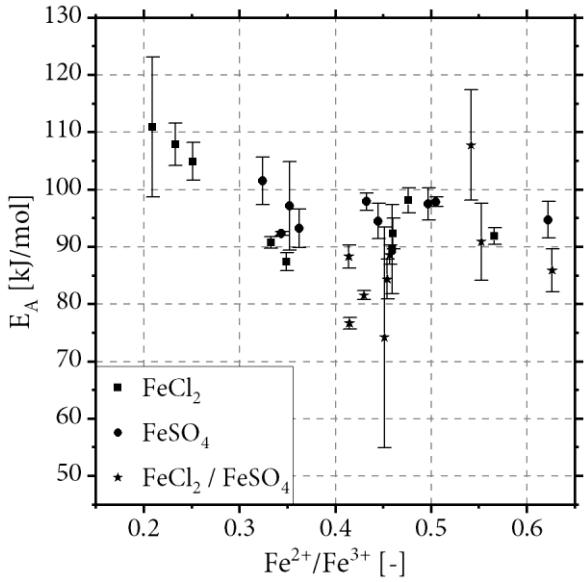

Figure II - 4.7: Dependency of activation energies (A1-model, TG-data) from the Fe^{2+}/Fe^{3+} ratio for all samples of HS2-series

Furthermore, the dependence of the activation energy on the Fe^{2+}/Fe^{3+}-ratio can be investigated. The plot is shown in Figure II - 4.7. No dependence or correlation, which would make the inclusion of Fe^{2+}/Fe^{3+}-ratio necessary in kinetics and conversion calculations, can be found.

4.1.3 Conversion Reaction

The *TG 209 F1 Libra* provides c-DTA data in the measurements of the Laux-samples, the commercial sample and the HS1 sample series. From this c-DTA data a transition temperature is derived via numerical analysis. A random exemplary data-set of c-DTA values is presented in Figure II - 4.8 (sample HS1-C, dotted line). At the beginning of the heating there is a bigger peak due to the initial heating until the constant heating rate is reached. A second peak is following in the temperature range of roughly 150-250°C, evoked by the thermal character of oxidation reaction. Later on in the temperature range of roughly 500-600°C, a third peak is observable in the theoretical region of conversion reaction (cf. chapter 2.1.4.2).

The analysis of the data is done via numerical derivation of the c-DTA values in a first step and smoothing the derivative afterwards due to artifacts from numerical derivation (Figure II - 4.8, solid line). Subsequent a peak analysis of the smoothed derivative is done in the region of the third peak, since there is only one proper peak above a Temperature of 500°C for all samples. The peak temperature is estimated as conversion temperature (T_C) of the second reaction step and determined to 557°C for sample HS1-C.

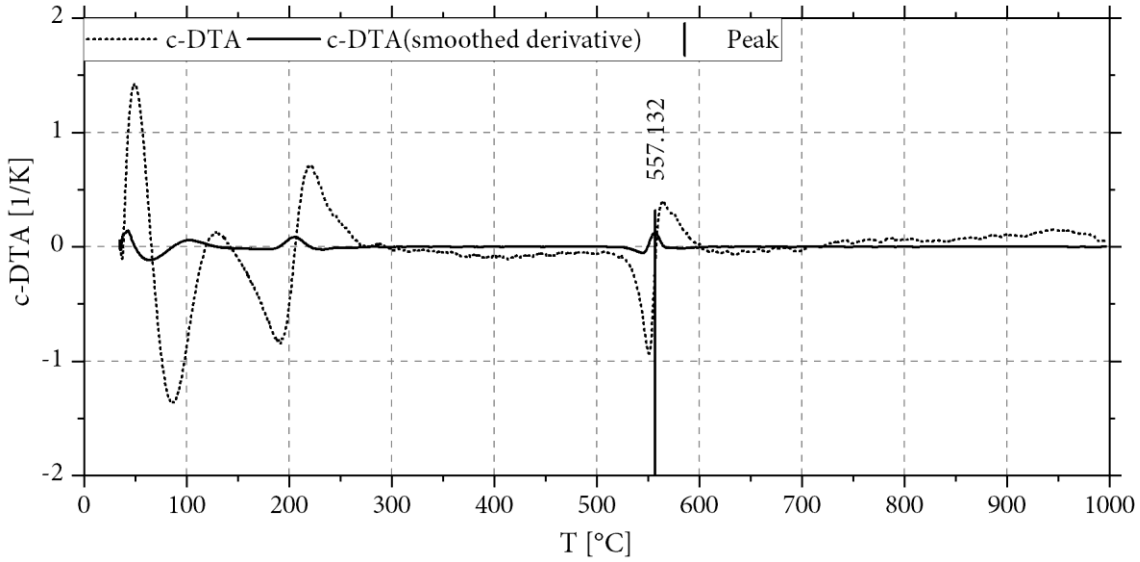

Figure II - 4.8: Presentation of peak-analysis from c-DTA data of sample HS1-C

All conversion temperatures (T_C) are presented in Figure II - 4.9 in dependency of the particle size and the various precursor materials used in synthesis of HS1-samples.

It can be clearly observed, that no strict dependency regarding the particle size is derivable from the data. But since all conversion temperatures of samples from $FeSO_4$ are significantly lower, the presence of chloride seems to increase the conversion temperature in general (cf. magnetites from precursor mixture).

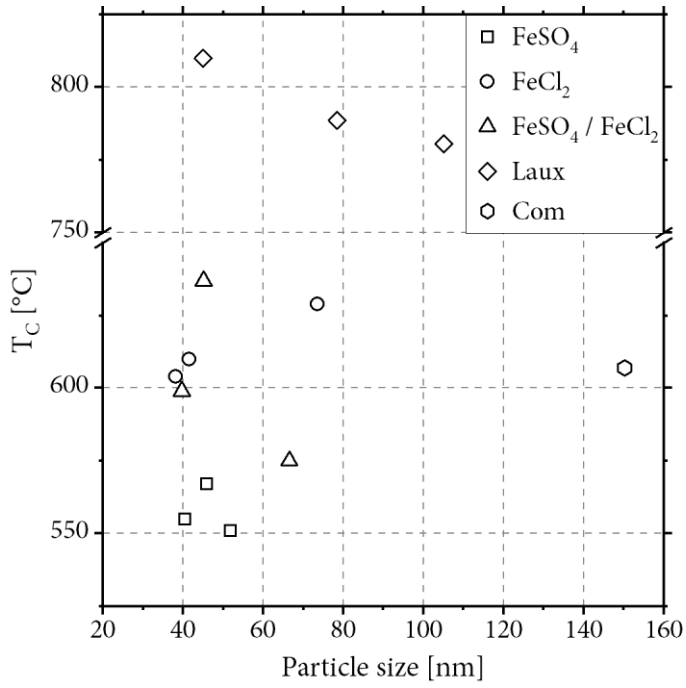

Figure II - 4.9: Conversion temperatures (T_C) dependent on particle size for all samples of HS1-series, Laux-samples and the commercial sample

Besides that, the presence of sulfate evokes a maximum conversion temperature at about 45nm particle size, while chloride products show a strict trend to higher conversion temperatures with increasing particle size.

The commercial product delivers a comparable conversion temperature although the particle size is more than double as high. The Laux-magnetites show a completely different behaviour since conversion temperatures are significantly (roughly 150-200°C) higher at comparable particle sizes. A trend towards lower conversion temperatures with increasing particle size is observable here, contrary to the trend of the magnetites from $FeCl_2$.

4.2 Differential Scanning Calorimetry

In contrast to the TG-technique, thermodynamic properties can be derived from the DSC data also. Thus in this study the data is evaluated regarding:

- Kinetics
- Enthalpies

The basic progress of the DSC curves is explained using example curves of samples HS2-A, HS2-J and HS2-S, as shown in Figure II - 4.10 (magnetites synthesized from all three material combinations). The evaluation of oxidation and crystallization reactions is also explained using these examples in the following chapters.

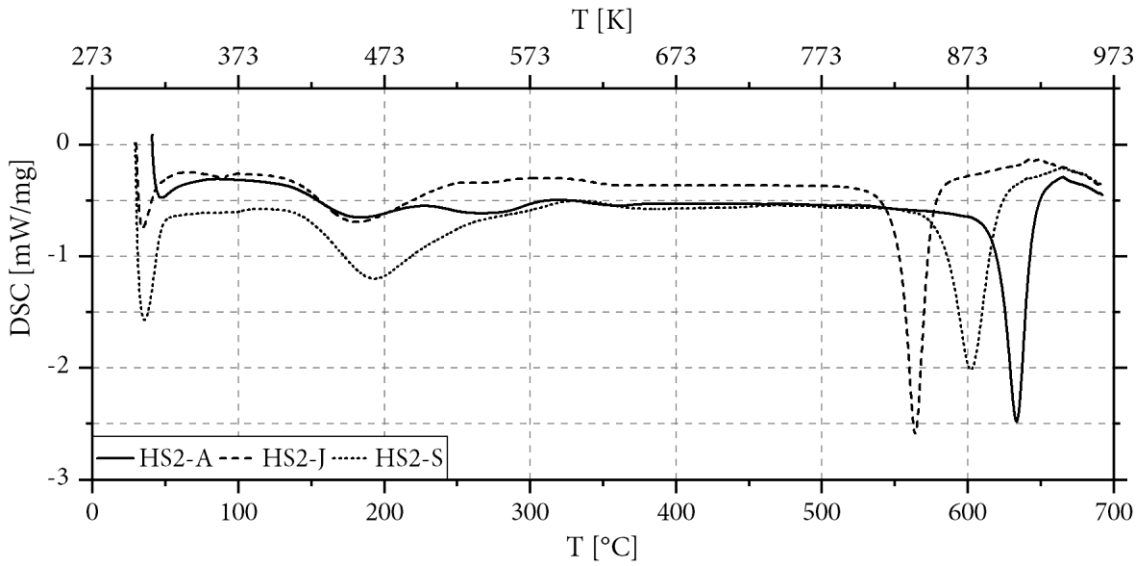

Figure II - 4.10: DSC-plot of sample HS2-A, HS2-J and HS2-S at heating rates of 20 K/min, measured with synthetic air flow of 20 mL/min. Exotherm peaks in downward direction.

The characteristic progress of the curves in Figure II - 4.10 is similar for all samples. At the beginning (<50°C), a pronounced drop in the exothermic direction is observable. This is a result from the initial heating process of the apparatus due to technical reasons and will not be further considered. At about 125°C, an exothermic peak begins, which extends to about 350°C. For sample HS2-A (magnetite from $FeCl_2$) the first peak is bimodal, while for sample HS2-J (magnetite from $FeSO_4$) the bimodal character is only weakly pronounced. Contrasting, for sample HS2-S (magnetite of $FeCl_2$/$FeSO_4$), only an unimodal peak is recognizable. The first peak is therefore differently pronounced for the magnetites from different synthesis materials, in some samples the split is also hardly recognizable or not present. Generally, the first peak can be assigned to the exothermic oxidation reaction (cf. chapter 2.1.4.1).

In the further progress of each measurement, starting from about 550°C a second peak occurs, which extends over a significantly smaller temperature range (up to about 650°C). This peak can be assigned to the crystal transformation reaction (cf. chapter 2.1.4.2), which is also exothermic. The second peak is always clearly unimodal for all samples, but a significant shift in the temperature regime can be recognized here, comparing the different samples.

In summary, it can already be stated here that the characteristic structure with two peaks, the first of which is sometimes split in two peaks, can be found in all samples. The exact shape and position of the peaks, however, is different for each individual sample.

In their work, Sanders and Gallagher [49] find comparable curves of TG and DSC as presented in Figure II - 4.11). The DSC curve also shows a double peak in the area of oxidation (mass increase). The TG curve also shows two sections in the mass increase. After a steep increase at the beginning, the curve flattens out and a further mass increase of about 0.5% takes place more slowly. However, the peak for recrystallization is very broad here from 500°C to approx. 800°C and is not accompanied by any mass loss. Furthermore, the mass increase almost corresponds to the exact theoretical value of 3.4%.

To estimate measurement errors, the three stated samples (HS2-A, HS2-J, HS2-S) were measured three times each referencing the empty crucible and additionally three times against a reference crucible with hematite of the same batch. The sample selection includes one sample from each starting material in the magnetite synthesis, so the determined standard deviations can be transferred to the other samples of the same synthesis material as error estimation.

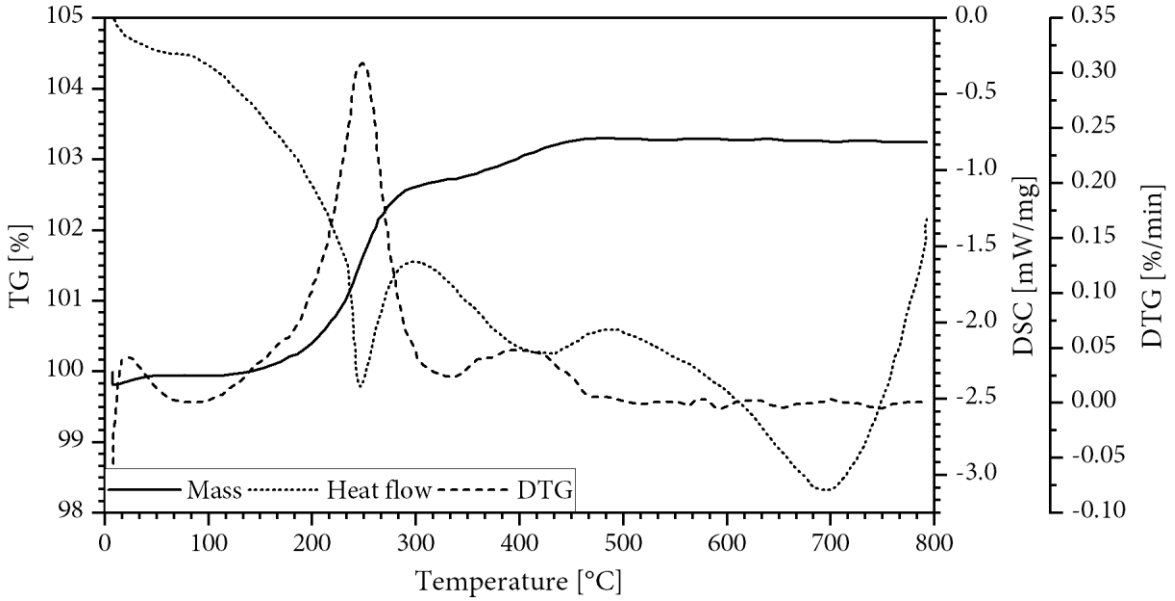

Figure II - 4.11: Literature data for the reactions of magnetite analysed with DSC and TG and DTG [49]

The evaluation of all measurements is carried out as explained in the following sections. Due to clarity, explicit listing of the three measurements is presented. Only the determined standard deviations are given and transferred to the samples of the same series.

4.2.1 Oxidation Reaction

The evaluation of the DSC signals has been explained in theory in chapter 2.2.2. In the following, the analysis of sample HS2-S is carried out as example. Figure II - 4.12 presents the DSC curve of sample HS2-S and the temperature interval of the first peak (115-333°C) is marked for clarification. Furthermore, the baseline of that peak is shown and the area between the signal and the baseline calculated by numerical integration (trapezoidal method, equation (2.25)) is highlighted. According to equation (2.23), the integral represents the enthalpy of reaction (ΔH_R). For sample HS2-S, a peak area and thus reaction enthalpy of 155.35 J/g (exothermic) could be determined. Furthermore, the conversion X for the oxidation reaction is depicted in Figure II - 4.12, as calculated with the help of the peak area according to equation (2.24). From the progress of conversion, the reaction kinetics is analysed analogously to TG-evaluation (cf. chapter 4.1.1).

Using the presented methods, the entire HS2 sample series is evaluated with regard to the heat of reaction (thermodynamics) and the reaction kinetics.

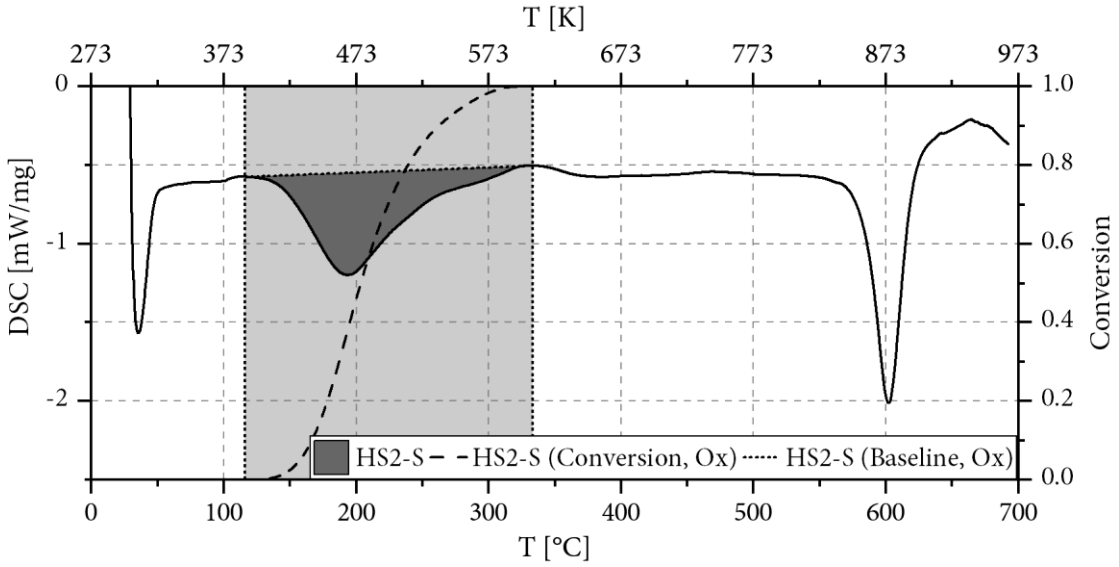

Figure II - 4.12: Exemplary evaluation of conversion and reaction progress from oxidation reaction with DSC-data from sample HS2-S.

4.2.1.1 Heat of Reaction

Similar to the exemplary determined reaction enthalpy of 155 J/g for sample HS2-S, the oxidation reaction enthalpies for all samples of the HS2-series have been determined. By means of the molar weight, the unit is converted into kJ/mol. For this purpose, the stoichiometry deviation is also included in the calculation of the molar weight of the sample, since the DSC signal refers to the sample mass (see chapter 0). The results are shown in Table II - 4.4, while the relative standard deviation (rel. Std.) is provided from the multiple measurements of samples HS2-A, HS2-J and HS2-S as already explained.

In order to visualize the data, it is plotted (cf. chapter 4.1.2) against the material characteristics in Figure II - 4.13. According to the considerations from chapter 0 with equation (2.5), a correlation between the Fe^{2+}/Fe^{3+}-ratio or the stoichiometry deviation should exist. The lower the Fe^{2+}-content, the lower the heat of reaction will be. Howerver, this is not recognizable in the corresponding Figure II - 4.13, which also shows a curve representing the theoretical enthalpies calculated by applying Hess's law to equation (2.12). It can be clearly deduced that the measured enthalpies do not fit the measured Fe^{2+}/Fe^{3+}-ratios. The reasons can either be an incorrect determination of the ratio or measurement errors of the DSC, whereby the latter reason can rather be excluded by the error bars (statistical error).

Table II - 4.4: Heat of reaction for oxidation reaction calculated from DSC-data for all samples of HS2-series

Sample	Precursor	δ	$M_{Magnetite}$	$\Delta_R H$		rel. Std.
			g/mol	J/g	kJ/mol	%
HS2-A	FeCl2	0.17	222.06	102.05	-22.66	
HS2-B	FeCl2	0.16	222.82	105.43	-23.49	
HS2-C	FeCl2	0.14	223.56	102.36	-22.88	
HS2-D	FeCl2	0.08	227.01	114.12	-25.91	
HS2-E	FeCl2	0.01	230.97	112.46	-25.98	10.5
HS2-F	FeCl2	0.02	230.40	108.10	-24.91	
HS2-G	FeCl2	-0.03	233.42	121.07	-28.26	
HS2-H	FeCl2	0.09	226.35	126.59	-28.65	
HS2-I	FeCl2	0.02	230.40	146.81	-33.82	
HS2-J	FeSO4	0.10	226.01	107.86	-24.38	
HS2-K	FeSO4	0.00	231.54	119.82	-27.74	
HS2-L	FeSO4	0.04	229.51	103.35	-23.72	
HS2-M	FeSO4	0.00	231.54	108.93	-25.22	
HS2-N	FeSO4	-0.06	234.69	105.39	-24.73	7.7
HS2-O	FeSO4	0.08	227.01	99.49	-22.58	
HS2-P	FeSO4	0.03	229.81	118.19	-27.16	
HS2-Q	FeSO4	0.09	226.68	115.93	-26.28	
HS2-R	FeSO4	0.08	227.34	103.75	-23.59	
HS2-S	FeSO4/FeCl2	0.05	228.90	168.92	-38.67	
HS2-T	FeSO4/FeCl2	0.02	230.40	199.44	-45.95	
HS2-U	FeSO4/FeCl2	0.05	228.90	206.04	-47.16	
HS2-V	FeSO4/FeCl2	0.03	230.10	223.32	-51.39	
HS2-W	FeSO4/FeCl2	0.03	230.10	225.59	-51.91	9.2
HS2-X	FeSO4/FeCl2	0.04	229.51	217.62	-49.95	
HS2-Y	FeSO4/FeCl2	-0.02	232.90	251.12	-58.48	
HS2-Z	FeSO4/FeCl2	-0.02	232.63	253.83	-59.05	
HS2-AA	FeSO4/FeCl2	-0.06	234.94	241.65	-56.77	

Contrary to the plot against the Fe^{2+}/Fe^{3+} ratio, it is noticeable that there is a linear correlation to the particle size (see Figure II - 4.14, left). Therefore, a linear regression was carried out for this dependency, which shows a very high correlation (correlation coefficient R^2=0.96) with the following equation:

$$\Delta_R H \left[\frac{kJ}{mol}\right] = -0.45 \cdot d_P[nm] - 10.7 \tag{2.54}$$

A dependence of the reaction enthalpy on the conductivity cannot be found (cf. Figure II - 4.14, right), and would also not be logically explainable. The correlation of particle size is all the more remarkable, as no dependencies were expected in this case either.

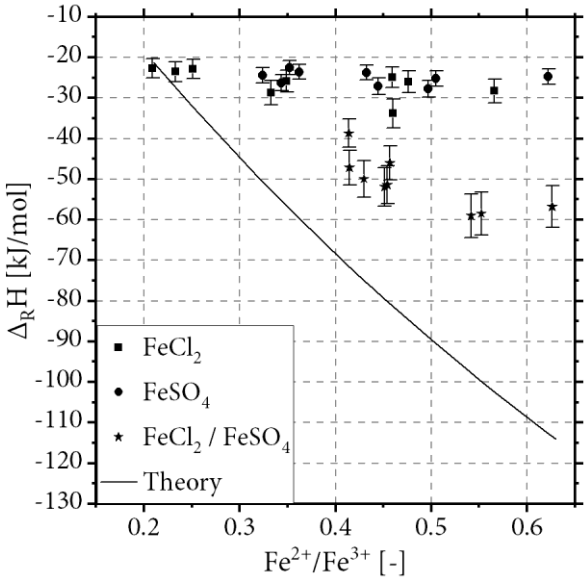

Figure II - 4.13: Reaction enthalpy of oxidation reaction versus the Fe^{2+}/Fe^{3+} ratio. Experimental values, calculated from DSC-data of HS2-series are presented in relation to the calculated theoretical values.

4.2.1.2 Reaction kinetics

With the conversion, calculated as explained in chapter 4.2.1, the further evaluation was carried out similar to chapter 4.1.1 and the different kinetic models were tested using the Coats-Redfern method (cf. Figure II - 4.2). A graphical representation is omitted here, the results of the calculations for example HS2-S (cf. Figure II - 4.12) are shown in Table II - 4.5.

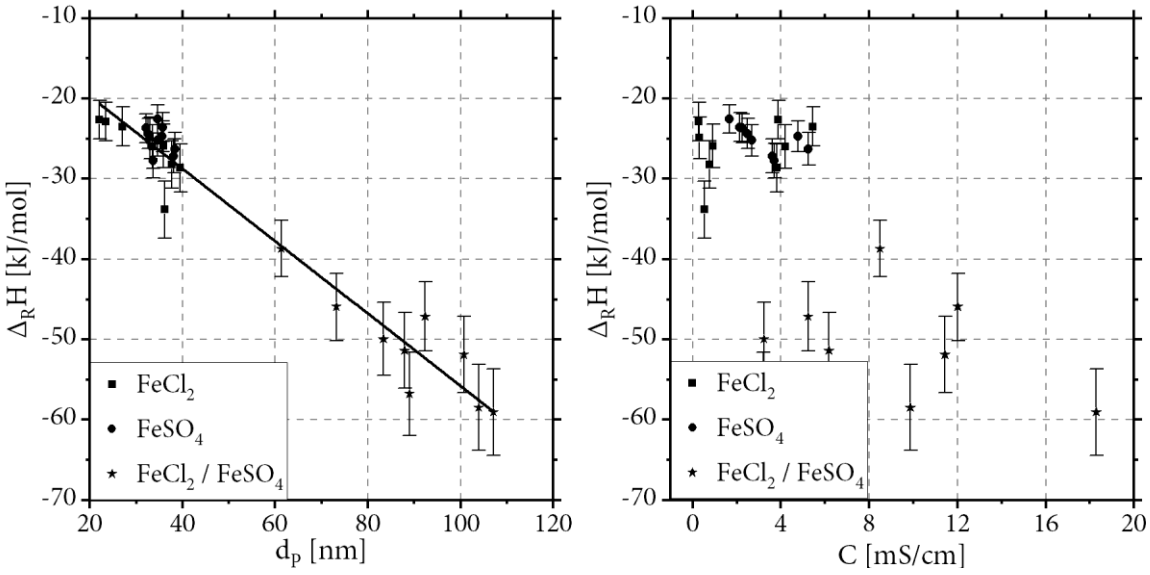

Figure II - 4.14: Experimental reaction enthalpies of oxidation reaction calculated from DSC-data of HS2-series versus particle size d_P (left) and sample conductivity C (right). Regression formula on the left: $\Delta_R H$=-0.45*dP-10.7; R^2=0.96.

Table II - 4.5: Regression coefficients and activation energies for all tested models on oxidation kinetics of sample HS2-S from DSC-data

Reaction order			Nucleation			Avrami-Eroveef			Contraction			Diffusion		
	E_A kJ/mol	R^2		E_A kJ/mol	R^2		E_A kJ/mol	R^2		E_A kJ/mol	R^2		E_A kJ/mol	R^2
F1/3	29.3	0.53	P3/2	14.5	0.37	A1	39.8	0.71	R2	31.3	0.57	D1	61.3	0.56
F3/4	34.9	0.64	P1/2	8.6	0.27	A3/2	23.5	0.66	R3	33.6	0.61	D2	66.8	0.60
F3/2	53.0	0.84	P1/3	2.8	0.07	A2	15.4	0.59				D3	76.2	0.68
F0	26.2	0.47	P1/4	-0.2	0.00	A3	7.3	0.40				D4	69.7	0.62
F1	39.8	0.71				A4	3.2	0.18				D5	105.2	0.84
F2	69.7	0.88										D6	57.4	0.53
F3	107.6	0.87												

For the sample HS2-S, the 2nd order reaction model (F2) provides the best regression coefficient or fit. But the 3rd order reaction (F3), the 3/2th order reaction (F3/2) and the diffusion model D5 also provide regression coefficients in a similar order of magnitude. Using the A1-model according to Avrami-Eroveef, which showed good regression in the TG analysis, no reasonable fit was achieved. On average over all samples of HS2-series, the second-order reaction (F2) provides the best congruence with the experimental results, which is why the following remarks also refer to this model.

Referring to the TG analyses, the activation energies for all samples of sample series HS2 were determined using the second-order reaction and presented in Table II - 4.6. The relative standard deviations were determined from the triple measurements of the samples HS2-A, HS2-J and HS2-S. In Table II - 4.6 it is particularly noticeable, that the determined activation energies of the samples from $FeSO_4$ show high discrepancies. While the samples HS2-J to HS2-M are in the range of 80 kJ/mol, the analyses of the samples HS2-N to HS2-R show values in the range of 125 kJ/mol. This fact cannot be explained so far.

The activation energies are also plotted against the particle size of the magnetites and the conductivity of the samples as shown in Figure II - 4.15 (analogously to Figure II - 4.5). Except from some outliers in the case of $FeSO_4$-magnetites there is a tendency towards higher activation energies with increasing particle size and increasing conductivity. These dependencies are also visible in Figure II - 4.16, which presents the projections of particle size and conductivity axes of Figure II - 4.15. However, the scattering of the values regarding the conductivities is high, thus a regression would be weak. In the range of low conductivities (0-8 mS/cm) there is a broad scattering of activation energies, which is also independent of the anions.

Table II - 4.6: Activation energies (2nd order reaction) for all samples of HS2-series from DSC-data

$FeCl_2$			$FeSO_4$			$FeSO_4/FeCl_2$		
Sample	E_A [kJ/mol]	Std. [%]	Sample	E_A [kJ/mol]	Std. [%]	Sample	E_A [kJ/mol]	Std. [%]
HS2-A	77.70		HS2-J	80.40		HS2-S	107.95	
HS2-B	82.16		HS2-K	78.65		HS2-T	118.11	
HS2-C	79.78		HS2-L	85.36		HS2-U	105.37	
HS2-D	96.21		HS2-M	85.86		HS2-V	111.35	
HS2-E	95.84	2.7	HS2-N	127.81	3.6	HS2-W	113.17	5.3
HS2-F	93.24		HS2-O	123.87		HS2-X	111.23	
HS2-G	96.34		HS2-P	129.61		HS2-Y	115.95	
HS2-H	96.34		HS2-Q	127.34		HS2-Z	120.30	
HS2-I	88.33		HS2-R	125.08		HS2-AA	109.14	
Mean	89.55		Mean	107.11		Mean	112.51	

The highest values of activation energy are provided from the five already stated $FeSO_4$-magnetites (Samples HS2-N to HS2-R). Considering these values as outliers (although no test is applicable here), reasonable linear correlation of increasing activation energy with particle size d_P is obvious. The linear regression (omitting outliers) delivers a R^2 of 0.82 with the function:

$$E_A\left[\frac{kJ}{mol}\right] = 0.426 \cdot d_P[nm] + 74.036[nm] \tag{2.55}$$

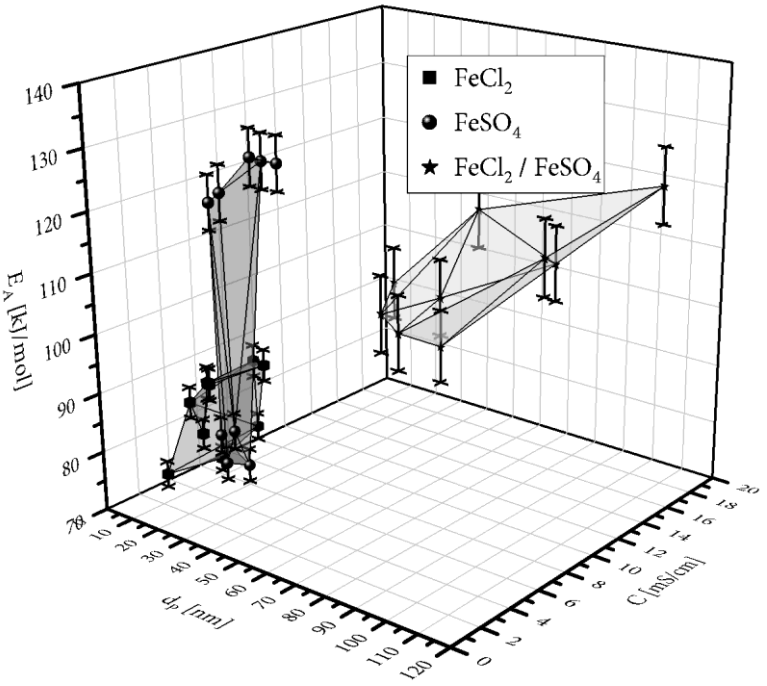

Figure II - 4.15: Plot of activation energies (2nd order model, from DSC-data) of oxidation from HS2-series in dependency of particle size d_P and conductivity C of the samples.

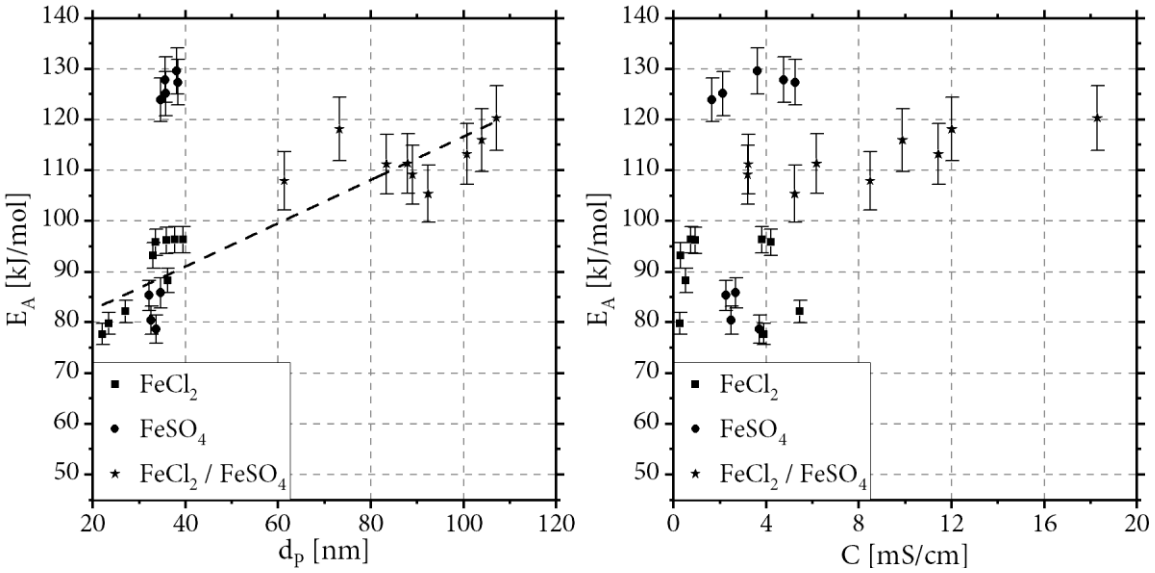

Figure II - 4.16: Plots of activation energies E_A (2^{nd} order model, DSC-data) of oxidation from HS2-series; Left: E_A vs. particle size d_P (regression without outliers in the top left corner); Right: E_A vs. conductivity C of the samples.

The dependency regarding sample conductivity also becomes clearer without outliers, but at higher conductivities, no significant increase is observable anymore. Linear regression results in correlation coefficients below 0.5, logarithmic correlation is even worse. It is concluded from this (similar to the results found with the TG analysis), that the conductivity has no correlating influence on the kinetics of the oxidation reaction.

Figure II - 4.17 presents the activation energy as a function of the Fe^{2+}/Fe^{3+} ratio. As a tendency, the activation energy increases with increasing Fe^{2+} content. However, the scattering is again very high, which is why a regression has not been applied. Reference is made to the fact that other variables, that were not explicitly considered here, may have an influence as e.g. the actual crystal structure.

4.2.2 Conversion Reaction

Comparable to the oxidation reaction, which was evaluated in the previous chapter, the DSC data is used to analyze the crystal transformation reaction (cf. chapter 2.1.4.2).

Figure II - 4.18 again shows the DSC curve of sample HS2-S, but the second peak is emphasized with its evaluation interval (540-640°C), the baseline and peak area generated by numerical integration and the calculated conversion curve. The reaction enthalpy (ΔH_R) determined in the example HS2-S is 123 J/g.

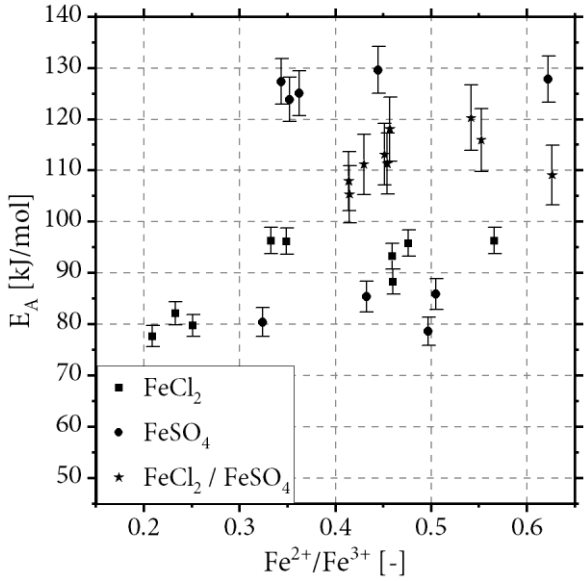

Figure II - 4.17: Plot of activation energies (2nd order model, DSC-data) versus the Fe^{2+}/Fe^{3+} ratio for all samples of HS2-series

4.2.2.1 Heat of Reaction

Table II - 4.7 lists the results of the reaction enthalpies for the sample series HS2. For the conversion of the DSC integral (J/g) into the substance-related quantity, the molar weight of maghemite with 159.7 g/mol from the literature (see Table II - 2.1) is utilized (oxidation reaction is completed). It is easy to see that the calculated results of the individual samples only vary within a small range.

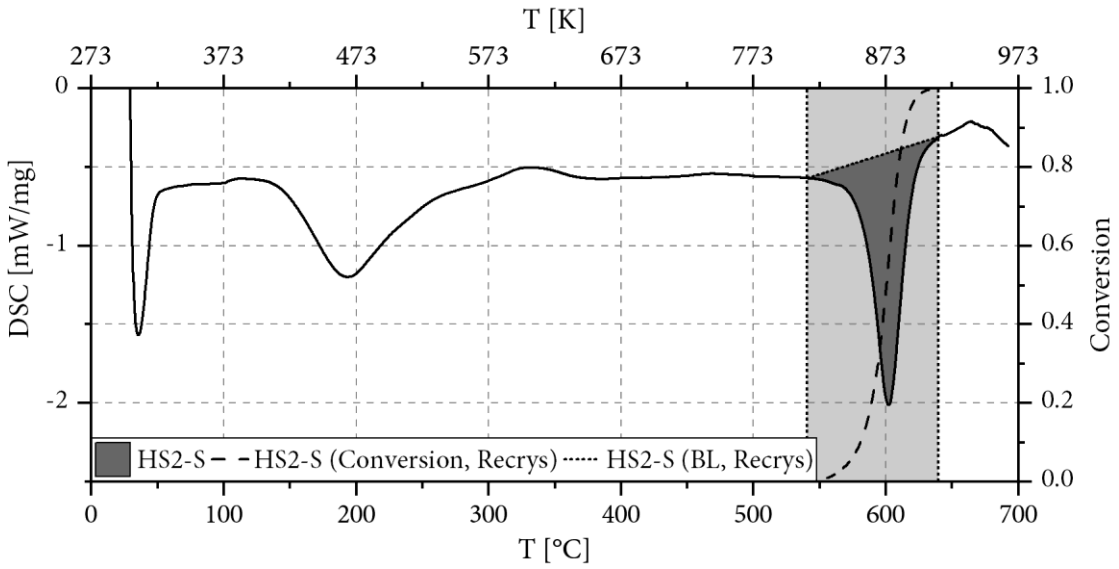

Figure II - 4.18: Exemplary evaluation of conversion and reaction progress from recrystallization reaction with DSC-data from sample HS2-S

Table II - 4.7: Heat of reaction for conversion or recrystallisation reaction calculated from DSC-data for all samples of HS2-series

$FeCl_2$			$FeSO_4$			$FeSO_4/FeCl_2$		
Sample	$\Delta_R H$ [kJ/mol]	Std. [%]	Sample	$\Delta_R H$ [kJ/mol]	Std. [%]	Sample	$\Delta_R H$ [kJ/mol]	Std. [%]
HS2-A	-19.09		HS2-J	-17.72		HS2-S	-20.24	
HS2-B	-20.24		HS2-K	-17.83		HS2-T	-23.90	
HS2-C	-19.13		HS2-L	-17.96		HS2-U	-21.21	
HS2-D	-19.19		HS2-M	-17.07		HS2-V	-18.08	
HS2-E	-19.76	2.7	HS2-N	-18.01	4.2	HS2-W	-18.38	3.4
HS2-F	-19.42		HS2-O	-17.81		HS2-X	-19.30	
HS2-G	-18.91		HS2-P	-17.58		HS2-Y	-20.00	
HS2-H	-22.42		HS2-Q	-18.09		HS2-Z	-20.16	
HS2-I	-19.99		HS2-R	-18.77		HS2-AA	-19.01	
Mean	-19.79		Mean	-17.78		Mean	-20.03	
Std.	1.08		Std.	0.45		Std.	1.75	

Slightly deviating in the comparison of all values are the somewhat lower enthalpies for the magnetites from $FeSO_4$ (-17.78±0.45 kJ/mol). The mean value of all reaction enthalpies is 19.23±1.53 kJ/mol. Within the limits of accuracy, this is an exact agreement with the value of 19.3 kJ/mol calculated from the literature data for the standard enthalpies of formation (cf. chapter 2.1.4.2).

No dependencies regarding the characterization parameters of the magnetite samples can be found. This absence is plausible, since for this reaction the transformation into maghemite has taken place before. This is exemplified in a plot of $\Delta_R H$ versus the Fe^{2+}/Fe^{3+}-ratio in Figure II - 4.19, which also shows the literature value as dotted reference line. Thus, the enthalpy of recrystallization reaction from literature is confirmed. Thermodynamically, the samples showed no difference regarding this point.

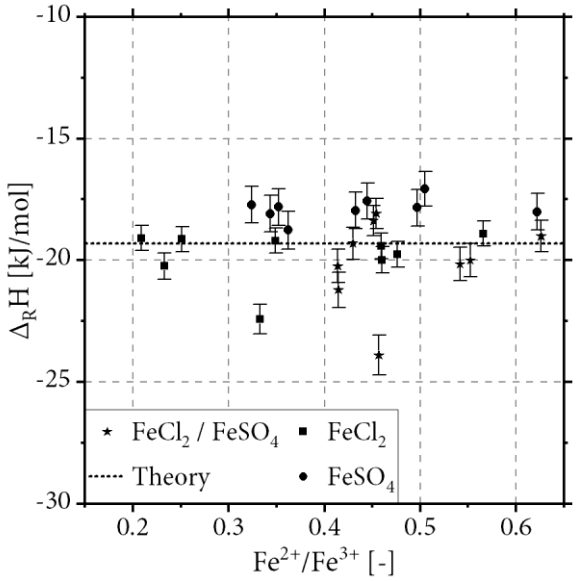

Figure II - 4.19: Plot of reaction enthalpies for conversion reaction of sample series HS2 calculated from DSC-data. Dashed horizontal: calculated reaction enthalpy from literature data.

4.2.2.2 Reaction kinetics

Following the same principle as in chapter 4.2.1.2, the DSC data of the second peak is also evaluated regarding the recrystallisation kinetics utilizing the conversion. As an example, the evaluation of activation energies and regression coefficients of all investigated kinetic models is listed in Table II - 4.8 for the sample HS2-S.

Table II - 4.8: Regression coefficients and activation energies for all tested models on oxidation kinetics of sample HS2-S from DSC-data

Reaction order			Nucleation			Avrami-Eroveef			Contraction			Diffusion		
	E_A kJ/mol	R^2		E_A kJ/mol	R^2		E_A kJ/mol	R^2		E_A kJ/mol	R^2		E_A kJ/mol	R^2
F1/3	506.9	0.92	P3/2	313.0	0.89	A1	0.0		R2	526.1	0.93	D1	967.8	0.90
F3/4	563.0	0.95	P1/2	231.2	0.89	A3/2	404.3	0.97	R3	549.4	0.94	D2	1021.3	0.92
F3/2	760.7	0.98	P1/3	149.4	0.88	A2	299.6	0.97				D3	1113.1	0.95
F0	476.7	0.89	P1/4	108.5	0.88	A3	195.0	0.97				D4	1049.0	0.93
F1	613.6	0.97				A4	142.7	0.97				D5	1425.9	0.98
F2	945.9	0.94										D6	925.5	0.88
F3	1358.0	0.84												

A graphical representation comparable to Figure II - 4.2 is omitted in this case. The regression coefficients in Table II - 4.8 reveal, that for the transformation reaction, in contrast to the oxidation, almost all models show a very good correlation with R^2 higher than 0.90 or even 0.95. The best values for sample HS2-S are provided by the D5-model and the F3/2-model, which has a slightly better congruence with experimental data across all samples on average. Consequently, Table II - 4.9 lists the calculated activation energies for all samples of the HS2 series according to the F3/2-model.

In general, the activation energies for the conversion reaction are significantly higher compared to the oxidation reaction, which is plausible due to the higher temperatures in the conversion reaction. In the comparison of the mean values for each individual magnetite precursor, the $FeSO_4$-magnetites stand out. The activation energy is more than 200 kJ/mol higher on average relating the further two precursor variants. Furthermore, the reproducibility of the samples made of $FeCl_2$ as precursor is worse with 25.4% rel. Std. (based on the triple measurement of sample A).

In order to determine further dependencies of the kinetics on the sample characteristics, the values are plotted versus the conductivity and the particle size of the crystallites in Figure II - 4.20. No significant correlations can be identified. Since from theory the reaction only represents a crystalline transformation without a reaction partner, these independencies are also plausible. Projections of the two dependencies from the 3D-view are therefore not presented.

Table II - 4.9: Activation energies (F3/2-model) for all samples of HS2-series from DSC-data

	$FeCl_2$			$FeSO_4$			$FeSO_4/FeCl_2$		
Sample	E_A [kJ/mol]	Std. [%]	Sample	E_A [kJ/mol]	Std. [%]	Sample	E_A [kJ/mol]	Std. [%]
HS2-A	464.42		HS2-J	897.05		HS2-S	760.68	
HS2-B	494.00		HS2-K	802.67		HS2-T	480.63	
HS2-C	684.45		HS2-L	733.71		HS2-U	442.76	
HS2-D	567.72		HS2-M	902.39		HS2-V	725.59	
HS2-E	687.90	25.4	HS2-N	956.33	7.4	HS2-W	804.99	4.1
HS2-F	753.30		HS2-O	886.50		HS2-X	623.54	
HS2-G	758.41		HS2-P	833.85		HS2-Y	593.98	
HS2-H	502.06		HS2-Q	886.48		HS2-Z	606.43	
HS2-I	662.31		HS2-R	735.85		HS2-AA	574.20	
Mean	619.40		Mean	848.32		Mean	623.65	

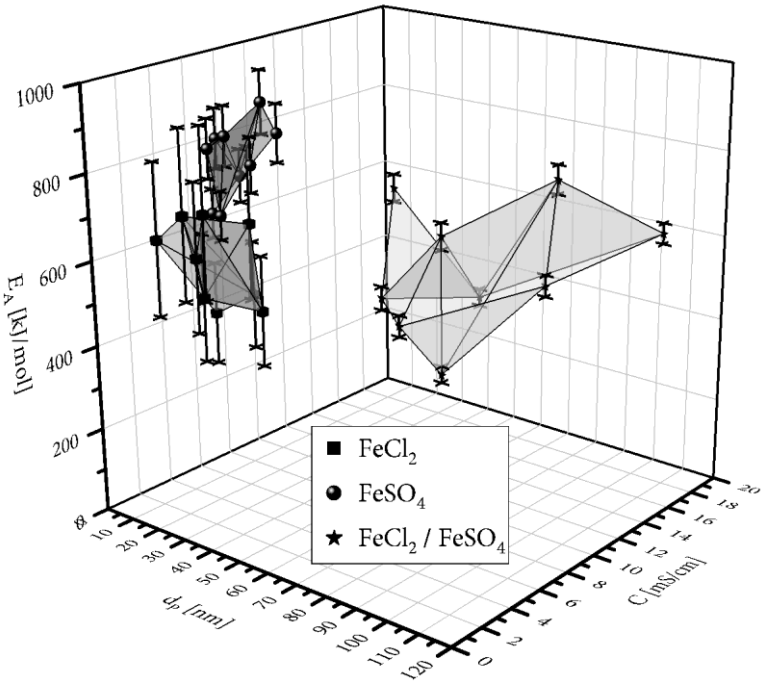

Figure II - 4.20: Plot of activation energies (F3/2-model, from DSC-data) of conversion reaction from HS2-series in dependency of particle size d_P and conductivity C of the samples.

In order to get a thorough picture, Figure II - 4.21 shows a plot of the activation energies (conversion reaction) for the sample series HS2 against the Fe^{2+}/Fe^{3+}-ratio. Again, no correlation can be observed, which is plausible. Due to the finished oxidation reaction, the Fe^{2+}/Fe^{3+} ratio should have no influence here. In contrast, the very broad scattering of the activation energies becomes obvious once again in this plot. This finding is opposed to the reaction enthalpy results (see chapter 4.2.2.1), which showed a high consistency for all samples. The high fluctuation here can only be explained in two ways for the reasons mentioned above:

- The reaction proceeds spontaneously with a high statistical range of variation for nucleation.
- The reaction is influenced by a parameter or material characteristic that is not included in the analysis of this work.

Summarizing, the results show the complexity of the system. It is difficult to make an exact prediction about progress of the conversion reaction based on the known material characteristics.

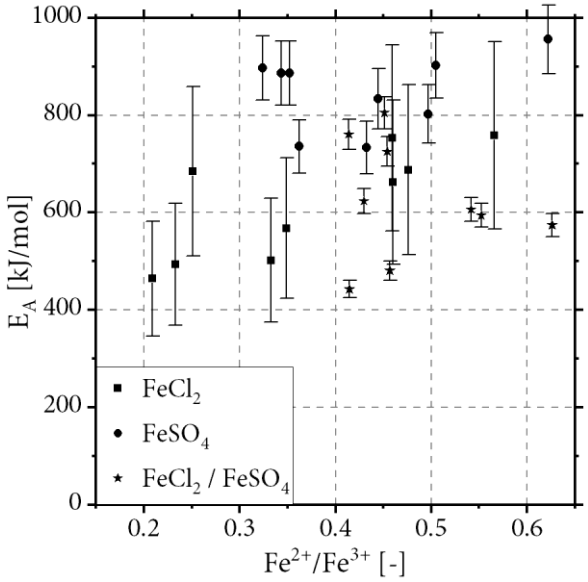

Figure II - 4.21: Dependency of activation energies for conversion reaction (F3/2-model, DSC-data) from the Fe^{2+}/Fe^{3+} ratio for all samples of HS2-series

4.2.2.3 Conversion Temperatures

In analogy to the conversion temperatures (T_C) from the c-DTA data (see chapter 4.1.3), T_C is also determined from the DSC curves, where T_C is the temperature of the second peaks' minimum (see Figure II - 4.18). The results for the HS2-samples are listed in Table II - 4.10.

It is noticeworthy, that the triple measurements of the samples HS2-A, HS2-J and HS2-S show extremely high reproducibilities with rel. Std. below 0.3%. Contrary to the above activation energy results, the scatter within the samples from the same precursor material is significantly lower than for the activation energies. Additionally, it can be derived, that the samples from $FeCl_2$ precursor have the highest transformation temperatures, while the samples from $FeSO_4$ provide the lowest values. This is a further contrast to the determined activation energies, considering the activation energy as temperature proportional "thermal energy". The mixed precursor samples deliver transformation temperatures between the first two precursor materials, which seems plausible. Furthermore, the values are in perfect agreement with the results from the c-DTA analyses of the TG evaluation of HS1-sample series (see chapter 4.1.3). A plot of T_C against particle size and conductivity is shown in Figure II - 4.22. Due to the low standard deviation, the error bars are omitted (clearer visualization). The plots indicate that there are no dependencies on the particle size and the conductivity of the samples. In contrast, it becomes clear that the precursor material in the magnetite synthesis does seem to exert an influence on the conversion temperature.

Table II - 4.10: Conversion temperatures T_C (second reaction step) for all HS2-samples evaluated from the minima in second DSC-peaks

$FeCl_2$			$FeSO_4$			$FeSO_4/FeCl_2$		
Sample	T_C [°C]	Std. [%]	Sample	T_C [°C]	Std. [%]	Sample	T_C [°C]	Std. [%]
HS2-A	603.4		HS2-J	568.8		HS2-S	601.8	
HS2-B	626.2		HS2-K	558.4		HS2-T	603.5	
HS2-C	621.5		HS2-L	571.8		HS2-U	578.5	
HS2-D	625.7		HS2-M	571.1		HS2-V	581.6	
HS2-E	624.5	0.2	HS2-N	571.5	0.3	HS2-W	587	0.3
HS2-F	623.2		HS2-O	567.7		HS2-X	578.7	
HS2-G	621.7		HS2-P	560.4		HS2-Y	592.7	
HS2-H	611.7		HS2-Q	562.9		HS2-Z	601.4	
HS2-I	615.9		HS2-R	561		HS2-AA	579.9	
Mean	619.31		Mean	565.96		Mean	589.46	

The presence of chloride as an anion raises the conversion temperature. Since the chloride concentration in the synthesis from the $FeCl_2/FeSO_4$ mixture was only half as high as in the synthesis from pure $FeCl_2$, the somewhat lower values of the samples from the mixture also fit very well into the pattern here.

The transformation temperatures for the Laux samples LXS-A, LXS-B and LXS-C from chapter 4.1.3, were clearly above 700°C. Thus, the DSC analysis of these samples is not possible with the *Netzsch DSC 204 cell*, because the peaks for the transformation reaction are above the possible temperature range of the apparatus.

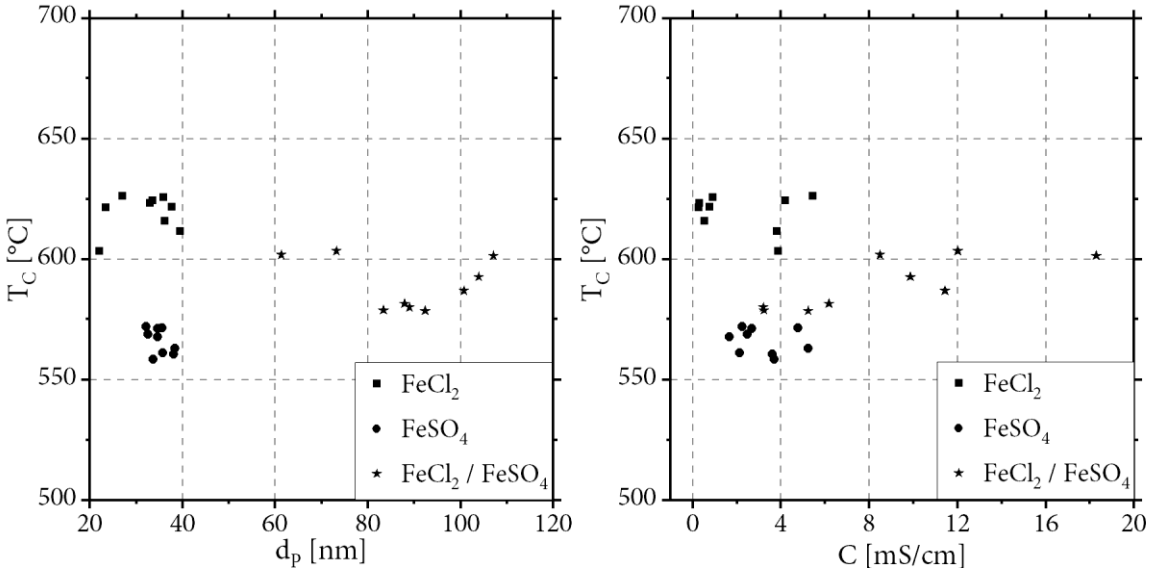

Figure II - 4.22: Diagrams of conversion temperatures T_C (second reaction step) for all HS2-samples evaluated from the minima in second DSC-peaks. Left T_C vs. particle size d_P; Right: T_C vs. sample-conductivity.

4.3 Comparison of Methods (TG & DSC)

Only from sample series HS2 both analyzing methods (TG and DSC) have been applied and data has been recorded. Therefore, a comparison can be made for these samples. For this purpose, the data of both methods is presented in a combined diagram. As example in Figure II - 4.23 samples HS2-A, HS2-J and HS2-S (one sample from each of the three precursor materials) are presented. The measurement conditions are comparable, as heating rates of 20 K/min were used in both methods and synthetic air with similar volume flows was used as purge gas.

The areas of the DSC peaks are colored in light grey analogously to the evaluation stated earlier (see Figure II - 4.12 & Figure II - 4.18), the area of the mass increase in TG is highlighted in dark grey comparable to Figure II - 4.1. A rough correspondence between the areas of mass increase in TG and the first peak in DSC is observable. However, the temperature range of the TG mass increases are entirely included in the peak range of the DSC, which are clearly broader. The onset of the DSC peaks is about 30-50°C below the beginning of mass increases (TG). The DSC-peaks further include the mass decrease always occurring after the increase, which were not considered in the TG evaluation in chapter 4.1.1. In particular, this is well observable in samples HS2-A and HS2-J. This fact can be taken as the main reason for the deviating kinetic models resulting from both methods, as it can also be deduced from this finding that the conversion curves show a different course.

From this first comparison it is furthermore derivable, that the oxidation reaction does not stop with the end of the mass increase, as the exothermic peak area in DSC continues. Conversely, it can also be concluded, that a process causing a loss of mass is superimposed on the oxidation. This could be, for example, the elimination of crystal water or anion compounds of the precursor from the crystal.

Additionally, it is noticeable that the sample HS2-A (synthesized from $FeCl_2$) at approx. 650°C again causes a stronger mass decrease after the second DSC peak. In this step, actually only a crystal rearrangement takes place, which in theory does not cause a mass change. The mass-decrease suggests that the crystal rearrangement again induces the removal of foreign substances from the crystal. The stated behavior is found for all samples of $FeCl_2$, whereas the samples of $FeSO_4$ show an almost constant mass after oxidation. For the samples synthesized from the precursor-mixture, a slower but steady mass decrease in TG takes place after the second DSC-peak is completed.

From these findings, it can be clearly concluded once again for industrial operation, that a magnetite processed directly after synthesis has a different behavior than e.g. an ideal magnetite, which has been tempered before the thermal analysis in laboratory preparation.

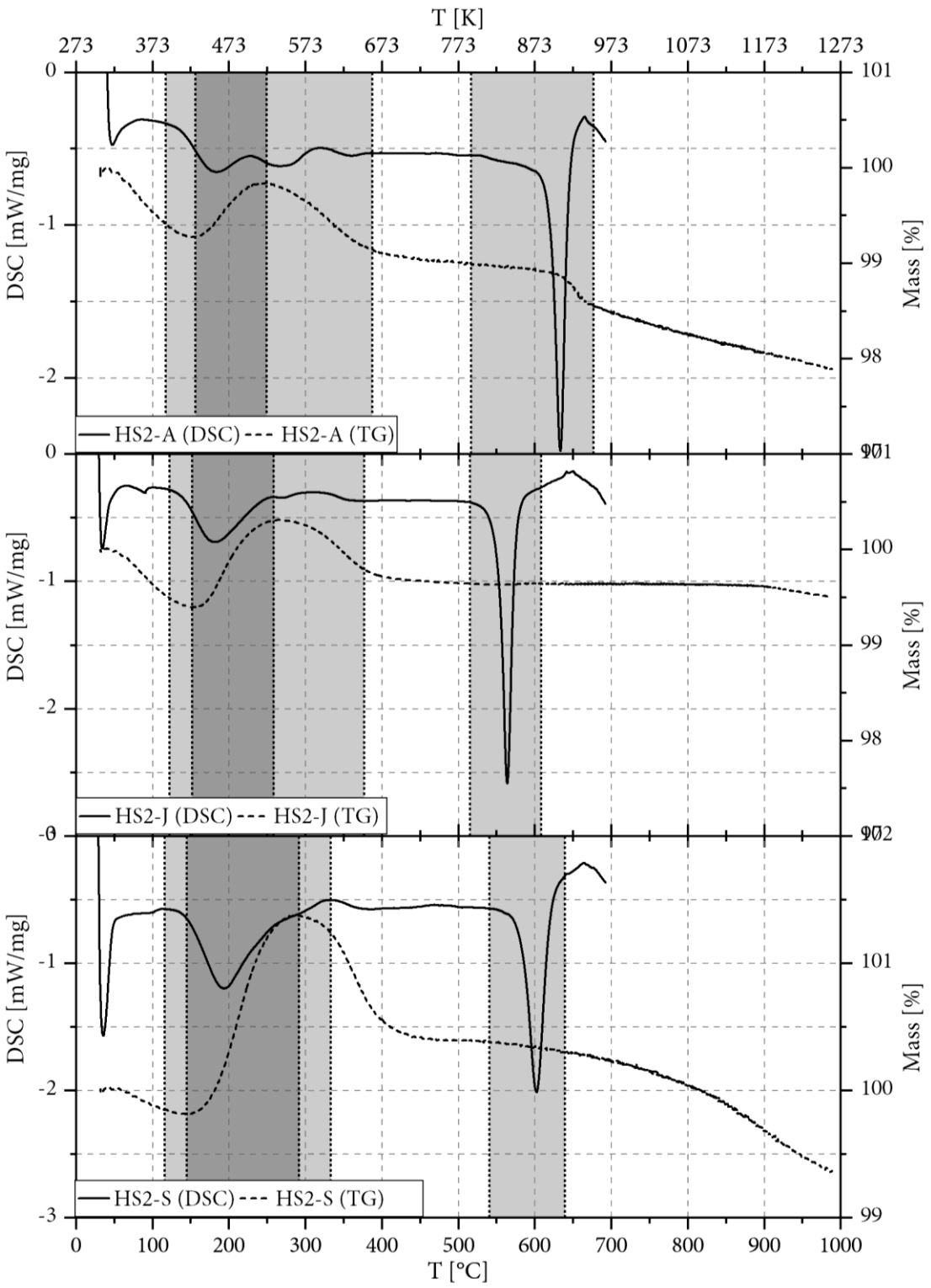

Figure II - 4.23: Comparison of TG and DSC data versus temperature with marked peak-areas (grey, DSC) and marked mass-increase (dark grey, TG). Top: sample HS2-A; Center: sample HS2-J; Bottom: sample HS2-S.

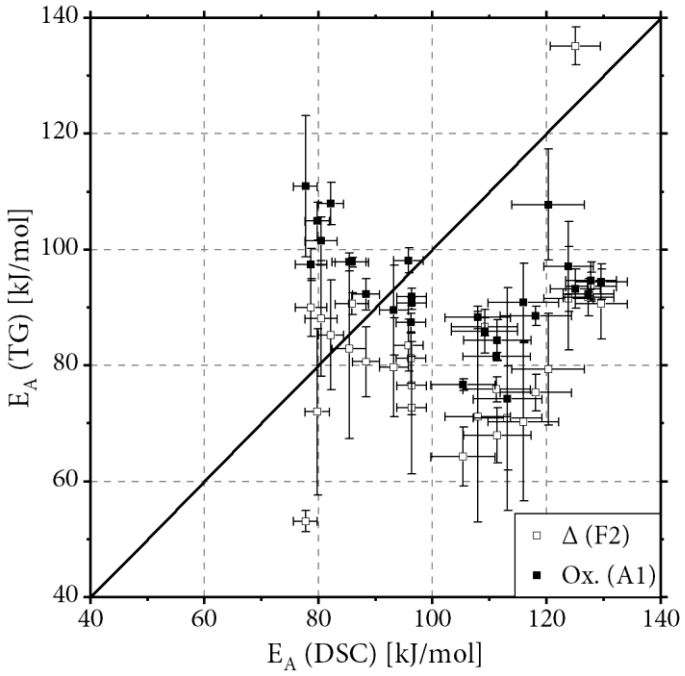

Figure II - 4.24: Comparison of activation energies (HS2-samples) for oxidation calculated from DSC-data (F2-model) with dedicated activation energies calculated from TG-data (oxidation curves with A1-model, difference curves with F2-model).

In addition to the stated general derivations from the combined original curves, the evaluated activation energies for the oxidation reactions are presented in Figure II - 4.24 as comparing diagram for both methods.

No correlation or comparability can be deduced from the diagram regarding the activation energies (the ideal correlation is indicated by the diagonal in the diagram). The finding supports the earlier thesis, that both methods do not provide any comparability or agreement for the oxidation reaction with regards to the evaluated kinetic data.

Besides the kinetics, thermodynamics are compared also. The stoichiometry deviation due to the Fe^{2+}/Fe^{3+} ratio should affect both, the mass increase and the reaction enthalpy for the oxidation reaction. Figure II - 4.25 therefore presents a comparison of the reaction enthalpies determined by DSC (see Table II - 4.4) with the mass increases in oxidation range determined from the TG data. Oxidation-results (Ox) as well as difference-curves (Δ) from TG data is used. Furthermore, the theoretical mass increase Δm for an ideal magnetite of 3.48% and the reaction enthalpy of -91.8 kJ/mol calculated from the standard enthalpies of formation for the reaction of such a magnetite to maghemite are indicated in Figure II - 4.25 as dotted lines.

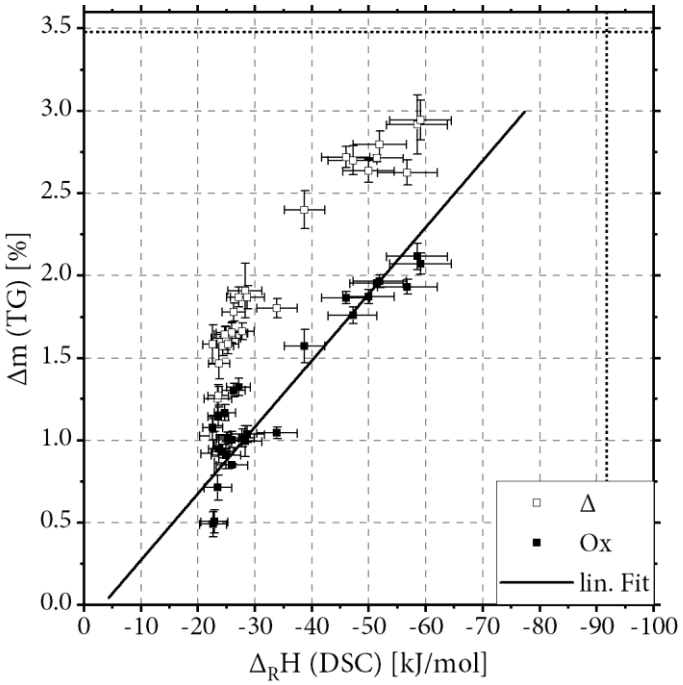

Figure II - 4.25: Comparison of reaction enthalpies for oxidation reaction, calculated from DSC-data, with mass increase in TG-analysis due to oxidation for HS2-samples. Dashed lines represent the dedicated values calculated from theory for ideal magnetite.

A very good correlation of reaction enthalpy and mass increase can be seen. The regression function with a regression coefficient of R^2=0.96 is:

$$\Delta m_{Ox} = -0.040 \cdot \Delta_R H - 0.131 \tag{2.56}$$

From the intercept (-0.131) it can be derived, that the regression passes the origin almost exactly and insertion of the theoretical enthalpy of -91.8 kJ/mol in equation (2.56) delivers a mass increase Δm of 3.54%, which almost exactly agrees with the assigned literature value of 3.48%. This congruence with the theory is remarkable and leads to the conclusion that the methods DSC and TG provide consistent results regarding the thermodynamics. However, mass increase and reaction enthalpy are depending on the Fe^{2+}/Fe^{3+}-ratio, as mentioned earlier. Thus, this finding is also an indication of errors in the measured Fe^{2+}/Fe^{3+}-ratios, since in the analysis of TG or DSC data regarding the ratio delivered no correlation.

Finally, it has to be stated, that combined with the findings from the original curves above (see explanation for Figure II - 4.23) the deviation of enthalpy and mass increase may also be caused by an endothermic evaporation process of e.g. crystal water.

The conversion reaction cannot be compared for both methods, since no data of similar samples is available (no c-DTA data of HS2-samples and no DSC-data of HS1-samples).

5 Interim conclusion & Outlook

In the first part of this work, the main reactions in the kiln have been considered. By means of thermal analysis, the reaction of magnetite as starting material to the intermediate maghemite and subsequently from maghemite to hematite has been investigated. Thermogravimetry (TG) and differential scanning calorimetry (DSC) have been applied for this purpose.

The comprehensive literature analysis showed that magnetite as a starting material can have very different properties (particle size, stoichiometric deviations, impurities) depending on its production process. These properties also influence the reaction behavior.

For this purpose, magnetites were specially produced on a laboratory scale (precipitation process) in order to analyze the influence of the different properties on the oxidation and subsequent recrystallization to hematite. The material characterization included the particle size analysis, determination of stoichiometry deviation (Fe^{2+}/Fe^{3+} ratio), and an estimate of impurities due to different anions (chloride and sulfate). However, the subsequent thermal analyses showed that the comparability of the laboratory-produced preparations with the magnetite from the Laux process (as model) is limited (e.g. significantly higher activation energies for oxidation and transformation). However, the mentioned different behavior of the magnetites depending on the different characteristics in the further course of the reaction was also observed in the experimental part.

The different magnetites were then evaluated via thermal analysis. The measured data were examined with respect to the thermodynamics and the kinetics of the reactions, focusing on the determination of the reaction kinetics and suitable model descriptions. It turned out to be fundamentally challenging to describe the kinetics as a function of the starting material characteristic. Moreover, the evaluation of the kinetics is strongly dependent on the selected analytical method. The following two chapters summarize the results for the two reaction steps oxidation and conversion reaction.

5.1 Oxidation Reaction

The oxidation reaction proceeds according to equation (2.7) or including stoichiometry deviation with equation (2.12). Although oxygen from the gas phase is involved as a reactant, no dependence on the oxygen partial pressure could be determined in the investigated range (relevant at industrial process, see chapter 3.2.1.1). The result is comparable with literature results, where an effect of the oxygen partial pressure was observed only at very low values [27]. The independence is valid for the

laboratory-scale analytical methods mentioned here. However, as explained in chapter 2.1.4.3, there are also macro-effects that have not been taken into account in the conducted measurements.

The analysis regarding the reaction kinetics revealed a very differentiated picture. In contrast to the literature (e.g. Gillot et al. [46]), there is a tendency for the activation energy (based on TG analyses) to decrease with particle or crystallite size (HS1 series, HS2 series and Laux magnetites).

The Laux magnetites show significantly higher activation energies compared to the precipitated magnetites from this work. It should be noted that the mentioned values for activation energies are also strongly dependent on the analysis method and the used evaluation model. The evaluation of the DSC data revealed (comparable to the literature) increasing activation energies for larger crystallites. A good approximation for the investigated range is given in equation (2.55).

In this work, no influence of impurities due to remaining electrolytes etc. on the oxidation reaction kinetics could be observed (HS2 series). However, magnetites from different precursor materials do behave different while oxidation. Magnetites precipitated chloride-containing solutions tended to have higher activation energies and thus higher conversion temperatures (see Table II - 4.6). However, a quantification of this fact is not feasible due to the scatter of the values.

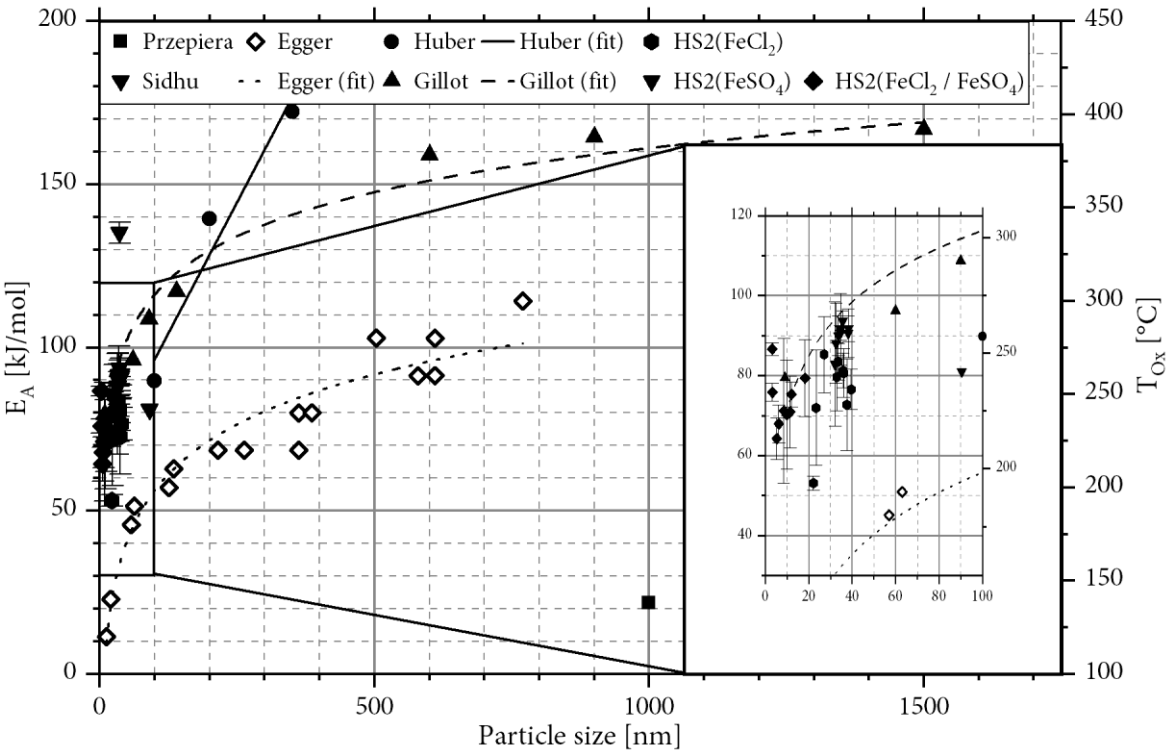

Figure II - 5.1: Results of activation energy (oxidation) versus particle size in comparison with literature values [18,27,44,46,47]. Filled signs indicate activation energies (E_A), hollow signs represent oxidation temperatures (T_{Ox}). Insertion is a zoom of the framed area in the diagram.

Regarding the modeling, the model of 2nd-order reaction was determined as the best description for the oxidation (TG & DSC) in contrast to literature, where different kinetic models for the oxidation reaction were considered as best fit.

Finally, the DSC data was also evaluated thermodynamically. The determined reaction enthalpies do not agree with the literature values. The influence of the Fe^{2+}/Fe^{3+}-ratio (equation (2.12), Figure II - 4.13), which can be derived from theory, could also not be demonstrated with the measurements. Probably the reason for this is the inaccuracy in the determination of the Fe^{2+}/Fe^{3+}-ratio. However, it is assumed that, in addition to the kinetics, the changed heat tone due to deviations in the Fe^{2+}/Fe^{3+}-ratio in particular has a significant influence on the kiln process. Looking at the strongly exothermic reaction, this should be taken into account in reactor modeling.

5.2 Conversion Reaction

The conversion reaction proceeds according to equation (2.18), which reveals that no mass change takes place during the reaction. The experimental analysis was therefore carried out using DSC and c-DTA.

With c-DTA and DSC, the conversion temperatures (T_C) were first determined, since they can be directly deduced from the signals. In their work, Feitknecht and Mannweiler [42] (S3) find a dependence of the conversion temperature on the chloride content of the magnetites. The results of this thesis are similar and show that the transformation temperature depends on the preparation of the magnetite. It can be deduced that magnetites from $FeCl_2$ precursor provide the highest conversion temperatures, magnetites from $FeSO_4$ precursor, on the other hand, have the lowest. The difference is on average about 55°C. Magnetites from the mixed precursor complete the trend with conversion temperatures between these two extrema. The finding is valid for the HS1 series samples as well as for the HS2 series. It is very striking that the transformation temperatures of the Laux magnetites are again approx. 150-200°C above the precipitates (see Figure II - 4.9).

Although the transformation temperatures do not fully describe the kinetics, they can be considered as a measure of the required activation energy. The kinetic analysis was performed for the HS2 sample series using the DSC data. On average, the kinetics of the conversion reaction is best described by the model of a 1.5th order reaction. This is contrary to some literature statements where different models are mentioned for this reaction step (e.g. AEG-A1 [47]). No dependencies on the characteristics of the starting material (magnetite) could be found. Moreover, the scattering

of the values is high, leading to difficulties in the evaluation of trends. In contrast to the conversion temperatures, the $FeSO_4$ magnetites exhibit significantly higher activation energies, which is not plausible.

The reaction enthalpies from the thermodynamic evaluation of the DSC data agree very well with the reaction enthalpy calculated from literature data from standard enthalpies of formation (Figure II - 4.19). As expected, there are no dependencies on other sample characteristics (of magnetite), since a homogenization of the characteristics (especially Fe^{2+}/Fe^{3+}-ratio) has previously taken place due to the oxidation.

For technical applications, the finding of magnetites from $FeCl_2$ exhibiting significantly higher conversion temperatures is decisive. Due to this behavior, the energy consumption is also significantly influenced by the higher temperatures required.

5.3 Outlook

The results from the analyses of this work are extensive. However, weaknesses have become apparent with regards to some of the used methods, which should be remedied by further refinement of the analytical methods. In particular, the determination of the Fe^{2+}/Fe^{3+}-ratio should be mentioned here. Analyses should also be carried out on the samples, e.g. using XRD, in order to be able to evaluate the phase composition of the materials.

In addition to the optimization of the analyses carried out, other decisive points are also relevant to enhance the description of processes taking place in the analyzed reactor/rotary kiln, which are briefly explained below.

5.3.1 Colorimetric investigations

Besides the chemical and physical (thermodynamics and kinetc) consideration of the reactions it is essential in pigment production to characterize the products regarding their coloristic properties. From literature it is known, that the color shades of iron oxides are particle size dependend [6,117]. In a first attempt to investigate the colorimetric properties of the hematites from reaction preparations of the material on white paper have been manufactured. The (remission) spectra of the samples have been recorded with a “UV-Vis-NIR spectrophotometer 5000” (Cary). Additionally, to the spectra, the L*a*b*-values (CIE-L*a*b* color system) have been measured with a “spectro-guide” spectrophotometer (BYK). In the first test-results high variances of the L*a*b*-values are observable. The method (especially of sample preparation in a mortar) has to be refined

to enable the finding of relevant differences in the color shades in further steps. Since the investigated rotary kiln process is applied in pigment production, the information of process impact on the color characteristics of the pigment would be very helpful.

5.3.2 Carbon combustion

As a minor component of the cast iron waste used in the Laux synthesis, carbon is incorporated. Carbon will burn at the temperatures prevailing in the rotary kiln. In order to be able to take the carbon combustion into account in the reactor modeling, the combustion can also be analyzed using thermal methods described in this part of the work.

Part III Solid transport in rotary drums

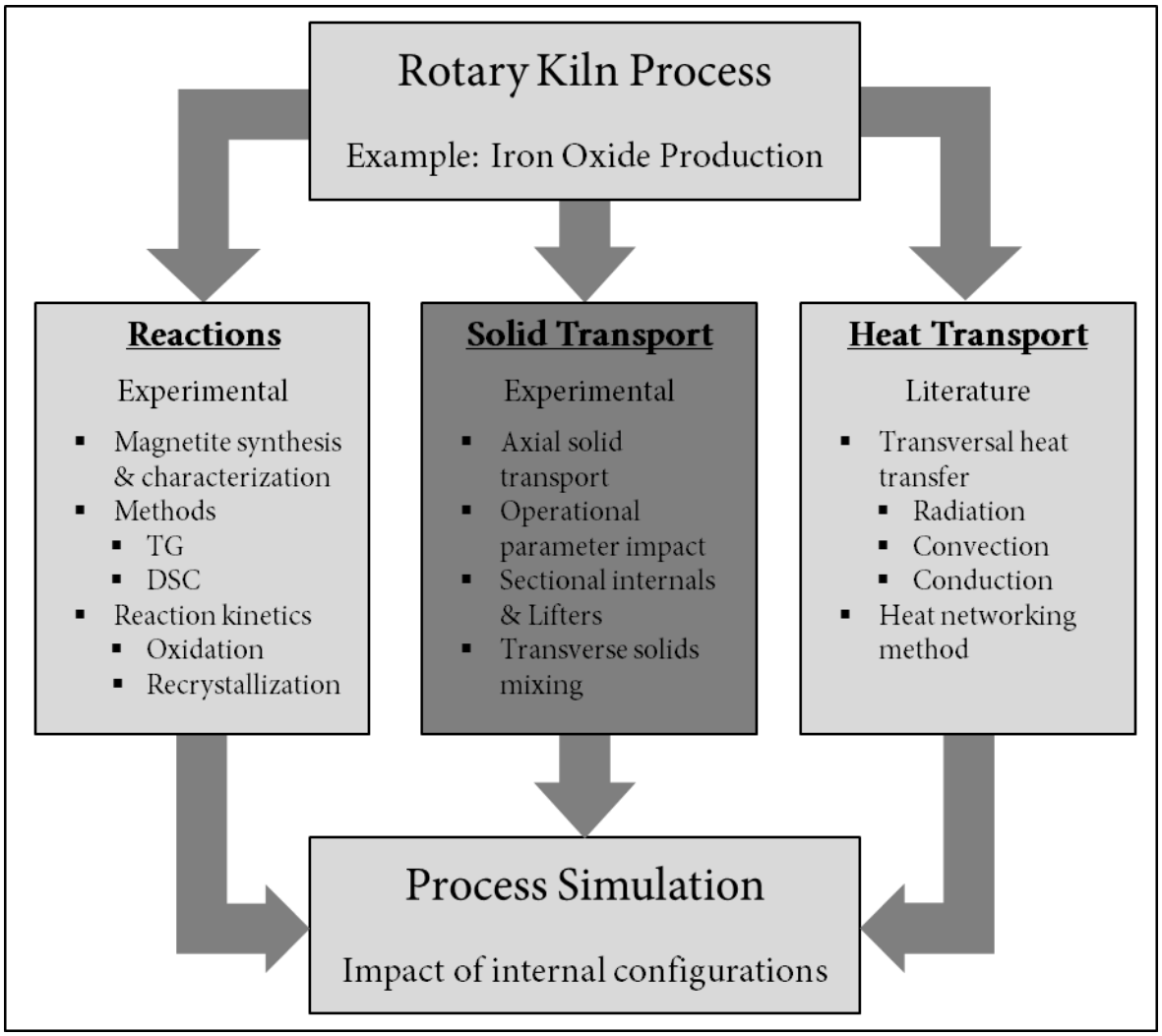

1 Introduction and motivation

A rotary kiln or drum basically consists of a cylinder rotating around its axis while being slightly inclined to the horizontal. At the upper end, the cylinder is charged with a bulk material, which passes the drum as a result of the rotary motion and leaves the tube at the lower end. This is shown schematically in Figure III - 2.1, with a more detailed description in chapter 2.1.

Rotary kilns are no recent invention and have been used in the processing of solids for a long time. The first patent for a rotary kiln was filed in Great Britain in 1885 by the British inventor Frederick Ransome for a new method of manufacturing cement [118–120]. Even though the first patent originated in Great Britain, the first successesful breakthroughs in the use of rotary kilns were reported in the USA [119].

From this moment, the spread of rotary kilns in cement production was unstoppable. Today, the fields of application of rotary kilns have expanded into many areas of thermal (reactive) treatment of solids, such as [119,121]:

- Reduction of ores [119,122] (including sulfide ores) [123]
- Burning of petroleum coke [119]
- Incineration of waste (esp. toxic waste) and pyrolysis [119,124–127]
- Production of polyphosphates [121]
- Thermal soil purification [128,129]
- Pigment production (white [130] and colored [131] pigments)
- Anorganic basic products, e.g. aluminum oxide [121,132]

Specht et al. [133] gave a good overview of the fields of application, in which the versatility of the reactor is clarified by the number of application areas. This versatility is certainly based on the advantages of the rotary kiln technology, which include e.g. [119]:

- High flexibility regarding the feed material characteristics
- Independence regarding the particle size (especially in contrast to e.g. fluidized bed reactors)
- Slurry like solids can be treated
- High temperatures up to 2000K are possible

Rotary kilns are therefore very robust process equipment, both from a mechanical and a process engineering point of view.

Huge experience exists in their design and operation, and they offer advantages that are crucial for some applications. However, systematic engineering and scientific research on rotary kilns with published results, begins a longer time after patenting. Sullivan et al. [134] were the first to publish a research paper providing an empirical description of the residence time. From this point on, there have been many different researchers and research groups that have studied and addressed the issue of solids transport in the rotary kiln. A more detailed introduction about the main findings and results will be given in the following chapter while explaining the current state of research.

The research groups have mainly dealt with the analysis of the rotary kiln behavior with regard to:

- Influence of operating parameters
- Transverse bulk solids transport and mixing
- Axial bulk transport and bed height profiles

The literature research usually distinguishes between axial transport, which is mostly carried out by analyzing the residence time, and transverse transport, i.e. the flow behavior of the material in the cross section of the rotary kiln. There are descriptions and explanations of the behavior of both in the literature.

Rotary kilns are usually individual and specially adapted to the process in which they are applied. In addition to the basic geometric dimensions (length, diameter), this also includes the potential use of a variety of different internals. These are for example:

- Dams / weirs
- Lifters and flights (high number of variations)
- Chains
- Sectional internals (mostly named as heat exchanger internals)

Besides these internals, all combinations of the mentioned options are possible and also further process steps / unit operations can be combined, e.g. a desagglomeration or grinding by means of grinding balls [129]. The extensive literature research performed for this thesis focused on the quantitative influences of these internals. Regarding dams, some authors provide descriptions of their impact. Lifters or flights have been discussed in various ways in numerous research papers and publications. The number is based on the multitude of options in the application, design and construction of lifters. However, the research work on lifters raises the question of transferability to practice, since the analyses and modeling of transverse transport indirectly assume axially continuous flights. In practice, often individual, axial segmented lifters are used.

A literature review on the influence of sectional internals in rotary kilns, on the other hand, was rather unsuccessful, except for the finding that they are used and that various types of construction have been patented as kiln linings. Duda [120] reported on the use of sectional internals ("Dietze" or "Azbe" bridge) in cement production in "long rotary kilns for drying", which are intended to improve heat exchange and mixing. However, quantitative descriptions are not given.

The motivation for further experimental investigations concerning rotary kilns is therefore the unknown (quantitative) influence of sectional internals on the process behavior of rotary kilns. The work focusses on this aspect and for this purpose, both axial and transverse transport are investigated.

With regard to the solids transport processes analyzed in this chapter, there is ambivalence between rotary drums and rotary kilns, since the kiln only differs by the prevailing temperatures. The findings on mechanical solids transport are transferable to other rotary drum applications.

2 Theoretical background and current state of research

In the following chapter, the state of the art in research and technology will be presented with a focus on the process engineering and solids transport in rotary kilns.

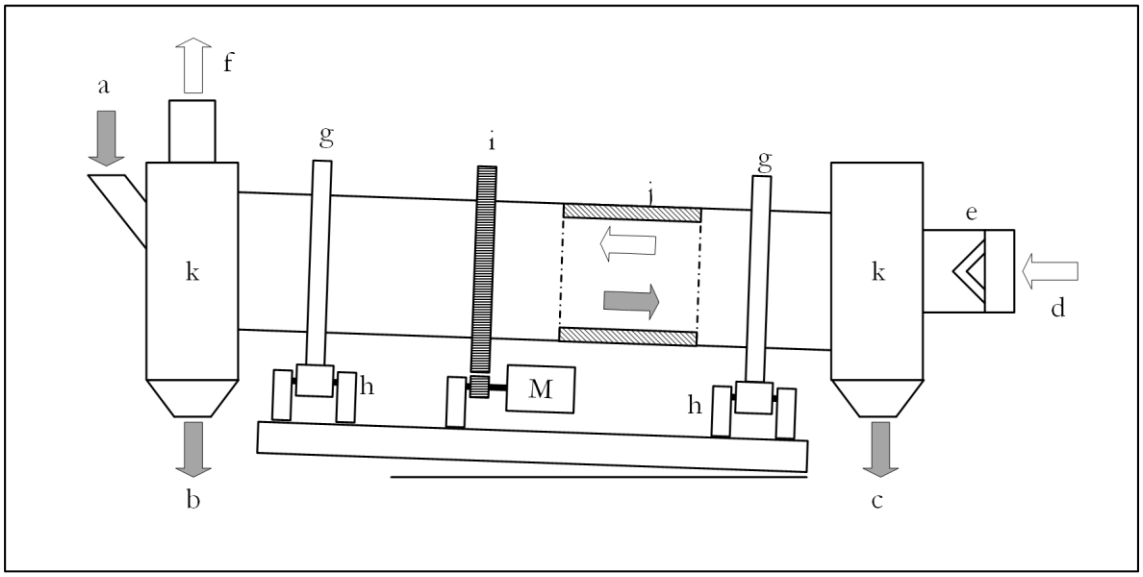

Figure III - 2.1: Sketch of rotary kiln with major construction characteristics (according to [121]). a: material inlet; b: dust/material outlet; c: material outlet; d: gas/air inlet; e: burner/firing; f: gas outlet; g: kiln tires; h: roller station; i: kiln drive (sprocket); j: kiln wall with lining; k: inlet/outlet housing

2.1 Industrial rotary drums / kilns

The areas of application of industrial rotary kilns have been presented in the introduction. Now the basic construction of rotary drums and rotary kilns and their operation will be explained. Figure III - 2.1 shows the typical structure of an industrial rotary kiln.

The kiln consists of a cylinder which is slightly inclined to the horizontal and rotates around its axis. To protect the drum shell (usually made of steel) from the high temperatures from inside, it is mostly lined with a refractory lining (j). The material flow (a) is introduced into the kiln via a chute and passes the drum from the higher to the lower part, where it leaves the kiln (c). Excess material and dust (partially) already leaves the kiln at the inlet (b). Air (d) is fed through fans (not shown), possibly together with fuel, into the burner or furnace (e) to produce the hot gas, which then flows through the kiln and leaves again at the opposite end (f). The drum is equipped with tires (g), which are mounted on the roller stations (h) and provide the rotating movement. The roller stations are mounted on one or more basements and usually provide the kiln inclination via a slight height difference. The rotary motion is generated by a motor (M) and transmitted to the toothed ring of the furnace (i) via a sprocket. The rotary kiln terminates in static housings (k) and is sealed against them in a suitable manner (e.g. segment sealing).

As presented in Figure III - 2.1, the furnace is directly heated and the material flow and the gas flow are countercurrent, which is the most common process mode. However, indirect heating is also possible, e.g. via the furnace shell (electrically or by means of firing). Furthermore, co-current flow of gas and solids is possible. The process control is adapted to the process task and the material properties in the design of the drum.

2.2 Transversal solid motion

The movement of the solids bed inside the rotary kiln is fundamental for the solids transport. This movement is generated by the rotation of the kiln and is therefore initially considered transversely, i.e. in the kiln cross-section in the following.

2.2.1 Types of motion

It is known, that various types of motion occur in the rotary kiln depending (among further parameters) on the rotational frequency. According to Henein et al., the influencing factors which determine this form of motion are as follows [135,136]:

- Particle size (distribution) (d_P)
- Particle shape
- Static angle of repose ()
- Drum diameter / Drum radius (D/R)
- Rotational speed (n)
- Local bed depth (filling degree, Φ).

Henein et al. propose the description of the bed behavior in diagrams as a plot of filling degree Φ versus the Froude number (Fr) [136]. Also by Henein et al. the following relationships were determined as scaling criteria for transverse solids transport.

$$[Fr]_M \left[\frac{D}{d_P}\right]_M^{\frac{1}{2}} = [Fr]_P \left[\frac{D}{d_P}\right]_P^{\frac{1}{2}} \tag{3.1}$$

$$[\Phi]_M = [\Phi]_P \tag{3.2}$$

This relation clarifies that the dimensionless Froude number (Fr), and the degree of filling have a great influence on the type of motion of the material.

The index M specifies the "model scale", P is equivalent to the "production scale". The Froude number is defined as a dimensionless number as follows and indicates the ratio of inertial force to gravity [119,137]:

$$Fr = \frac{\omega^2 \cdot R}{g} = \frac{inertia}{gravity} \tag{3.3}$$

Gravity is represented by the gravitational constant g, while inertia in the case of circular motion in rotary tubes is represented by the centrifugal force with the radius R and the angular velocity ω. Among other authors, Mellmann has published a summary on the types of motion in the transverse plane of rotary drums [138]. Depending on the influencing variables already mentioned, the

following three main types of motion occur in the cross-section of (unmodified) rotary tubes, which in turn can be broken down into sub-forms:

- Slipping motion
  - Sliding
  - Surging
- Cascading („tumbling“) motion
  - Slumping
  - Rolling
  - Cascading
- Cataracting motion
  - Cataracting
  - Centrifuging

The types of motion are represented graphically in Figure III - 2.2 in exemplary sketches.

At low Froude numbers and with low friction between the wall material and the solids, "slipping" (Figure III - 2.2, a) occurs as a type of motion. In this condition, the tube wall rotates "under the solid bed". In sliding-mode, the bed does not move, while in surging mode, the bed is lifted very slightly before sliding down at the wall again without internal displacements of particles.

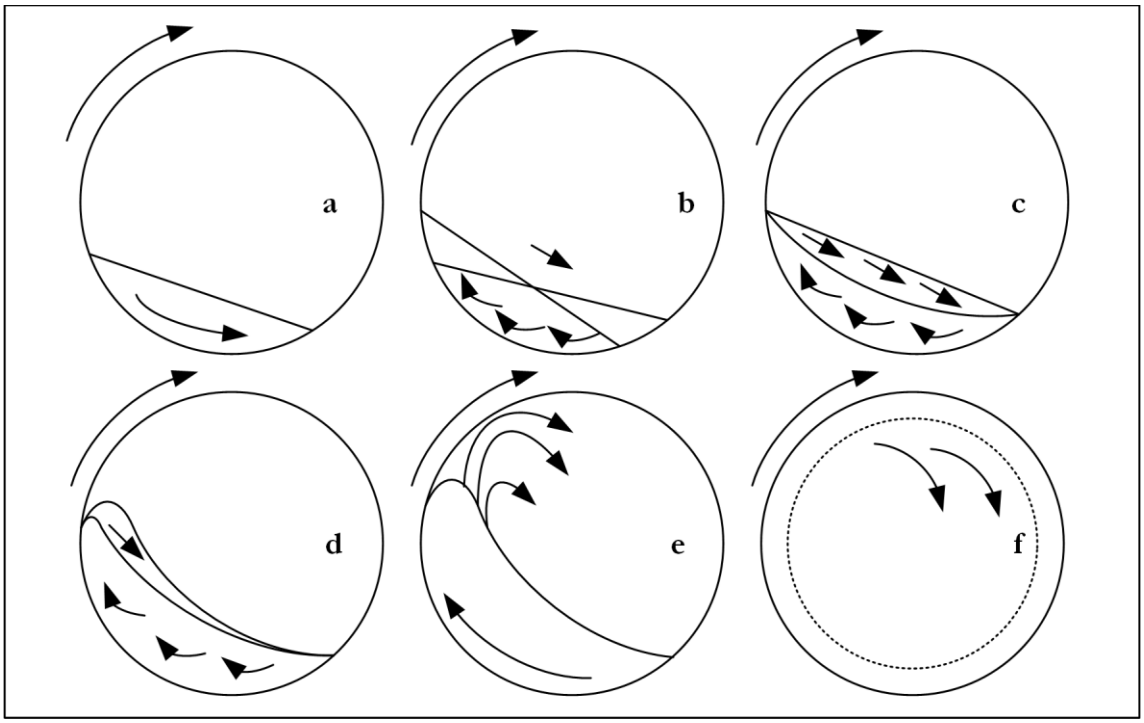

Figure III - 2.2: Different types of transverse solid motion in rotating cylinders (according to [119,135,138]). a: slipping; b: slumping; c: rolling; d: cascading; e: cataracting; f: centrifuging

Cascading motion occurs at higher friction between the solid bed and the wall. The solid bed is lifted during slumping (Figure III - 2.2, b) and a certain amount from the upper area then slides down the surface before this process is repeated. As the rotational speed or Froude number is further increased, the intermittent slumping changes to a continuous process called rolling motion (Figure III - 2.2, c). Material is continuously lifted from the lower bed by the rolling motion and trickles down again at the surface in a film of particles (cascading layer). The solid bed surface is almost flat. With further increases in rotational speed, cascading (Figure III - 2.2, d) begins, and the solid bed is shaped similarly to a kidney in the cross sectional view.

When higher rotational speeds or Froude numbers are exceeded, individual particles are accelerated by the rotary motion in such a way that they escape from the bed into the gas phase, which is then called cataracting (Figure III - 2.2, e). This type of motion is frequently used in ball mill grinding [137,139]. If the critical rotational frequency n_C is exceeded, centrifuging occurs (Figure III - 2.2, f). The critical frequency can be determined by a force equilibrium [139]:

$$n_C = \frac{1}{\pi}\sqrt{\frac{g}{2D}} \tag{3.4}$$

The different types of motion merge into one another depending on the influencing variables already mentioned. Table III - 2.1 provides reference values for these criteria. As in the previous list, the slipping motion is again subdivided into a sliding and a surging motion, with surging representing a kind of transition between sliding and slumping. The basis for Table III - 2.1 is the experimental investigation and empirical modeling of bed bahavior by Henein [135,136] and Mellmann [138].

Rotary kilns are almost exclusively operated in rolling motion. As already explained, a steady state is created where the solid bed can be divided into two regions. In the region close to the wall, the solid particles are lifted laminarly by the rotary motion until they reach the surface. Then they trickle down in a rolling layer on the solid bed surface. This surface layer is called the active layer, since the essential processes such as mixing and heat exchange with the gas phase take place in this layer.

Table III - 2.1: Types of transverse solid motion in rotating cylinders and the regarding process parameters [138]

Basic form	Slipping motion		Cascading motion			Cataracting motion	
Subtype	Sliding	Surging	Slumping	Rolling	Cascading	Cataracting	Centrifuging
Physical Process	Slipping		Mixing			Crushing	Centrifuging
Froude number	$0<Fr<10^{-4}$		$10^{-5}<Fr<10^{-3}$	$10^{-4}<Fr<10^{-2}$	$10^{-3}<Fr<10^{-1}$	$0.1<Fr<1$	$Fr\geq1$
Filling degree	$\Phi < 0.1$	$\Phi > 0.1$	$\Phi < 0.1$	$\Phi > 0.1$		$\Phi > 0.2$	
Wall friction	$\mu_W < \mu_{W,c}$	$\mu_W \geq \mu_{W,c}$	$\mu_W > \mu_{W,c}$			$\mu_W > \mu_{W,c}$	
Application	No use		kilns and reactors; rotary dryers and coolers; mixing drums			Ball mills	No use

The frequent use of the rolling motion is also a reason for the high number of different analyses and modeling approaches for this type of motion. Basically the description of the active layer in shape and size is in focus. Mellmann et al. describe the behavior based on mass- and momentum equations with additional experimental input [140]. Furthermore the flow conditions have been analyzed by e.g. Perron et al. [141] who used a rheological approach to describe the flow. Boateng [142] describes the flow with a continuum model. Nowadays the modeling of rotary drums is mostly performed with CFD ([143]) or DEM-methods [144,145], where velocity fields of the particles and flow regions can be directly deduced.

The presented knowledge on the transverse types of motion is exclusively applicable to bare drums without any internals. Depending on the design, these internals can massively influence the solids transport in the transverse direction.

2.2.2 Mixing & Segregation

Rotary kilns are also frequently used as mixing units in solids processing technology, and the state of mixedness of the solids in the kiln also influences the performance of the rotary kiln as a reactor. This is because good mixing results in homogeneous solids heating and also homogeneous qualities [146]. The mixing of solids is generally attributed to two basic mechanisms (analogously to mixing technology) [147,148]:

1. Convection as transport of particle groups from one place to another ("dividing and rearranging").
2. Diffusion as the random movement of individual particles towards each other.

Additionally, shear mixing can be stated, which is a combination of the two mechanisms in slipping solid layers.

To mix the particles, they must be mobilized by an externally generated motion (e.g. stirring etc.). However, one characteristic of solids is the segregating behavior if the individual particles have different properties with respect to particle size, solid density or particle shape etc. Potentially also interactions between the individual particles affect the segregation [147,149]. Thus particle mixing is always related to the overlaid demixing or segregation, which are [148]:

1. Agglomeration (due to preferential self-agglomeration of one component)
2. Flotation segregation (of coarse particles in a vibrating bed)
3. Percolation (fine particles trickle down through coarse particles)
4. Trajectory segregation (of moving particles)

Mixing in rotating drums has been intensively investigated and is still being further studied nowadays (e.g. [150–152]). In the transverse direction of the drum, mixing is dominated by convection with superimposed diffusion [147]. The description of mixing is connected to the types of motion. Often the rolling motion is targeted, which causes the diffusive layer (active layer).

Percolation is one of the main effects for segregation in rotary drums, if the already mentioned differences in particle characteristics (especially particle size) of the individual particles in the bulk material are present [146]. However, the flotation effect also plays a role, because about 20% size difference is sufficient for segregation in the cross section. The higher the difference, the faster the segregation occurs [147].

In order to describe mixing processes, a brief introduction to the theory of mixing analysis will be presented in the following. The mixing quality at a specific time (t) can be described by the variance (s^2) of the sample concentrations (c) of N samples at different locations (i) [110]:

$$s_t^2 = \frac{\sum_{i=1}^{N}\left(c_{i,t} - \bar{c_t}\right)^2}{1 - N} \tag{3.5}$$

The ‘better’ the mixture is (homogenization), the lower the variance (or standard deviation) becomes, since in the case of the optimal mixture the samples all have the same concentrations. However, the variance describes the mixing condition as a function of the number of samples. A suitable possibility to overcome this is the application of the Lacey mixing index M, which describes the mixing state in the interval from 0 (complete segregation) to 1 (statistically totally mixed). For

this purpose, the theoretical variances of the completely segregated/unmixed state and the fully mixed state have to be known in addition to the current variance. The state of complete segregation can be described by [110]:

$$\sigma_{seg}^2 = c \cdot (1 - c) \tag{3.6}$$

The variance of the statistically fully mixed state is specified with the incorporation of the sample size (K particles in the sample) with [147]:

$$\sigma_{mix}^2 = \frac{\sigma_{seg}^2}{K} = \frac{c \cdot (1 - c)}{K} \tag{3.7}$$

The experimental Lacey mixing index M at the current time t ($M_{t,exp}$) can be calculated using the two former relations with [150,153]:

$$M_{t,\mathrm{exp}} = \frac{\sigma_{seg}^2 - s_t^2}{\sigma_{seg}^2 - \sigma_{mix}^2} \tag{3.8}$$

Opposite to the mixing index, the intensity of segregation (S) or the segregation index is also used in the literature as well [154]:

$$S = \sqrt{\frac{\sum_{i=1}^{N}(c_i - \bar{c})^2}{N - 1}} \tag{3.9}$$

As can be seen easily, the description is similar to the already introduced relation (3.5) and thus the same information is given with the segregation index.

The progress of the mixing process itself can be considered as a kinetic process when applying the mixing index over the time (M_t). It is common to use the 1st order kinetics, which can be related to the time or the number of revolutions n_R [153,155]:

$$M_t = M_\infty \cdot \left(1 - e^{-k \cdot n_R}\right) \tag{3.10}$$

Finally, the mixing process can be described in its progress via the two parameters mixing index in the steady state (M_∞) and the rate constant k. The 1st order kinetics is usually a sufficient description, even though for example 2nd order kinetics have been applied also [153]. Khakhar et al. propose values for the rate constant of mixing of sugar crystals and sugar balls for different filling degrees in the range of 0.03 to 0.50 rev^{-1} [154].

2.3 Axial solid motion

The solid transport in axial direction is the result of the transverse transport in an axially inclined rotary drum. The mobilization of the solid bed via rotation and the axial inclination result in a continuous axial displacement of the solids in the drum.

Different modeling approaches can be used to describe the axial solid transport. In the following, some models described in the literature are introduced and explained. A distinction is made between empirical models (chapter 2.3.1) and the Saeman model (chapter 2.3.2). Finally, the axial dispersion model (chapter 2.3.3) is introduced, which is used in the data analysis in this work.

The central parameter in the description of the axial solid transport is the residence time (t) or the mean residence time ($\bar{t}$, MRT) in the rotary kiln, since this time is essential for the reactions or similar processes taking place.

2.3.1 Empirical models

Basic systematic analyses on the axial solid motion in rotary drums have been performed by Sullivan et al. in 1927 [134], who first investigated the functional dependencies of mean residence time $\bar{t}$ from the geometric dimensions and properties of the drum (length L, diameter D etc.) as well as from the operational parameters (rotational speed n, dum slope β, feed mass flow $\dot{m}_F$ etc.) and the characteristics of the bulk material (angle of repose θ etc.). They found the latter variables to be significant in the design and operation of rotary drums and gave a first empirical equation to describe the residence time [134].

$$\bar{t} = 1.77 \cdot \frac{L}{D} \cdot \frac{\sqrt{\theta}}{n \cdot \beta} \cdot factor \tag{3.11}$$

The authors already propose a “factor”, which is 1 for bare drums and can be used to introduce corrections for different constrictions of the drum. The authors declare the accuracy to <6% for equation (3.11). No influence of the feed mass flow was observed in their studies.

In the early 1950s the US Geological survey provided another formula for the mean residence time, which additionally includes the freeboard gas velocity G and the feed rate F as well as a material constant B (function of particle diameter) [119,156]:

$$\bar{t} = \frac{0.23 \cdot L}{\beta \cdot n^{0.9} \cdot D}\left(\pm 0.6 \frac{B \cdot L \cdot G}{F}\right) \tag{3.12}$$

It is important to mention, that the variables are not in metric units here. Comparing both equations reveals that the dependencies regarding drum length and diameter as well as drum inclination are equal. Regarding rotational speed a slight difference (power of 0.9) is introduced and no material characteristic is needed (repose angle, θ). The braced, second optional part includes a material constant and additionally gas velocities and feed rates have been considered, which is new.

A further model has been developed by Chatterjee et al. as criteria equation based on dimension analysis to calculate the MRT ($\bar{t}$) as one important value in the description of axial solid transport in bare drums [157,158]:

$$\bar{t} = 0.1026 \cdot \frac{L^3}{\dot{V}} \cdot \left(\frac{\theta}{\beta}\right)^{1.054} \cdot \left(\frac{\dot{V}}{L^3 \cdot n}\right)^{0.981} \cdot \left(\frac{L}{D}\right)^{1.1} \tag{3.13}$$

The authors themselves stated, that neglecting the exponents in equation (3.13) close to unity reveals a similarity to equation (3.11) as stated earlier by Sullivan (constant has to be fitted). However, they insist that the feed rate definetly influences residence time. Chatterjee also investigated drums with end constriction dams or conical parts [158,159] and found that dams enhance the residence time and hold-up in the drum.

2.3.2 Saeman model

One of the best known models which is widely used in dimensioning and layout until today is the Saeman-model from 1951 [160]. The basic assumptions in the derivation of the model are presented in Figure III - 2.3.

The Saeman model is based on the description of the path of one particle or a control volume on its way along the rotary drum. The solid bed is shaped like a segment of a circle in the cross section (see Figure III - 2.3, left). The surface of the solid bed is creating a cord through the circle. A particle out of the solid bed is transported in the solid bed by the circular movement until it reaches the surface. After reaching the surface, the particle is assumed to slide down on the top of the bed in the active or cascading layer (cf. chapter 2.2). While slipping down, it moves a short distance in axial direction which is connected to the radius R of the drum, the filling degree (bed height h, which is connected to the length of the cord) and the drum inclination β. Furthermore, the dynamic angle of repose θ is affecting this process. For rotary drums with higher loads it can be observed from experiments that the filling degree is not constant in axial direction (see Figure III - 2.3, right). The filling degree is decreasing from the inlet end of the drum to the outlet end. Since the mass and volume of the bulk material are constant, the effect is evoked by a higher axial particle velocity. By the change in the solid bed height h the cord for cascading is changing in axial direction, too. Therefore the description according to Saeman is written as a first order ordinary differential equation (ODE) regarding the bed height h [156,160,161]:

$$\frac{dh}{dx} = \frac{3 \cdot \dot{V}}{4 \cdot \pi \cdot n} \cdot \frac{\tan(\theta)}{(2Rh - h^2)^{\frac{3}{2}}} - \frac{\tan(\beta)}{\cos(\theta)} + \frac{dR}{dx} \tag{3.14}$$

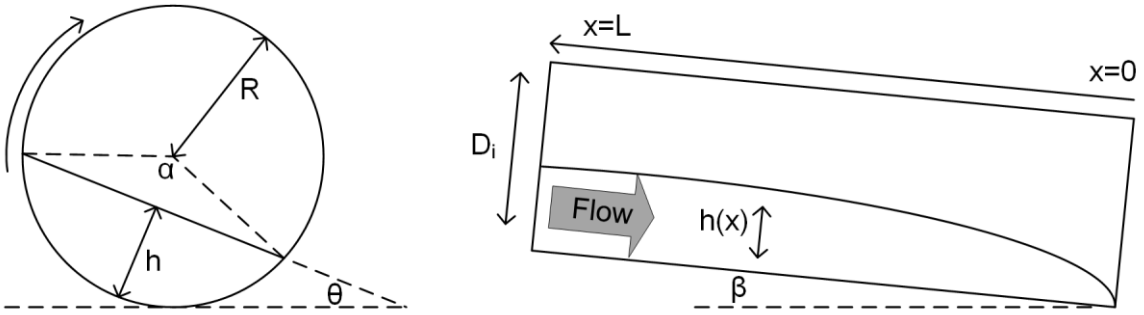

Figure III - 2.3: Sketch of the rotary drum with basic description of the Saeman-model. Left: cross sectional view with the solid bed on the ground; right: side-view with typical solid bed shape in axial direction

This mathematical description can be used for arbitrary drums (e.g. conical in the so called Roto-Louvre type driers), if a functional description of the radius in axial direction is available. Usually the drum is a cylinder and thus the expression dR/dx=0, which leads to:

$$\frac{dh}{dx} = \frac{3 \cdot \dot{V}}{4 \cdot \pi \cdot n} \cdot \frac{\tan(\theta)}{(2Rh - h^2)^{\frac{3}{2}}} - \frac{\tan(\beta)}{\cos(\theta)} \tag{3.15}$$

Similar relations as description of the solid bed even for horizontal drums have been found by others [162,163]. The ODE can be solved numerically, if a boundary condition (height at the beginning) is known. For rotary drums with free discharge end, the boundary condition is the particle diameter d_P [161,164,165]:

$$h(x = 0) = d_P \tag{3.16}$$

Otherwise for rotary drums with constriction dams at the discharge end [161,166]:

$$h(x = 0) = h_{dam} \tag{3.17}$$

Specht et al. introduced the dimensionless “bed-depth”-number Bd from parameters in equation (3.15) with a transition from volumetric feed rate to mass feed rate $\dot{m}_F$ to [133,167]:

$$Bd = \frac{3 \cdot \dot{m}_F \cdot \tan(\theta)}{4 \cdot \pi \cdot n \cdot \rho_b \cdot R^3} = \frac{inertia}{centrifugal\ force} \tag{3.18}$$

Using this Bd-number they propose as boundary condition for the filling degree Φ at x=0:

$$\Phi = 1.75 \cdot Bd^{0.5} \tag{3.19}$$

Besides the numerical solution, Danish et al. and Liu et al. [164,166] developed analytical solutions of the Saeman-ODE, which will not be further evaluated here, since numerical methods are applied in this work.

In order to use and apply the model, the cross sectional area A_{cross} of the solid bed in each increment of the numerical integration of equation (3.15) can be calculated from the bed height h via geometric considerations [168]:

$$A_{cross} = \frac{r^2}{2} \cdot \left[2 \cdot \cos^{-1}\left(1 - \frac{h}{r}\right) - \sin\left(2\,cos^{-1}\left(1 - \frac{h}{r}\right)\right)\right] \tag{3.20}$$

The cross section is integrated numerically as well and results in the hold-up volume V_{hold}. Afterwards, the mean residence time can be calculated from this hold-up and the volumetric flow-rate or mass flow rate to the hydrodynamic residence time τ_{hyd}:

$$\tau_{hyd} = \frac{V_{hold}}{\dot{V}} = \frac{m_{hold}}{\dot{m}} \tag{3.21}$$

In conclusion the Saeman-model combines the geometry of the drum as well as operational parameters and characteristics of the bulk material and leads to the bed height profile (orthogonal to solid bed surface) of the solid bed in the bare drum. The model is used until today to model the solid bed in rotary drums [169,170]. Although it was originally developed for bare cylinders or conical drums, it has also been used to model the behavior of rotary drums with diverse constriction dams etc. [162,171].

2.3.3 Axial dispersion model

The axial dispersion model has been used and proven its capability in a wide range of applications. It's proposal is dedicated to Danckwerts [172], who used it in the investigation and modeling of fluid-processing reactors [173]. The material flow is described by the one dimensional Fokker-Planck equation, which consists of two main effects taking place at the same time. Convective material transport is superimposed by dispersive/diffusional material transport. Diffusional transport in one dimension can be depicted by the second Fick's law to [60]:

$$\frac{\partial c}{\partial t} = D_x \cdot \frac{\partial^2 c}{\partial x^2} \tag{3.22}$$

D_x is the diffusion or dispersion coefficient in the observed dimension. In case of this application in drums or tubes the observed dimension is the axial direction. With superimposed convection the one dimensional axial dispersion model is [173–175]:

$$\frac{\partial c}{\partial t} = D_x \cdot \frac{\partial^2 c}{\partial x^2} - v_x \cdot \frac{\partial c}{\partial x} \tag{3.23}$$

v_x is the velocity in the observed dimension. In order to determine the coefficients in equation (3.23), its dimensionless manifestation is used [60]:

$$\frac{\partial C}{\partial \theta} = \left(\frac{D_x}{v_x L}\right) \cdot \frac{\partial^2 C}{\partial z} - \frac{\partial C}{\partial z} = \frac{1}{Pe} \cdot \frac{\partial^2 C}{\partial z} - \frac{\partial C}{\partial z} \tag{3.24}$$

The coefficient in this equation is a dimensionless group called as Peclet-number (Pe) and describes the relation of convective flow and dispersive motion:

$$Pe = \frac{v_x L}{D_x} \tag{3.25}$$

If Peclet-numbers are small (nearly zero), backmixing is high (nearly perfect) and the model describes a continuous stirred-tank reactor (ideal). The other way around ideal plug flow can be assumed for large Peclet-numbers. Small deviations from plug-flow can be assumed at Peclet numbers above 100 [60].

The partial differential equation (3.24) can be solved analytically for different boundary conditions. For open-open boundary conditions (no disturbances in flow at the inlet and outlet end) and small extends of dispersion (Pe > 100) the curves of the residence time distribution (density distribution, E) have a symmetrical shape and the solution of the differential equation (3.24) is [60,175]:

$$E_\theta = \bar{t} \cdot E = \frac{1}{\sqrt{4\pi Pe}} \cdot \exp\left[-\frac{(1-\theta)^2}{4Pe}\right] \tag{3.26}$$

The symmetrical shape of the RTD-curve is similar to the Gaussian distribution. With residence time on the abscissa the Gaussian distribution is presented in equation (3.27).

$$E = \frac{1}{\sqrt{2\pi\sigma^2}} \cdot \exp\left[-\frac{(t-\bar{t})^2}{2\sigma^2}\right] \tag{3.27}$$

A comparison of equations (3.26) and (3.27) leads to the following expression (dimensionless dispersion, σ_θ^2) to calculate the Peclet-number from the Gaussian distribution [60,176,177]:

$$\sigma_\theta^2 = \frac{\sigma_t^2}{\bar{t}^2} = \frac{2}{Pe} = 2 \cdot \left(\frac{D_x}{v_x L}\right) \tag{3.28}$$

For further determination the Gaussian distribution is fitted to the measured RTD-curves (E) via least squares-method. The two fit factors are mean residence time ($\bar{t}$, maximum of distribution) and the standard deviation or variance (σ^2). The two parameters are used to calculate the Peclet-number according to equation (3.28) and thus the amount of axial back-mixing in the drum or the axial dispersion coefficient. Peclet-numbers in the range of

The mean axial velocity $\bar{v}_x$is calculated from the drum length L and the mean residence time $\bar{t}$ with:

$$\bar{v}_x = \frac{L}{\bar{t}} \tag{3.29}$$

The use of the axial dispersion model is advantageous especially in scientific investigation, since information on axial transport and dispersion effects can be derived at once. Abouzeid et al. [178] and Rutgers [179] conducted stimulus response experiments with rotary drums and demonstrated the applicability of the axial dispersion model with the assumptions made earlier (symmetric distribution). They found the dispersion to increase with rotational speed and decrease with drum inclination while feed rate had no significant effect. Abouzeid et al. additionally found, that dimensionless dispersion only depends on residence time with [180]:

$$\log\left(\sigma_\theta^2\right) = 2.68 \cdot \log(\bar{t}) - 7.62 \tag{3.30}$$

This information therefore allows scaling of the RTD meaning, that increased MRT always leads to higher standard deviation or a wider distribution.

Rutgers found axial dispersion coefficients down to 0.04 cm^2/s, Sheritt et al. [174] conclude a range of axial dispersion coeffients in bare drums from 10^{-7} to 10^{-4} m^2/s.

2.4 Internals in rotary drums

Rotary kilns and dryers are often individually adapted to the process in which they are applied. The bare rotary kilns considered so far can be equipped with a wide variety of internal components, whose basic types have been named in the introduction. These internals also influence the material transport [133].

The simplest internals are weirs or dams. These represent a circular constriction of the cross-section and are often installed at the outlet end [161]. As a result, the material in the solid bed is retained by the dam, increasing the hold-up and thus also the residence time [157]. Sullivan already gave a modified formula for this based on equation (3.11) by adjusting the factor [134,161]:

$$factor = \exp\left[\left\{\left(0.12 \cdot \frac{L}{D} - 3.86\right) \cdot log\left(\frac{2.5 \cdot \dot{V}}{n \cdot \dot{V}}\right) + e^{2.3-0.32 \cdot \frac{L}{D}} - 1\right\} \cdot \frac{h_{dam}}{D - 2 \cdot h_{dam}}\right] \tag{3.31}$$

The impact of dams has been considered in many studies. Chatterjee et al. report that a dam at the outlet end leads to an almost flat solid bed in the axial direction [157] and also influences the dependencies with regard to the operating parameters speed, inclination and feed rate [158]. In addition, back-spillage occurred in the experiments with dams, which indicates a capacity limitation.

Scott et al. [171] tested the applicability of the models of Saeman and Kramers and Crookewit, respectively, to rotary drums with dams (as weirs or tapered dams at the outlet end as well as mounted centrally in the drum). They found a very good agreement between the modeled axial bed height profiles and the experimental determination and concluded a good applicability of the models even for variable cross sections. Ndiaye et al. [170] also successfully used the Saeman model to calculate the solid bed height profile in an industrial rotary kiln with an outlet dam.

Besides dams, the impact of further internals is considered in the following.

2.4.1 Lifters & Flights

Lifters and flights are frequently used in rotary drums in the field of drying [181,182]. These are shovel like constructions mounted parallelly to the axis from the inside wall of the drum. The intention of installation is lifting a portion of the bulk material from the solid bed at the bottom of

the rotary drum and spread it in the gas phase. The use of lifters consequently increases the mass- and heat-transfer coefficient and the mass- and heat-transfer surface [119,183].

Many different types and designs of lifters or flights are known. As an example, a cross-sectional view of a rotary drum with installed straight lifters is shown in Figure III - 2.4 (left). The number and shape of the lifters used or selected depends (to a large extent) on the treated material, and it is also common to use different shapes in the axial direction, adapted to the changing material properties while processing [182].

In Figure III - 2.4 on the right (a-i) examples for the different shapes of lifters and flights are presented to illustrate the variety. The naming of the lifters shown in Figure III - 2.4 differs slightly in the literature, thus in this work the following nomenclature is used:

a: Straight lifters/flights [184]

b: Rectangular lifters [184]

c: Angular lifters (2 segments, 2S) [185,186]

d: Angular lifters (3 segments, 3S) [187,188]

e: (Semi-)Circular lifters [182]

f: Extended circular lifters / J-Lifters [119,184]

g: Equal angular distribution (EAD) lifters [189,190]

h: Equal horizontal distribution (EHD) lifters [191]

i: Centrally biased distribution (CBD) lifters [190,192]

The listing also includes exemplary literature passages in which the respective form is mentioned, described or analyzed.

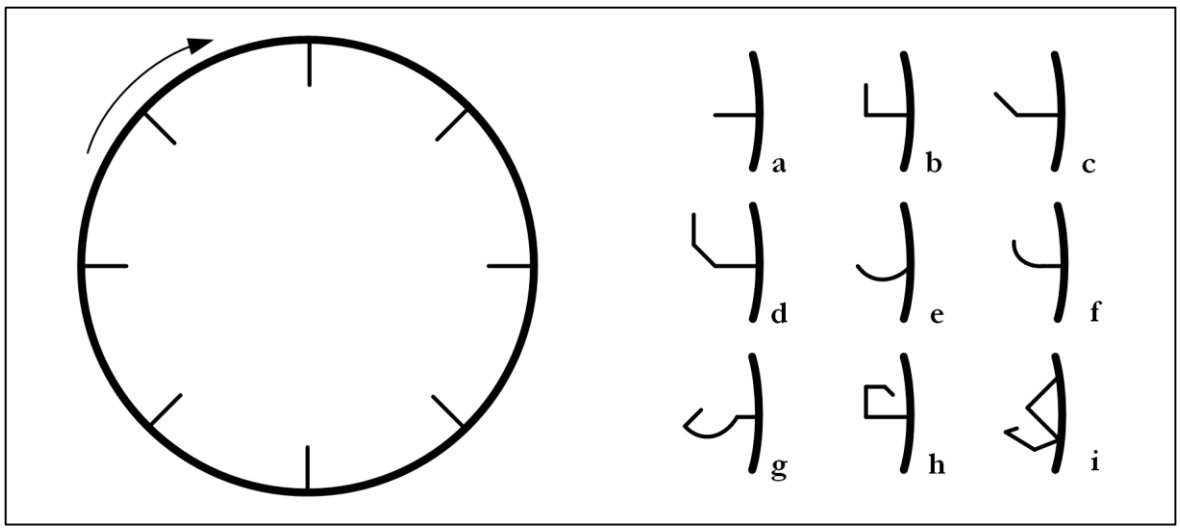

Figure III - 2.4: Sketch of the cross section of a rotary drum with (straight) lifters (left); lifter types: a: straight; b: rectangular; c: angular (2 segments); d: angular (3 segments); e: circular; f: J-lifter/extended circular; g: EAD; h: EHD, i: CBD

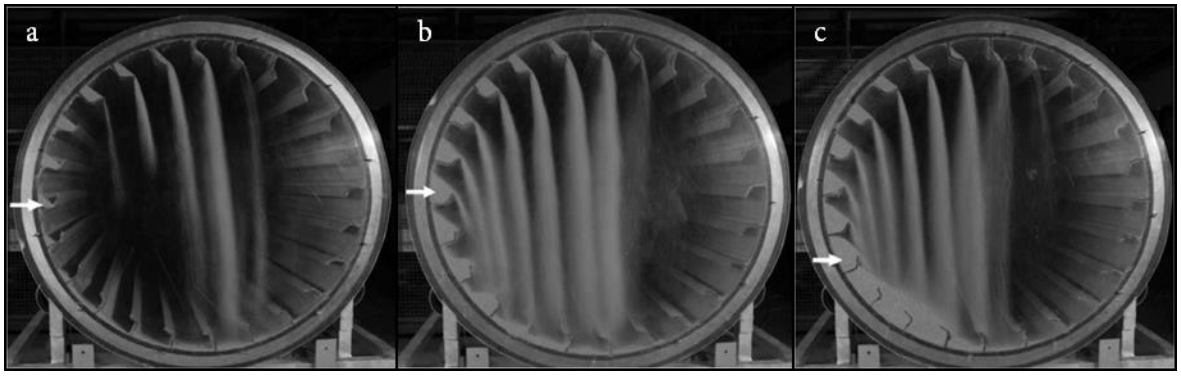

Figure III - 2.5: Flighted rotary drum at different loading states, clockwise rotation; a: under-loading; b: design-loading; c: over-loading (adapted from [185])

Straight lifters, as the simplest design, are often used for adhesive materials, while the other shapes tend to be used for better or free-flowing bulk materials [182]. However, the design of lifters is also based on the discharge or trickling behavior of the same in the cross section of the rotary drum. In this field, image analysis has been frequently applied as an experimental methodology. Figure III - 2.5 shows an example of images from the cross-section of a rotary drum with lifters at different filling degrees, as published by Ajayi [185].

The presented pictures illustrate the trickling behavior in the cross-section of the rotary drum for three fundamentally different filling conditions. In Figure III - 2.5 (a), only a small amount of solids is provided in the drum and following the lifters are not completely filled. Therefore the discharge only takes place in a small part of the cross-section, which is clearly above the 9 o'clock position (arrow) in the direction of rotation (clockwise). In the third picture (Figure III - 2.5, c) the filling degree is too high, since the lifters are overfilled and a part of the solid bed cannot be taken up by the lifters. Additionally the unloading of the lifter begins before the 9 o'clock position (arrow). The second picture (Figure III - 2.5, b) represents the optimal loading of the drum in the shown configuration, since all material is lifted up and the lifters are fully filled. Extensive experimental research has been performed by Karali et al. on the field of unloading behavior [193–196] and finding the optimal loading of the drum. From experimental results they provide the following relation to calculate the optimum drum loading for rectangular lifters [194]:

$$fd_{design} = 4.5D^{-0.77}L^{0.60}d_P^{0.043}(\tan(\theta))^{0.35}\rho_b^{0.013}Fr^{0.052}n_F^{0.941}\left(\frac{l_2}{l_1}\right)^{0.839} \quad (3.32)$$

The coefficient l_2/l_1 describes the ratio of tangential and radial part of the rectangular lifter and n_F is the number of installed flights.

Besides the experimental investigation also the modeling of the unloading behavior was in focus to deduce the process behavior. Baker [184] performed calculations with geometric considerations. The main issue is the changing geometry of the filling area in the cross sectional plane while the rotation. Kelly [191] used such considerations to propose the design of EAD and EHD flights. Lastly, it has to be mentioned that also stochastic modeling has been applied in the field of cross sectional unloading of flights [197].

In addition to the main objective of improving the heat transfer between the material and the gas flow, the lifters also impact on the axial material transport. Afacan et al. [198] found that the installation of 8 (straight) lifters had no impact on residence time. The axial dispersion coefficients are higher compared to bare drums and a range of 10^{-5} to 10^{-3} m^2/s is provided by Sheritt et al. [174].

Experiments regarding axial solid transport in flighted drums have been performed by Bongo Njeng et al. [199,200] for straight and rectangular lifters and by Hatzilyberis et al. for EAD and EHD lifters [189]. Bongo Njeng et al. provide relations to calculate residence time and axial dispersion coefficients based on dimension analysis and experimental data:

$$\bar{t} = 0.26 \cdot \frac{\rho_b L D^2}{\dot{m}_F} \cdot \left(\frac{N^2 D}{g}\right)^{0.08} \cdot \left(\frac{D_o}{D}\right)^{-0.36} \cdot \theta^{0.87} \cdot S^{-1.12} \cdot \left(\frac{\dot{m}_F}{\rho_b N L D^2}\right)^{0.84} \cdot \left(\frac{4S}{\pi D^2}\right)^{-5.53} \cdot \left(\frac{\rho_b}{\rho_t}\right)^{0.77} \cdot \left(\frac{L}{D}\right)^{1.1} \tag{3.33}$$

$$D_{ax} = 1.20 \cdot 10^7 \left(\frac{\dot{m}_F}{\rho_b}\right)^{-0.87} \cdot (n \cdot \beta)^{1.67} \cdot (\theta \cdot d_P)^{0.43} \cdot L_s^{0.21} \cdot D_i \tag{3.34}$$

Hatzilyberis et al. provide a correlation to calculate the impact of EAD/EHD flights regarding residence times in relation to bare drums:

$$\bar{t}_L = \left(a \cdot n_F^b\right) \cdot \bar{t} \tag{3.35}$$

The coefficients of the stated equation are given with a=1.12 and b=0.44. Besides the more simple lifters, various special forms of lifters have been analyzed, e.g. axially inclined lifters, which impose

an axial movement (analogous to screw conveyors) on the material in addition to the lifting in the transverse plane [201].

Since gas-flow is affecting the axial particle motion due to the intensified contact, e.g. Baker [202] and Renaud et al. [203] performed experiments and derived models to quantify the impact of gas-flow. Model approaches have also been developed regarding the axial solid transport by e.g. Karali et al. [204] or by Thibault et al. [205] incorporating neural network methods.

Summarizing it has to be stated, that a huge amount of research is available in the topic of lifters. However, common to all of the very careful conducted analyses mentioned above is that they either refer to the cross section or they consider the lifters as continuous in axial direction. The former case also includes the hidden assumption, that the lifter devices are continuous or "infinitely long" in axial direction.

2.4.2 Sectional internals

Sectional internals are only rarely mentioned in the literature. They are usually entitled as ‘heat exchanger internals’, since they are frequently used with this objective.

Duda reports about sectional internals in rotary kilns as ceramic heat exchanger internals [120]. In the explanations, 3 or 4 sections/sectors are mentioned, which consist of ceramic refractory material. They are named Dietze bridge (3 sections, after the inventor Dietze [206]) and Azbe bridge (4 sections, after the inventor Azbe [207,208]), respectively. An exemplary schematic representation of the structure in the drums cross-section is shown in Figure III - 2.6.

Since the first patents mentioning sectional internals (Azbe & Dietze [206,207]) in the mid of the 20th century, many other patents on ceramic heat exchangers or sectional internals have been published. These essentially relate to the design of the internals. Andersen [209] shows 6 sections, where the section walls can be additionally equipped with fins e.g. for conveying. Rochelsberg publishes a type of construction with 8 sections [210]. In order to improve the construction of the Dietze bridge, various types of construction [211–214] have been published also from recent past. Regarding the Azbe bridge, further types of construction are also patented [215].

Besides the stated types of sectional internals, more special types of construction are also known, e.g. Dussossoy patented a helix-shaped design of sections in axial direction [216,217] or a tube in tube construction as proposed by Reayney [218]. Furthermore, other materials than ceramic have been used in the construction of sectional internals [219].

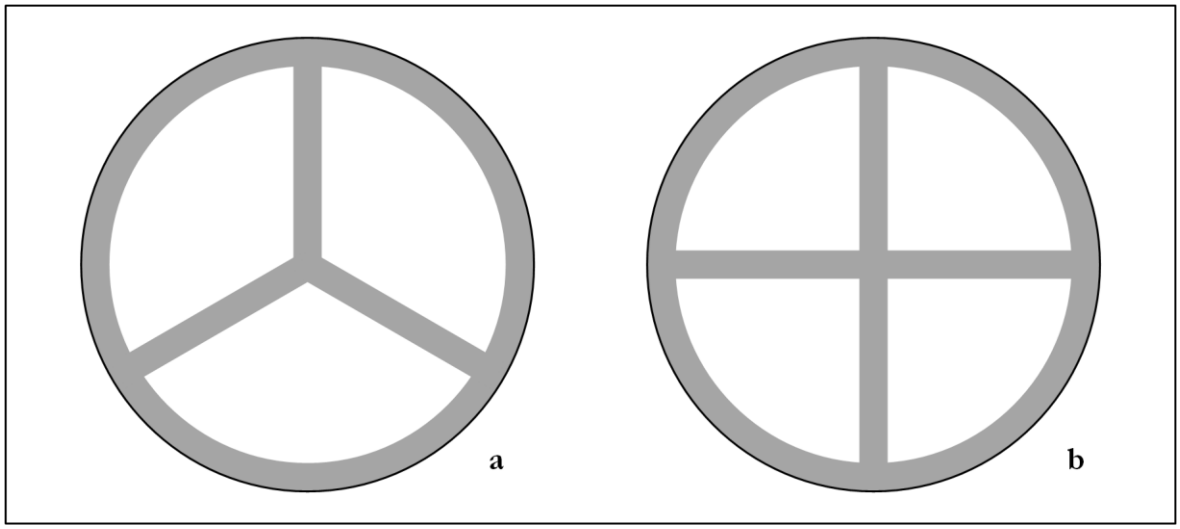

Figure III - 2.6: Schematic cross sectional view into a rotary drum with sectional internals; a: 3 sections or Dietze-bridge; b: 4 sections or Azbe-bridge (adapted from [120]).

The impact of sectional internals regarding the process behavior has not been researched or documented to the author's knowledge (process engineering view). Duda indicates the division of gas and solid flows and an associated improvement of heat exchange as well as mixing as the main purposes for the installation of sectional internals. However, the effects are not quantified. For cement kilns, the internals increased the kiln capacity by 8-12% and lowered the exhaust gas temperature by 80-100°C [120].

In the scientific literature, only one publication is found, in which Xu and Ma made a simulation for a "multi-cavity kiln" in catalyst manufacturing [220]. The internal structure of the described kiln is essentially the same as presented in Figure III - 2.6 (a). They cite the extraordinary uniformity of the temperature and thus the improved uniformity of the product quality as an advantage for the use of sectional internals.

2.4.3 Further internal structures

In addition to the mentioned and well known internals, there are numerous other possible internal structures. To illustrate this fact and to show the resulting complexity of the subject 'rotary drum internals', a few more types will be mentioned here:

- Trefoil shaped patterns of the cross section [119,221]
- Structures with a squared cross section (helical in axial direction) [222]
- Roto-areated drier with central pipe inducing gas into the solid bed [223,224]
- Diverse devices to improve the mixing of the solids [225]
- Especially in dryers: cross type internals, simplex internals, quadrant internals [137,226]
- Pipes in axial direction for heating or cooling purposes in dryers or coolers [227]

As can be seen, in general the only limit is the constructability of the internals. These complex types of internals will not be further considered in this work.

3 Experimental

In this chapter the experimental setup for the conducted experimental investigation of solid transport and process behavior for rotary drums with different internals is presented.

3.1 Description of the Apparatus

A completely new, innovative and optically accessible experimental setup has been developed in this work, to investigate the solid transport processes. It is focused on a maximum of flexibility in the feasible measurements, since many different configurations will be tested.

The main aims while construction considerations have been:

- Flexibility in dimensions to be able to perform experiments in different scales
- Flexibility in operational parameter settings
- Flexibility in mounting different internals or internal structures
- Full optical accessibility to apply visual/optical measuring-techniques

Based on further examples of optically accessible process equipment as e.g. spiral jet mills [228–230] or flotation investigation equipment [231], different setups of the apparatus have been created [232]. They enable the analysis of solid transport in axial direction as well as in transversal direction, which will be shown in the following chapters. All configurations basically consist out of a base frame as mounting device with a roller station and the lab-scale rotary drum models (further called models) itself.

The development process was CAD-guided (Autodesk Fusion 360®) and Lasercutting and 3D-printing (filament and resin) have been used while manufacturing.

3.1.1 Axial flow configuration 1

The first configuration to measure the axial material flow by means of residence time (RT) is presented in Figure III - 3.1 with a description adapted from [233]. It can be considered as the first stage of expansion of the apparatus.

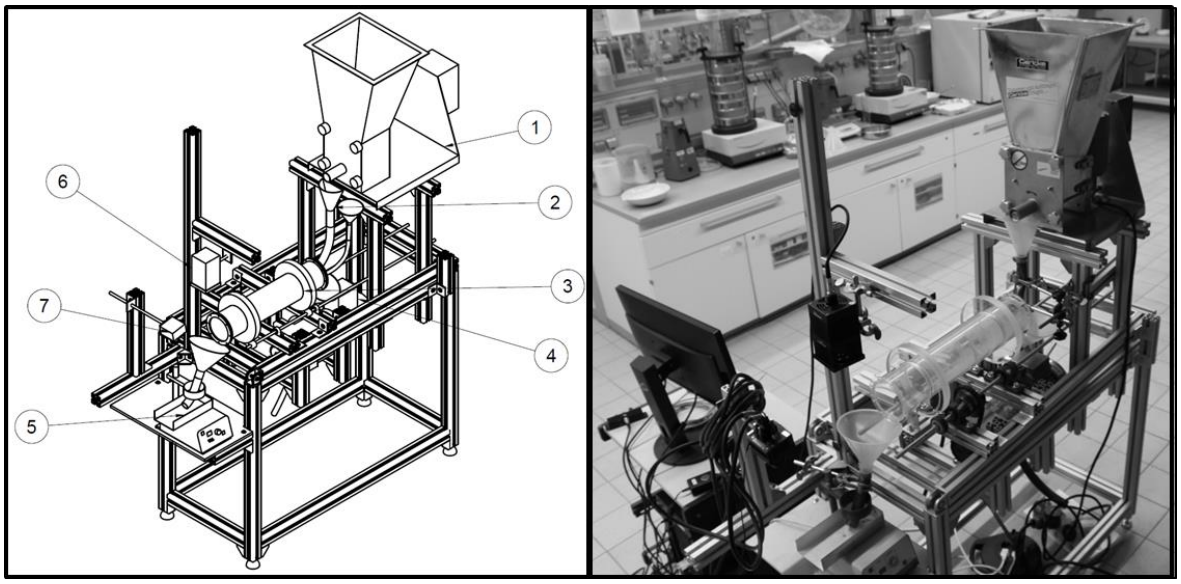

Figure III - 3.1: Representation of the laboratory equipment for axial flow measurements in configuration 1; a: sketch; b: photo [233]

The apparatus is mounted on a base frame. The feed mass flow is delivered by a screw conveyor (Figure III - 3.1, No. 1; Gericke GLD75, 50W). The screw conveyor is equipped with a screw of 35 mm in diameter. The motor of the conveyor is frequency-controlled, thus the conveyor can deliver variable mass flow rates via different rotational speeds. The screw conveyor is equipped with a hopper which is used as storage volume for bulk material. The feed mass flow is conducted to the feed inlet of the rotary drum with a funnel and a chute, manufactured out of a hose (Figure III - 3.1, No. 2). The drum itself (Figure III - 3.1, No. 3) has two tires and is mounted on the roller station consisting of two axes (threaded rods) with four rollers. The drum's tire at the outlet end is used to prevent the axial drifting of the drum through inclination with a tiny horizontal roller. The distance between both axes can be changed to support drums with different diameters and the mounting of the axes can be used for drums with different lengths. One of the axes is equipped with a sprocket to transfer the power by a chain drive. The power is delivered by a motor (Figure III - 3.1, No. 4) with integrated variable mechanical transmission (Heynau H-Trieb, 250W), thus different rotational speeds can be set to the rotary drum.

The solid mass flow at the outlet end is falling down into a funnel ending on a vibration conveyor (Figure III - 3.1, No. 5; Retsch DR100) with modified chute. The cross section of the funnel is bigger than the drum's cross section to guarantee collecting all material coming out of the drum. The vibration conveyor is optically accessible from the top and illuminated by a lamp (Figure III - 3.1, No. 6). The top of the conveyor is observed by a camera (Figure III - 3.1, No. 7; Vieworks VC-

2MC-C340EO). The camera view allows the observation of the whole cross section of the chute. The camera is triggered with a computer via a frame grabber (Xtium-CL_MX4_1).

The rotary drum itself is constructed out of polymethyl-methacrylate (PMMA), which is transparent. It is based on a simple tube and has two flanges at both ends to easily mount and exchange internals, constriction dams etc. The internals are constructed as slide-in modules. An example of a configuration equipped with 3 sections and the dam at the inlet end is presented in Figure III - 3.2.

For all investigations the length of the tube is 500mm, the inner diameter is 100mm. The inlet end is equipped with a constriction dam with inner diameter of 60mm to prevent back spillage of the particle feed, the free cross section is therefore reduced to 36% at the inlet end. This inlet constriction dam is used for all configurations in this work.

3.1.2 Axial flow configuration 2

The second configuration to measure the axial solid flow is essentially based on the first configuration, but is enhanced and improved in a few parts. The apparatus is shown in Figure III - 3.3 adapted from [234] and can be considered as the second stage of apparatus development.

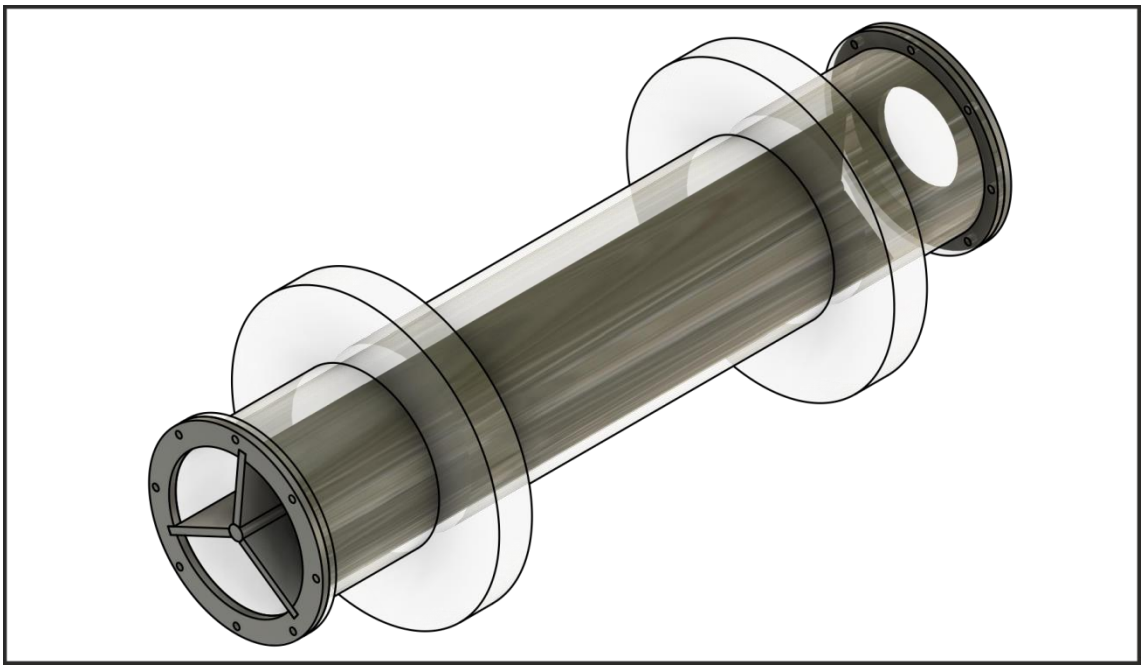

Figure III - 3.2: Exemplary sketch of three sections slide in module (L=450mm) and the inlet dam (d_i=60mm) mounted to the bare drum. Construction material is PMMA, grey color of mounted parts is chosen for visualization.

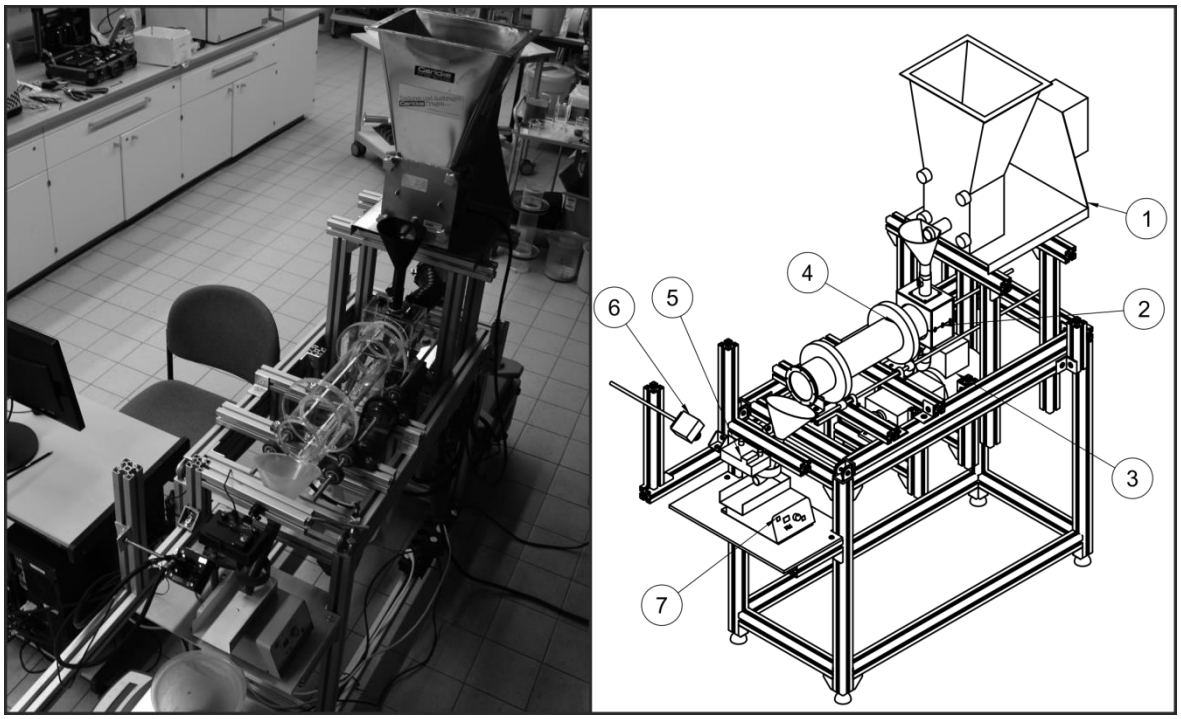

Figure III - 3.3: Representation of the laboratory equipment for axial flow measurements in second configuration ; a:photo; b: sketch [234]

At three main points modifications have been made compared to configuration 1:

1. The screw of the feed conveyor (Figure III - 3.3, No. 1) has been exchanged to a screw of 15mm in diameter to provide easier solid dosing.
2. The light source above the vibration conveyor (Figure III - 3.3, No. 5) is changed to an LED-Panel and the position of the light source is moved and optimized for better handling.
3. The funnel and the inlet chute (Figure III - 3.3, No. 2) have been modified as explained in the following in more detail.

In order to be able to perform measurements with additional gas-flow in the system, the connection of a fan has to be provided. Therefore the static pipe or hose has to be connected to the rotating drum. Adapted from the basic industrial construction, a housing for the inlet end was constructed, which furthermore contains a new inlet chute. It is presented in Figure III - 3.4.

The housing is easy to open via flipping aside the top part of it in order to mount or remove the drum with the back end flange. The inlet funnel on top of the housing is removable and adjustable in height for that purpose. An adapter to connect the pipe to a fan is located at the back end of the housing (Figure III - 3.4, right). The bottom is formed as a funnel itself to collect the back spillage material. The complete housing is constructed in PMMA to gain optical access. The gap between housing and the drum's outer wall is sealed with self-sticking foam adapted from window sealing

systems. In order to enlarge the friction between the drum and the roller station, sandpaper is glued at the drum's tires.

3.1.3 Transversal flow configuration

As explained in theory, besides the axial solid transport the transversal solid transport is also very important and the impact of different internal structures has to be investigated. The presented apparatus is adapted to provide the possibility of these measurements. The apparatus is presented in Figure III - 3.5 as an overview and with the modifications for cross sectional measurements in particular. The description can also be found in [235].

The base frame is the same as described before for the axial flow measurements. The inclination angle is set to 0°. The roller station is extended with two additional rollers near the rollers at the outlet end to mount the short cross section model. The camera position (Figure III - 3.5, No. 2) is changed to optimize the view in axial direction. An endocentric objective is used to watch the complete cross section of the model during the experiments.

The model is lighted with a ring type lamp (Figure III - 3.5, No. 1) from the observation side (front) to guarantee a homogeneous and uniform illumination of the circular surface of the model.

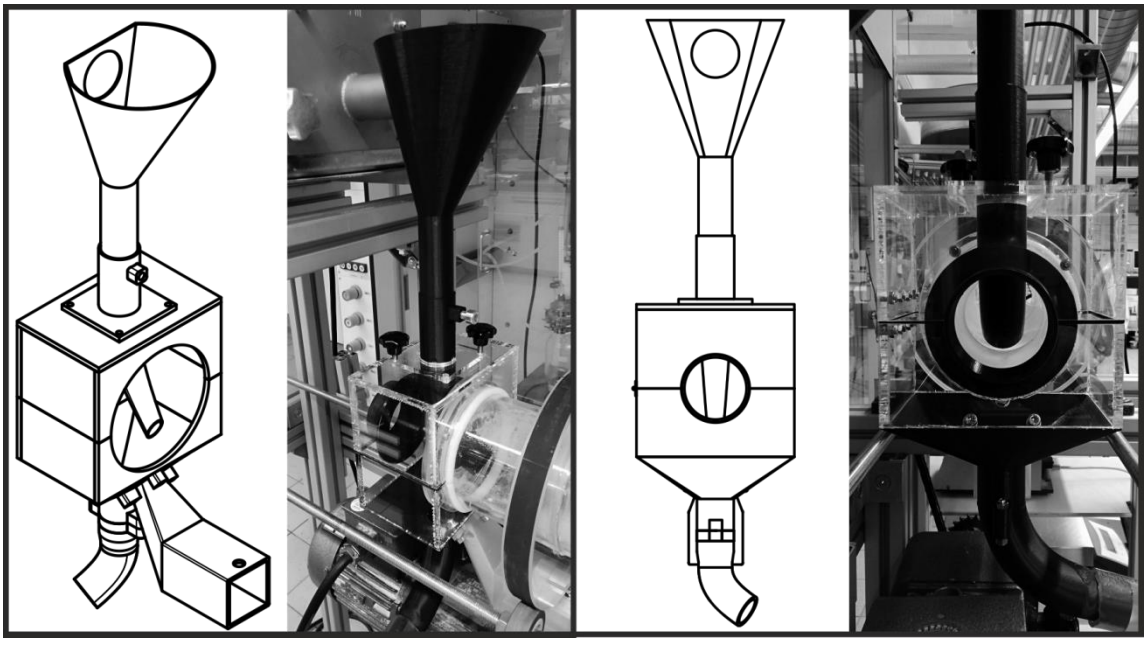

Figure III - 3.4: Left: Sketch and photo of a total view of the inlet housing; Right: Sketch and photo of the back side view of the inlet housing.

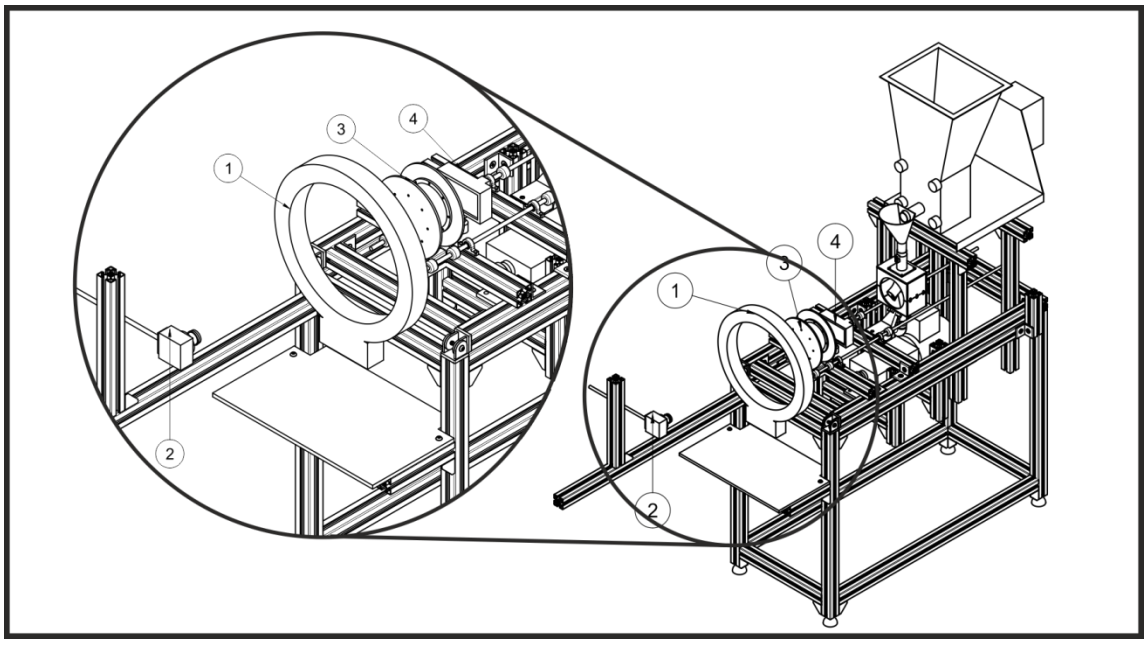

Figure III - 3.5: Rotary drum apparatus in transversal flow configuration; 1: Ring type lamp; 2: High-speed camera; 3: Cross-sectional rotary drum model; 4: LED-panel

Besides the ring type lamp, the setup can be illuminated from behind via a plane LED-panel (Figure III - 3.5, No. 4). On the back plate of the model a white paper is installed as diffusor to guarantee a uniform backlight illumination. This enables the possibility of taking shadowgraph-pictures of the solid bed in the cross section.

The cross section model itself (Figure III - 3.5, No. 3) consists out of three parts, namely the cylindrical part of tube with flanges at both ends and two cover plates which are mounted to the drum via the flanges. The length of the cylinder part is 60mm. The cover plates are serving as drum tires at the same time and transmit the rotary motion from the roller station to the drum. The inner diameter of the drum is 100mm and the outer diameter of the cover plates at both ends is 260mm. As material again PMMA is used to get the full optical accessibility of the apparatus. The filling of the drum is possible through a radial hole in the cylinder wall which is closed with a plug. To prevent disturbances in the interaction between wall and particles the plug ends at the plane of the inner wall. Exemplary pictures of the laboratory setup are additionally represented in Figure III - 3.6 to provide an impression of the setup.

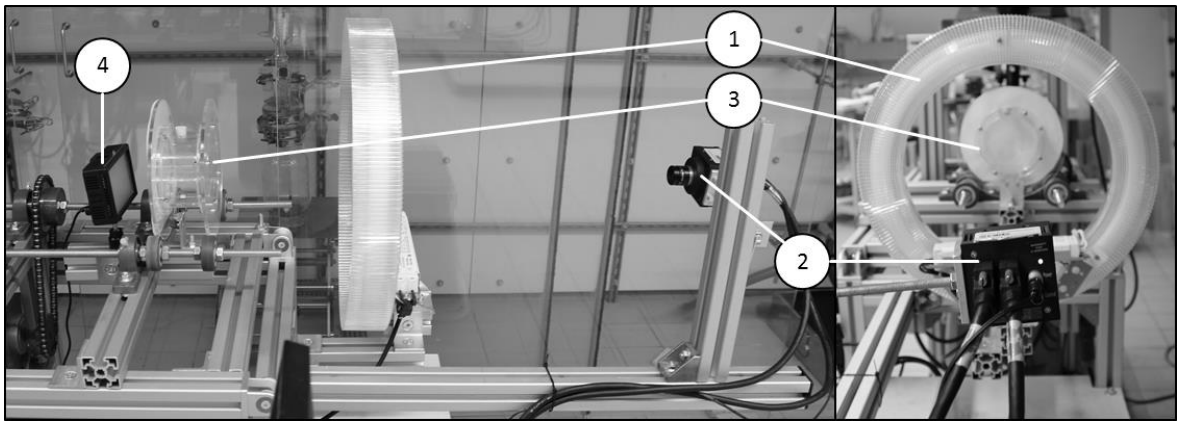

Figure III - 3.6: Left: side view photo from the experimental setup; right: photo of experimental setup showing the camera perspective (1: ring-type lamp; 2: camera; 3: cross-section model; 4: LED-Panel) [235]

3.2 Solid material

As known from literature, segregation effects can take place in a rotary drum. The aim of this part of the work is to understand the process behavior of the rotary drum apparatus in its different configurations. Following, the prevention of effects caused by the solid material, which could lead to misunderstanding or misinterpretation of the generated data, is focused. Therefore, the solid material was chosen by the following aspects:

- The material needs to be homogeneous
- Narrow particle size distribution
- Uniformity in particle shape (spherical)
- Uniformity in density of the particles (no mixture of materials or gangue in particles)
- Possibility of recycling of the material

Furthermore, the tracer-material needs to be similar to the bulk material in most characteristics. Glass particles perfectly fulfill the desired aspects mentioned above in contrast to e.g. natural sand with a gangue. In the different investigations two particle size fractions have been used (100-200µm and 800-900µm). As tracer material black-colored glass particles have been used, which leads to color as the only distinction between the two materials. In order to manufacture that tracer, a part of the material was colored with water soluble dye (simplicol® textile dye, 'midnight black'). After each experimental run the used mixture of bulk and tracer is collected, washed with water, dried and sieved afterwards. This technique allows full recycling of the material although there is no usable particle characteristic to separate bulk and tracer. All known or measured characteristics of the solid materials used in this work are given in Table III - 3.1.

Table III - 3.1: Characteristics of the solid materials utilized in this work

		Small particles		Large particles	
Property		**Bulk**	**Tracer**	**Bulk**	**Tracer**
Color		white	black	white	black
Particle size	µm	100-200	100-200	800-900	800-900
Sphericity	-	≥ 0.89	≥ 0.89	≥ 0.89	≥ 0.89
Bulk density	kg/L	1.454 ± 0.002	1.331 ± 0.002	1.493 ± 0.002	1.424 ± 0.002
Solid density	kg/L	2.50	2.50	2.50	2.50
stat. repose angle	°	18.9 ± 0.7	23.6 ± 1.0	14.5 ± 0.7	20.7 ± 1.0
dyn. repose angle	°	30.0 ± 1.0	33.0 ± 1.0	27.3 ± 0.6	29.4 ± 0.6

Besides the particle size, the static angle of repose (H-W-S Labortechnik, DIN ISO 4324) and the bulk density (HLL Landgraf, DIN ISO 697) were measured. The dynamic angle of repose is measured with the cross sectional apparatus described before [235]. Other particle characteristics (particle size, sphericity, solid density) are known from the product data sheet of the manufacturer (Sigmund Lindner GmbH). The particle size range is verified before each run via the recycling method containing the sieving step. Sieving is performed with a Retsch AS200 sieving machine with sieves of 200µm and 800µm respectively.

3.3 Axial flow measurements

The experimental procedure with the described apparatus (3.1.1 & 3.1.2) uses a non invasive analyzing method without a need for sampling. In a first step the experiment is conducted with the data acquisition working as an inline technique (picture acquisition). In a second post-processing step, the data is examined using digital image processing techniques. Therefore, the measurements are described in two steps. In general the method is the same for both axial flow configurations although there are slight distinctions regarding the mass balance according to back-spillage.

3.3.1 Description of the routine

The experiments in axial flow analysis were conducted referring to the following procedure [233] with axial flow configuration 1:

1. The hopper of the screw conveyor is filled with bulk material and the chosen parameters for rotational speed, drum slope and mass-flow rate are set and checked.
2. The apparatus is run to steady-state conditions, differences in mass-flowrate at the outlet are below 3%. The frequency of the vibration conveyor at the outlet end is adjusted until a thin particle film is generated.
3. Dyed tracer is injected (25g) in <1s and the video/picture acquisition is started simultaneously. The tracer injection is considered as pulse function (Dirac impulse).
4. All equipment and the experiment is stopped when the tracer completely left the drum. The times needed for that event are determined in preliminary experiments with a safety time.
5. The weight of the solid material inside the drum is determined as hold-up.
6. The photo sequence of the outlet flow is analyzed as illustrated in chapter 3.3.2.

The experiments using the axial flow configuration 2 are conducted in the same way, but the inlet housing enables quantitative determination of the back spillage mass and therefore balancing afterwards. Two steps are added as follows after step 2 and 4 [234]:

2b The drum and the feed screw are stopped and the collecting vessels behind the inlet and outlet end of the drum are emptied from the material needed for steady state setting. The weight of the vessels is determined, and the vessels are repositioned at the drums ends.

4b The masses of the collecting vessels and therefore the weights of the material at the outlet and inlet end of the drum are measured.

The data acqisition works via taking photos of the vibration conveyor surface with the particles using the high-speed camera in defined, triggered time intervals. The analyzing rate (2 pictures/second for axial flow configuration 2) is high compared to the measured residence times while keeping the handling of the data amount feasible. With axial flow configuration 1 the sampling rate was higher in some experiments. The exposure times are low (5 ms), due to the observation of moving objects/particles. In order to guarantee the same possibility and probability for each particle to be visible on the picture, the whole cross section of the chute (100mm) is

evaluated. Since no particle should be analyzed twice, the observation area is small in flow direction (7mm).

The bulk glass particles are nearly invisible, since they are illuminated by the LED panels and the surface-preparation of the vibrating chute in white color. Consequently, a very high contrast to black tracer particles is generated to improve sensitivity of the technique.

The result of the measurement is a picture sequence of the particles or the particle flow at the end of each experiment.

3.3.2 Analyzing methodology

After the experiment is physically finished, the data (picture sequence of analyzed area on the vibration conveyor) is examined with the software ImageJ® via digital image analysis. The first picture of the sequence is subtracted from each following picture as blind value, in a first step. Afterwards, the ratio of black area to the analyzed area is determined, which is proportional to the number of tracer particles in each photo. In addition, the number of tracer particles is proportional to their concentration, since a thin (mono) layer of particles is created on the vibration conveyor as described before. The black area is measured with a defined and fixed threshold for all pictures in the whole picture sequence. The time from experimental start is connected to the picture numbers via the camera setup (trigger intervals). In conclusion, a plot of the black area fraction (A_{tracer}) against time directly leads to the equivalent of the residence time distribution.

Numerical integration (trapeze method) of all area fraction values over time and subsequent division of each value by the total integral results in the normalized cumulative distribution (F(t)), with F(∞)=1.

$$F(t) = \frac{\int_0^t A_{tracer}\, dt}{\int_0^\infty A_{tracer}\, dt} \tag{3.36}$$

The density distribution (E(t)) is calculated in the following via numerical differentiation, since the relation between F(t) and E(t) is generally known to [60,236]

$$E(t) = \frac{dF(t)}{dt} \tag{3.37}$$

After the calculation of the density distribution (E(t)) the Gaussian distribution (equation (3.27)) is fitted to E(t) via least squares method utilizing standard deviation and mean residence time as fit factors. Further evaluation of the distribution concerning the axial dispersion model has already been described in chapter 2.3.3.

Figure III - 3.7 presents an exemplary diagram of cumulative distribution and density distribution from an experiment with the fitted Gaussian distribution. As example a bare drum (DC1) measurement with the axial flow configuration 1 apparatus and the parameter set n=3.8 1/min, β=4.3° and $\dot{m}_F$=9.5 kg/h is shown.

The calculated MRT from the shown fitted Gaussian distribution in the example of Figure III - 3.7 is 125s, the standard deviation (of Gaussian distribution) is 3,7s. Thus the spread of the distribution can be estimated by 6σ to 22.2s (because in this case more than 99% of the Gaussian distribution is covered). Utilizing the drum length, the axial velocity is determined to 0.004m/s according to equation (3.29). The calculated Peclet-number is 2270 (Equation (3.28)) and thus the axial dispersion coefficient is $8.82 \cdot 10^{-7}$ m²/s, which means the axial mixing is rather low and the flow regime can be assumed as plug flow.

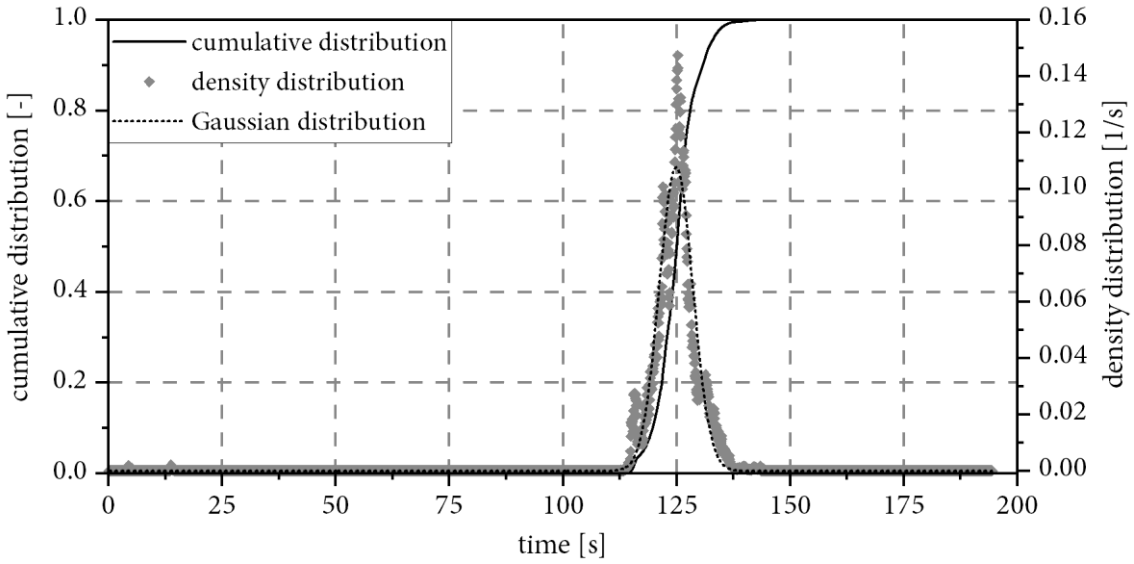

Figure III - 3.7: Examplary diagram of measured residence time distribution. Axial flow configuration 1, bare drum (DC1) with operational parameter set: n=3.8 1/min, β=4.3° and $\dot{m}_F$=9.5 kg/h

3.3.3 Design of experiments

The experimental design is based on the variation of the operational parameters rotational speed n, feed mass flow $\dot{m}_F$ and axial drum inclination angle or slope β. The parameter combinations are chosen by a full factorized design with three factors on two stages (cube). Furthermore, the extension of this basic design to a central composite design was considered (with elongation-factor of 1.3 for starpoint experiments) in the development and in the setting of the parameter space. The parameter combinations of the executed experiments are presented in Table III - 3.2.

Besides the basic experiments some of the investigated configurations have been tested with further parameter combinations in an extended design. Exp.-No. 10 to 13 provide an extended or mirrored design regarding the feed mass flow. As materials, referring to Table III - 3.1 the small particles (bulk & tracer) have been used in all experiments. Additionally, in some cases, during the midpoint experiment (Exp.-No. 09LT), the large tracer particles (see Table III - 3.1) have been used to check the influence of segregating particles on the axial flow or residence time behavior.

Many different internal structures have been tested as scope of this work. They will be declared as drum configuration (DC) in the following. The structures are presented related to the axial flow configuration which was used for the measurements. At least the basic DOE has been conducted with every drum configuration.

Table III - 3.2: Design of experiments (full factorized design, three factors on two stages) for the chosen parameter combinations in the experiments

	Exp.-No.	Rotational speed n [1/min]	Slope β [°]	Feed rate $\dot{m}_F$ [kg/h]
Basic	01	3.8	1.3	9.5
	02	11.0	1.3	9.5
	03	3.8	4.3	9.5
	04	11.0	4.3	9.5
	05	3.8	1.3	16.0
	06	11.0	1.3	16.0
	07	3.8	4.3	16.0
	08	11.0	4.3	16.0
	09	7.3	3.0	13.5
Extension	09LT	7.3	3.0	13.5
	10	3.8	1.3	3.5
	11	11.0	1.3	3.5
	12	3.8	4.3	3.5
	13	11.0	4.3	3.5

3.3.3.1 Axial flow configuration 1

With the axial flow configuration 1 basically the bare drum and a constriction dam at the outlet end have been tested as literature benchmarks as well as the first measurements with sectional internals. Figure III - 3.8 presents the basic drum dimensions in a side view sketch. Furthermore, the different drum configurations (DC), which have been analyzed with the axial flow configuration 1, are presented in a cross sectional view. A description is also given in [233].

The first configuration (Figure III - 3.8, DC1) represents the bare drum without any internals or constriction dams at the outlet end. As already described in chapter 3.1.1 the drum length was L=500mm and the inner drum diameter D_i=100mm. At the inlet end, a dam was used with inner diameter of D_i=60mm, reducing the free cross section to 36% at the inlet end.

In the second configuration (Figure III - 3.8, DC2) the outlet end is equipped with an additional exit dam. The inner diameter of the dam is 80mm. Thus the free cross section is reduced to 64%, or the cross sectional shrinkage (CSS) is 36% respectively. The first two configurations have already been analyzed and described in literature as mentioned in the theory.

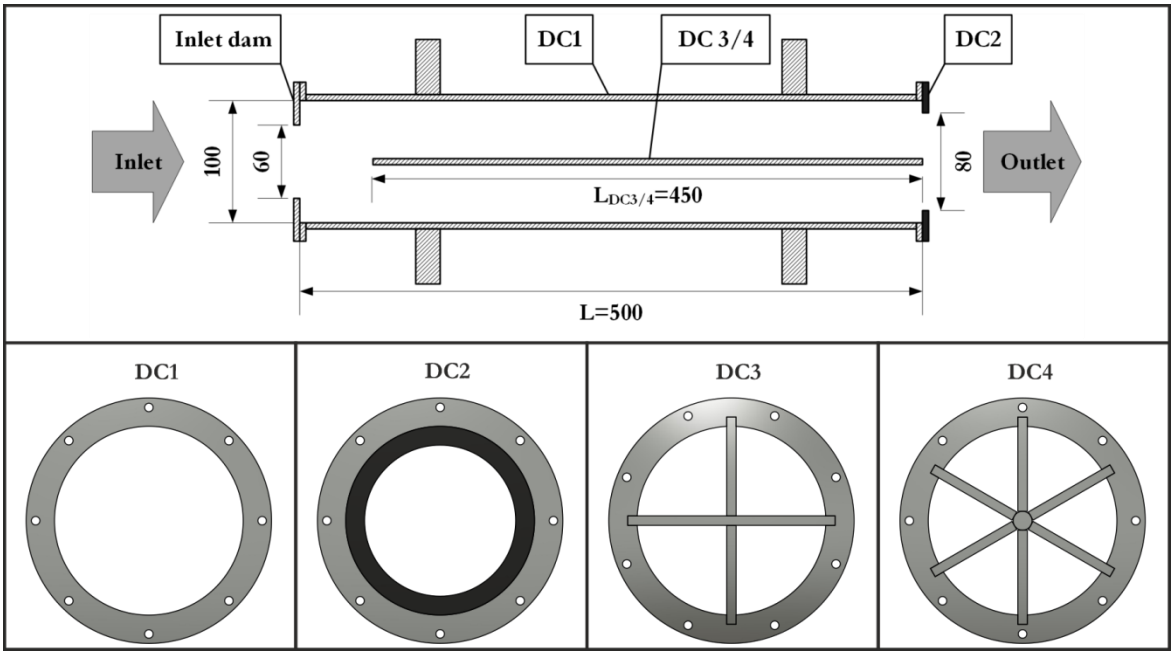

Figure III - 3.8: Top: Side view sketch of the rotary drum with exemplary drum configurations (DC, values in mm); Bottom: View from outlet end presenting cross sections of the used drum configurations (DC1: free discharge/bare drum; DC2: outlet dam; DC3: four sections; DC4: six sections). Adapted from [233]

The third configuration (Figure III - 3.8, DC3) is based on the basic design of sectional internals with compartments. The cross section of the drum is divided into four equal sections (comparable to the Azbe-Bridge). The sections have a length of 450mm beginning at the outlet end because a clearance for the inlet chute is needed at the drums inlet end. No restriction dam is added at the discharge end. The thickness of the construction material (PMMA) is 5mm thus the free cross section in DC3 is reduced to 87.3%. The last configuration of this study (Figure III - 3.8, DC4) is based on configuration DC3, but having six equal sections now. The free cross section is reduced to 80.9% here.

The basic design of experiments (cf. Table III - 3.2) has been applied to each of the drum configurations, conducting each experiment three times to gain statistical parameters. This results in a total of 108 Experiments.

3.3.3.2 Axial flow configuration 2

With the axial flow configuration 2, basically two different types of internals have been investigated, namely sectional internals and lifters/flights.

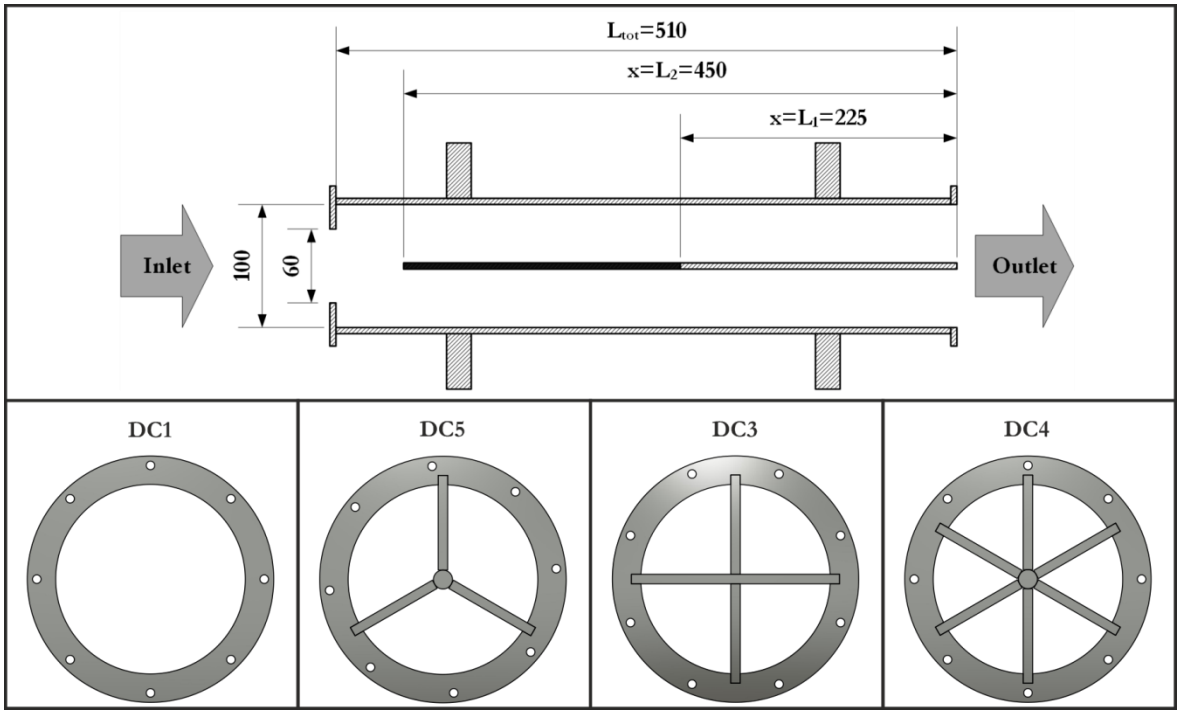

Figure III - 3.9: Top: Sideview-sketch of the drum with all dimensions and different lengths of internals, all values in mm); Bottom: Sketch of cross sections of the used drum configurations (DC). DC1: bare drum; DC5: 3 sections; DC3: 4 sections; DC4: 6 sections. Adapted from [234]

Sectional internals:

First, all investigated configurations related to sectional internals are shown in Figure III - 3.9. The first measurements with sectional internals (DC1, DC3 & DC4) with the axial flow configuration 1 have been repeated with the modified experimental setup (AFC 2, see chapter 3.1.2). Additionally, a new configuration (DC5) was added, containing 3 sections (related to the Dietze-bridge, cf. chapter 2.4.2). Furthermore, the axial length of the sections has been varied in two stages. A long version with L_2=450mm (clearance at the inlet end needed), simulating the full occupancy of the drum with sectional internals (similar to chapter 3.3.3.1). In a shorter version the internal length was halved to L_1=225mm, in order to investigate the impact of the internal length. In the axial cut in Figure III - 3.9 (top) the geometric structure of all configurations is presented, the middle-bar in the drum representing one section spoke. All lengths are measured from the outlet end. As nomenclature, a combination of drum configuration (DC) and length (L) with DCxLy is used in the following to indicate the full drum configuration.

Lifters:

As mentioned above, next to the sectional internals the apparatus was additionally utilized to investigate the impact of lifters [237]. Besides another run with the bare drum, rectangular lifters in two configurations have been installed, as presented in Figure III - 3.10.

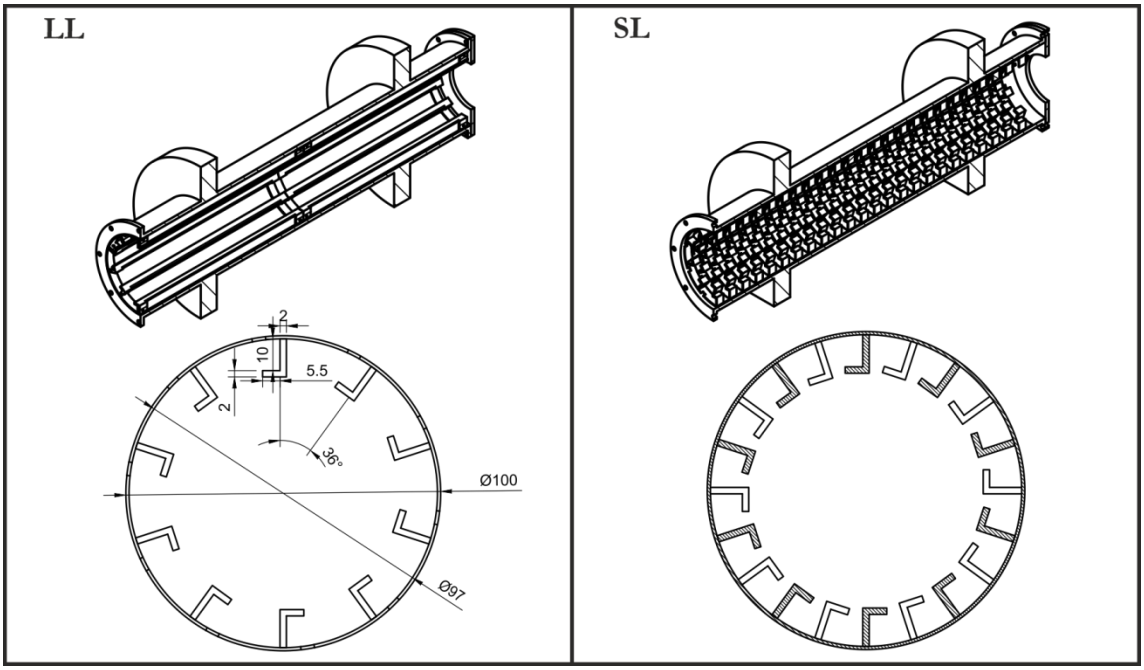

Figure III - 3.10: Axial cuts of the rotary drum with both lifter configurations (long lifters, LL and short lifters, SL) as well as cross sectional view of both configurations with the lifter dimensions (all values in mm). Adapted from [237].

Both lifter configurations have been constructed as slide-in modules, manufactured from “Tough-PLA” (filament-printer, Ultimaker® S5) and “clear-resin” (resin-printer, Formlabs® 2) via 3D-printing. The first configuration (Figure III - 3.10, left) represents long and continuous lifters covering the whole axial length of the drum (long lifters, LL, see chapter 2.4.1) the second configuration (Figure III - 3.10, right) represents single lifter shovels in axial direction (short lifters, SL).

Although both configurations look totally different inFigure III - 3.10, the SL-configuration is based on the LL-configuration. The theoretic hold-up is kept equal, in order to guarantee the comparability of both lifter models. In detail, the geometry of the lifters in cross sectional direction is equal and the total axial length of both lifter configurations (SL/LL) is the same. The total length for the SL-configuration is calculated as the sum of all axial lengths of the short lifters. By slicing in axial direction every 10mm and rotating each slice about half of the “lifter angle” (δ = 36°/2 = 18°) the SL configuration is created. This arrangement is also common in industrial practice (see introduction and chapter 2.4.1).

Both lifter configurations use rectangular flights. The geometries and sizes of the cross section are presented in Figure III - 3.10. In both lifter configurations, 10 flights are equally distributed in the circumference of the drum (36° between two flights). The cross sectional dimensions are the same. Summarizing, the only distinction of the configurations is the axial length of the flights. In the LL-configuration the axial length of flights equals the drums length of 510mm. The axial flight segment length in SL-configuration is 10mm, equal to the radial flight dimension.

Additional gas-flow:

Using the possibility of applying gas streams with AFC2, first orienting measurements have been performed for the bare drum. Additionally, the impact of an internal influencing the gas flow (‘swirl generator’) has been tested (see chapter 5.4).

3.4 Transversal flow measurements

The transversal flow measurements are also working with an experimental procedure utilizing a non invasive, camera based analyzing method without a need for sampling. The basic apparatus has been described before (chapter 3.1.3). The technique is also working in two steps (picture acquisition & evaluation) analogously to axial flow measurements.

The transversal flow measurements have been conducted for bare drum, sectional internals and different flights. The experimental routine is basically the same, while the image analysis is distinct, since different parameters are in focus here. Therefore, the description is divided according to the different investigations.

3.4.1 Bare drum & sectional internals

In the analysis of the cross section of the bare drum or the impact of sectional internals on the transversal solid transport, especially the flow patterns, are in focus. Also mixing and segregation is an important topic, therefore, in the analysis two different materials (bulk & tracer) are used to investigate the mixing process and the flow patterns. The main issue in the development of the routine was the moving position of the solid bed when sectional internals are installed, since only the solid bed should be analyzed. In Figure III - 3.11 an exemplary sketch of the experimental setup (cross section model & camera) and the used internal configurations is presented. The naming of the internals refers to the axial flow models (DCx).

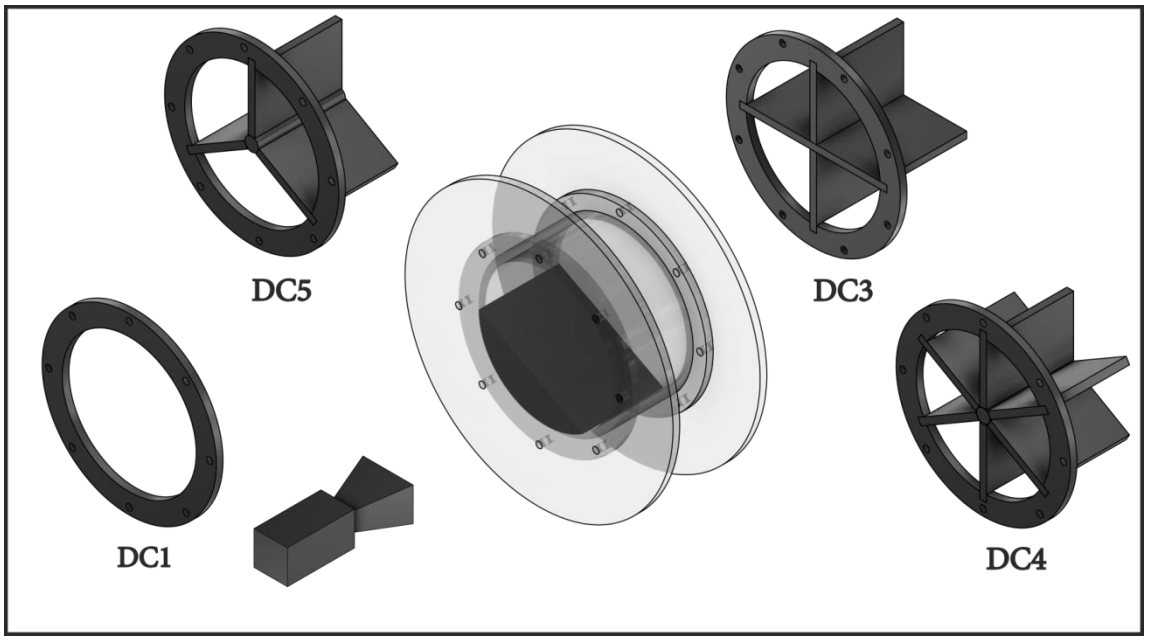

Figure III - 3.11: Sketch of the cross sectional measurements and the used internal configurations (DC1: bare drum; DC5: sectional internals with 3 sections; DC3: sectional internals with 4 sections; DC4: sectional internals with 6 sections).

3.4.1.1 Description of the routine

The description of the experimental routine has already been provided in [235]. The camera is adjusted with the frame grabber to specified triggered time intervals (50 fps, exposure time is set to 0.25 ms, due to illumination conditions). The experiments were conducted as follows:

1. The rotational speed of the drum is set with the gear-motor and checked with the empty cross section model.
2. The cross-section model is filled with white beads of the material combination under consideration and the surface is flattened carefully. The tracer-beads are filled carefully on top without mixing the two fractions.
3. The cross section model is closed with the plug (cf. chapter 3.1.3) and mounted to the roller station. The initial position is marked.
4. The ring type front light is activated and the experiment is initiated by starting the camera and the motor of the apparatus.
5. The experiment is stopped after 1800 frames of the camera. In preliminary experiments this number was determined to ensure complete mixing with a safety factor.
6. The cross section model with the mixed beads is set back to the initial position, the front light is deactivated and the plane back light is activated.
7. A second video is taken with the backlight illumination (shadowgraph pictures) with the experimental conditions and the same material in the drum.
8. The photo sequences/videos are saved and analyzed as illustrated in 3.4.1.2.

The horizontally layered initial state (see step 2) is used for all conducted experiments. After the physical completion of the experiment the results are two videos/picture sequences of the cross section. Further data processing is done afterwards in a post-processing step using digital image processing techniques.

3.4.1.2 Analyzing methodology

The pictures are analyzed with the software ImageJ®, the steps of analysis have also been explained in [235]. The two picture sequences will be called front light sequence (FLS) and back light sequence (BLS) in the following. In a first step, the cross section of the inner drum is cropped from the pictures to eliminate disturbing and needless information and to optimize the subsequent calculation by reducing the amount of data for both picture sequences (FLS & BLS). Afterwards the BLS is analyzed by thresholding the dark solid-bed area and determining the surrounding

borderline for each image. Therefore the region of interest (ROI) in analyzing the particles (only particle bed should be analyzed) is created for each image. This is necessary because while measuring with sectional internals the solid bed has a different shape and is positioned on different cross sectional coordinates in each picture. The ROIs (borderlines) from shadowgraph pictures are transferred to the corresponding pictures of the FLS afterwards. Now the solid bed region can be cropped out of the picture of the complete cross section as shown in the example in Figure III - 3.12 for a bare drum experiment. The area around the solid bed is masked in black by this calculation.

In the next, step a grid is overlaid on the prepared pictures, which is the equivalent to the step of sampling in conventional analyzing methods for mixing processes. The grid is fixed globally to the pictures. A reasonable size of grid cells, which can also be considered as "sample cells", is identified in preliminary experiments. For this purpose, the mixing progress was evaluated with different cell sizes (different pixel numbers in the rectangular cell) and thus particle number in a cell. Due to the different position and shape of the solid bed in each picture and the globally fixed grid, the main issue is the analysis of the outer solid bed borders. The grid size should be small to overcome this problem, resulting in a higher amount of data and less particles in each box. Therefore, the chosen cell size of 144 pixels (~15 particles) is a tradeoff between accuracy, amount of data and computing capacity. The size of sample cells is the same in all conducted measurements to guarantee comparability. An example is presented in Figure III - 3.13.

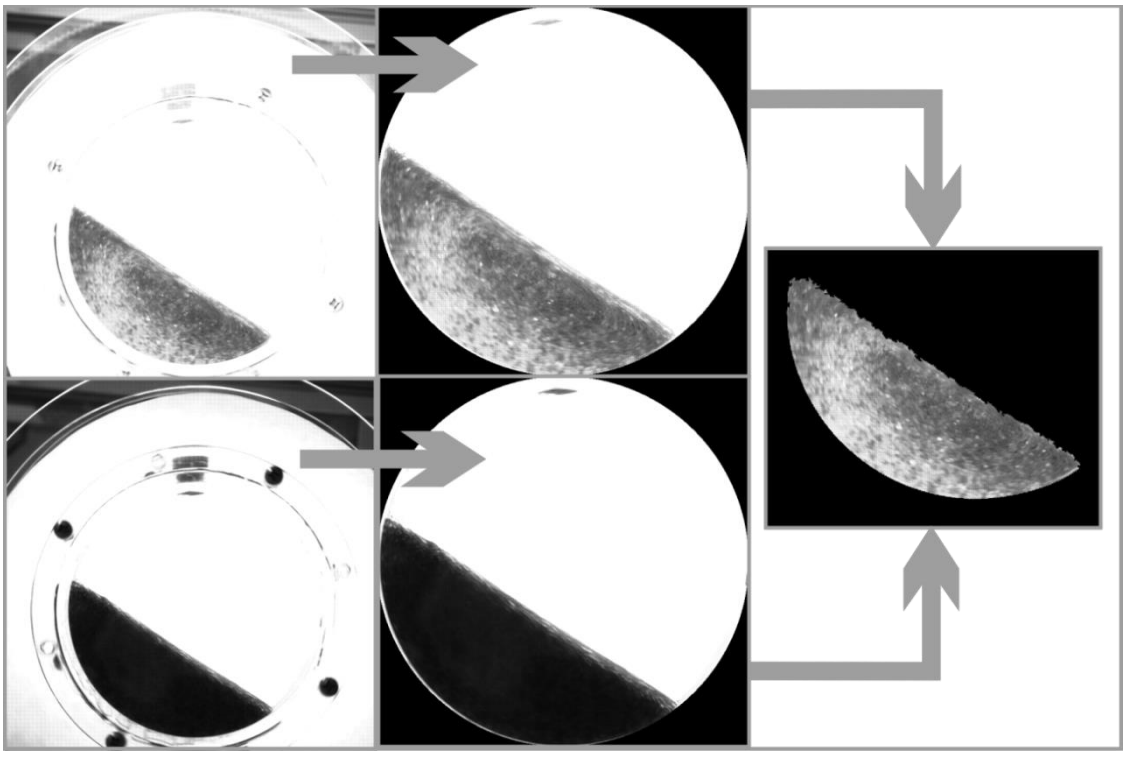

Figure III - 3.12: Exemplary processing steps of the images for a bare drum experiment (n=11 min^{-1}; Φ=0.3; MC1) after one rotation.

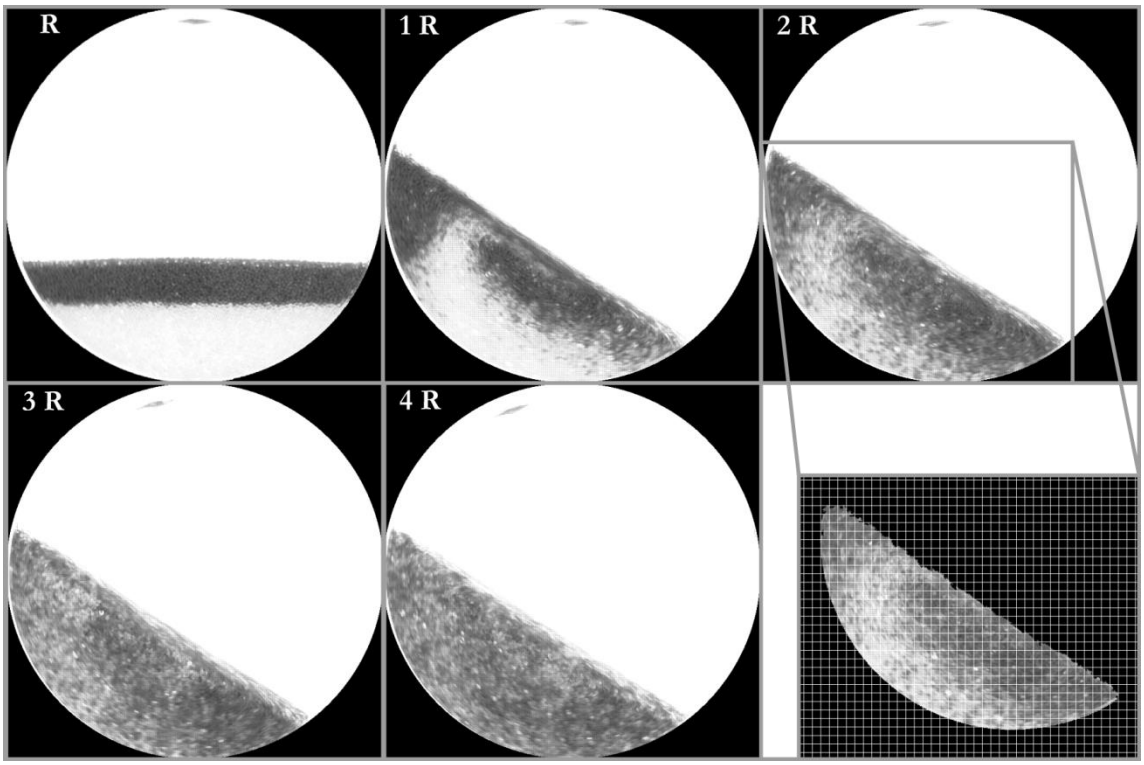

Figure III - 3.13: Exemplary pictures for a bare drum experiment (n=11 min^{-1}; Φ=0.3; MC1) after several rotations (top left corner). At the right bottom corner: example of the selected solid bed for data evaluation with the overlaid grid is presented (according to [235])

The mean grey value (MGV_i) of each grid box (location, i) is calculated in ImageJ® as equivalent to the concentration of black/white particles for each picture. While the surrounding area is masked in black (MGV=0) only cells with MGV>20 are transferred to further examination steps. This guarantees no surrounding area is affecting the analysis and minimizes error due to the border region (black background & bed).

Concluding, no invasive sampling is needed and there are no process interruptions and material loss although the complete amount of solids in the cross section is analyzed. The result is a matrix with local MGV ($MGV_{i,t}$) for each image or time step. The processing procedure is automated to increase throughput of measurements.

The matrix is used afterwards to calculate the concentrations c in each grid box or sampling area. An area from the first frame is analyzed concerning the mean grey value containing only white bulk-material (MGV_{min}; c=0). The same determination is performed with an area containing only black tracer material (MGV_{max}; c=1). All MGV in the matrices (for each time step) of the experimental run are transformed into concentrations ($c_{i,t}$) by linear scaling:

$$c_{i,t} = \frac{MGV_{i,t} - MGV_{\min}}{MGV_{\max} - MGV_{\min}} \tag{3.38}$$

These concentrations are used to perform the calculations of the standard deviation and following the mixing degree as explained in chapter 2.2.2.

3.4.1.3 Design of experiments

The rotational speed (n) and the filling degree (Φ, defined as the volumetric occupancy of the drum or one section divided by the total volume of the drum or section) of the drum were varied based on a statistical design of experiments, shown in Table III - 3.3.

These 9 experiments were conducted with different internal structures of the cross section apparatus including the bare drum and sectional internals with 3, 4 and 6 sections respectively. The internal structures are named as drum-configurations (DC1, DC5, DC3 and DC4, consistently with the axial flow measurements) and presented in Figure III - 3.14.

Besides the equipment configuration also the materials used in flow analysis have been varied in order to simulate a segregating and a non segregating system. Two different material combinations (MC) of large and small bulk particles and large tracer particles (according to Table III - 3.1) have been used as shown in Table III - 3.4.

Finally, in order to gain statistical information, the midpoint experiment (n=7.3 rpm Φ=0.2) was executed three times for error estimation (88 experiments in total).

Table III - 3.3: Design of experiments for operational parameters (n: rotational speed, Φ: filling degree) in transverse flow and mixing analysis with bare drum and sectional internals

Exp.-No.	n [1/min]	Φ [-]
01	3.8	0.1
02	7.3	0.2
03	11.0	0.3
04	3.8	0.1
05	7.3	0.2
06	11.0	0.3
07	3.8	0.1
08	7.3	0.2
09	11.0	0.3

Table III - 3.4: Investigated material combinations (MC) in transverse flow and mixing analysis with bare drum and sectional internals

		Small particles	Large particles	
Property		Bulk	Bulk	Tracer
Color		white	white	black
MC1	m.-%		50	50
MC2	m.-%	50		50

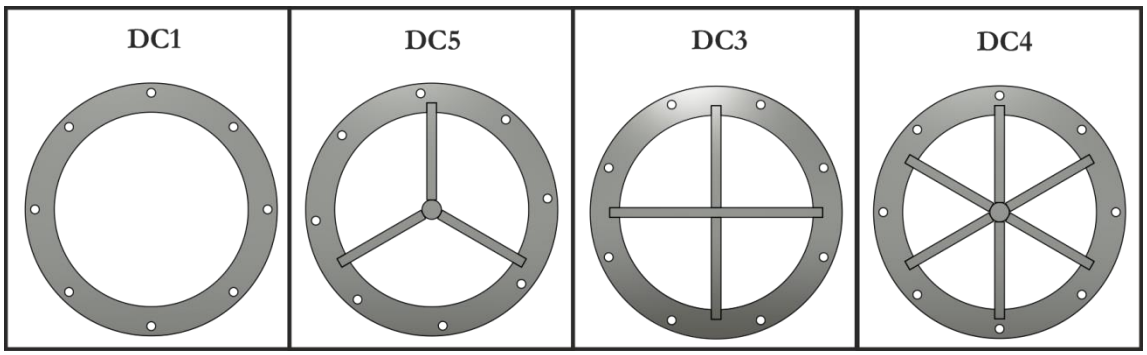

Figure III - 3.14: Drum configurations (DC) used in the transversal flow and mixing analysis

3.4.2 Flighted rotary drums

In the analysis of the cross section of flighted rotary drums, especially the loading and unloading of the flights and thus the solids distribution in the gas phase is essential. Since flights induce a high degree of mixing and the cascading of the particles itself induces high dispersion, mixing in the cross-section is not investigated.

The aim in the development of the routine was the compatibility to the already given apparatus and less effort in the adaption of the routine. The main issue was to provide a good contrast in the image acquisition to facilitate image analysis. In order to provide a good contrast, the white diffusor at the back plate of the cross section model (cf. chapter 3.1.3) was exchanged to a black paper.

3.4.2.1 Description of the routine

The routine is adopted from the bare drum routine (cf. chapter 3.4.1.1), although some changes had to be implemented. The camera setup is the same as for bare drum measurements (50 fps, exposure time is set to 0.25 ms), and the following steps have been done while execution:

1. The rotational speed of the drum is set with the gear-motor and checked with the empty cross section model.
2. Disassembling of the front wall of the drum and preparing the inner walls of the drum with antistatic-spray.
3. Insertion of the flight-model under investigation (models are explained in the following). The models prevent the usage of the radial filling hole.
4. The cross-section model is filled with white beads of the size under consideration. The amount of beads is calculated to the desired filling degree.
5. The front plate is reassembled and the cross section model is mounted to the roller station. The solid/gas surface should be horizontal.
6. The ring type front light is activated and the experiment is initiated by starting the camera and the motor of the apparatus.
7. The experiment is stopped after 1800 frames of the camera.
8. The photo sequence/video is saved and analyzed as illustrated in chapter 3.4.2.2.

At the end of the experiment the result is a video/picture sequence of the cross section. Further data processing is once more done afterwards in a post-processing step using suitable digital image processing techniques.

3.4.2.2 Analyzing methodology

The pictures are analyzed with the software ImageJ®. The steps of analysis are conducted as explained in the following. The procedure is visualized in the related Figure III - 3.15.

First of all, the pictures of the video sequence are prepared by cropping the inner of the drum from the pictures to reduce the data amount. Next, the gas-phase of the drum, specified as the inner circle contacting the flights, is cropped again. The flights itself and the material hold-up in the drum are omitted with this procedure. From the gained pictures the area fraction occupied by the white solid curtains (f_{OA}) is analyzed. A reasonable threshold (range of gray values) is determined visually in preliminary experiments, for this purpose. The threshold serves as decision point to count pixels as part of a particle or background and thus separating background and solids.

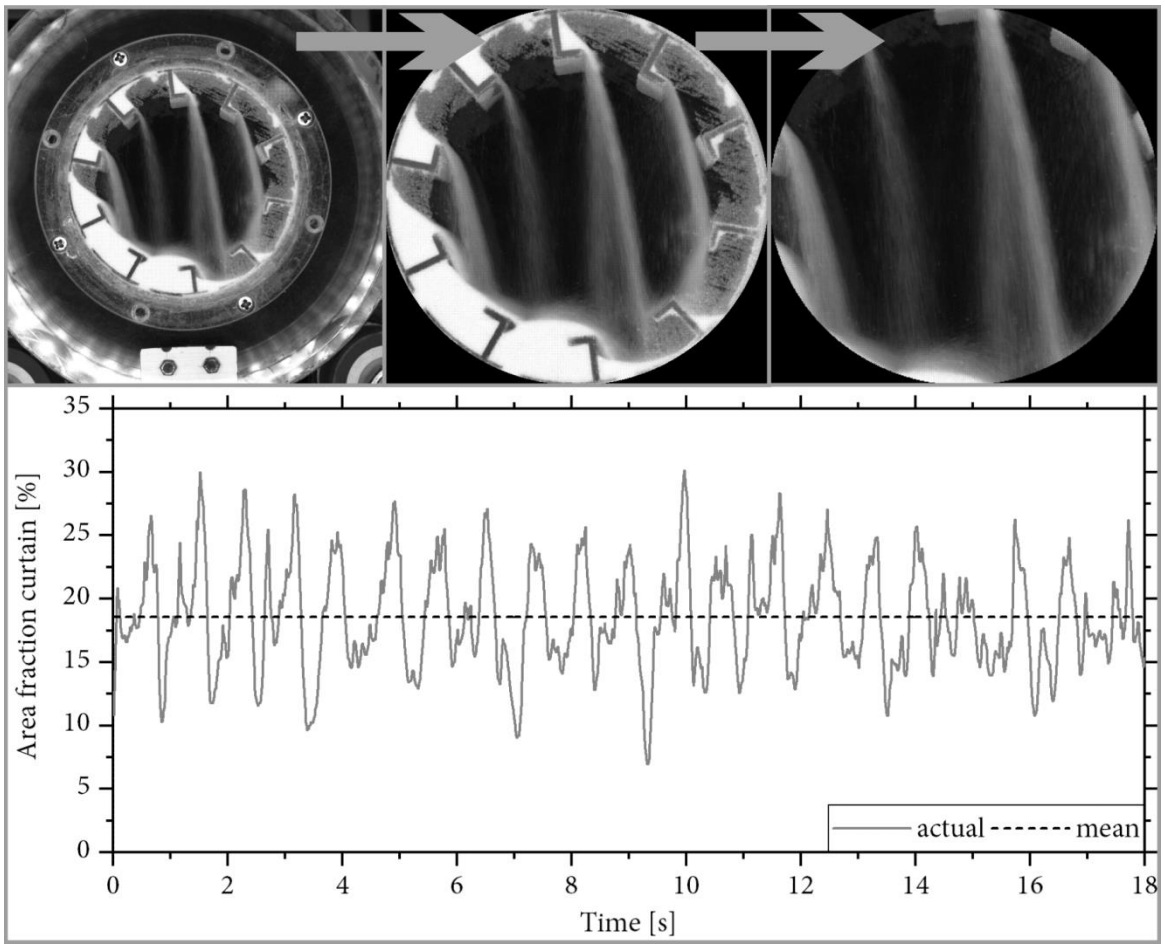

Figure III - 3.15: Exemplary visualization of the "lifter analysis"-routine; parameters: rotational frequency 7.3 min^{-1}, filling degree 15%, small white particles 100-200 µm

Since the calculations are performed for each picture of the sequence, afterwards the values of the area fraction are plotted against the time. As can be seen easily, the unloading is a periodic procedure. Therefore, the mean value of f_{OA} (mf_{OA}) over the measured time is calculated.

Finally, this mean value is a measure of occupied gas phase in the cross section and therefore represents a measure of "trickling-density". Further evaluations are performed with the mean value regarding the operational parameters afterwards.

3.4.2.3 Design of experiments

The rotational speed (n) and the filling degree (Φ, defined as the volumetric occupancy of the drum or one section divided by the total volume of the drum or section) of the drum were varied based on a statistical design of experiments, shown in Table III - 3.5. Preliminary experiments revealed that filling degrees of 20% already led to the overloading state and higher filling degrees as e.g. 30% (cf. Table III - 3.3) provide no further information.

Table III - 3.5: Design of experiments for operational parameters (n: rotational speed, Φ: filling degree) in transverse flow and unloading characteristics in flighted rotary drums

Exp.-No.	n [1/min]	Φ [-]
01	3.8	0.10
02	3.8	0.15
03	3.8	0.20
04	7.3	0.10
05	7.3	0.15
06	7.3	0.20
07	11.0	0.10
08	11.0	0.15
09	11.0	0.20
10	3.8	0.05
11	7.3	0.05
12	11	0.05

Each of the 12 experiments is furthermore conducted with both particle sizes. All experiments were conducted once for each investigated drum configuration except Exp.-No. 5 (midpoint), which was executed 3 times in order to gain statistical information of reproducibility. Furthermore, the DOE was applied to eight different flight internals installed in the cross section apparatus as will be described in the following. This results in a total of 240 experiments.

Via CAD-construction and 3D-printing various flight models have been created. The focus is on the investigation of the impact of axial flight length. Therefore, each type of flight is at least investigated in two different axial lengths.

L-Flights:

Four different configurations of L-Flights have been used. The flight dimensions in the cross section are equal to the configurations applied in axial solid transport investigation (see Figure III - 3.10). The basic model (L_{cont}) considers axially continuous flights, while the second model is equal to the short lifters from Figure III - 3.10 (L_{10mm}). Additionally, to these models one configuration of the short lifters with 20mm length in axial direction is constructed (L_{20mm}). At least a model based on the short lifters is created, where the flights have additional front side walls in the height (5.5mm) of the tangential lifter element ($L_{10mm,closed}$). Thus, closed single lifter buckets are created. All configurations are exemplarily presented in Figure III - 3.16. The nomenclature of the explained models has been given in braces and will be used in the following evaluations.

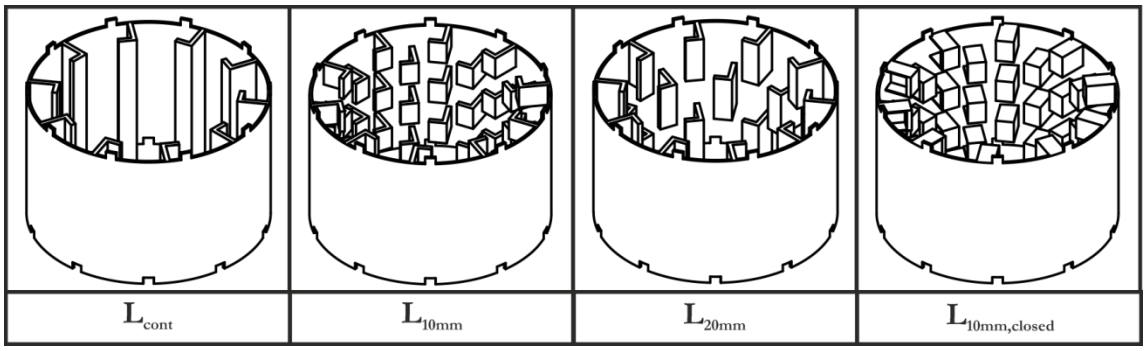

Figure III - 3.16: Sketches of the different versions of L-type flights analyzed regarding the transversal solid transport.

EAD- / EHD-Flights:

In order to perform tests with distinct flight designs as known from literature (see chapter 2.4.1), different types of flights have been created. Since EAD and EHD flights should be optimized regarding the dispersion of solids in the gas-phase these types are chosen. Both models have been constructed in a continuous version (EAD_{cont}, EHD_{cont}) and in a modified way with 10mm of axial length analogously to the L-flights (EAD_{10mm}, EHD_{10mm}). The configurations have been presented in Figure III - 3.17.

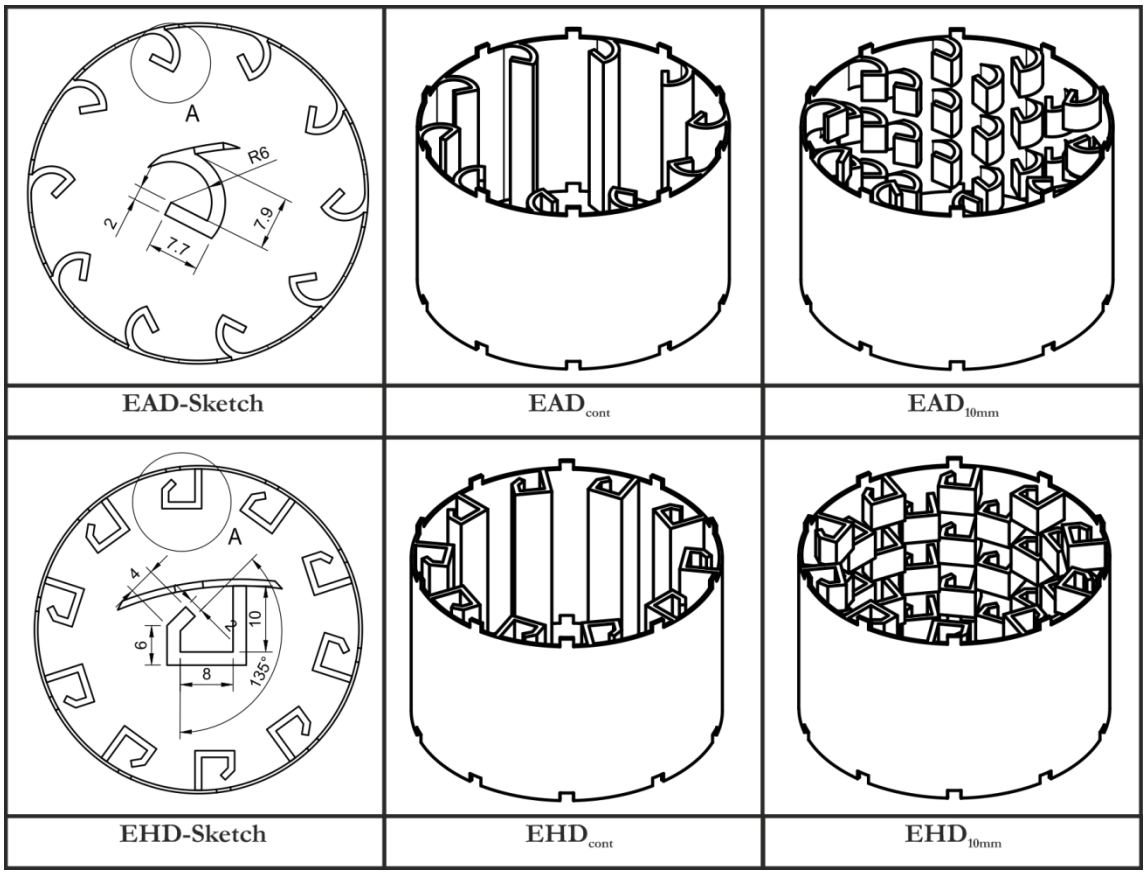

Figure III - 3.17: Sketches of the different versions of EAD- and EHD-flights analyzed regarding the transversal solid transport. All dimensions in mm.

4 Results & Discussion

In this chapter the magnitude of experimental results is presented and discussed. The presentation of results is structured as already explained in the description of the experimental setup (chapter 3).

4.1 Axial solid transport

First of all, the axial solid transport investigations are presented. The main results here are the residence time distributions. In order to provide a good comparison, the characteristic values as MRT, axial dispersion coefficient and hold-up are presented

4.1.1 Axial flow configuration 1

The evaluations provided for axial flow configurations 1 have been published already in [233]

4.1.1.1 Mean residence time (AFC1)

The measured MRT-values for all investigated configurations (DC1-DC4) are listed in Table III - 4.1.

Table III - 4.1: MRT-values of all experiments conducted with AFC1, calculated from RTD-curves

		Exp. Run			Mean	Std.	rel. Std.			Exp. Run			Mean	Std.	rel. Std.
	Exp. -No.	1 [s]	2 [s]	3 [s]	[s]	[s]	[%]		Exp. -No.	1 [s]	2 [s]	3 [s]	[s]	[s]	[%]
DC1	1	232	260	257	250	15.4	6.2	DC3	1	888	887	877	884	6.1	0.7
	2	116	112	113	114	2.1	1.8		2	352	252	362	322	60.8	18.9
	3	125	110	114	116	7.8	6.7		3	427	399	388	405	20.1	5.0
	4	50	46	47	48	2.1	4.4		4	133	133	137	134	2.3	1.7
	5	215	233	216	221	10.1	4.6		5	824	781	776	794	26.4	3.3
	6	90	86	92	89	3.1	3.4		6	310	315	316	314	3.2	1.0
	7	131	129	130	130	1.0	0.8		7	432	402	412	415	15.3	3.7
	8	48	53	55	52	3.6	6.9		8	163	132	130	142	18.5	13.1
	9	92	92	99	94	4.0	4.3		9	259	256	251	255	4.0	1.6
DC2	1	382	388	398	389	8.1	2.1	DC4	1	809	957	916	894	76.4	8.5
	2	181	194	212	196	15.6	8.0		2	542	543	556	547	7.8	1.4
	3	138	118	116	124	12.2	9.8		3	416	432	447	432	15.5	3.6
	4	73	66	69	69	3.5	5.1		4	176	180	172	176	4.0	2.3
	5	276	295	297	289	11.6	4.0		5						
	6	149	149	149	149	0.0	0.0		6	510	522	519	517	6.2	1.2
	7	100	100	99	100	0.6	0.6		7	489	487	471	482	9.9	2.0
	8	58	53	58	56	2.9	5.1		8	169	168	169	169	0.6	0.3
	9	118	114	121	118	3.5	3.0		9	374	367	346	362	14.6	4.0

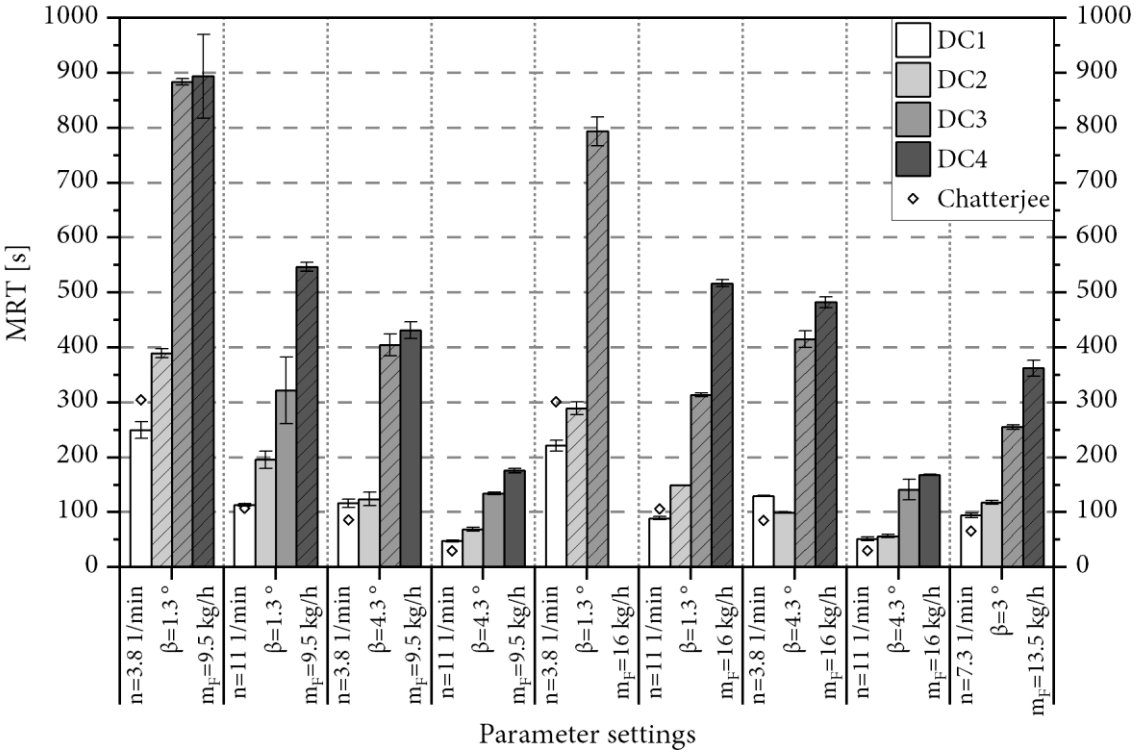

Figure III - 4.1: Diagram of MRT-values calculated from the RTD-curves (axial flow configuration 1); column hatchings indicate the occurence of back-spillage in these experiments, rhombic points represent calculated MRT according to the model of Chaterjee et al. [158] (adapted from [233])

The mean values (three executions) of MRT for all experiments and configurations are illustrated in Figure III - 4.1 graphically. The standard deviations (std.) and relative standard deviations (rel. std.), also represented as error bars in Figure III - 4.1, indicate that the methodology provides good reproducibility for all parameter combinations. The column hatchings in the diagram indicate that back-spillage occurred in these experiments, which means feed material leaves the rotary drum at the inlet end. Furthermore, a MRT is indicated (rhombic points) which is calculated by the theoretical model of Chatterjee (cf. chapter 2.3.1).

This model was used to check the plausibility of the values measured with the bare drum (DC1). Good congruence with the literature model is found concerning the trends, although especially in both experiments with low inclination and low rotational speed a higher deviation is observable. In Figure III - 4.1 similar trends regarding the set of operational parameters are obvious for all drum configurations. However, compared to the bare drum (DC1) the absolute MRT-values are significantly higher with configurations DC2–DC4. The increase in MRT is qualitatively plausible for DC2 with installed exit dam, since the dam inhibits the axial particle flow and leads to increased hold-up as presented later. Increased MRT due to constriction dams has also been found by Chatterjee [157]. Due to the similar dependencies of operational parameters, a description of the

MRT-gain regarding the bare drum (DC1) with constant additional values (Δ) and constant increase factors (IF) is evaluated:

$$\Delta_{DCx} = MRT_{DCx} - MRT_{DC1} \tag{3.39}$$

$$IF_{DCx} = \frac{MRT_{DCx}}{MRT_{DC1}} \tag{3.40}$$

The calculated results are listed in Table III - 4.2 and presented graphically in Figure III - 4.2.

The evaluation delivers a wide spread of Δ-values (–30 to 140 s), revealing a similar pattern regarding the operational parameters as MRT itself. However, the correlation between MRT and Δ-values with $R^2 = 0.42$ is rather weak (cf. Figure III - 4.2.). IF is within the range of 0.77 (outlier Exp. 07) to 1.72. The mean of the IF (MIF) with 1.32 increase or 32 %, respectively, is in the range of cross section shrinkage (CSS, [%]) evoked by the constriction dam (36 %). A first approach to calculate the constriction dam impact is multiplying the calculated MRT, e.g., according to Eq. (3.13) with the CSS [233]:

$$\bar{t} = 0.1026 \cdot \left(1 + \frac{CSS}{100}\right) \cdot \frac{L^3}{\dot{V}} \cdot \left(\frac{\theta}{\beta}\right)^{1.054} \cdot \left(\frac{\dot{V}}{L^3 n}\right)^{0.981} \cdot \left(\frac{L}{D}\right)^{1.1} \tag{3.41}$$

Table III - 4.2: Calculated additional values (Δ) and increase factors (IF) of MRT based on comparison with the bare drum (DC1) for AFC1 (adopted from [233])

Exp.-No.	n	β	$\dot{m}_F$	DC1	DC2			DC3			DC4		
				MRT	MRT	Δ	IF	MRT	Δ	IF	MRT	Δ	IF
	[1/min]	[°]	[kg/h]	[s]	[s]	[s]	[-]	[s]	[s]	[-]	[s]	[s]	[-]
01	3.8	1.3	9.5	250	389	140	1.56	884	634	3.54	894	644	3.58
02	11	1.3	9.5	114	196	82	1.72	322	208	2.83	547	433	4.81
03	3.8	4.3	9.5	116	124	8	1.07	405	288	3.48	432	315	3.71
04	11	4.3	9.5	48	69	22	1.45	134	87	2.82	176	128	3.69
05	3.8	1.3	16	221	289	68	1.31	794	572	3.59			
06	11	1.3	16	89	149	60	1.67	314	224	3.51	517	428	5.79
07	3.8	4.3	16	130	100	-30	0.77	415	285	3.19	482	352	3.71
08	11	4.3	16	52	56	4	1.08	142	90	2.72	169	117	3.24
09	7.3	3	13.5	94	118	23	1.25	255	161	2.71	362	268	3.84
		mean		124	166	42	1.32	407	283	3.15	447	336	4.05
		rel. STD		52.9	62.4	115	22.5	61.3	65.2	11.4	48.3	48.2	19.3

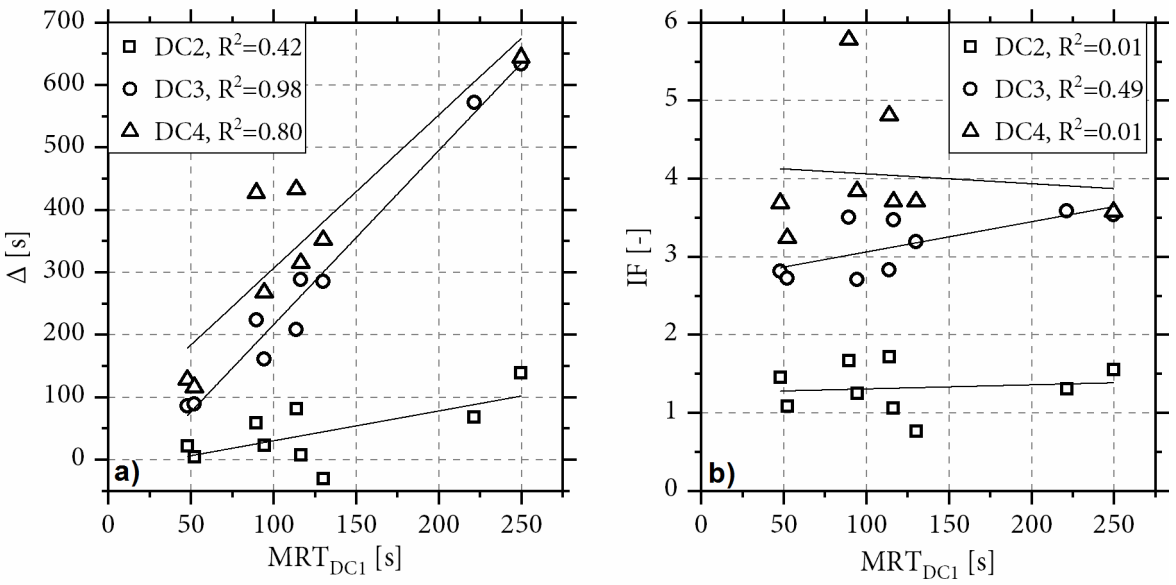

Figure III - 4.2: a) Diagram of Δ-values against the MRT of DC1 with regression analysis; b) Diagram of IF-values against the MRT of DC1 with regression analysis (adopted from [233])

Attention has to be paid on this approach due to precision, since the relative standard deviation of IF (rel. σ_{IF}) regarding the full DOE with 22% including all experiments suggests further influencing factors as e.g. operational parameters. The occurrence of back-spillage and therefore reaching capacity limits additionally influences the results. Further research is needed here with different dam diameters as well as operational parameter settings.

The impact of sectional internals (DC3, DC4) on MRT is remarkably higher compared to the constriction dam. Figure III - 4.1 reveals similar trends regarding the operational parameters, thus two possible explanations come to mind.

First, the behavior of sectional internals is considered similarly to constriction dams. However, the CSS of DC3 (13%) and DC4 (19%) is lower than the shrinkage of the dam while MRT is increasing above DC2-values. Concluding, the mechanism evoked by sectional internals is completely different to dams.

In the second explanation approach, sectional internals are considered to divide the drum into N equal compartments and therefore the drum would behave like N single drums. Thus, a constant factor of N should describe the increase in MRT compared to the bare drum. The Δ-values of DC3 are correlating well with the MRT (R^2=0.98, cf. Figure III - 4.2.), and MRT-increase is larger if MRT itself is high in the bare drum. This suggests a dependency of increase from operational parameters. The IF of DC3 (range 2.71 to 3.59) has a mean value of 3.15 with rel. STD of 11% (cf. Table III - 4.2). That means IF-fluctuation is much lower than for the constriction dam, but it deviates significantly from the section number N=4.

Discussing configuration DC4, MIF increases to 4.05 with a rel. STD of 19% (range 3.24 to 5.79). Although the section number rises by 50% from 4 to 6, MIF is increasing only slightly compared to DC3. It has to be stated, that particularly the IF of Exp. 02 and Exp. 06 deliver higher values and back-spillage superimposes the findings.

Summarizing, a description using constant factors based on the section number N is not possible. Further research is needed, quantifying the back-spillage and expanding the parameter space, to find a suitable and quantitative description or model.

4.1.1.2 Hold-up (AFC1)

The determined hold-up-values for all investigated configurations (DC1-DC4) are listed in Table III - 4.3, and displayed in Figure III - 4.3 graphically.

Table III - 4.3: Hold-up values of all experiments conducted with AFC1, determined as material in the drum after each experiment.

	Exp. Run			Mean	Std.	rel. Std.		Exp. Run			Mean	Std.	rel. Std.
Exp.	1	2	3				Exp.	1	2	3			
-No.	[g]	[g]	[g]	[g]	[g]	[%]	-No.	[g]	[g]	[g]	[g]	[g]	[%]
	DC1							DC2					
1	683	689	698	690	7	1.1	1	794	778	633	735	89	12.1
2	450	444	435	443	8	1.8	2	738	626	732	699	63	9.0
3	314	322	381	339	36	10.7	3	661	756	761	726	57	7.8
4	166	143	142	150	14	9.0	4	239	220	258	239	19	8.0
5	588	599	572	586	14	2.3	5	1371	1160	1225	1252	108	8.6
6	1088	1200	1199	1162	64	5.5	6	960	924	949	945	18	1.9
7	888	871	904	887	17	1.9	7	1086	1060	1048	1065	19	1.8
8	335	363	368	355	18	5.0	8	473	471	508	484	21	4.3
9	603	591	618	604	13	2.2	9	760	734	710	735	25	3.4
	DC3							DC4					
1	1018	1020	1012	1017	4	0.4	1	1143	1183	1066	1131	59	5.2
2	949	937	930	939	9	1.0	2	995	1000	987	994	7	0.7
3	1226	1249	1275	1250	25	2.0	3	804	808	798	803	5	0.6
4	362	326	345	344	18	5.3	4	457	433	414	435	22	5.0
5	1476	1469	1474	1473	4	0.3	5						
6	1471	1469	1460	1467	6	0.4	6	1521	1514	1495	1510	13	0.9
7	1064	1062	1098	1075	20	1.9	7	1645	1670	1636	1650	18	1.1
8	921	916	899	912	12	1.3	8	1201	1207	1209	1205	4	0.3
9	1238	1258	1249	1248	10	0.8	9	1278	1300	1298	1292	12	0.9

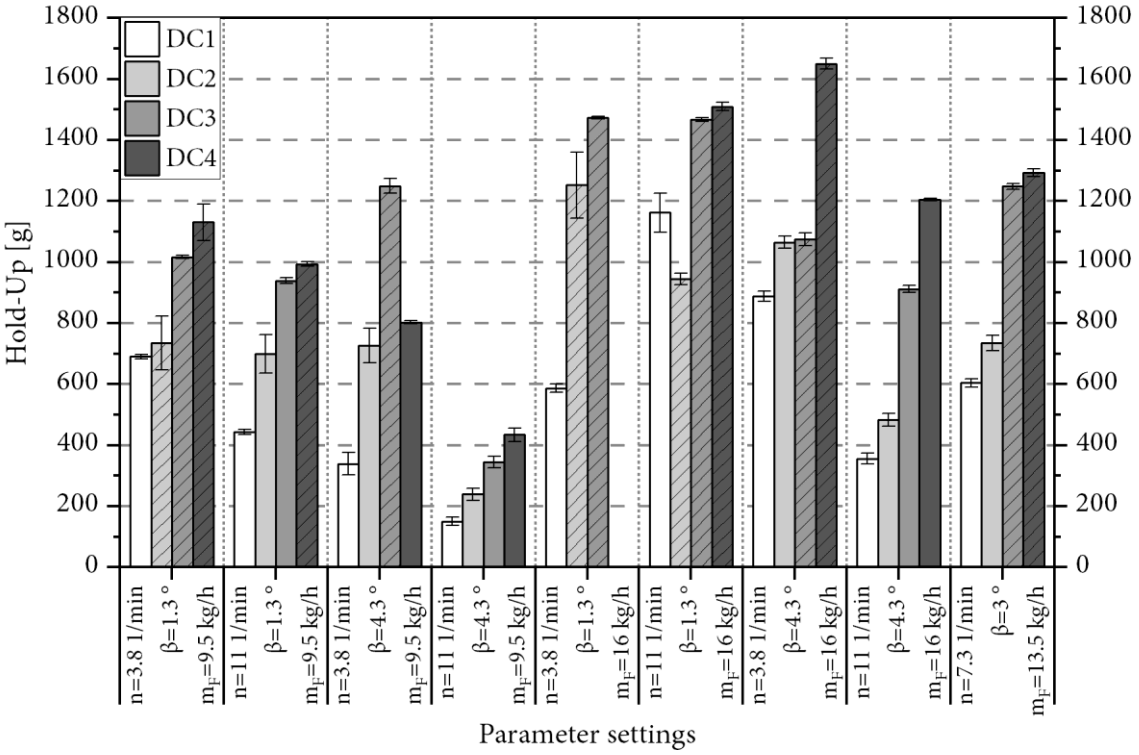

Figure III - 4.3: Comparative diagram of hold-up values for each experiment and configuration; column hatchings indicate back-spillage in these experiments. (adapted from [233])

The pattern in Figure III - 4.3 is different in comparison to the one presenting MRT (Figure III - 4.1). As the column hatchings in the bars indicate, back-spillage occurred in some experiments with internals and constriction dam (DC2-DC4). This suggests capacity limits for the investigated combination of operational parameter setting and system-configuration. Figure III - 4.3 reveals higher hold-ups with exit dam and sectional internals compared to the bare drum (DC1). Sectional internals create a further increase compared to the exit dam, although CSS for DC3/DC4 is lower, which undermines the different mechanism already stated. The data delivers no strict maximum hold-up to indicate the occurrence of back spillage (BS), e.g. with DC2 in Exp. 07 no BS occurred, although the hold-up is higher than in Exp. 01 with back-spillage. Back-spillage reduces the effective feed rate to the drum. Therefore, no strict correlation between MRT and hold-up exists for the measured data in this part of the work. A calculation of BS is performed via hold-up and feed rate utilizing the hydrodynamic residence time τ_{hyd}. The back spillage mass flow $\dot{m}_{BS}$ reduces the feed rate $\dot{m}_F$ to an effective mass flow $\dot{m}_{eff}$ through the drum:

$$\dot{m}_{eff} = \dot{m}_F - \dot{m}_{BS} \tag{3.42}$$

Via the hold-up m_{HU} and the hydrodynamic residence time the back spillage mass flow is calculated to:

$$\dot{m}_{BS} = \dot{m}_F - \frac{m_{HU}}{\tau_{hyd}} \tag{3.43}$$

If the value of $\dot{m}_{BS}$ is zero or negative, no back spillage occurs; a positive value represents the back spillage mass flow. This mass flow is related to the feed rate in the back spillage ratio or fraction f_{BS}:

$$f_{BS} = \frac{\dot{m}_{BS}}{\dot{m}_F} \tag{3.44}$$

The ratio of back spillage and feed rate is defined as back-spillage ratio (BSR). It is observable that the BSR and thus the system override are increasing with a growing number of sectional internals.
The occurrence of back spillage in the experiments is not congruent to the calculated back spillage. This reveals some deficiency in the data. It is clearly observable, that back spillage is higher with sectional internals in experiments where back spillage occurred. This is plausible due to higher MRT with sectional internals.
The back spillage is not higher for DC4 in Exp. 01 although MRT is slightly higher. But in theory back spillage occurs in nearly all experiments referring to DC4, which is plausible due to higher MRT.

Table III - 4.4: Calculated back spillage ($\dot{m}_{BS}$) and back spillage ratio (f_{BS}) for all conducted experiments

	DC1		DC2		DC3		DC4	
Exp.-No.	$\dot{m}_{BS}$ [kg/h]	f_{BS} [-]	$\dot{m}_{BS}$ [kg/h]	f_{BS} [-]	$\dot{m}_{BS}$ [kg/h]	f_{BS} [-]	$\dot{m}_{BS}$ [kg/h]	f_{BS} [-]
1	-0.4		2.7	0.28	5.4	0.56	4.9	0.52
2	-4.5		-3.4		-1		3	0.31
3	-1		-11.6		-1.6		2.8	0.3
4	-1.9		-2.9		0.3	0.03	0.6	0.06
5	6.5	0.4	0.4	0.03	9.3	0.58		
6	-30.8		-6.8		-0.8		5.5	0.34
7	-8.6		-22.5		6.7		3.7	0.23
8	-8.6		-14.9		-7.2		-9.7	
9	-9.6		-9		-4.1		0.7	0.05

Exp.-No. 5, configuration DC4 (Table III - 4.4) depicts a combination of maximum section number, a high feed rate and a low rotational speed as well as inclination of the drum and therefore could not be executed because unexpectedly back spillage was too high so draining through the inlet funnel into the drum was stopped and a backlog in the inlet chute developed. The deficiency of the data is one reason for the modifications of the apparatus performed in the axial flow configuration 2.

4.1.1.3 Axial dispersion, D_{ax} (AFC1)

The axial dispersion coefficient as a measure for axial mixing in the rotary drum is calculated from the variance of the distribution as shown in equation (3.28). The determined D_{ax}-values for all investigated configurations (DC1-DC4) are listed in Table III - 4.5, and presented in Figure III - 4.4 graphically for all conducted experiments. The error bars suggest, that the exact determination of the coefficient is difficult because errors of different characteristic values of the distribution run into the calculation (equation (3.28)).

Taking the error bars into account, Figure III - 4.4 shows that D_{ax} is only changing very slightly for all configurations (DC1-DC4) in a magnitude of about $1 \cdot 10^{-5}$ to $1 \cdot 10^{-6}$ m²/s except for some outliers. The average values fit very well into literature data where others found the axial dispersion coefficient to be in a range of $1 \cdot 10^{-4}$ to $1 \cdot 10^{-7}$ m²/s [174] (range of the diagram in Figure III - 4.4). The values for DC1/DC2 and DC3/DC4 with sectional internals are not differing significantly.

Therefore, no significant additional axial dispersion is introduced by sectional internals, although in MRT-analysis a different mechanism was proposed.

Table III - 4.5: Calculated axial dispersion coefficients (D_{ax}) for all experiments (all values in [10^{-6} m²/s]

Exp. -No.	Exp. Run 1	2	3	Mean	Std.	rel. Std. [%]	Exp. -No.	Exp. Run 1	2	3	Mean	Std.	rel. Std. [%]
	DC1							DC2					
1	1.8	2.8	2.3	2.3	0.5	21.0	1	0.8	2.0	1.6	1.5	0.6	40.6
2	5.1	6.7	5.1	5.6	0.9	16.4	2	2.9	0.9	1.1	1.6	1.1	66.8
3	0.9	3.6	1.8	2.1	1.4	65.7	3	4.9	0.6	0.6	2.1	2.5	119.0
4	9.0	12.3	12.1	11.1	1.9	16.8	4	2.1	3.9	3.2	3.1	0.9	30.4
5	6.0	5.8	5.2	5.7	0.4	7.1	5	4.5	2.6	2.0	3.0	1.3	41.9
6	7.2	9.1	9.4	8.6	1.2	13.6	6	2.2	2.2	2.0	2.1	0.1	6.5
7	3.8	4.3	3.9	4.0	0.3	7.1	7	0.1	0.1	0.8	0.3	0.4	135.2
8	29.2	15.4	13.2	19.3	8.7	45.0	8	0.6	0.3	11.3	4.1	6.3	154.3
9	1.7	2.8	1.7	2.0	0.6	30.6	9	0.8	0.8	0.7	0.8	0.1	9.0
	DC3							DC4					
1	0.6	0.7	1.0	0.7	0.2	25.4	1	4.2	1.4	2.2	2.6	1.4	55.5
2	2.1	12.1	3.5	5.9	5.4	91.5	2	1.6	1.7	1.8	1.7	0.1	4.2
3	1.4	2.1	2.0	1.8	0.4	21.7	3	5.9	5.2	5.5	5.5	0.3	6.1
4	0.9	2.3	2.6	1.9	0.9	47.7	4	21.5	21.0	21.9	21.5	0.5	2.1
5	1.3	0.7	1.2	1.1	0.3	27.2	5						
6	3.0	2.9	2.7	2.9	0.2	5.8	6	1.9	1.6	1.3	1.6	0.3	17.7
7	3.8	2.4	2.3	2.8	0.8	28.3	7	6.8	5.8	6.4	6.3	0.5	7.5
8	27.4	7.0	4.4	12.9	12.6	97.6	8	6.9	7.6	10.5	8.3	1.9	22.9
9	1.4	2.5	2.8	2.2	0.7	32.5	9	4.3	8.8	7.0	6.7	2.3	33.9

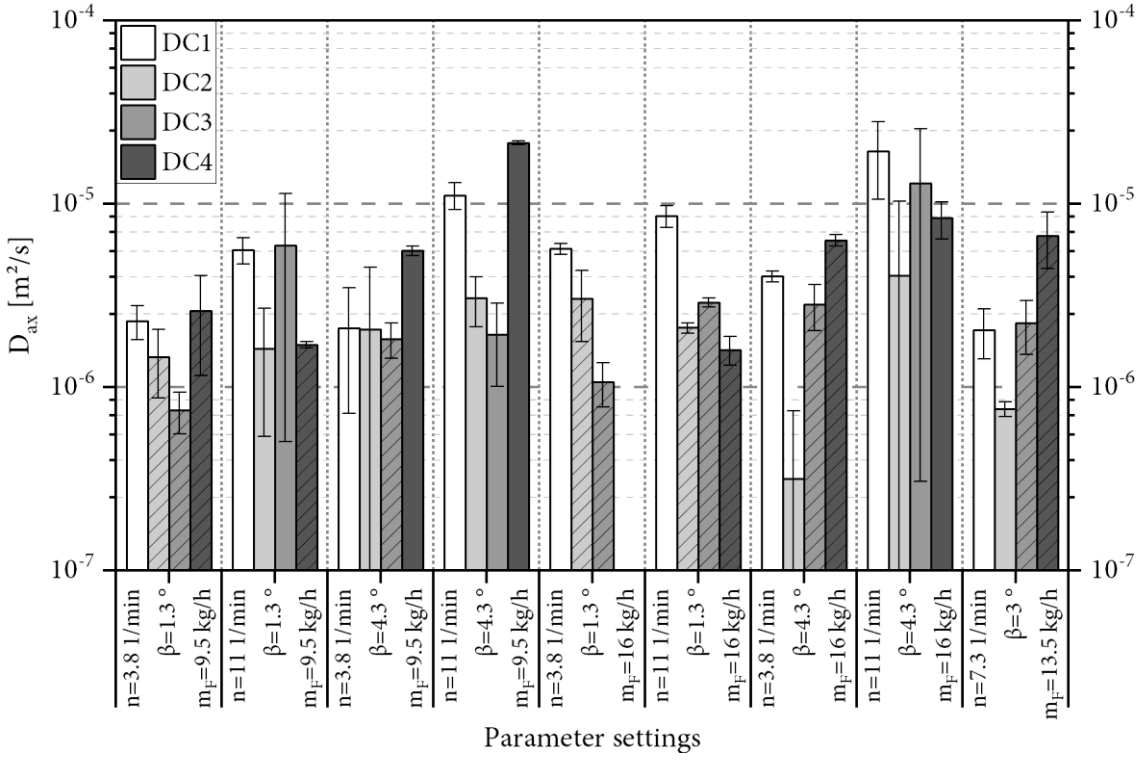

Figure III - 4.4: Calculated axial dispersion coefficients (D_{ax}) for all experiments, column hatchings indicate back-spillage in these experiments (adapted from [233])

4.1.1.4 DOE-Analysis (AFC1)

The analysis of effects is based on a linear model due to the DOE-design, testing each parameter on two stages. Effects deliver the direction and magnitude of impact on an attribute A due to the conducted parameter changes. In Table III - 4.6 the calculated effects (eff.) are presented with the experimental F-value (F_{exp}). The theoretical F-value (F_{theo}) with significance level of 95% is determined to 4.49. A comparison of the two F-values leads to the significance decision (sign.) of the particular parameter or parameter combination, which is additionally given in Table III - 4.6 (s=significant; ns=not significant). The last information in Table III - 4.6 is the coefficient (coeff.), which can be used in the linear model according to the following equation (depending on the considered attribute (A), A has to be exchanged by e.g. MRT etc.:

$$A = b_0 + a_1 \cdot n + a_2 \cdot \beta + a_3 \cdot \dot{m}_F + a_{12} \cdot (n \cdot \beta) + a_{13} \cdot (n \cdot \dot{m}_F) + a_{23} \cdot (\beta \cdot \dot{m}_F) \quad (3.45)$$

With this (linear) equation, all attributes can be calculated in the investigated parameter space. Due to deviation from linearity, attention has to be paid on the calculated values. The deviation from linearity is checked with the midpoint experiment (Exp. 09). In Table III - 4.7 calculated attribute values from equation (3.45) are presented with the experimental results and the deviation. Hold-up calculations deliver satisfying congruence, while MRT- and D_{ax}-calculations have higher deviation.

Figure III - 4.5 presents the main effects calculated from the experimental design graphically. Effects are dimensionless and provide the magnitude of influence on the attribute (e.g. MRT) due to the investigated parameter. Effects for DC4 cannot be calculated because of missing data of Exp. 05.

All main effects are statistically significant for every configuration (cf. Table III - 4.6). The interaction-effects of the three investigated parameters are also statistically relevant, thus varying only one factor at a time leads to incomplete data. The whole system has to be considered at once.

Table III - 4.6: Effects, experimental F-value, significance decision and coefficients of multiple linear regression analysis for MRT, D_{ax} and hold-up

			n	β	$\dot{m}_F$	$n \cdot \beta$	$n \cdot \dot{m}_F$	$\beta \cdot \dot{m}_F$
		b_0	a_1	a_2	a_3	a_{12}	a_{13}	a_{23}
Mean residence time								
DC1	eff.		-104	-82	-9	30	-1	18
	F_{exp}		4787.43	2995.38	33.46	409.89	0.79	139.04
	sign.		s	s	s	s	ns	s
	coeff.	445.1	-21.5	-71.2	-6.0	2.8	-0.1	1.8
DC2	eff.		-108	-169	-46	59	16	27
	F_{exp}		3665.28	8921.95	664.93	1093.87	82.13	234.77
	sign.		s	s	s	s	s	s
	coeff.	808.5	-39.1	-132.3	-20.0	5.5	0.7	2.8
DC3	eff.		-397	-304	-20	125	20	29
	F_{exp}		5559.91	3275.52	14.38	548.18	13.68	30.09
	sign.		s	s	s	s	s	s
	coeff.	1582.2	-98.1	-224.9	-17.7	11.5	0.8	3.0
Axial dispersion coefficient								
DC1	eff.		7.62E-06	3.59E-06	4.10E-06	4.52E-06	1.45E-06	9.26E-07
	F_{exp}		133.86	29.75	38.82	47.00	4.88	1.97
	sign.		s	s	s	s	s	ns
	coeff.	0.0	0.0	0.0	0.0	0.0	0.0	0.0
DC2	eff.		9.91E-07	3.19E-07	3.33E-07	1.38E-06	4.15E-07	-7.02E-07
	F_{exp}		3.81	0.39	0.43	7.41	0.67	1.91
	sign.		ns	ns	ns	s	ns	ns
	coeff.	0.0	0.0	0.0	0.0	0.0	0.0	0.0
DC3	eff.		4.30E-06	2.22E-06	2.32E-06	8.01E-07	1.66E-06	3.67E-06
	F_{exp}		18.65	4.99	5.44	0.65	2.79	13.61
	sign.		s	s	s	ns	ns	s
	coeff.	0.0	0.0	0.0	0.0	0.0	0.0	0.0
Hold-up								
DC1	eff.		-98	-287	342	-263	120	34
	F_{exp}		281.64	2432.29	3449.84	2028.86	422.97	34.78
	sign.		s	s	s	s	s	s
	coeff.	379.6	-10.8	39.1	4.9	-24.3	5.1	3.5
DC2	eff.		-353	-279	337	-181	-91	-45
	F_{exp}		846.83	529.33	771.64	222.93	56.57	13.59
	sign.		s	s	s	s	s	s
	coeff.	-148.7	47.6	89.5	93.5	-16.8	-3.9	-4.6
DC3	eff.		-288	-329	344	-246	203	-148
	F_{exp}		9701.15	12614.53	13829.97	7072.66	4837.20	2556.05
	sign.		s	s	s	s	s	s
	coeff.	794.2	-87.1	252.5	31.1	-22.8	8.7	-15.2

Table III - 4.7: Exemplary calculated values for MRT, D_{ax} and Hold-up for Exp. 09 according to equation (3.45) and experimental values of Exp. 09

attribute		DC1	DC2	DC3
MRT (exp.)	s	94.3	156.8	255.3
MRT (calc.)	s	122.7	117.7	409.2
Deviation	%	30.1	24.9	60.3
D_{ax} (exp.)	m^2/s	2.05E-06	7.60E-07	2.23E-06
D_{ax} (calc.)	m^2/s	7.94E-06	2.25E-06	4.17E-06
Deviation	%	287.8	195.6	87.0
Hold-up (exp.)	g	604.0	734.6	1248.0
Hold-up (calc.)	g	599.0	793.1	1078.7
Deviation	%	0.8	8.0	13.6

Figure III - 4.5 a) presents negative effects on MRT, since increasing of the parameters leads to reduced MRTs. The feed-rate has only negligible influence on the MRT in the investigated parameter space. Effects concerning DC3 are significantly higher, which means the impact of variations in the parameter setting for this configuration is stronger and the system has a higher sensitivity. The adjustment of MRT is in practice realized most precisely with the rotational speed, since the slope is usually fixed. In Table III - 4.6, coefficients are delivered to calculate MRT dependent on the operational parameters with equation (3.45).

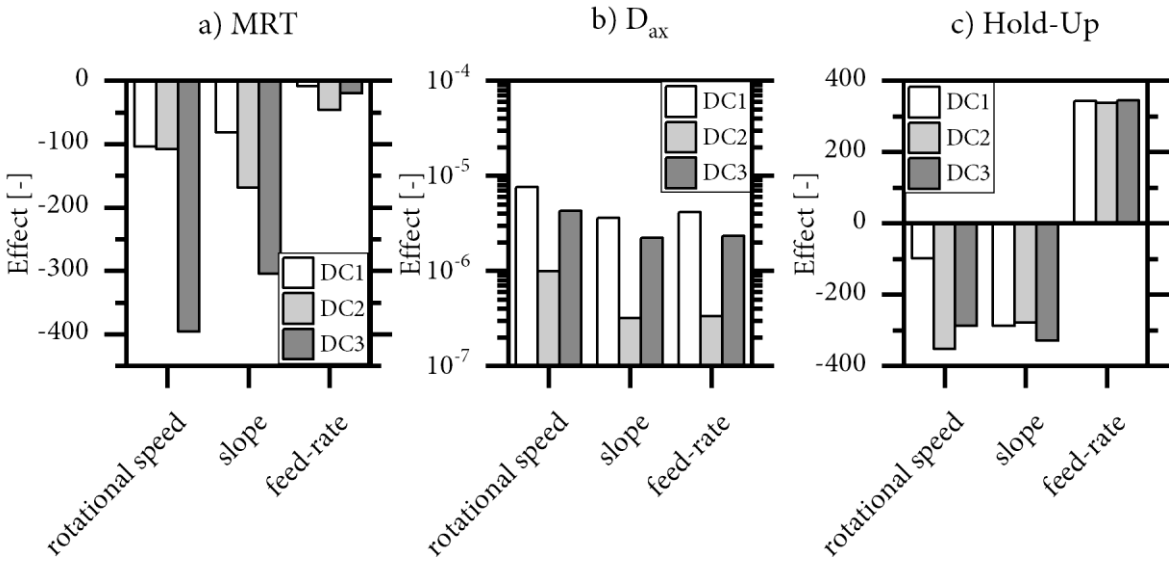

Figure III - 4.5: Effects of experimental parameters, calculated from the DOE on a) MRT, b) D_{ax} c) Hold-up calculated from DOE (adapted from [233])

Attention has to be paid on this approach, since the check with midpoint experiments delivers significant deviation from the linearity assumed in the model. This was expected due to non-linearity of literature models (e.g. equation).

Regarding the axial dispersions, Figure III - 4.5 b) reveals no significantly different dependencies of D_{ax} from the operational parameters for sectional internals (DC3). Compared to the bare drum, the exit dam has a higher impact on the effects here. Due to the forced hold-up by the dam, the influence of parameter changes is lower, since the revolutions each particle is experiencing within the drum statistically is equalized.

Considering the hold-up, the behavior is dependent on the whole set of operational variables once more, which is presented in Figure III - 4.5 c). Similar influences of slope and feed rate on the hold-up have been found for all configurations. Contradicting, the rotational speed has minor impact on hold-up for bare drums compared to DC2/DC3.

4.1.2 Axial flow configuration 2 & Sectional internals

The results which have been achieved with the axial flow configuration 2 investigating sectional internals have already been published in [234]. With AFC2 the bare drum, and sectional internals with varying section number (3, 4 & 6) and section lengths (L1/L2) have been analyzed (cf. chapter 3.3.3.2). Table III - 4.8 shows all the measured and evaluated data, the mean residence time (MRT), hold-up and axial dispersion coefficients (D_{ax}). The values for DC1 are assigned to the length L2, since L2 with 450mm is closer to the length of the drum (510mm).

4.1.2.1 Mean residence time (AFC2 & sections)

The experimental MRT-results are presented graphically in Figure III - 4.6 in order to analyze trends and dependencies visually. Since the variation of the operational parameters already covers three dimensions and additionally the drum configuration has been changed, a multi-dimensional plot is not possible.

Table III - 4.8: Results of mean residence time (MRT), hold-up and axial dispersion coefficient (D_{ax}) for all axial flow measurements with AFC2 (adapted from [234])

		MRT [s]				Hold-up [g]				D_{ax} [x10^{-6} m²/s]			
Sections		1	3	4	6	1	3	4	5	1	3	4	6
Exp.-No.		DC1	DC5	DC3	DC4	DC1	DC5	DC3	DC4	DC1	DC5	DC3	DC4
	1		503	669	1008		894.6	960.2	1038.7		0.73	0.84	0.78
	2		214	264	384		617.2	759.9	972.5		2.18	1.65	0.82
	3		202	239	337		653.2	805.2	975.0		1.55	1.10	1.13
	4		79	89	122		214.7	244.2	335.2		7.89	6.36	4.02
L1	5		490	660	991		967.7	1036.0	1098.9		0.81	1.00	0.67
	6		195	247	374		850.1	934.8	1034.9		1.59	0.98	0.35
	7		209	254	375		988.5	1169.0	1461.3		1.80	2.04	1.02
	8		78	90	123		350.7	404.8	566.6		5.14	4.64	3.60
	9		162	186	260		661.2	749.3	1056.8		2.50	1.61	1.64
	1	320	740	940	1372	679.1	920.3	986.4	1006.5	0.68	1.71	1.31	0.19
	2	146	282	368	507	420.4	811.6	910.3	986.9	3.43	0.93	0.24	1.02
	3	147	271	355	522	418.2	789.4	1024.8	1272.2	2.45	0.57	0.84	1.14
	4	58	102	129	179	155.6	277.4	365.7	488.8	13.18	2.69	1.56	1.30
L2	5	311	736	927	1312	729.5	990.8	1053.7	1071.4	0.62	3.40	2.03	0.76
	6	129	268	364	493	595.6	902.8	968.4	1041.0	4.30	0.94	0.63	0.90
	7	145	281	368	524	663.5	1165.6	1296.1	1349.7	2.54	1.26	0.95	0.94
	8	57	100	129	181	253.9	452.5	589.1	838.1	10.28	2.30	1.73	1.19
	9	107	208	262	369	424.2	884.2	1044.9	1174.6	3.72	2.05	0.72	0.94

Therefore, Figure III - 4.6 presents the results of the MRT in two stacked bar charts. The grey-shades refer to the equipment configuration or number of sections, respectively. The upper diagram exhibits the results of the shorter sectional internals (L1), the lower diagram displays the results of the longer sectional internals (L2, indicated with hatchings). From this representation, a multitude of trends can be evaluated:

- In general the MRT is dependent on the combination of operational parameters set for each experiment.
- In direct comparison to the EC1-results, MRT-values calculated by the models of Chatterjee and Saeman (cf. chapter 1) are displayed. A reasonable congruence is obvious, except some outliers. This congruence is a good validation of the measurements and the dependencies due to operational parameters and literature models. Higher deviations have been found at Exp. 01/05 with the Saeman-model and at Exp. 03/07 with the Chatterjee-model. The deviation of the Saeman-model is evoked by the occurrence of back-spillage, as explained later.

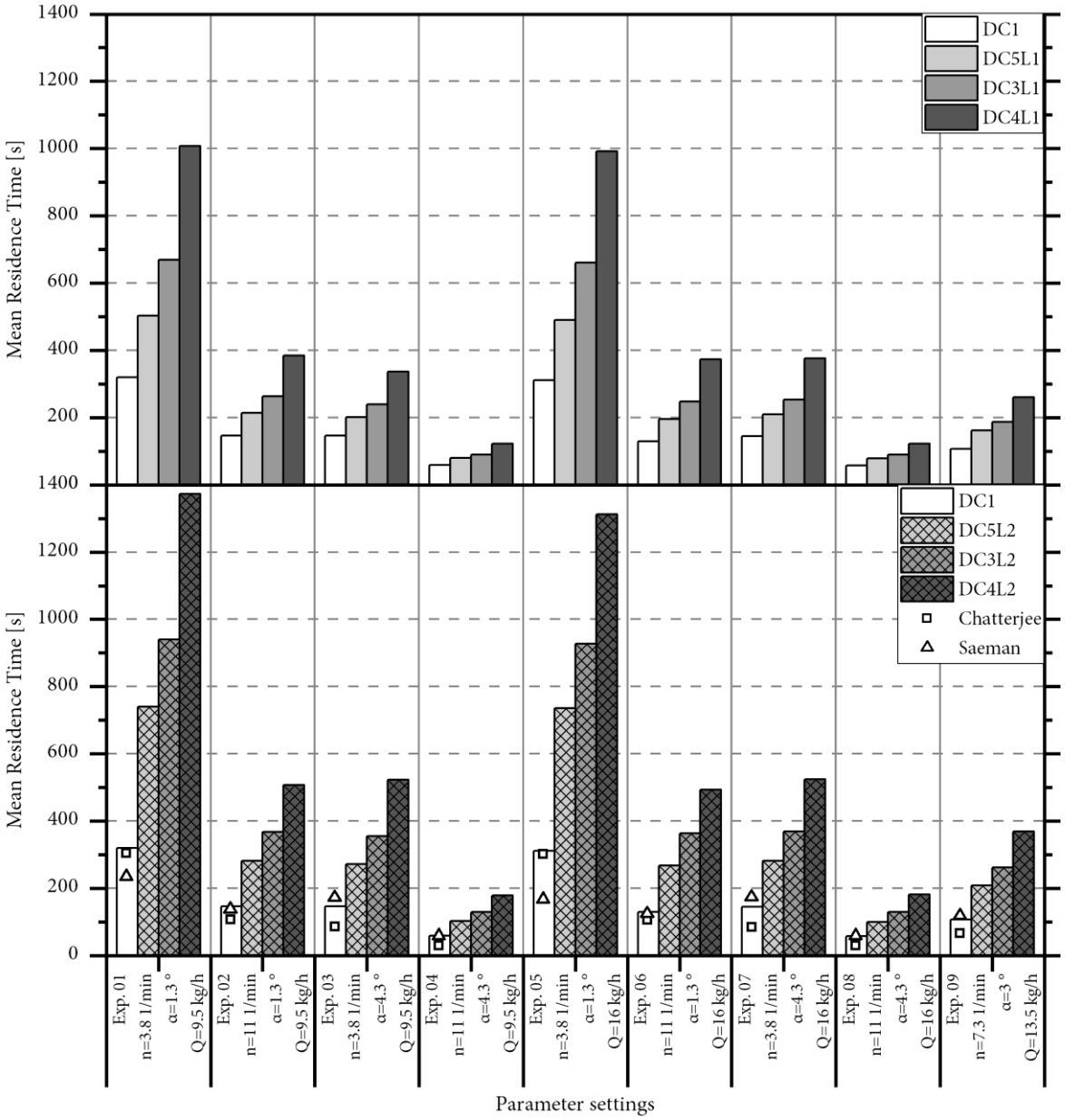

Figure III - 4.6: Diagram of MRT-values calculated from the RTD-curves (axial flow configuration 2); squares represent calculated MRT according to the model of Chaterjee et al. [158]; triangles represent calculated MRT according to the Saeman-model (chapter 2.3.2); hatchings indicate the different internal length (adapted from [234])

- An increase of the feed mass flow has only very little effect on residence time when all other parameters are kept constant (cf. Exp 01/05; Exp. 02/06 etc. for all configurations).
- The rotational speed of the drum has a very large impact on the residence time (cf. Exp. 01/02; Exp. 03/04 etc. for all configurations). A higher rotational speed leads to significant shorter MRT.
- The inclination angle of the drum also has a very large effect on the MRT (cf. Exp. 01/03; Exp. 02/04 etc. for all configurations). Significantly lower MRTs have been measured with higher inclination angles of the drum.

- The observed trends are also represented in the effect-analysis (as presented later) and explained in detail there.

The above trends concerning the three operational parameters are valid for the bare drum and all internal configurations of the drum. They are also valid for both lengths of the sectional internals. As additional novelty, trends due to the number of sections and the lengths of the sectional internals are obvious.

Since the dependencies regarding the operational parameters are similar, an analysis of increase factors is conducted. The factors between MRT of the bare drum and the MRT with different configurations (IF_{EC}) are evaluated for each experiment. Furthermore, a comparison of the longer and the shorter version is performed (IF_L). The results are presented in Table III - 4.9.

Additionally to the visual findings in Figure III - 4.6, it is clearly observable from the mean increase factors (MIF) in Table III - 4.9, that:

- The number of sections is influencing the MRT. A higher section number leads to an increase in MRT. This is valid regardless of the internal lengths.
- The length of the sectional internals additionally impacts the MRT due to longer MRT with higher lengths of the sectional internals. However, the MIF_L-results with factors of roughly 1.4 show, that doubling the lengths of sectional internals (L2=2*L1) does not lead to a doubling in MRT.

Table III - 4.9: Results of increase factor analysis (IF_{EC}) for MRT between different drum configurations and between different internal lengths (IF_L)

	IF_{EC}						IF_L		
	L1			L2					
No.	DC5	DC3	DC4	DC5	DC3	DC4	DC5	DC3	DC4
1	1.57	2.09	3.15	2.32	2.94	4.29	1.47	1.40	1.36
2	1.46	1.80	2.62	1.93	2.51	3.46	1.32	1.40	1.32
3	1.38	1.63	2.30	1.85	2.42	3.56	1.35	1.48	1.55
4	1.36	1.53	2.10	1.75	2.21	3.07	1.29	1.44	1.46
5	1.58	2.13	3.19	2.37	2.99	4.23	1.50	1.40	1.32
6	1.51	1.92	2.89	2.07	2.82	3.82	1.37	1.47	1.32
7	1.45	1.75	2.60	1.95	2.55	3.63	1.35	1.45	1.40
8	1.38	1.59	2.16	1.76	2.26	3.19	1.28	1.42	1.48
9	1.52	1.75	2.44	1.95	2.46	3.47	1.28	1.40	1.42
Mean	1.47	1.80	2.61	1.99	2.57	3.64	1.36	1.43	1.40
rel. Std.	0.06	0.12	0.16	0.11	0.11	0.12	0.06	0.02	0.06

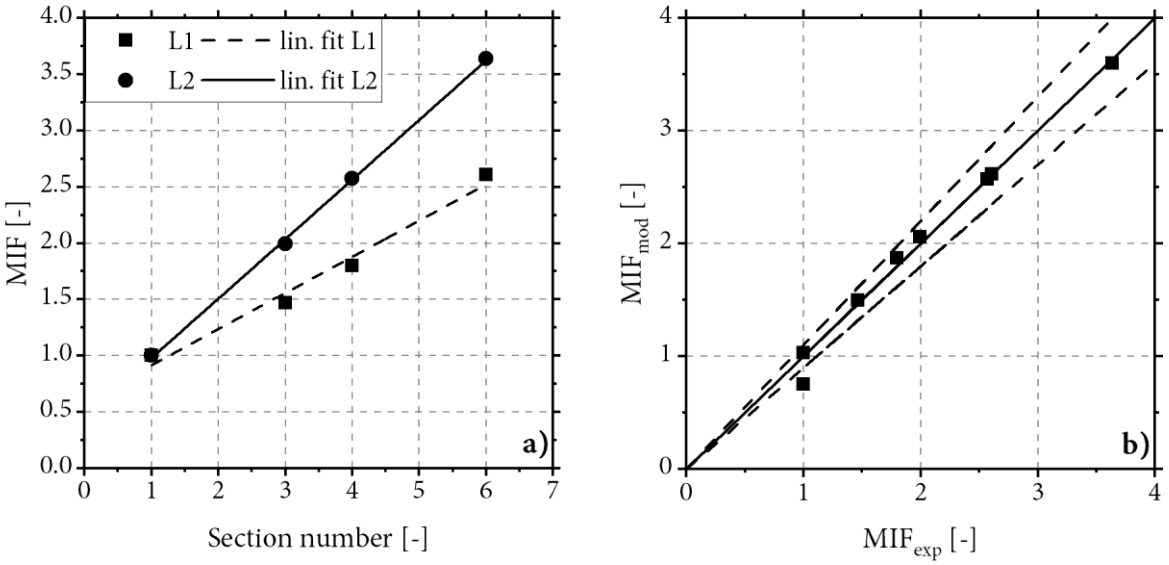

Figure III - 4.7: a) Mean increase factors and linear fits (R^2 above 0.95). Slope for L1-fit is 0.3 and for L2-fit 0.5 respectively; b) Diagram comparing the experimental MIF-values and the modeled MIF-values in the modeling of MRT impact due to sectional internals. Dashed lines indicate ± 10% deviation margins (adapted from [234]).

The mean factors are presented graphically in Figure III - 4.7 a). A factor of 1 is set for the bare drum with an assumption of 1 as section number. Both lengths give an excellent linear correlation (R^2 above 0.95), indicating a linear increase of the MIF with section number. The slope regarding long internals (L2) is 0.5 and for short internals (L1) 0.3 respectively.

The slope itself is therefore dependent on the internal length. In order to evaluate a function describing the MRT-behavior of rotary drums with sectional internals, an approach of a family of linear functions according to the following equation is chosen:

$$MIF_{mod} = a\lambda^b \cdot N + a\lambda^b = a\lambda^b \cdot (N+1) \tag{3.46}$$

The factor λ is the dimensionless fraction of drum length occupied by sectional internals (λ_1=0.45; λ_2=0.9). This factor is fitted in a polynomial approach with two fit parameters (a, b) via least squares method to the experimentally determined MIF-values. The function describing MIF finally is:

$$MIF_{mod} = 0.54\lambda^{0.46} \cdot N + 0.54\lambda^{0.46} = 0.54\lambda^{0.46} \cdot (N+1) \tag{3.47}$$

A very good congruence is achieved as presented in the diagram in Figure III - 4.7 b), comparing experimental and modeled MIF-values. There is only one outlier leaving the 10% deviation

margins, namely the modeled factor describing the pseudo bare drum at L1. Although the model equation is dimensionless, the scale up validity of the model has to be checked in further measurements with different drum dimensions.

Concluding, based on the experimental findings, a calculation approach based on an increase factor according to the bare drum-MRT is developed. For industrial practice and design calculations, the MRT for bare drums according to the operational parameters can be determined according to existing models (e.g. Saeman or Chatterjee). Afterwards, it has to be manipulated with the MIF according to the drum configuration.

4.1.2.2 Back-Spillage (AFC2 & sections)

For some experiments or parameter settings, the system shows an overrun. That means, solid material is unwantedly coming out of the drum on the inlet end, which is called back-spillage. The amount of back-spillage (mass flow $\dot{m}_B$) measured in the experiments is calculated as fraction f_{BS} of the feed mass flow rate (cf. equation (3.44)).

A comparison of the data presented in Table III - 4.10 also reveals a pattern. Similar to the residence time, back-spillage is also dependent on the operational parameters. With higher feed mass flow rates or lower inclination angles of the drum, the risk of back-spillage increases massively. If it occurs, the amount of back spillage is increasing in the same manner. These observations have also been found by Liu et al. and Chatterjee et al. for bare drums or drums with constriction dams [158,161]. Back spillage thus behaves antiproportionally to the MRT, which is plausible presupposing similar hold-ups in the drum, as will be discussed later.

Besides dependencies on the operational parameters, the mean values of f_{BS} (cf. Table III - 4.10) reveal clear trends regarding the equipment configuration. A higher number of sections or an increase of the sectional internal length reduces the capacity of the drum in terms of volume or mass flow conducted through the drum. Three experiments (Exp. 01/05/06) lead to back spillage in all equipment configurations. Therefore, these experiments are evaluated graphically in Figure III - 4.8. Linear correlations between section number and f_B are observable (all correlation coefficients above 0.95) regardless the investigated experiment or internal structure.

Table III - 4.10: Back spillage-results for all measurements as fraction of the feed mass flow rate f_{BS}

Exp.-No	DC1	L1 DC5	L1 DC3	L1 DC4	L2 DC5	L2 DC3	L2 DC4
1	0.33	0.39	0.51	0.66	0.59	0.64	0.76
2	0.00	0.00	0.00	0.15	0.03	0.16	0.34
3	0.00	0.00	0.00	0.00	0.00	0.00	0.18
4	0.00	0.00	0.00	0.00	0.00	0.00	0.00
5	0.50	0.59	0.67	0.78	0.71	0.77	0.84
6	0.00	0.08	0.21	0.43	0.32	0.39	0.56
7	0.00	0.00	0.01	0.19	0.12	0.27	0.48
8	0.00	0.00	0.00	0.00	0.00	0.00	0.00
9	0.00	0.00	0.00	0.00	0.00	0.01	0.24
Mean	0.09	0.12	0.16	0.25	0.20	0.25	0.38

The slopes are in the range of 0.07 to 0.12 for all configurations and thus comparable. With the longer versions (lengths nearly congruent to drum length) even the bare drum (1 section) fits into the linear correlation as presented in the linear fits in Figure III - 4.8. The absolute amount of back-spillage is affected by the experiment-number and thus the set of operational parameters. Furthermore, the length of the sections impacts on the absolute amount of back-spillage, but the impact is not constant considering the different operational states. Additionally, f_{BS} evoked by different internal lengths at constant operational states converges with section number.

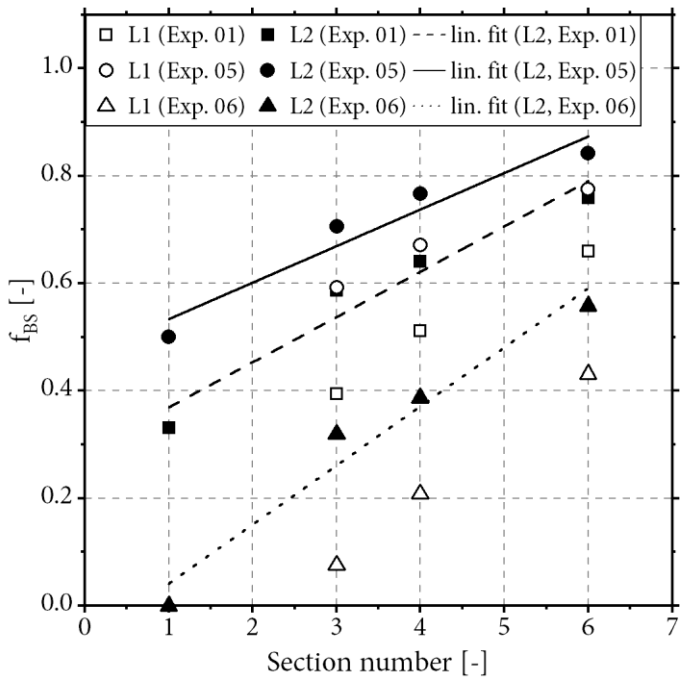

Figure III - 4.8: Evaluation of back spillage fraction in dependency of the section number for experiments 01, 02 and 06. The linear fits deliver correlation coefficients (R^2) above 0.95 and slopes in the range of 0.07 to 0.12 (adapted from [234])

As first "rule of thumb" for the design of rotary drums with sectional internals in practice, it can be deduced from these findings, that each additional section reduces the capacity of the drum by approximately 12%. This is a conservative estimation, since the impact is lower with shorter length of sectional internals.

To complete the relationship between feed mass flow and residence time, the experimental data of hold-up is taken into account and the hydrodynamic residence times are calculated via an adjustment of equation (3.43):

$$\tau_{hyd} = \frac{m_{HU}}{\dot{m}_F \cdot (1 - f_{BS})} \tag{3.48}$$

The results are presented in Table III - 4.11 together with the relative deviation of the hydrodynamic residence time from the experimentally determined MRT.

The mean values of relative deviation are all equal or below 10%, which is a good congruence taking into account, that the experimental results used in the calculations always include an error. The overall mean deviation is calculated to 8.4%.

This finding is a further indication of capacity limits, since it proves that the changes in MRT are evoked by lowering the effective mass flow passing the drum as represented by equation (3.48).

Table III - 4.11: Calculated hydrodynamic residence times [s] with relative deviation from the measured MRT (adapted from [234])

	τ_{hyd} [s]							rel. deviation [%]						
		L1			L2				L1			L2		
Exp.	DC1	DC5	DC3	DC4	DC5	DC3	DC4	DC1	DC5	DC3	DC4	DC5	DC3	DC4
1	385	559	746	1156	845	1041	1581	20.4	11.3	11.5	14.7	14.2	10.8	15.2
2	159	234	288	433	316	409	567	8.8	9.1	9.3	12.9	12.0	11.1	11.9
3	158	248	305	369	300	388	585	8.2	22.8	27.8	9.6	10.5	9.5	12.1
4	59	81	93	127	105	139	185	1.1	2.5	3.4	3.9	2.9	7.4	3.5
5	329	534	710	1102	757	1014	1521	5.8	9.0	7.6	11.1	2.9	9.3	15.9
6	134	207	266	409	298	355	530	3.9	6.1	7.3	9.6	11.5	-2.3	7.5
7	149	222	267	407	297	397	581	3.3	6.5	5.1	8.5	5.5	7.7	10.9
8	57	79	91	127	102	133	189	0.6	0.8	0.9	4.1	1.9	3.1	4.0
9	113	176	200	282	236	281	410	6.5	8.6	7.1	8.2	13.3	7.5	11.0
							Mean	6.5	8.5	8.9	9.2	8.3	7.1	10.2

4.1.2.3 Hold-up (AFC2 & sections)

As described in the experimental procedure (chapter 3.3.3.2) the retained mass is measured after each experimental run as hold-up. The results are presented graphically in Figure III - 4.9.

In analogy to the MRT, the characteristic trends can be found here, too. Sectional internals lead to an increase in hold-up, which is plausible due to the higher residence times and the relationship of hydrodynamic MRT (equation (3.48)).

However, in contrast to the MRT values, the pattern of the hold-up masses is not as clear. The reason for this is the back spillage, as explained earlier.

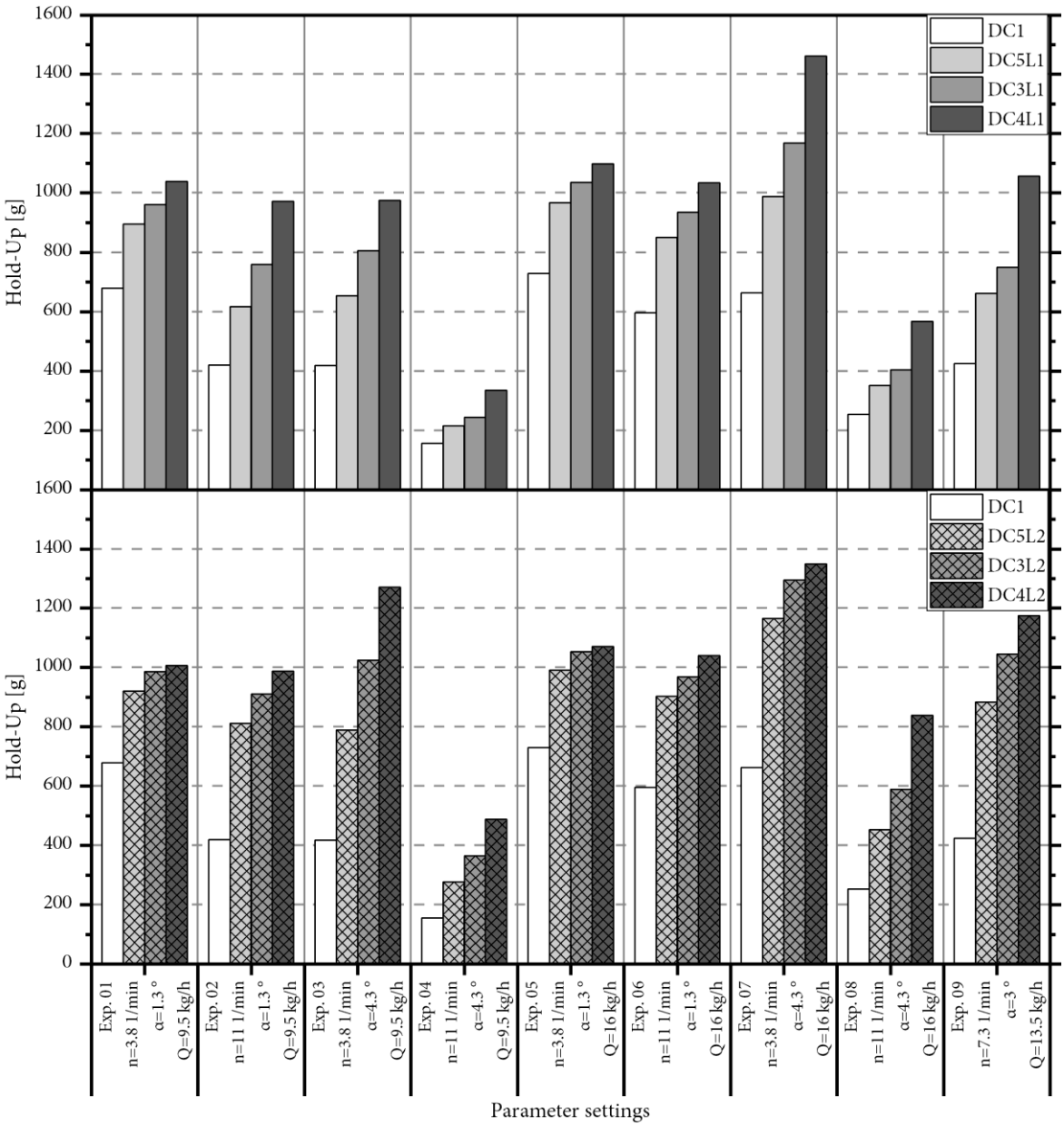

Figure III - 4.9: Comparative diagram of Hold-up values for each experiment and drum configuration (sectional internals analyzed with AFC2); column hatchings indicate different internal length (adapted from [234])

For most configurations, the capacity limit concerning solid hold-up seems to be reached. A higher mass flow / volume flow cannot be transported through the drum. Especially for the experiments with low rotational frequency and low inclination angle (cf. Exp. 01/05 for all configurations) the hold-up is almost independent from the feed mass flow rate and also from the number of sections. Even an increase of the internal length does not lead to higher hold-ups here. The capacity limits seem to be reached already. In contrast to this finding, however, the MRT is increasing further. This can be explained by the increase in back-spillage, reducing the effective mass flow passing the drum. This is what causes a higher MRT for a similar hold-up in the drum.

Therefore, it can be concluded that rotary drums with sectional internals have a specific capacity limit concerning the retained volume or hold-up mass. Overfilling beyond this limit is not possible, a further increase of the feed volume flow simply results in an increase in back spillage flow.

4.1.2.4 Axial dispersion, D_{ax} (AFC2 & sections)

In analogy to the evaluation of axial flow configuration 1 measurements (chapter 4.1.1.3), the explained method is used to provide information on the residence time distribution and therefore on the axial mixing in the drum. The values (cf. Table III - 4.8) are presented in Figure III - 4.10.

First of all, Figure III - 4.10 shows that all axial dispersion coefficients are in the range of 10^{-4} to 10^{-7} m^2/s (range of the diagrams). This is exactly the range of measured values for bare drums delivered in the literature by Sherritt et al. [174] and also found in earlier measurements [174,233]. Except a few outliers the values are very narrow to $1x10^{-6}$ m^2/s.

The data indicates that axial mixing is reduced by sectional internals with increasing section number, particularly for the short internal configurations. The reason for this is an estimated change in mixing mechanism as described for the cross section in [235]. Mixing in the bare drum takes place in the active layer, which is not that distinct when sectional internals are used. The active layer is dependent on the operational parameters, particularly the rotational speed, evoking the different values of D_{ax} for different operational states. Focusing on the lower diagram with the longer internal configuration the dispersion coefficients are nearly constant to a value of 10^{-6} m^2/s regardless the operational parameters. This supports the approach of changed solid movement.

Comparing the changes caused by the sectional internals with the variation due to parameter settings, their impact is comparable. Since changes of operational parameters are usual in industrial practice, the influence of sectional internals on the axial mixing is considered as negligible.

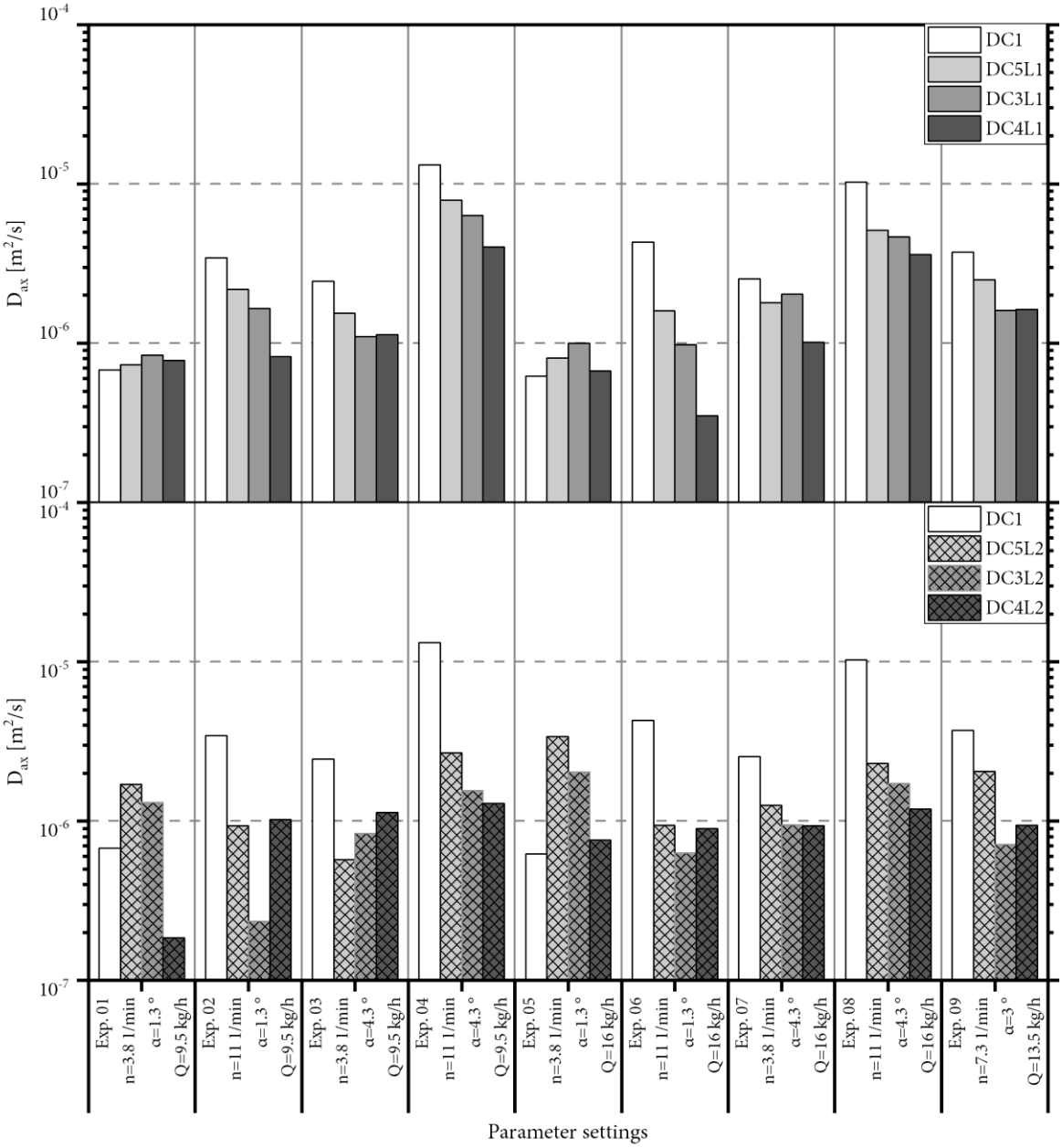

Figure III - 4.10: Calculated axial dispersion coefficients (D_{ax}) for all investigations with sectional internals and AFC2, column hatchings indicate different internal length (adapted from [234])

4.1.2.5 DOE analysis (AFC2 & sections)

In analogy to the evaluation presented in chapter 4.1.1.4, the statistical design of the experimental runs enables the analysis of the effects or sensitivities on the measured values created by the parameter changes. Effects or sensitivities are the mean differences in a measured quantity introduced by the investigated parameter changes. The results are shown in Figure III - 4.11.

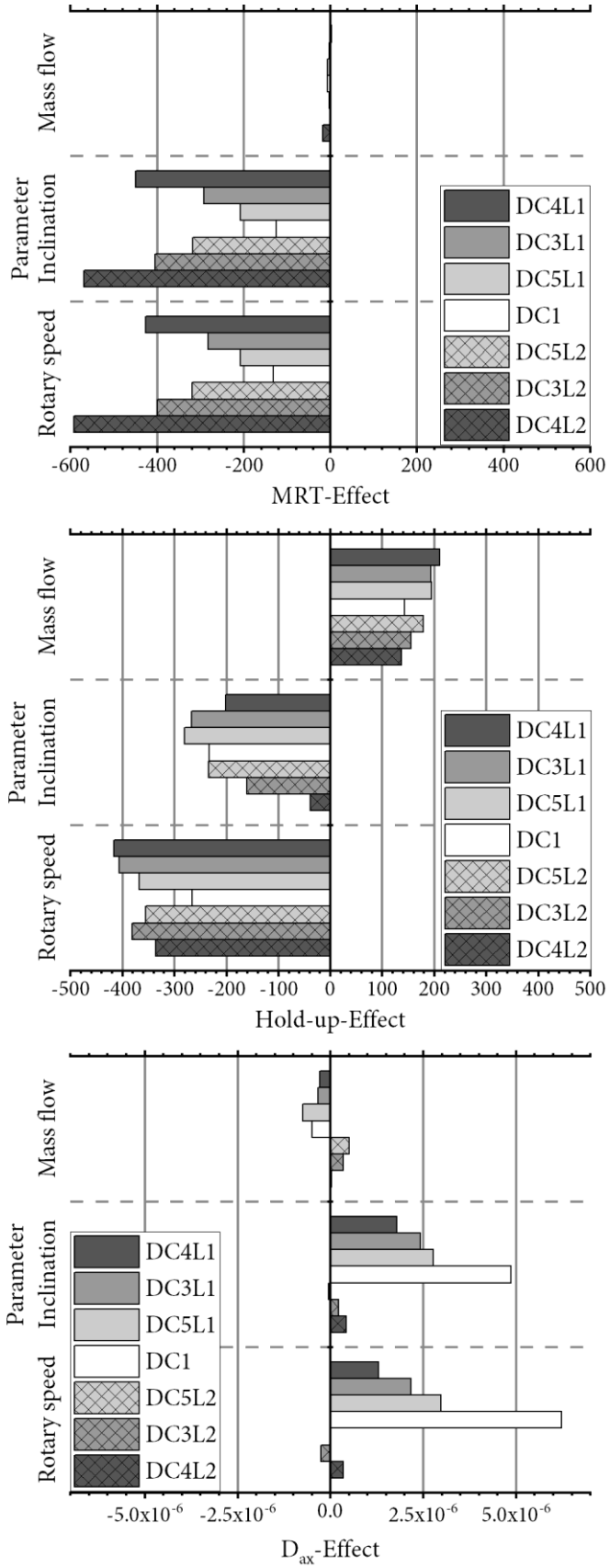

Figure III - 4.11: Effects of experimental parameters, calculated from the DOE on MRT, D_{ax} and Hold-up from AFC2 measurements with sectional internals (adapted from [234])

All diagrams are structured similarly and the bare drum (DC1) is the central value because of its benchmark character. The effects on MRT (Figure III - 4.11, top) prove the finding, that mass flow is not affecting the MRT at all. This is valid for all drum configurations in the investigated parameter space. Further effects of the other operational parameters are negative. This is plausible because increasing the inclination or rotational speed of the drum leads to lower MRT. The effects evoked by drum inclination compared to rotational speed of the drum are nearly equal considering each configuration. Comparing the different equipment configurations, the increasing number of sections leads to higher impact of parameter changes. That means higher sensitivities of the system. The trends are equal regardless to the length of the internals. However, the absolute effects are significantly higher with the longer internal version. Thus the system sensitivity is dependent on the internal lengths. Sectional internals are therefore ideal in applications where e.g. the residence time has to be adjusted very precisely (e.g. production of catalysts [220] etc.).

Considering the effects on the drums hold-up now (Figure III - 4.11, middle), impact of the mass flow on the hold-up is observable in contrast to MRT. A higher feed mass flow leads to higher hold-ups in the drum. Keeping in mind that there is no impact on MRT automatically evokes the need for higher back-spillage reducing the effective mass or volume flow passing the drum. Sectional internals slightly emphasize the impact of mass flow changes, but there is no clear trend regarding section number. Changes in drum inclination affect the hold-up in the drum, but sectional internals (short version) have no significant additional impact compared to the bare drum. The sensitivity is comparable to the bare drum in its magnitude. The evaluation of long sectional internals produced lower impact with increasing section number. With high section numbers (DC4L2) the influence of inclination on hold-up becomes more and more negligible. Keeping the back-spillage results in mind, this is also an indicator for capacity limits. The highest impact on hold-up is generated by the drums rotary speed in the investigated parameter space. Comparing the different equipment configurations, a different pattern to MRT-effects is observable. The rotary speed effects with sectional internals are higher in comparison to the bare drum, but in contrast to MRT-effects the section number has no further significant impact. Furthermore, the length is not additionally influencing the effect. Again, the explanation to this finding is back spillage.

The last diagram in Figure III - 4.11 (bottom) shows the effects on the axial dispersion coefficient or axial mixing. Again, the mass flow is not strongly influencing the axial mixing. The impact of parameter changes in inclination and rotational speed on axial mixing is comparable. Additional sections decrease the sensitivity in the shorter version, while the effects for the long internal version

are much smaller (one magnitude). This finding fits to the evaluations regarding axial dispersion coefficients, where nearly constant dispersion coefficients have been found and is undermined by the switch in particle movement, no longer comparable to bare drums as found in [235]. Thus, with sectional internals the axial mixing becomes more and more independent from operational parameters with increasing section number or length of internals. Because the magnitude of dispersion coefficients is rather constant, this also supports the conclusion in the evaluation of axial dispersion coefficients, that axial mixing in general is not affected significantly by sectional internals. Since rotary drums have low axial dispersion and are satisfactorily estimated as plug-flow reactor, sectional internals emphasize this characteristic behavior. No further attention has to be paid on axial mixing or broad RTDs with sectional internals.

Further analysis of the DOE is not feasible because the check of midpoint experiments shows that the deviation of linear models is very high. This is plausible considering the models of Chatterjee or Saeman with nonlinear dependencies concerning inclination or rotational speed of the drum.

4.1.2.6 Qualitative observations (AFC2 & sections)

The full optical accessibility of the drum reveals additional phenomena of the solid bed which are analyzed and described qualitatively.

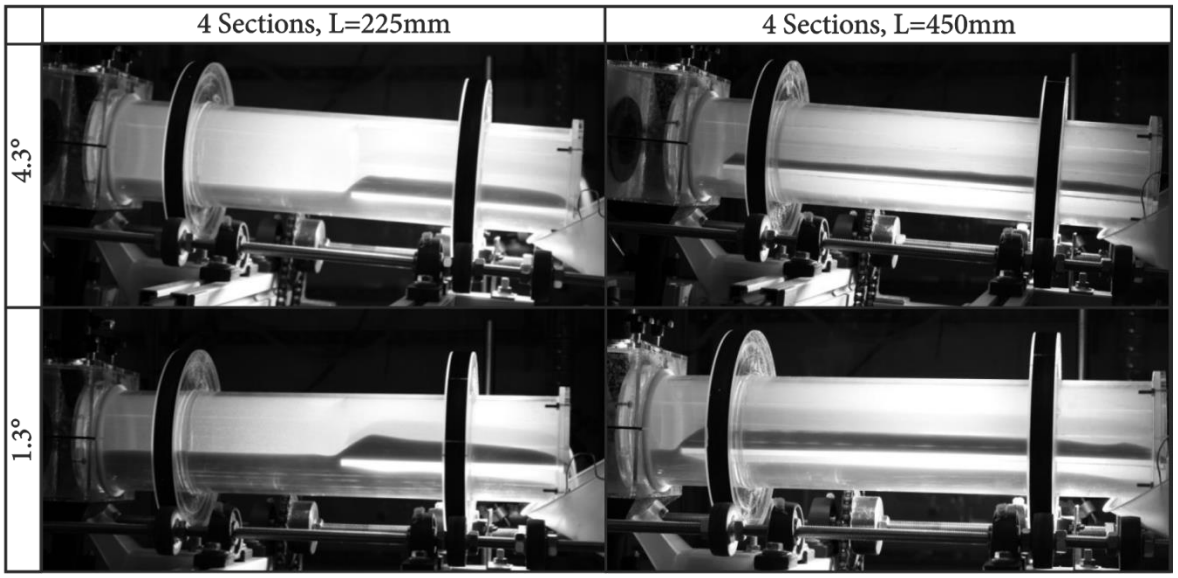

Figure III - 4.12: Exemplary shadowgraph pictures of the side view for the configuration DC3L1 and DC3L2 with: 11 rpm; 9.5 kg/h; top: inclination 4.3°; bottom: inclination 1.3° (adapted from [234])

An observation of the drum with a horizontal side view along the drum's axis directly leads to the axial shape of the solid bed. In Figure III - 4.12 four different states are exemplarily presented.

The pictures in Figure III - 4.12 have been taken as shadowgraph pictures with a LED illumination from behind the drum to enhance the visibility of the solid bed. The two vertical dark bars in each picture are evoked by the treads of the drum's tires. The horizontal dark areas show the shadows of the solid bed in the drum. The bright line below the solid bed in the right part of the drum (outlet end) is the radial front face of one section spoke (PMMA) enlightened by the backlight illumination. Both pairs of pictures are made with the same drum configuration (DC3, 4 sections) and each vertical pair has the same length. The experimental conditions (feed rate and rotational speed) are equal, only the drum's inclination is distinct. The cross sectional position of the spoke towards the viewer is nearly horizontal in all pictures.

As can be seen clearly from the measured data (see chapters 4.1.2.1 & 4.1.2.3), the inclination has a massive impact on hold-up and residence time. This can also be observed qualitatively in the heights of the solid beds. The solid bed height in the lower picture with a lower inclination is significantly higher, especially at the beginning of the sectional internal part (transition region between bare drum and sectional internals. The bed height in the bare drum part is additionally clearly higher in the lower picture.

Furthermore, looking from the outlet end of the drum, the characteristic solid bed profile predicted by the Saeman-model for the bare drum can be recognized, although the model originally was developed for bare drums. An exception to this finding is the transition region from sections to bare drum. Due to the filling of the segments, a negative slope of the solid bed height is created, since a part of the solid material is flowing backwards, when the section is lifting above the solid bed of the bare drum.

In the bare drum part (inlet end) the solid bed height is nearly constant. This is plausible because the sectional internals increase hold-up and residence time (see experimental data) and therefore the solid bed is retained backwards to the inlet end. This behavior for retained solid beds in rotary drums is also known from investigations in rotary drums with constriction dams by Kramers et al. and Scott et al. [162,171].

This qualitative observation leads to the conclusion that a mathematical modeling of the solid transport in rotary drums with sectional internals with a modified Saeman-model should be feasible, as will be explained in chapter 4.3.2.

4.1.3 Axial flow configuration 2 & Lifters

The results regarding axial flow with different lifter setups have been published in [237] and have been achieved with the AFC2 measurement setup. Besides the two lifter configurations introduced in chapter 3.3.3.2, a further run with the bare drum configuration (DC1) has been performed. All results are presented in Table III - 4.12.

The DOE has been extended compared to the measurements presented until here for lower feed mass flow rates in order to reduce back spillage. The midpoint experiment (Exp.-No. 9) was executed for three times to gain statistical data.

4.1.3.1 Mean residence time (AFC2 & lifters)

The experimental results of the mean residence time (MRT) are displayed graphically in Figure III - 4.13, in order to visualize trends and dependencies. Corresponding to the previous chapters, a bar chart is chosen, since a multi-dimensional plot is not possible.

Table III - 4.12: Results of mean residence time (MRT), hold-up and axial dispersion coefficient (D_{ax}) as well as back-spillage-ratio f_B for all measurements

Exp.-No.	n [min^{-1}]	β [°]	$\dot{m}_F$ [kgh^{-1}]	MRT [s]			Hold-up [g]			D_{ax} [$x10^{-6}$ m^2s^{-1}]			f_{BS} [-]		
				NL	SL	LL	NL	SL	LL	NL	SL	LL	NL	SL	LL
1	3.8	1.3	9.5	298	371	482	674.5	592.6	802.4	0.74	0.22	0.24	0.33	0.48	0.42
2	11.0	1.3	9.5	130	132	251	362.4	419.7	677.6	2.69	6.07	0.81	0.00	0.00	0.01
3	3.8	4.3	9.5	144	127	209	381.8	380.9	589.4	1.86	6.92	1.55	0.00	0.01	0.00
4	11.0	4.3	9.5	52	47	110	136.6	147.2	281.5	27.29	53.97	6.18	0.00	0.02	0.00
5	3.8	1.3	16.0	292	346	474	761.8	608.7	873.8	0.59	0.64	0.34	0.50	0.65	0.60
6	11.0	1.3	16.0	118	127	215	549.8	566.8	809.9	2.47	3.65	0.87	0.00	0.12	0.16
7	3.8	4.3	16.0	146	150	185	672.3	746.7	849.1	1.91	3.70	1.65	0.00	0.14	0.06
8	11.0	4.3	16.0	51	44	101	241.7	254.4	457.4	18.41	36.93	6.20	0.00	0.02	0.01
9a	7.3	3.0	13.5	110	89	160	427.5	313.9	629.1	2.83	8.41	2.47	0.00	0.04	0.01
10	3.8	1.3	3.5	334	367	613	356.3	414.7	625.6	0.27	1.18	0.38	0.00	0.00	0.02
11	11.0	1.3	3.5	136	148	347	151.0	161.5	362	6.45	6.71	1.45	0.00	0.04	0.03
12	3.8	4.3	3.5	144	129	246	152.9	122.8	239.9	3.77	7.18	2.17	0.00	0.00	0.00
13	11.0	4.3	3.5	48	55	110	96.0	75.1	104.9	53.96	50.26	8.76	0.00	0.05	0.01
		DOE-Mean		154	164	270	381.9	369.6	561.7	9.48	14.30	2.54	0.06	0.12	0.10
9b	7.3	3.0	13.5	103	92	167	391.1	306.4	306.4	3.76	1.76	1.55	0.00	0.12	0.00
9c	7.3	3.0	13.5	88	89	165	330.3	328.8	328.8	5.97	8.03	1.63	0.00	0.11	0.01
			Mean	100	90	164	383.0	316.4	421.4	4.19	6.06	1.88	0.00	0.09	0.01
			STD	9	1	3	40.1	9.3	147.1	1.32	3.05	0.41	0.00	0.04	0.00
			rel. STD [%]	9.4	1.5	1.7	10.5	2.9	34.9	31.5	50.3	22.0	10.0	40.7	24.4

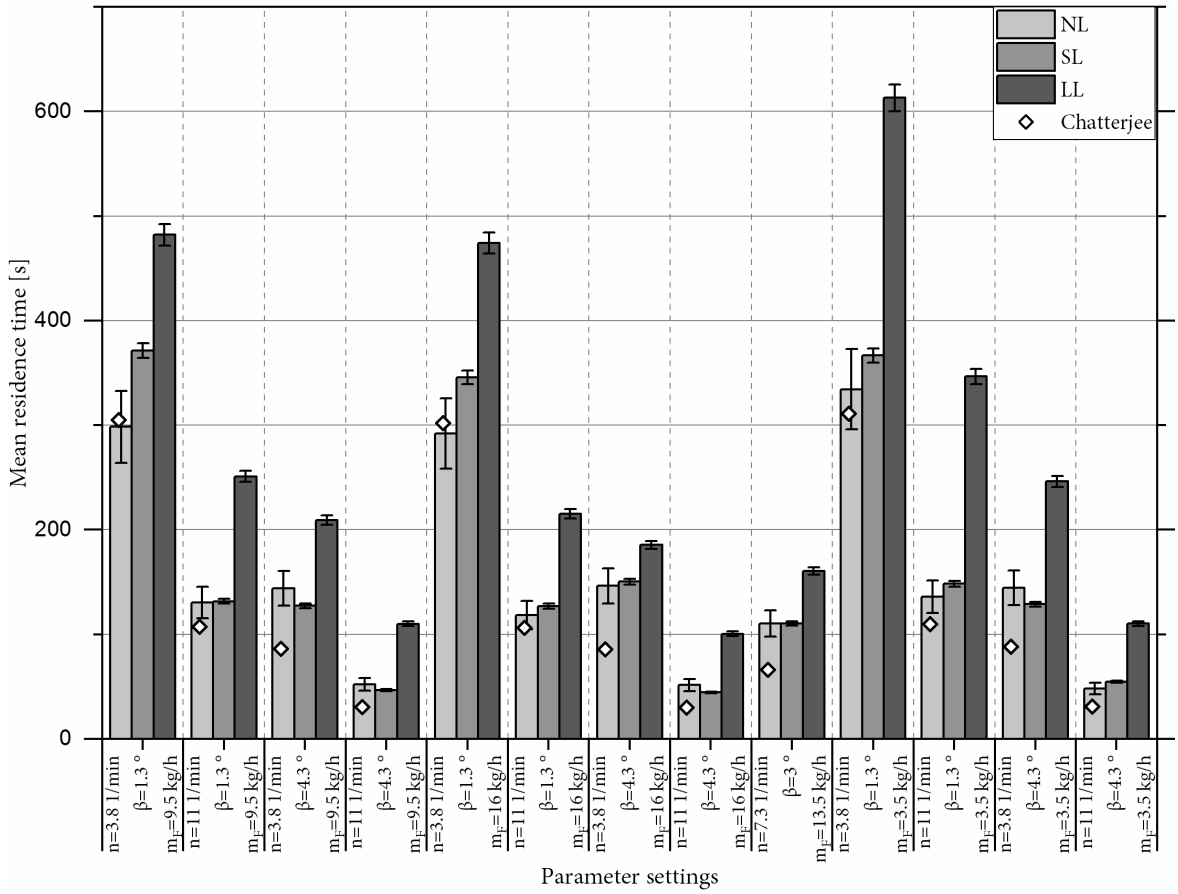

Figure III - 4.13: Comparative diagram of the MRT-results for all experiments with the investigated lifter configurations utilizing AFC2 (adapted from [237])

The error bars (rel. STDs in Table III - 4.12 below 10%) in Figure III - 4.13 show a good accuracy of the measured data. From this diagram a multitude of trends can be evaluated:

- Generally, the MRT is dependent on the combination of operational parameters applied in each experiment.
- An increase of the feed mass flow has only very little effect on residence time when all other parameters are kept constant (cf. Exp 01/05/10; Exp 02/06/11 etc.).
- The rotational speed of the drum has a very large impact on the residence time (cf. Exp. 01/02; Exp 03/04 etc.). A higher rotational speed leads to significantly shorter MRT.
- The inclination angle of the drum also has a very large effect on the MRT (cf. Exp. 01/03; Exp 02/04 etc.). Lower MRTs have been measured with higher inclination angles of the drum.
- The stated general trends regarding the three operational parameters are similar for all investigated internal configurations of the drum.
- The MRT in both lifter configurations is higher compared to the drum in general (except some outliers regarding SL-configuration). This can also be taken from the mean results in Table III - 4.12, with the order of LL = 270s > SL = 164s > NL = 154s for the DOE-mean.

- However, the increase in MRT for the SL-configuration is significantly lower than the increase evoked by LL-configuration, although the theoretical hold-ups provided by lifters in both configurations are the same. This is the clear evidence, that the axial configuration or segment length has to be considered next to the cross sectional investigation itself.

Analogously to the previous chapters, a first check of the results regarding plausibility is done by comparison of the NL-configuration with calculated MRT-data regarding the model of Chatterjee [158] for bare drums in Figure III - 4.13. The data reveals slightly lower calculated MRT-values in the regime of low residence times for the Chatterjee model. However, at higher residence times the modeled MRT fits very well. A further check of plausibility is generated by testing the measured MRT against the hydrodynamic residence time τ_{hyd}, which is calculated including the back-spillage fraction f_{BS} (see next chapter) according to equation (3.48). The results are presented in Figure III - 4.14 a, indicating a slightly systematic deviation to higher hydrodynamic residence times compared with MRT calculated from the RTD-curves. However, values are all in the range of ±20% error.

The increased MRT for the LL-configuration is furthermore checked against the correlation of Hatzilyberis et al. [189], who provided a correlation of MRT-increase based on bare drum results for continuous rectangular lifters:

$$\bar{t}_{LL} = \left(a \cdot n^{b}\right) \cdot \bar{t}_{NL} \tag{3.49}$$

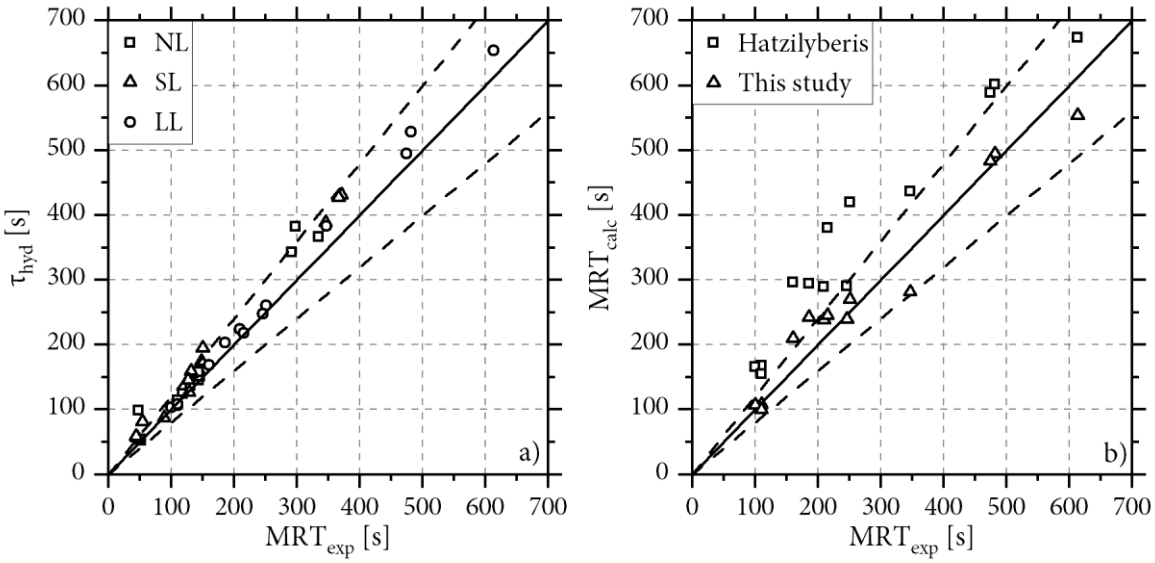

Figure III - 4.14: a) Comparative diagram of the MRT from evaluation of RTD-curve and the hydrodynamic MRT calculated from feed rate, back spillage and hold-up measurements; b) Comparison of experimental MRT-data with calculation approach from Hatzilyberis with different sets of coefficients (legend). Dotted lines indicate ± 20% deviation margins (adapted from [237])

Table III - 4.13: Coefficients from eqaution (3.49)

Coefficient	Hatzilyberis	Our work (LL)
a	1.12	1.25
b	0.44	0.21

The coefficients a and b in equation (3.49) are presented in Table III - 4.13.

A reasonable correlation is observable in Figure III - 4.14 b. This is a surprising finding, since the geometries of the drum and lifters used by Hatzilyberis et al. have been distinct to the investigated LL geometry. Thus, the correlation seems to be somewhat robust.

However, there is a systematic deviation to higher calculated residence times as depicted in Figure III - 4.14 b. Therefore, a new fit to the MRT-data regarding the coefficients was performed via least squares method. The coefficients are given in Table III - 4.13 and results are presented graphically in Figure III - 4.14 b as well. They show a good congruence to the experimental data. A calculation of MRT in rotary drums with continuous lifters based on bare drum correlations is therefore possible. MRT for short lifters have to be estimated in the range of bare drum-values and values for continuous lifters.

4.1.3.2 Back-Spillage (AFC2 & lifters)

Corresponding to the already stated results for some experiments or parameter settings, the system is overrun, and back-spillage occured. The amount of back-spillage measured in the experiments is presented as fraction of the feed mass flow rate (equation (3.44))

The results are presented in Table III - 4.12. A comparison of the data also reveals a pattern here. Like for the residence time, back-spillage is also dependent on the operational parameters. With higher feed mass flow rates or lower inclination angles of the drum, the risk of back-spillage increases. If it occurs, the amount of back spillage is increasing in the same manner. Back spillage thus behaves antiproportionally to the MRT, which is plausible under assumption of similar hold-up volumes in the drum, as will be discussed later. These observations have also been found by others for bare drums or drums with constriction dams [158,161].

Although the trends regarding operational parameters are comparable, the three investigated configurations differ systematically regarding back spillage. From the DOE-means in Table III - 4.12 the following ranking is derived: NL = 0.06 < LL = 0.10 < SL = 0.12. It is obvious, that this order is not antiproportional to the MRT-order. Additionally has to be stated, that the NL- and SL-configuration deliver comparable hold-ups (Table III - 4.12). Summarizing these facts, the higher

back-spillage of SL- compared with NL-configuration is remarkable. The increase in back-spillage for the LL-configuration is plausible because of the higher drum filling. However, with SL-configuration the filling roughly stays constant, but back-spillage is significantly higher. This finding can only be explained by a different flow pattern. A superimposed "pseudo back flow" is proposed, considering the lifter creating a plough-like behavior when passing the solid bed. The bulk material is forced to flow symmetrically to the front and to the back. Additionally, solids are falling out of the lifter nearly symmetrically to the back- and to the frontend, when it rises above the solid bed.

4.1.3.3 Axial dispersion, D_{ax} (AFC2 & lifters)

The axial dispersion coefficients (D_{ax}) were evaluated from the measured data via the variance of the Gaussian distribution as explained earlier. The values from Table III - 4.12 are presented graphically in Figure III - 4.15.

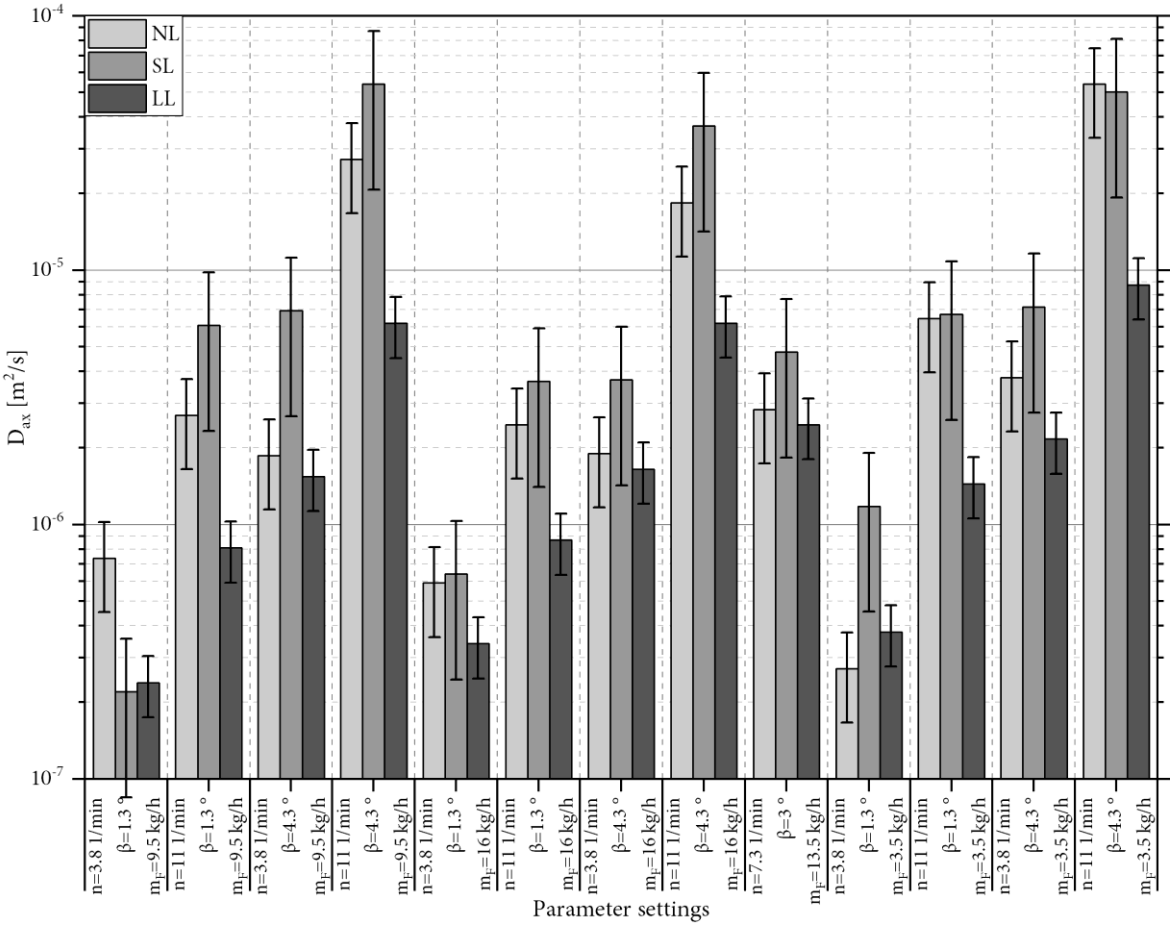

Figure III - 4.15: Diagram of all evaluated axial dispersion coefficients (D_{ax}) for the investigated lifter configurations with AFC2 (adapted from [237])

First of all, the axial dispersion coefficients are in the range of 10^{-4} to 10^{-7} m²/s (range of the diagram), as already found for the other investigations already presented. This is in the range of measured values for bare drums in the literature [174,199] and has also been found in earlier measurements. Bongo Njeng et al. found the same range of values for a flighted rotary drum with straight or rectangular lifters [199].

The error bars derived from the rel. STD of Exp. 09 indicate a higher range of errors compared to e.g. MRT. The reason for this is the need of two measured values (both with errors) in the calculation of D_{ax}. Nevertheless, important dependencies can be deduced from the data:

- D_{ax} is increasing with increasing rotational frequency (cf. Exp. 01/02; 03/04 etc.). This finding is plausible since the rising Froude-number leads to an increase in the active layer and therefore in mixing of the solids.
- With increasing inclination angle, D_{ax} is also rising (cf. Exp. 01/03; 02/04 etc.). Again this is plausible, since the higher inclination leads to higher axial movement in the active layer and therefore to higher statistical displacement and mixing.
- No significant influence of D_{ax} regarding the chosen feed rate $\dot{m}_F$ is observable.
- The trends are similar for all investigated configurations, although they deliver distinct values for D_{ax} at every parameter configuration. The order regarding internal configurations is (LL=2.54 < NL=9.48 < SL=14.30 each value x 10^{-6} m^2s^{-1}), which can be taken from the DOE-mean in Table III - 4.12.
- The LL-configuration delivers the lowest axial dispersion coefficients in all experiments. Axial mixing is therefore lower than in the bare drum and the residence time distribution is narrower. An estimated reason for this is the disturbance of the active layer on top of the solid bed by the lifter internals, since mixing takes place mostly in the active layer.
- Contrary to e.g. the MRT-results, the SL-configuration provides the highest axial dispersion coefficients (except two outliers, Exp. 01/13). This can be explained with material falling out of the lifters forwards or backwards in axial direction during the lifting process. This promotes the axial mixing by forced displacement that does not occur in the bare drum or with long lifters.

The trends regarding the internal structure are measurable and plausible. The higher axial dispersion with short lifters additionally proves the different flow patterns observed by MRT- and back-spillage investigations. It is a further evidence for the proposed “pseudo back-flow”.

Based on elaborations of Sai et al. and Sheritt et al. [174,238] a criteria equation to estimate D_{ax} in rotary drums with lifters was proposed by Bongo Njeng et al. [199]:

$$D_{ax} = 1.20 \cdot 10^7 \left(\frac{\dot{m}_F}{\rho_b}\right)^{-0.87} \cdot (n \cdot \beta)^{1.67} \cdot (\theta \cdot d_P)^{0.43} \cdot L_s^{0.21} \cdot D_i \quad (3.50)$$

The parameter L_s in equation (3.50) is interpreted has the area occupied by solids in the lifters and given with [199]:

$$L_s = \frac{N_L - 1}{2} \cdot A_{hor} \quad (3.51)$$

A_{hor} means the occupied area in the horizontal lifter (9 o'clock-position). Since that value is difficult to measure in practice, in our case a fully filled lifter is assumed here and with all other given quantities, the axial dispersion coefficients have been calculated according to equation (3.50). The results are plotted compared to the experimentally determined values in Figure III - 4.16 a.
Considering the experimental error, a good congruence has been achieved for LL-configuration, which has also been the basis for Bongo Njeng et al., although a slight systematical deviation to higher modeled values is observable. The systematical deviation of short lifters (Figure III - 4.16 a, SL) is also clearly observable. Therefore, the model equation was modified regarding the lifter coefficient L_S and the ratio of drum length L and lifter length L_L is introduced:

$$D_{ax} = 1.20 \cdot 10^7 \left(\frac{\dot{m}_F}{\rho_b}\right)^{-0.87} \cdot (n \cdot \beta)^{1.67} \cdot (\theta \cdot d_P)^{0.43} \cdot (L_s \cdot \frac{L}{L_L})^{0.21} \cdot D_i \quad (3.52)$$

Results of the calculations of equation (3.52) are compared with the experimental values for the SL-configuration and presented in Figure III - 4.16 b. A very good congruence has been achieved, proving that the axial length of lifters is influencing the solid flow and axial mixing.
However, comparing the changes caused by the internal structure with the variation due to parameter settings (rotational frequency and inclination), the latter impact is comparable.

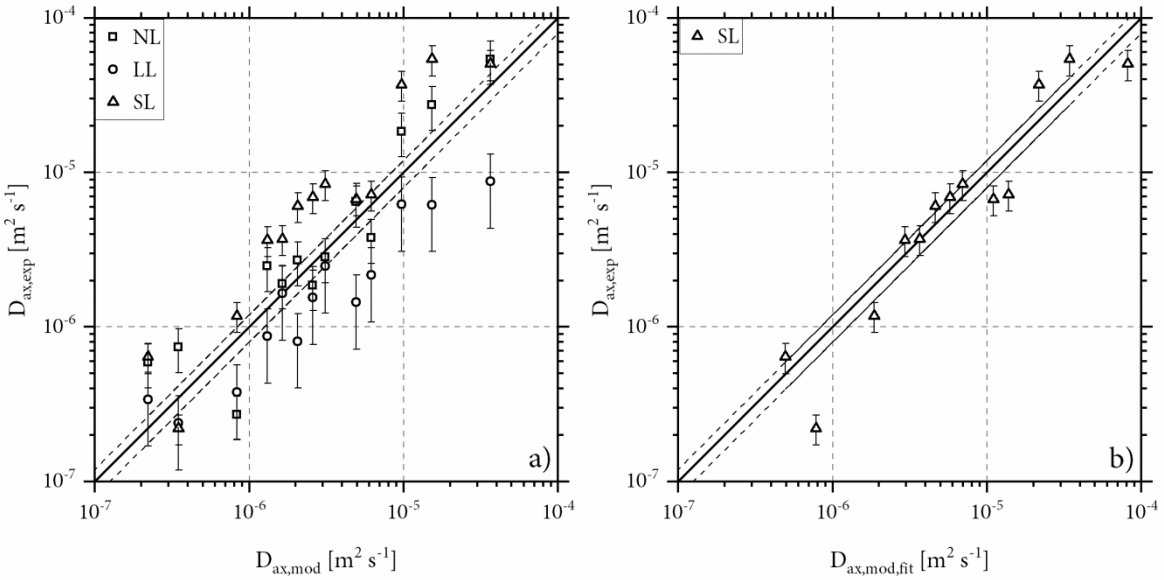

Figure III - 4.16: a) Comparison of experimental axial dispersion coefficients of this study with calculated values according to equation (3.50) [199]; b: Comparison of experimental D_{ax}-values for short lifters from this study with calculated values according to modified model equation (2.33). Dashed lines indicate ± 20% error margins. (adapted from [237])

4.1.3.4 Qualitative observations (AFC2 & lifters)

Besides the quantitative results mentioned before, considerable qualitative differences in the unloading and spreading behavior of the different flights have also been noticed during the extensive experiments by views inside the drum. This is exemplary presented in Figure III - 4.17.

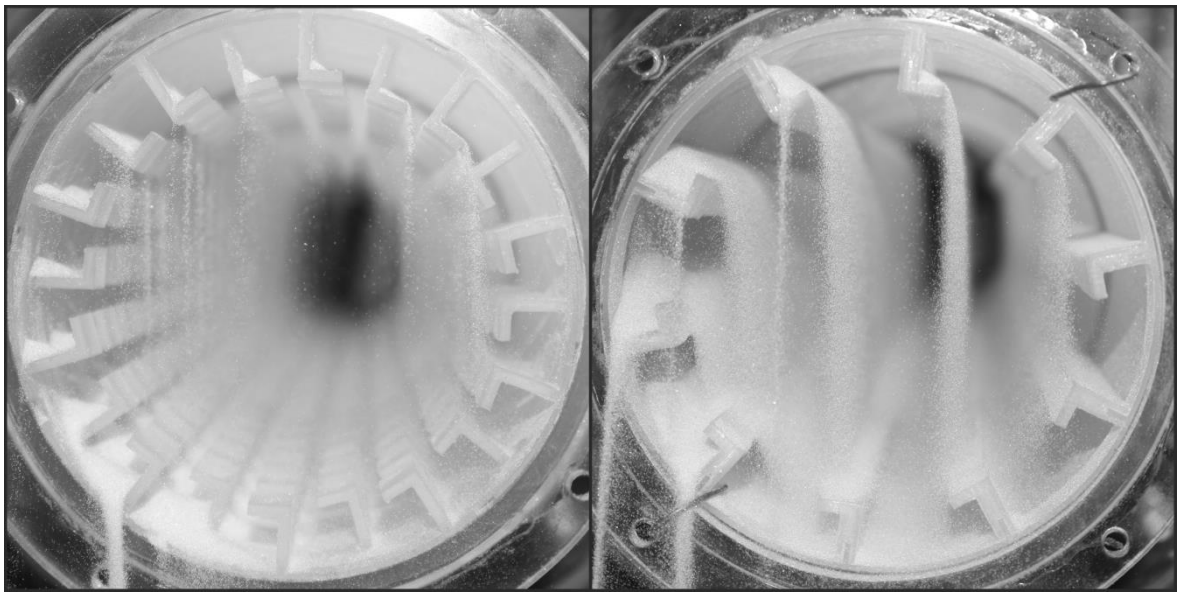

Figure III - 4.17: Axial views into the drum from the outlet end, parameter settings according to Exp. 09 (n=7.3 min^{-1}, β=3°, $\dot{m}_F$=13 kg s^{-1}); left: SL-configuration; right: LL-configuration. (adapted from [237])

The pictures have been converted to gray scale images, as this improves the contrast and visibility of the white particles and facilitates the qualitative comparison. Comparing both images, it can be clearly observed that the bulk density in the air is significantly worse for the SL-configuration and almost no solid material is in the airborne phase. The picture comparison also mirrors the quantitative measurement results from Table III - 4.12, where the hold-up increases significantly for the LL-configuration. Thus, the influence on the MRT is also plausible and in general the differences between both configurations are visually comprehensible.

Qualitatively, the discharge process of the LL-configuration (Figure III - 4.17, right) reveals exactly the patterns already known from many optical cross-section analyses. Focusing on the lifters on the left side in both configurations, which are approximately in the 9 o'clock-position, considerable differences in the filling degree are observable. While for the LL-configuration a solid-profile analogous to cross-section analyses is recognizable, the short lifters differ significantly here. They are almost not filled and the decay of solid filling in axial direction is predominant. This can also be derived from the low hold-ups with short lifters (Table III - 4.12). Based on these findings, a first modeling approach is developed in the following to investigate the effects of the lifter length in more detail.

4.2 Transversal solid transport

Besides the axial flow investigations, the transversal solid transport has also been analyzed as already described in the experimental description (cf. chapter 3.4). Different characteristics of the material flow regarding the considered internal drum configurations are in focus.

4.2.1 Bare drum & Sectional internals

The bare drum results as well as the impact of sectional internals have already been published in [235,239]. The utilized routine is explained in chapter 3.4.1. As example in Figure III - 4.18, the mixing progress for the experiment using DC1 and MC2 with 7.3 rpm and a filling degree of 0.2 is plotted in multiple ways. The standard deviation (as description of mixing state, equation (3.5)) is plotted against the number of revolutions together with deviation lines of ±20% calculated from the steady state as upper and lower border and set to the diagram (dashed lines). Furthermore, the experimental mixing index $M_{t,theo}$ is plotted in combination with the continuous (black) graph, depicting the fitted theoretical curve of $M_{t,theo}$. The theoretical mixing index is calculated from the experimental values by fitting the parameters M_∞ and k via least squares method.

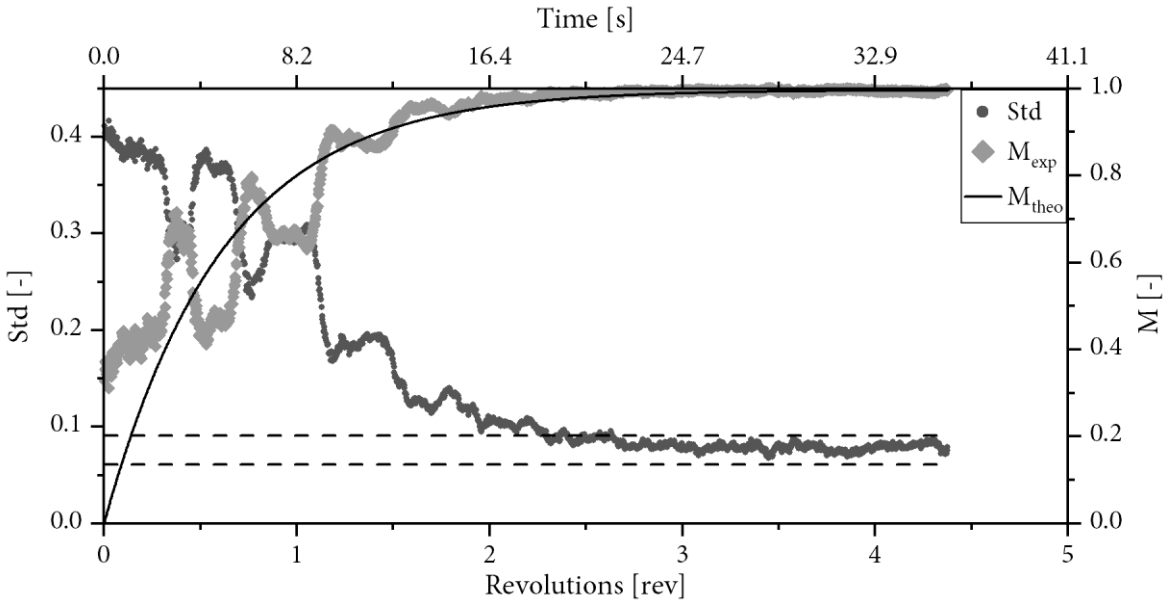

Figure III - 4.18: Diagram of standard deviation of local concentrations (goodness of mixing) versus number of revolutions for the experiment (DC1; MC1; n=7.3 min^{-1}; Φ=0.2) as well as experimental (M_{exp}) and fitted theoretical (M_{theo}) Lacey mixing indices for the same experiment (adapted from [235])

In order to provide a better and more visual and intuitive understanding of the values provided later in Table III - 4.14, the mixing progress is visualized for different drum configurations and material combinations for the first three rotations in Figure III - 4.19. The differences in mixing progress are easily observable, especially the development of the characteristic kidney-type core with smaller particles (white) for the bare drum with the segregating system (DC1-MC2).
Further description of the different impacts on mixing rate and goodness of mixing is delivered in the two following chapters adapted from [235].

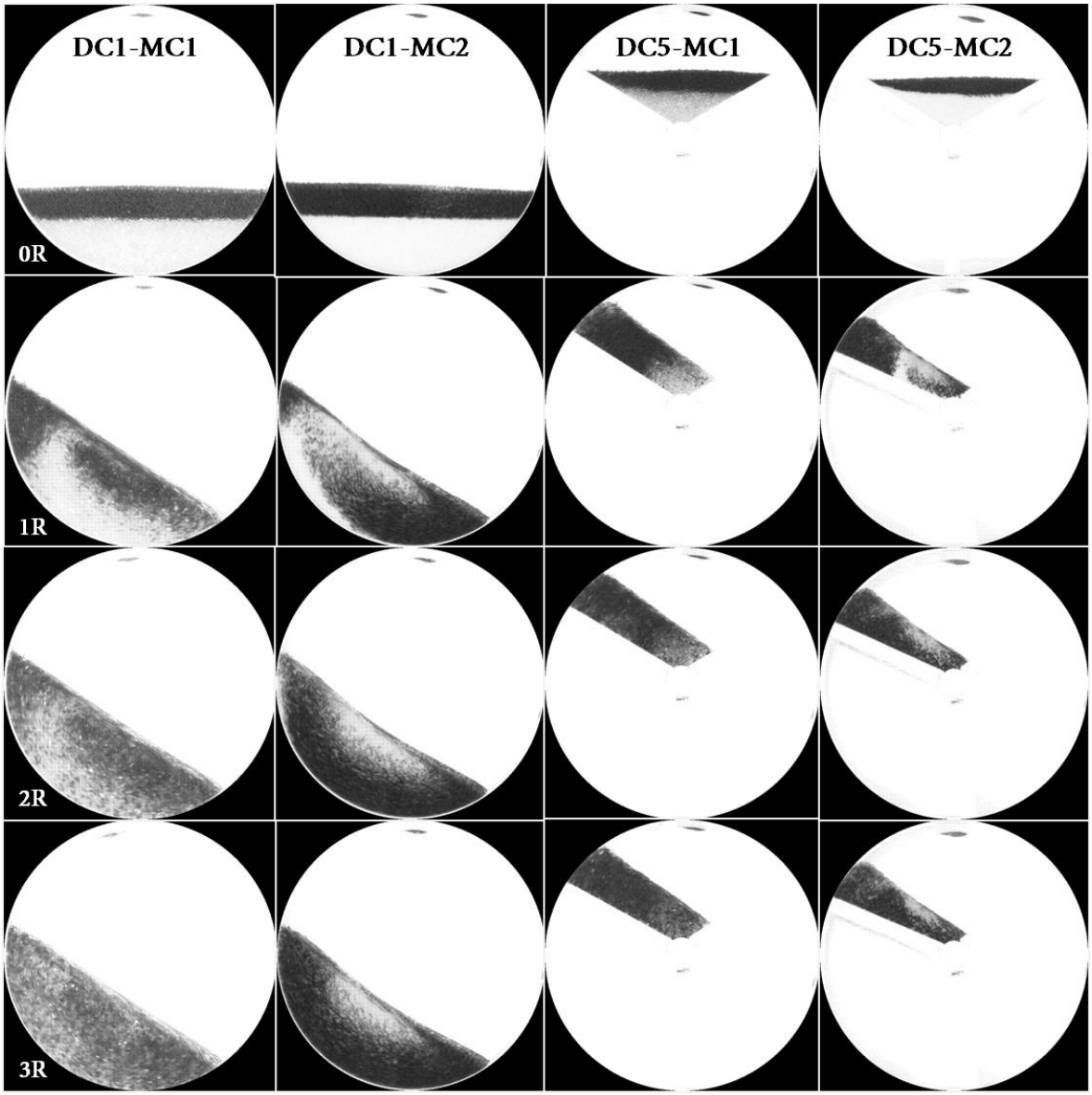

Figure III - 4.19: Exemplary mixing progresses in the first 3 rotations for bare drum (DC1) and three sections (DC5). Mixing of particle system with uniform size (MC1) and segregating particle system are presented for each configuration. Operational parameters in all pictures: rotational speed 11 rpm; filling degree: 0.3 (adapted from [235]).

Table III - 4.14: Results of mixing rate and mixing index for all conducted experiments (adapted from [235])

Config.	Exp.-No	n [1/min]	Φ [-]	MC1 M	MC1 k [1/rev]	MC2 M	MC2 k [1/rev]
DC1	1	3.8	0.1	0.99	3.17	0.79	4.75
	2	3.8	0.2	0.99	2.32	0.79	4.51
	3	3.8	0.3	0.99	2.32	0.93	3.42
	4	7.3	0.1	0.96	4.40	0.81	3.77
	5	7.3	0.2	1.00	1.62	0.89	3.02
	6	7.3	0.3	1.00	1.23	0.84	1.98
	7	11.0	0.1	0.94	3.10	0.91	3.33
	8	11.0	0.2	0.94	1.43	0.92	2.31
	9	11.0	0.3	0.99	0.96	0.82	3.53
	Mean Values			**0.98**	**2.28**	**0.86**	**3.40**
DC5	1	3.8	0.1	0.79	4.75	0.84	16.82
	2	3.8	0.2	0.86	5.56	0.88	6.19
	3	3.8	0.3	0.94	2.33	0.84	3.08
	4	7.3	0.1	0.93	5.05	0.83	6.43
	5	7.3	0.2	0.97	5.53	0.80	4.94
	6	7.3	0.3	0.96	2.20	0.87	2.37
	7	11.0	0.1	0.88	4.93	0.85	3.77
	8	11.0	0.2	0.86	2.44	0.77	5.33
	9	11.0	0.3	0.96	2.26	0.82	3.41
	Mean Values			**0.91**	**3.90**	**0.83**	**5.81**
DC3	1	3.8	0.1	0.81	7.98	0.90	4.97
	2	3.8	0.2	0.91	5.96	0.96	2.98
	3	3.8	0.3	0.90	1.53	0.95	2.52
	4	7.3	0.1	0.86	4.97	0.91	7.74
	5	7.3	0.2	0.90	2.45	0.84	2.78
	6	7.3	0.3	0.90	2.67	0.91	2.02
	7	11.0	0.1	0.90	2.03	0.84	5.06
	8	11.0	0.2	0.87	3.35	0.84	2.15
	9	11.0	0.3	0.91	1.49	0.88	1.71
	Mean Values			**0.88**	**3.60**	**0.89**	**3.55**
DC4	1	3.8	0.1	0.84	16.63	0.87	9.29
	2	3.8	0.2	0.89	6.90	0.94	3.64
	3	3.8	0.3	0.85	4.14	0.94	2.55
	4	7.3	0.1	0.82	24.33	0.86	9.89
	5	7.3	0.2	0.86	2.04	0.97	4.52
	6	7.3	0.3	0.91	1.57	0.89	2.32
	7	11.0	0.1	0.76	10.03	0.86	3.97
	8	11.0	0.2	0.86	2.94	0.92	3.25
	9	11.0	0.3	0.89	2.44	0.89	1.44
	Mean Values			**0.85**	**7.89**	**0.90**	**4.54**

rel. Std. = 1.25% (MC1 M) | rel. Std. = 5.28% (MC1 k) | rel. Std. = 9.00% (MC2 M) | rel. Std. = 19.05% (MC2 k)

rel. Std. = 5.00% (MC1 M) | rel. Std. = 9.24% (MC1 k) | rel. Std. = 4.47% (MC2 M) | rel. Std. = 6.92% (MC2 k)

rel. Std. = 0.54% (MC1 M) | rel. Std. = 33.91% (MC1 k) | rel. Std. = 4.23% (MC2 M) | rel. Std. = 11.37% (MC2 k)

rel. Std. = 4.38% (MC1 M) | rel. Std. = 59.69% (MC1 k) | rel. Std. = 4.80% (MC2 M) | rel. Std. = 27.44% (MC2 k)

4.2.1.1 Mixing rate

The mixing rate k in Table III - 4.14 is given as specific mixing rate per revolution [1/rev] to provide the change of mixing goodness with one revolution as an easily comparable measure. Following to that, the mixing time is decreasing for higher rotational speeds if mixing rates (k) are equal, since more revolutions take place in the same time interval.

Figure III - 4.20 presents diagrams for the experimental mixing rates from Table III - 4.14 to observe trends more easily.

MC1 (same size of bulk and tracer particles):

On the left side of Figure III - 4.20 (MC1, s. Table III - 3.4) it is shown, that the mixing rate is decreasing with higher filling degrees. This is plausible because a higher amount of material has to be mixed at the same conditions and mixing needs more time, which is known from literature [150,151,154,240,241]. In addition, it can be seen clearly that the drum configuration (DC) is influencing the mixing rate. The mixing rates for DC1 (bare drum) in nearly all experiments of the DOE are lower than the ones with installed sectional internals (DC2-4).

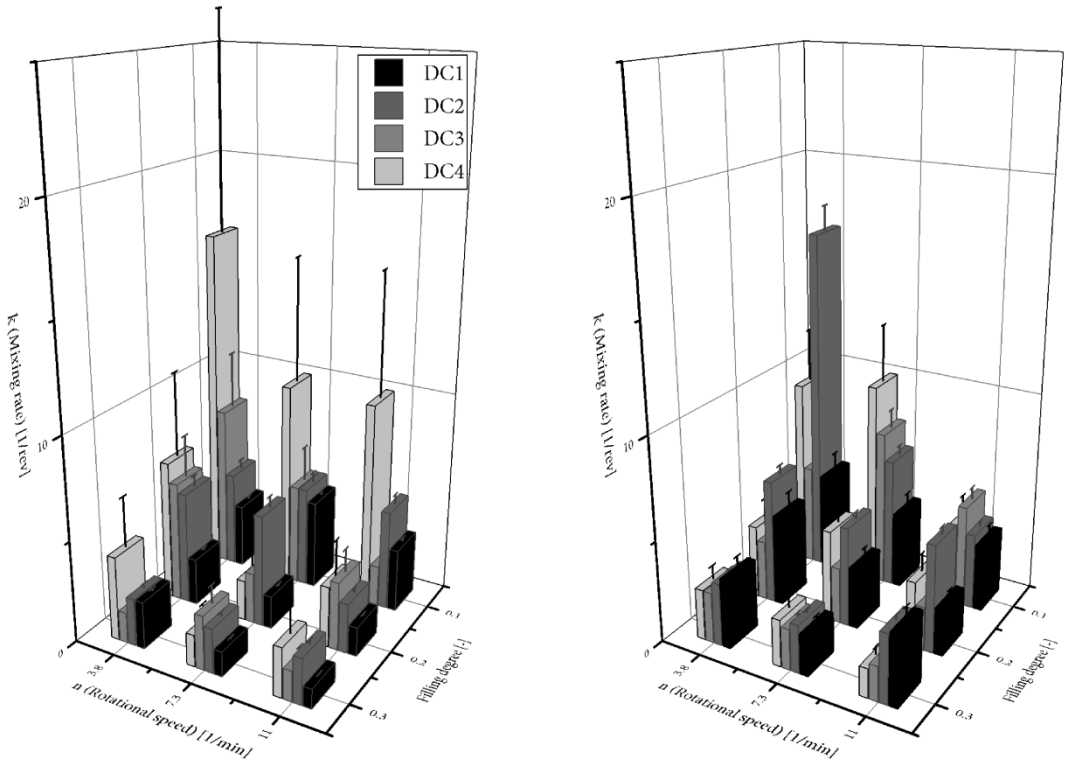

Figure III - 4.20: Mixing-rates for all experiments, MC1 on the left and MC2 on the right (adapted from [235])

This can also be observed by comparing the mean values of the mixing rates for one DC in Table III - 4.14. The increase in the mixing rate due to sectional internals is particularly high for lower filling degrees (Φ=0.1). Furthermore, it is higher for low rotational speeds (n=3.8 rpm). The reason for this is an estimated switch in mixing mechanism. Mixing in the bare drum is driven by the constantly present cascading layer on the top plane of the solid bed, which has a magnitude varying with the rotational speed [146,154,242]. With sectional internals the mixing is more likely affected by the periodical change in the shape of the solids' bed cross section (as described later in 4.2.1.3 via aspect ratio). This changing shape is independent from the rotational speed. Therefore the sectional internals lead to better results in mixing kinetics especially for low rotational speeds.

In the investigated range of rotational speeds, the mixing rates are more likely independent for the bare drum (DC1) while the mixing rate is higher with lower rotational speed when sectional internals are used (DC 3,4&5).

Besides that, there is a trend concerning the influence of section numbers N on the mixing rate. While at high rotational speeds and high filling degrees the section number leads to minor or negligible increases in mixing rate, the influence of the section number increases with lower rotational speeds. The same trend can be observed for lower filling degrees.

MC2 (small bulk and large tracer particles):

On the right side of Figure III - 4.20 the data for MC2 (Table III - 3.4) is presented. In comparison with the MC1 data, the mixing rates for higher filling degrees (0.2 and 0.3) increased obviously. Particularly the mixing rates of DC1 (bare drum) compared to sectional internals are higher. Thus the sections are not as advantageous as they were for uniform particle sizes (MC1) but they are not significantly worse. Now, in most cases the mixing rates are similar for all equipment configurations except from some outliers. At low filling degrees and low rotational speeds the advantage of sectional internals due to already described reasons can be observed once again. However, here there is no clear trend concerning the number of sections because mostly the configuration with three sections (DC5) provides the highest mixing rates.

Summarized, the mixing kinetics is affected positively by using the sectional internals due to higher or comparable mixing rates than for bare drums. MC2 is the more realistic case in real industrial processes because the particle size distributions are typically not that narrow. Moreover, the handling of materials with differing particle sizes is one major advantage of rotary kilns. Following this, the presented results for MC2 are more realistic in practice.

4.2.1.2 Goodness of mixing

The goodness of mixing is presented as Lacey-Mixing index (M_∞) in Table III - 4.14 for all experiments. The range of values for the mixing index is between 0 and 1 in general. A value of 1 represents a statistically perfect mixed state. In Figure III - 4.21 the values are presented as a diagram.

MC1 (same size of bulk and tracer particles):

On the left side of Figure III - 4.21 it is obvious, that highest mixing indices have been achieved in the bare drum (EC1) and nearly in every configuration the perfectly mixed state was reached at the end of the experiments. For all further equipment configurations the goodness of mixing is worse with mixing indices below 1 in most cases. Furthermore, there is a trend towards lower mixing indices with higher number of sections in the model when comparing the same parameter settings. This can additionally be evaluated from the mean values for each equipment configuration in Table III - 4.14. Besides this, there is a tendency towards lower mixing indices with lower rotational speeds for all equipment configurations.

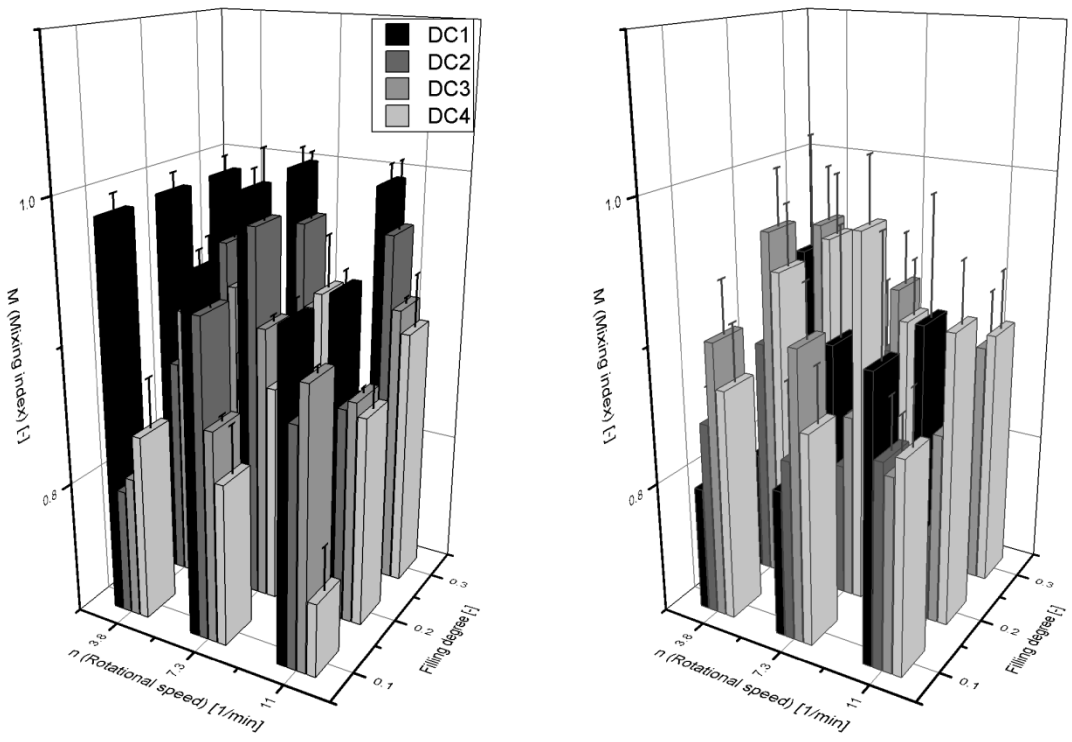

Figure III - 4.21: Lacey-Mixing-indices for all experiments, MC1 on the left and MC2 on the right (adapted from [235])

Additionally, with lower filling degree the mixing index is decreasing. The last two findings superimpose the decrease of mixing goodness with increasing section number.

The estimated reason for these findings again is the proposed switch in the mixing mechanism. A cascading layer with high diffusion rates to obtain a high stochastic mixing is not that distinct with sectional internals. Only when the whole solid bed is sliding down the inner walls, particles are cascading. This mechanism is connected with high changing rates concerning the aspect ratio (as will be explained later). Higher filling degrees lead to more distinctive cascading and thus higher stochastic mixing. This explains the occurrence of lower mixing indices at lower filling degrees.

MC2 (small bulk and large tracer particles):

On the right side of Figure III - 4.21 the data for material configuration MC2 is presented which describes a segregating system. Clearly, mixing indices are decreasing due to segregation of the system by different particle sizes in the bulk material compared to MC1-data. Besides that, the variance is increasing (error bars). The decrease in goodness of mixing is relatively high for the bare drum (DC1). While installation of sections with MC1 resulted in lower mixing indices, now the trend is the other way around. Mixing indices in the segregating system are higher with more installed sections. The number of sections is not as important as their presence itself. This can also be observed from the mean values of the mixing indices for the different equipment configurations in Table III - 4.14. While the mean mixing index for three sections (DC5) is slightly lower than for the bare drum, it is higher for the other configurations with sectional internals. A clear trend concerning the number of sections cannot be derived from the data. This will be subject of further investigations. Additionally, the trends concerning rotational speed and filling degree are not as distinct as for MC1 with particles of the same size.

The advantage of sectional internals in mixing segregating systems can also be explained with the shift in mixing mechanism. In bare rotary drums the segregation is evoked by percolation of smaller particles in the cascading layer [147,240]. As already stated, the cascading layer is not distinct with sectional internals. Furthermore the periodic forced change of bed shape attenuates the formation of segregation patterns. In order to visualize the process for segregating systems, the mixing progress is presented for three sections (DC5) exemplary in Figure III - 4.22.

The different shape and position of the solid bed can be observed clearly, which evokes different positions of the smaller particles (white) in the bed. Due to the dynamic of this process, no pseudo static core is created compared to the bare drum (cf. Figure III - 4.19, DC1-MC2).

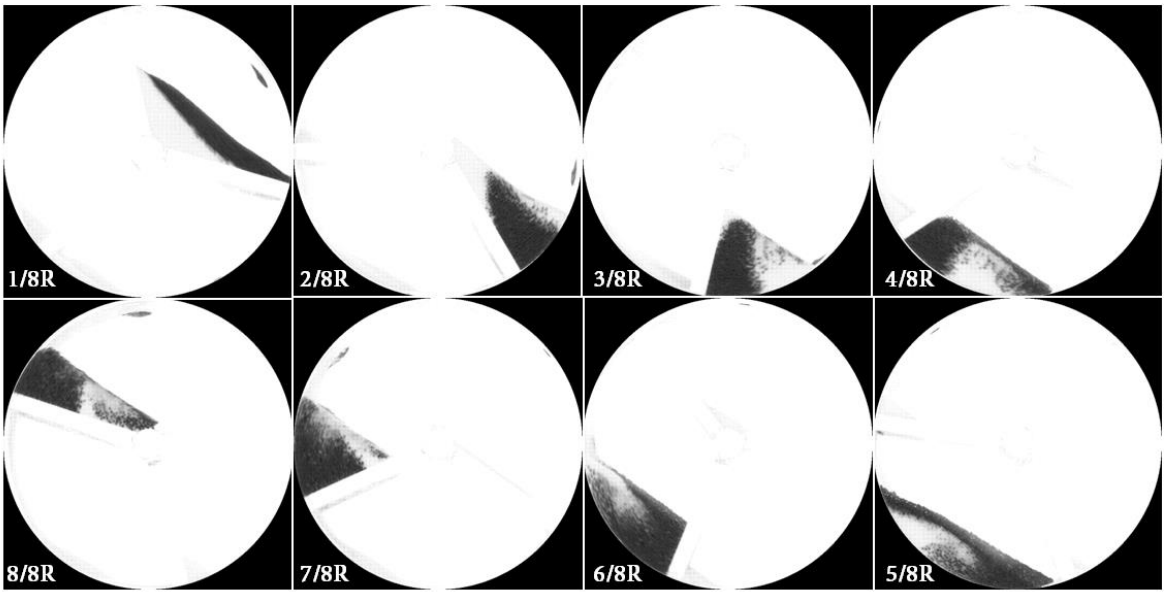

Figure III - 4.22: Mixing progresses at different states while the first rotation for three sections with the segregating system (EC2-MC2). Rotational speed 11rpm, filling degree 0.3 (adapted from [235])

Concluding, the goodness of mixing should not be affected negatively by sectional internals overall, because in real systems the particle sizes are mostly not uniform and the distribution can be wider than in the investigated model system. Additionally, the observed decay in goodness of mixing in uniform particulate systems is smaller for practically reasonable filling degrees (above 0.2).

4.2.1.3 Experimental observation & mechanism

The surface area is one of the most important parameters influencing the heat transport in rotary kilns. It is therefore essential to describe the influence of the sectional internals concerning this parameter.

The shadowgraph recordings from the experiments gave a first impression of the solid bed behavior in rotary drums with sectional internals. They are used to observe the changing shape of the solid beds cross section and the constantly renewing surfaces of the solid bed. First of all, the perimeter of the shadow is measured as well as the aspect ratio as a measure for the shape of the cross section. The perimeter and aspect ratio are measured with ImageJ (checking “Perimeter” and “Shape descriptors” in the menu “Analyze>Set Measurements”. In ImageJ the aspect ratio is defined as the ratio of major and minor axis of a fitted ellipse. As an example, the values perimeter (black) and aspect ratio (grey) for an experiment using EC2 and MC1 with 7.3 rpm and a filling degree of 0.2 are presented for two rotations in Figure III - 4.23.

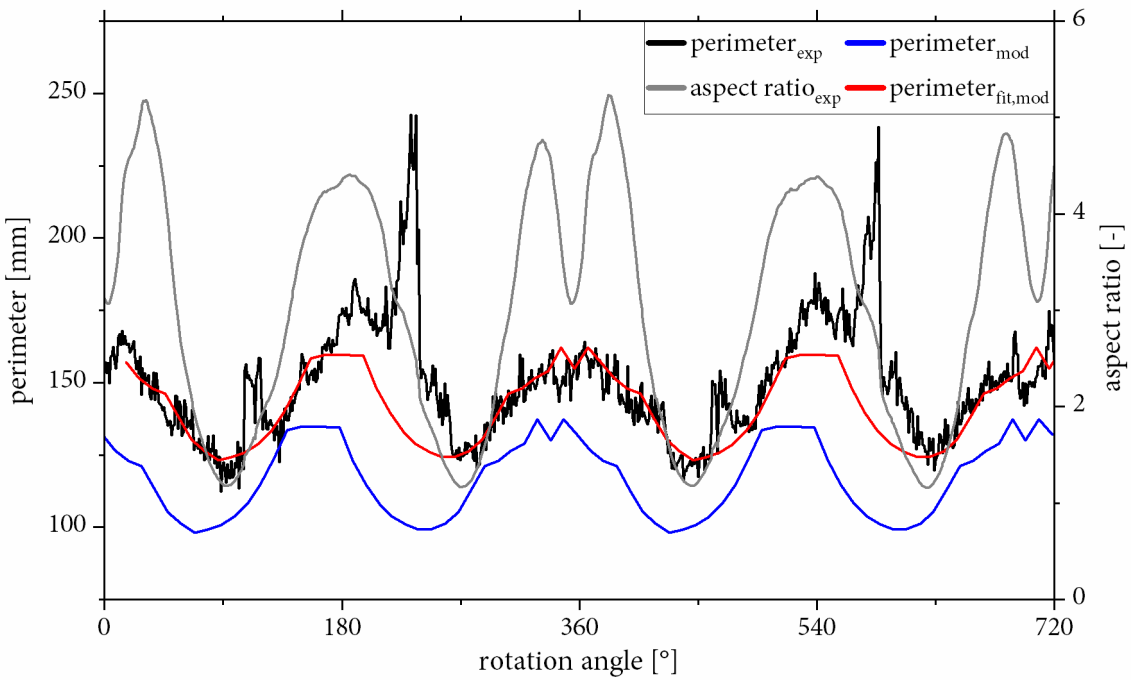

Figure III - 4.23: Diagram of solid-bed perimeter and aspect ratio from shadowgraph images (EC2; MC1; n=7.3; Φ=0.2) for 2 rotations and solid-bed perimeter from Geogebra® model (adapted from [235])

It can be seen clearly, that the aspect ratio and thus the shape of the solid bed cross section area is changing periodically in a range of roughly 1-5. Besides that, the perimeter of the solid bed shadow changes periodically from this shape variation. Because the solid bed shape is changing constantly and the walls made of PMMA are nearly invisible, a separated evaluation of the different contact lengths respectively phase interfaces between gas and solid (g/s) as well as between solid and wall (s/w) for the automated digital image analysis procedure is not possible. Thus, a modeling approach was set up to generate a deeper understanding of the sections impact on exchange surfaces, which will be explained later (chapter 4.3.1)

4.2.2 Lifters

The achieved results regarding the cross sectional investigation of different lifter types according the procedure explained in chapter 3.4.2 are presented in the following. First the continuous lifter experiments are shown, followed by the segmented lifters and a final comparison of lifter types.

4.2.2.1 Continuous lifters

The mean values of the area fraction in the drums cross section which is occupied by solids (mf_{OA}) have been determined and are listed regarding the DOE (see chapter 3.4.2.3) in Table III - 4.15.

Table III - 4.15: Mean values of the area fraction of solids occupying the gas-phase in the cross section mf_{OA} with continuous lifters

	small particles			large particles		
Exp.-No.	L_{cont}	EHD_{cont}	EAD_{cont}	L_{cont}	EHD_{cont}	EAD_{cont}
1	6.83	3.25	3.88	10.77	3.60	4.24
2	7.87	2.86	4.83	7.44	2.41	3.91
3	6.94	2.79	4.14	6.04	1.49	3.76
4	15.46	5.03	10.97	16.83	7.55	10.52
5	14.46	5.29	8.74	12.69	3.73	8.12
6	15.61	9.58	10.55	9.37	3.03	6.06
7	23.87	6.72	17.83	26.98	9.74	14.22
8	21.60	8.27	16.59	11.84	6.36	12.15
9	19.40	9.01	16.34	16.09	3.95	10.40
10	3.35	0.12	1.54	7.19	0.83	5.77
11	10.58	0.28	5.85	13.56	0.56	12.58
12	13.58	0.21	5.95	17.28	1.02	15.21
DOE-mean	13.30	4.45	8.93	13.01	3.69	8.91
Errors						
Std.	1.31	0.15	0.62	1.10	0.30	0.27
rel. Std.	8.21	2.91	7.21	9.63	8.50	3.33

First of all, it is obvious from the variation of the numbers that the experimental parameters impact on the occupied area. Furthermore, the different flight designs also affect the occupied area. In order to visualize the data, in Figure III - 4.24 diagrams of the area fraction regarding the filling degree are presented. Additionally, the data is separated for each investigated rotational frequency. For each lifter design and solid material (filled signs: small particles, hollow signs: large particles) a dedicated diagram is created.

The visualization reveals different patterns:

- The magnitude of occupied area is similar for the different materials (with equal other parameter settings), which is plausible.
- The characteristic progress of mf_{OA} regarding the filling degree is similar for each rotational speed, but the rotational speed itself is impacting on mf_{OA}.
- mf_{OA} increases with the rotational speed for constant filling degrees.
- mf_{OA} indicates a maximum at roughly 10% filling degree in nearly all configurations (except Figure III - 4.24 f). Either the maximum value stays constant for further filling or mf_{OA} even decreases.
- As can also be taken from the DOE-means in Table III - 4.15, the lifter type ranking of mf_{OA} for constant rotational speeds and solid material is L>EAD>EHD (for both materials).

The relative standard deviations (Table III - 4.15) and related error bars in Figure III - 4.24 show a good reproducibility of the data. Summarizing, the L-lifters turned out to be the most effective lifter type for the investigated system, assuming that the occupied area is a measure for solid material in the gas phase and thus intensified heat transfer. This finding is remarkable, since the construction of this lifter type is the easiest regarding industrial purposes and EHD or EAD lifters should be optimized for a more effective system (cf. 2.4.1).

The observed pattern of mf_{OA} regarding the filling degree is similar to literature findings of e.g. Karali et al. [192,194], who investigated the filling degree in the first unloading flight (at roughly 9 o'clock position). This filling degree in the first unloading flight (when leaving the solid bed) is similar to the amount of solids showering in the gas phase while the unloading process. The similarity therefore validates the experimental data.

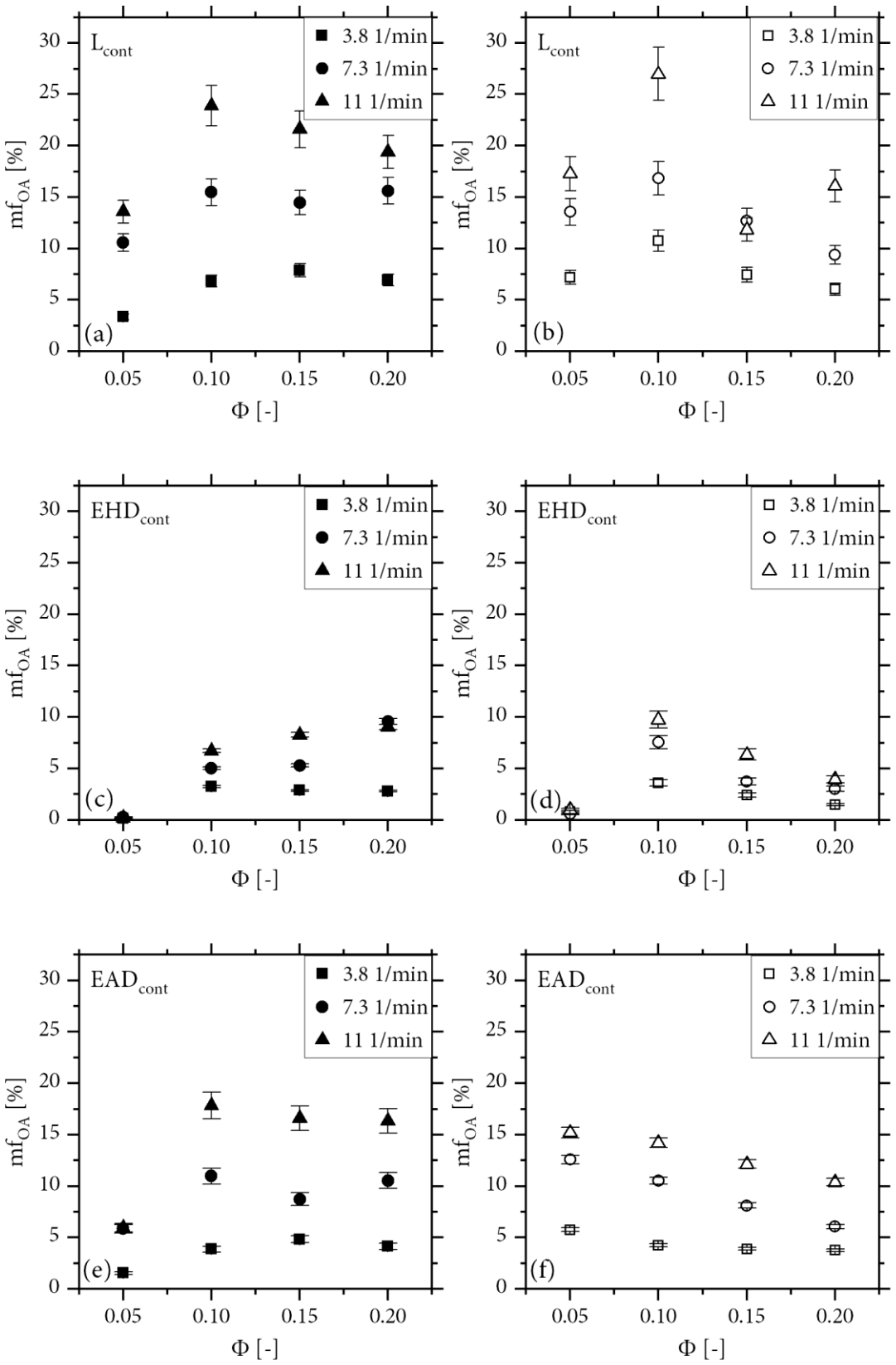

Figure III - 4.24: Diagrams of mean occupied area fractions of the gas-phase in the cross section (mf_{OA}) with continuous lifters in dependency of the drums filling degree Φ. a/c/e or filled symbols with small particles, b/d/f or hollow symbols with large particles.

Table III - 4.16: Mean values of the solid occupied gas-phase in the cross section with small particles and segmented lifters

Exp.-No.	L_{10mm}	$L_{10mm.closed}$	L_{20mm}	EHD_{10mm}	EAD_{10mm}
01	1.15	4.66	4.81	2.50	1.26
02	2.22	8.41	3.72	1.61	1.37
03	2.56	7.75	4.18	1.36	1.53
04	1.78	15.53	7.41	2.81	2.42
05	5.11	16.44	10.74	2.83	2.17
06	4.83	19.24	9.84	3.07	2.49
07	5.91	24.39	11.61	6.36	3.40
08	6.47	24.93	18.61	6.41	3.28
09	4.22	22.32	16.38	6.34	3.12
10	1.84	5.32	2.95	1.30	0.19
11	1.77	12.76	6.53	3.36	1.01
12	3.27	18.92	10.36	5.73	0.99
DOE-mean	3.43	15.06	8.93	3.64	1.94
			Errors		
Std.	0.86	3.30	1.53	3.40	0.44
rel. Std.	20.80	25.98	15.80	60.11	16.75

4.2.2.2 Axially segmented lifters

Analogously to chapter 4.2.2.1, the experimental data for the investigated axially segmented lifters is listed in Table III - 4.16 regarding small particles.

The data visualization is presented in Figure III - 4.25. Although the theoretic hold-up of the segmented lifters is equal to the continuous lifters, huge differences in the mf_{OA} values can be observed (see different ordinate scalings). The data also reveals some patterns:

- The characteristic progress is similar for all rotational speeds, although the L10mm configuration reveals some deviations.
- The increase of rotational speed leads to higher mf_{OA} with equal filling degrees.
- Again a maximum of mf_{OA} can be derived visually, but it shifted to 0.15 compared to the continuous lifter data.
- Comparing the DOE-means of the 10mm configurations L-type and EHD lifters provide similar values (~3.5%) and the EAD-flights are even worse (~2%). The different characteristic behavior observed for continuous lifter types are not present any more. The ranking of lifter types now is EHD>L>EAD (although deviations are very small).

- Comparing the three L-type configurations, the closed lifter version provides the best performance, while the 20mm version is second best. This is a further proof that the axial length (or front side walls) massively impacts on the lifter performance.

In Table III - 4.17 the measured mf_{OA}-values for axially segmented lifters with large particles are listed.

The related data visualization is given in Figure III - 4.26. The diagrams as well as the DOE-means from Table III - 4.17 show, that the large particles downgrade the performance regarding mf_{OA} values once more compared to continuous lifters. Obviously the maximum patterns regarding the filling degree are not existent any more (except EAD-flights), and mf_{OA}-values are constantly decreasing for increased filling degrees in almost all data sets.

The estimated reason for the findings is the ratio of axial lifter length (10mm) and particle size (0.8mm), which are in a similar magnitude. The ratio is roughly 10 and the large particles behave more likely as single balls than as a continuous bulk material. The lower repose angles (dynamic and static) are further measures for this effect.

Summarizing, for axially segmented lifters, the lifter type itself becomes more and more irrelevant the shorter the axial length is. However, the trends and dependencies regarding rotational frequency of the drum and filling degree (operational parameters) are similar for all configurations (except some outliers) and can be taken as universally valid. The impact of the rotational speed on mf_{OA} is higher than the impact of the filling degree.

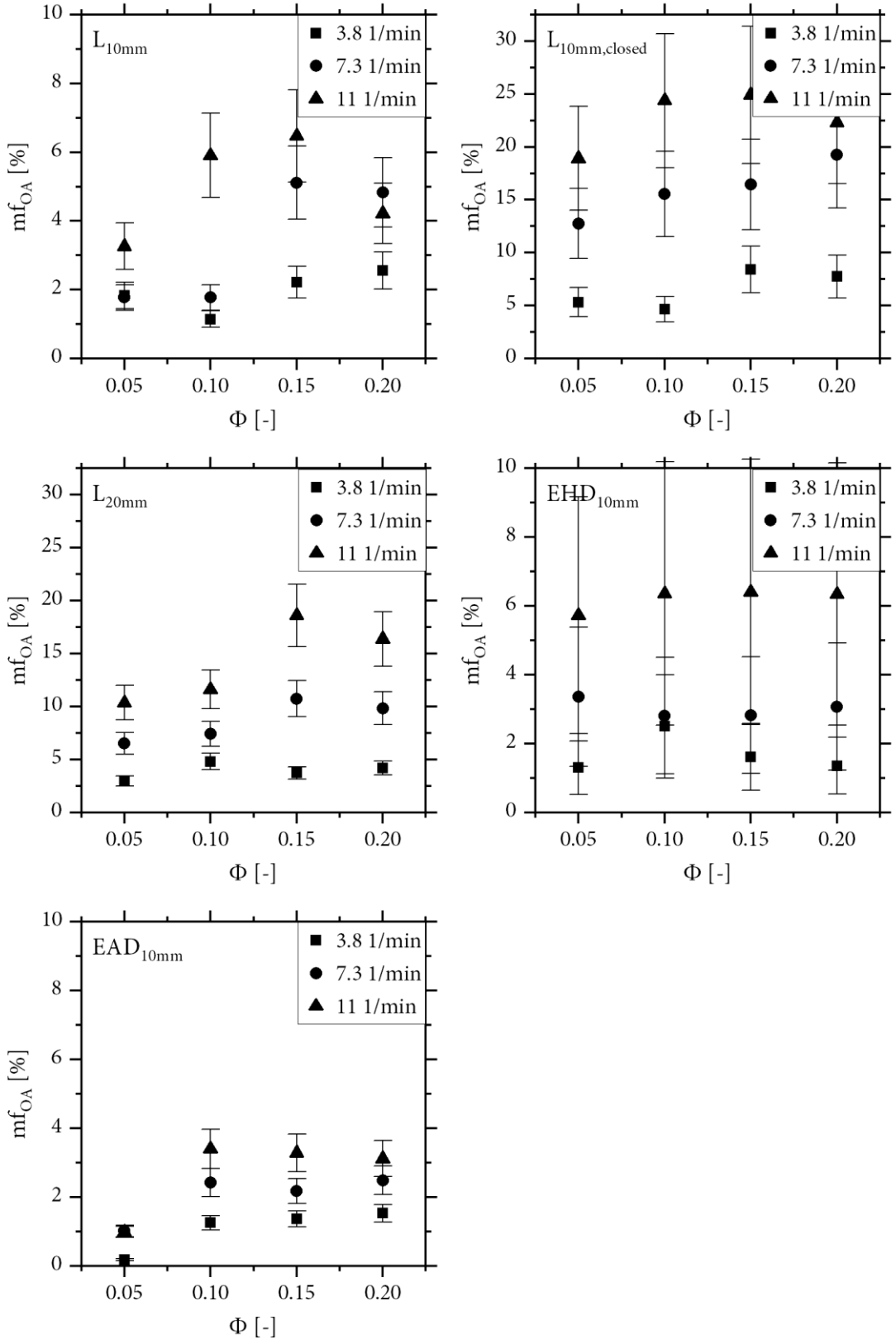

Figure III - 4.25: Diagrams of mean occupied area fractions of the gas-phase in the cross section (mf_{OA}) with axially segmented lifters in dependency of the drums filling degree Φ. All data is provided for small particles, lifter configurations in the top left corners.

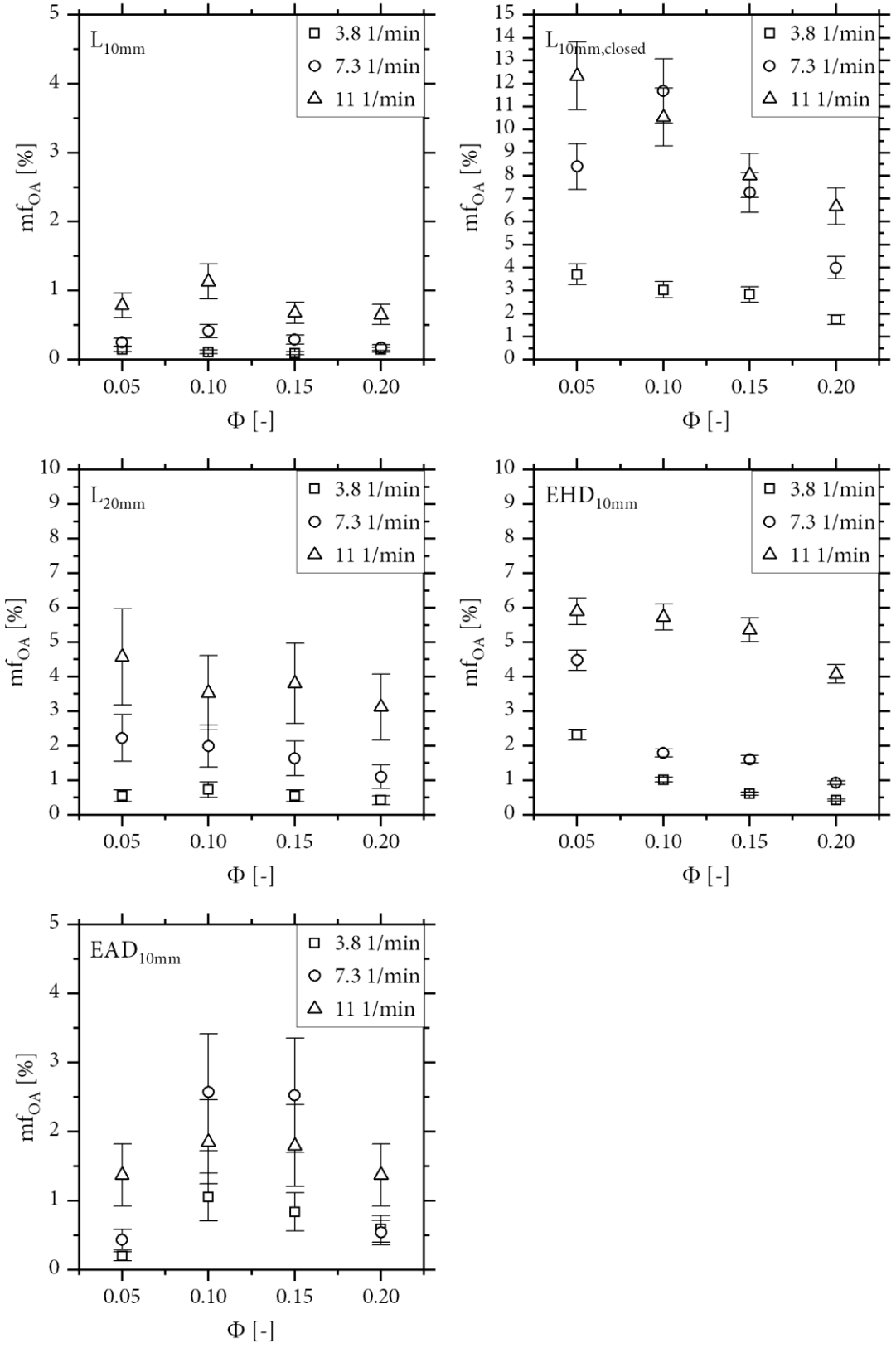

Figure III - 4.26: Diagrams of mean occupied area fractions of the gas-phase in the cross section (mf_{OA}) with axially segmented lifters in dependency of the drums filling degree Φ. All data is provided for large particles, lifter configurations in the top left corners.

Table III - 4.17: Mean values of the solid occupied gas-phase in the cross section with large particles and segmented lifters

Exp.-No.	L_{10mm}	$L_{10mm.closed}$	L_{20mm}	EHD_{10mm}	EAD_{10mm}
1	0.11	3.04	0.73	1.02	1.05
2	0.10	2.84	0.55	0.61	0.84
3	0.14	1.74	0.43	0.43	0.59
4	0.41	11.69	1.99	1.79	2.57
5	0.29	7.27	1.64	1.61	2.53
6	0.18	4.00	1.10	0.93	0.54
7	1.13	10.55	3.53	5.74	1.85
8	0.68	8.02	3.81	5.36	1.80
9	0.65	6.67	3.12	4.08	1.37
10	0.15	3.71	0.55	2.32	0.19
11	0.25	8.39	2.22	4.48	0.44
12	0.79	12.33	4.58	5.90	1.37
DOE-mean	0.41	6.69	2.02	2.86	1.26
			Errors		
Std.	0.08	0.95	0.77	0.10	0.62
rel. Std.	22.50	11.94	30.57	6.55	32.83

4.2.2.3 Visual comparison of lifter types

Besides the comparison of data given in the former chapters a graphical visualization is presented in the figures of this chapter to optically validate and emphasize the findings.

In Figure III - 4.27 the continiuous versions of the three investigated lifter types are presented under operation. It can be clearly observed, that the L-type flight has the best unloading behavior and the EHD-flight provides the worst showering characteristics. This is in total congruence to the findings from chapter 4.2.2.1. In the pictures of EAD and EHD flight the unloading on the right part of the drum is special, since they unload on the backside of the lifter blade ahead. This is the reason for the worse performance of both types. Additionally, it can be observed that due to the lifter geometry the loading of EAD and especially EHD flights in the solid bed is not working properly.

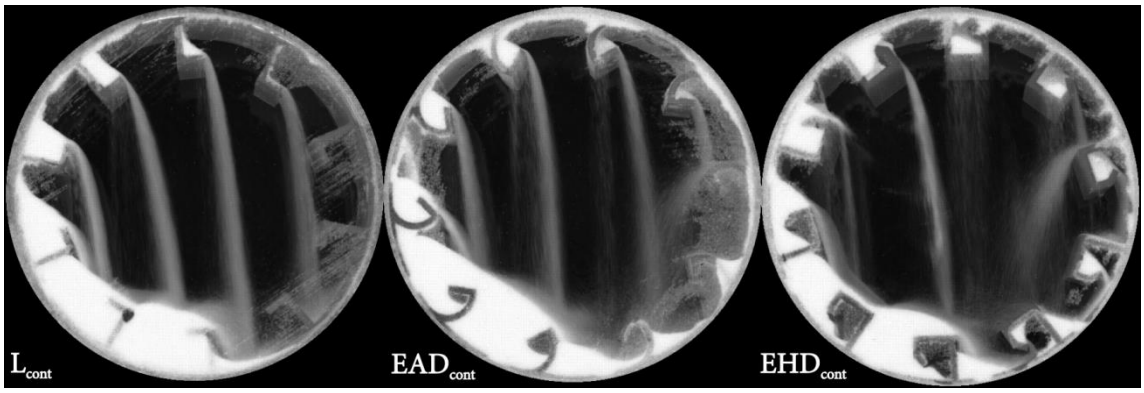

Figure III - 4.27: Exemplary comparison of the investigated continious flights under operation with small particels (Exp.-No. 08; n=11 min-1; θ=0.15).

Figure III - 4.28 presents the related axially segmented (10mm axial length) versions of the investigated lifter types. In direct comparison to the continuous lifters it is obvious that the solid loading in the gas phase is almost not existent. This finding validates the congruent results from chapter 4.2.2.2. Comparing the pictures to the related continuous flights it can be seen, that the filling degree in the flights is significantly lower. The mechanism is the drainage of particles in axial direction until the angle of repose is reached. In the unloading state therefore the material is unloading in three directions and the lifter is emptied very fast. The behavior is independent of the used lifter type.

In Figure III - 4.29 all investigated L-type flights are compared, as they are especially focused in this work. The impact of the axial lifter length on the solid density in the gas phase can be observed very clearly in the comparison. The visual ranking is $L_{cont}>L_{10,closed}>L_{20}>L_{10}$. The pictures provide clear evidence of the axial lifter length impact on the performance.

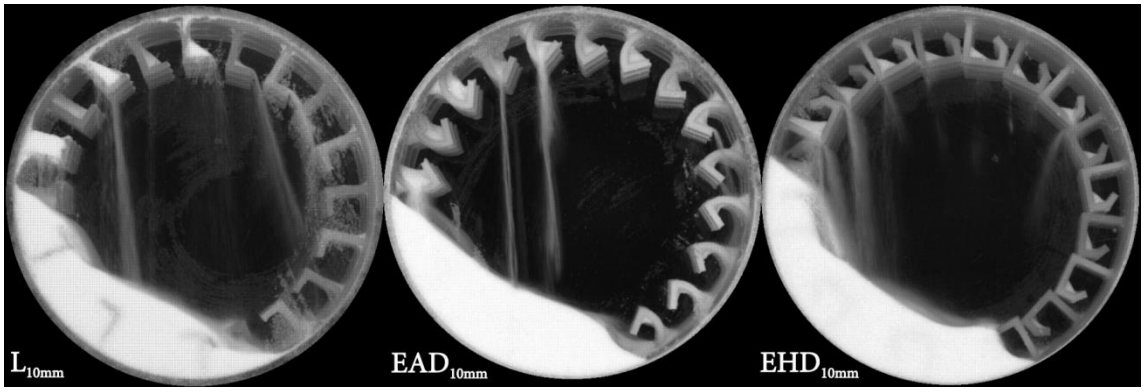

Figure III - 4.28: Exemplary comparison of the investigated axially segmented lifters under operation with small particles (Exp.-No. 08; n=11 min-1; θ=0.15).

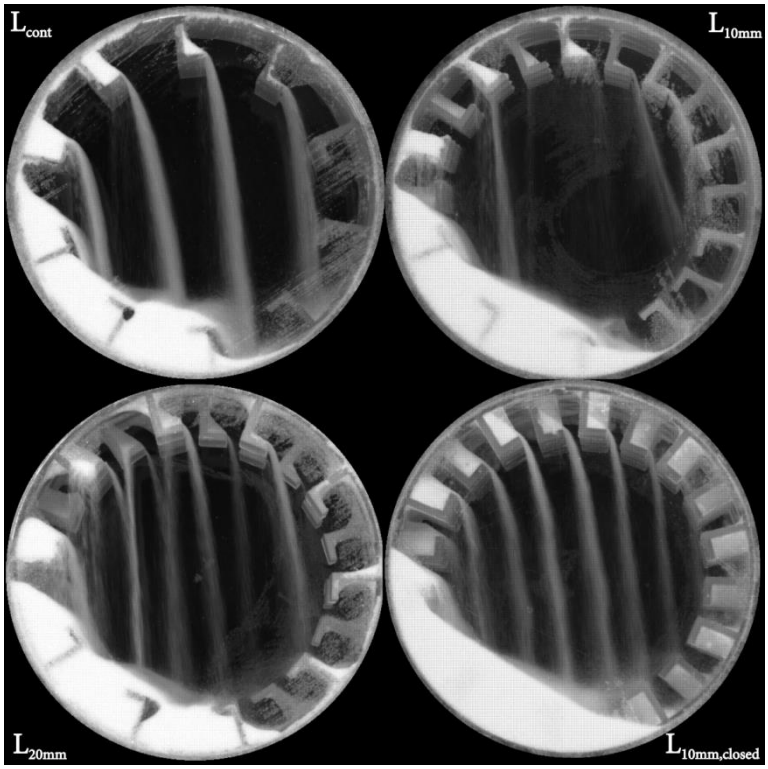

Figure III - 4.29: Exemplary pictures from the investigated L-type lifters in operation mode with small flights (Exp.-No. 08; n=11 min-1; θ=0.15).

Furthermore, the special impact of front side walls ($L_{10,closed}$) is presented, as the walls prohibit the axial particle drainage. This leads to smaller but more and very uniform solid curtains.

A presentation of the related pictures under operation with large particles is omitted, since the results are qualitatively similar.

Summarizing, the impact of the axial lifter length on the solid transport in rotary drums could be clearly shown in this work.

4.3 Modeling approaches

From the experimental data and the qualitative observations stated in chapters 4.1 & 4.2, modeling approaches have been derived to further evaluate the data or to predict the process behavior of the investigated drum configurations. In the following, these approaches and the results will be explained.

4.3.1 Transversal considerations with sectional internals

In contrast to the cross section of a rotary kiln or drier without sectional internals, where only g/s and s/w interfaces are significant to describe, the s/w surface has to be divided into two different parts with sectional internals [243]. Here, the outer wall of the drum with a connection to the systems' surrounding and inner walls, separating the sections have to be considered. Contact to the outer wall is leading to heat exchange with the drums outside due to conduction through the wall, comparable to systems without sectional internals. However, the heat flux through the inner walls is not leaving the system. Thus three different surfaces (g/s, Figure III - 4.30 blue line; solid/outer wall (s/w_o), Figure III - 4.30 green line; solid/inner wall (s/w_i), Figure III - 4.30 red line) have to be monitored or calculated for one rotation.

4.3.1.1 Modeling approach

Therefore a model was built in Geogebra® to enable the stated calculations. The modeling is strongly connected to the experimental findings (chapter 4.2.1) and the validation of the model with these findings, which is described later. As example, the modeling is illustrated for three sections (DC5) and a filling degree of 0.2. The main problem in modeling or mathematical description is the changing shape of the solid bed cross section for every angle of rotation, with installed sectional internals (visualization in Figure III - 4.30). Additionally, the basic geometry or construction is changing while one rotation. E.g. the solid bed is not in contact with the outer wall and thus does not contain the circular part of the outer wall or drum shell in each position. Therefore, the modeling uses triangles (Figure III - 4.30, red area) and a circular sector (Figure III - 4.30, grey area) as basic geometries.

The model describes one section (similar to the experimental part) rotating around the center (as shown in Figure III - 4.30 with different cases). The upper border (g/s-surface, Figure III - 4.30, blue line) of the solid bed is always horizontal, analogously to the behavior of water in the section.

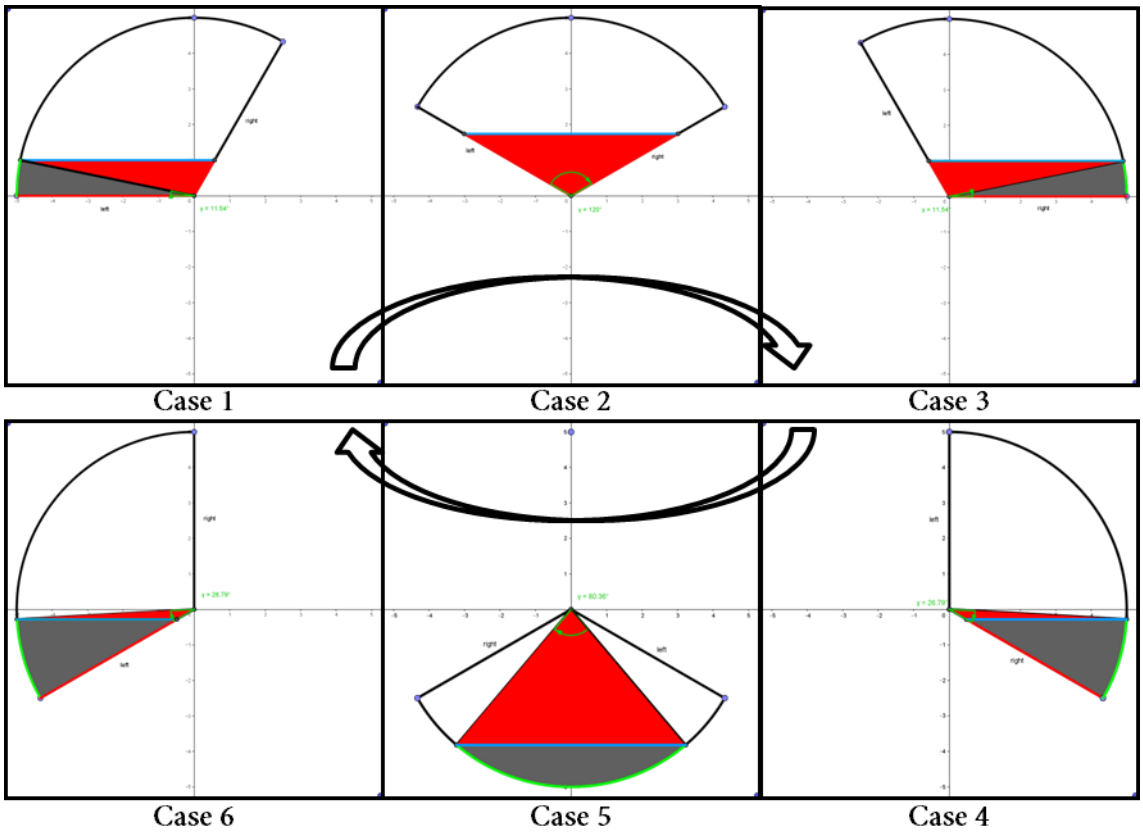

Figure III - 4.30: Exemplary modeling of the solid bed and the phase interfaces of a rotary drum with sectional internals with Geogebra® for 3 sections (DC5) and Φ=0.2 (adapted from [235])

The section is rotated around the center and for each rotation angle the area beneath the border (blue line) is calculated as solid bed cross section. The altitude of the g/s-borderline is fitted to the desired filling degree (Φ), defined as the area occupied by solids divided by the whole area of the section.

Each time the solid bed is changing its basic shape (e.g. switch in contacted walls or included basic geometries), the model is adapted by selecting the needed geometrical description.

Table III - 4.18 presents, whether the geometric component is added (+) or subtracted (-) to calculate the complete cross section depending on the aimed filling degree (visualization in Figure III - 4.30). Besides that, the different walls of the section contacting the solid bed are displayed.

Six different cases have to be considered in modeling the example of three sections (DC5) and a filling degree of 0.2 while one rotation. Other filling degrees or other section numbers lead to different numbers of cases. The transition rotation angles between the cases are not shown because they are depending on the filling degree and configuration. For example, case 5 (solid bed shape identical to the bare drum, Figure III - 4.30, case No. 5) is not present at high filling degrees. Due to the filling heights, the solid bed would also contact the inner section walls in this occasion.

Table III - 4.18: Example of different cases in modeling the solid bed cross section and the phase interfaces of rotary drums with sectional internals with Geogebra® for 3 sections (EC2) and Φ=0.2 (adapted from [235])

	geometric components		involved walls		
			radial section walls		
case-no.	triangle	circular sector	circle	left	right
1	+	+	x	x	x
2	+	-		x	x
3	+	+	x	x	x
4	-	+	x		x
5	-		x		
6	-	+	x	x	x

In order to reduce calculation effort, symmetry effects are considered. There is symmetry along the vertical diameter of the drum (cases 1+3 and 4+6) for all configurations and filling degrees, also observable in Figure III - 4.30 (180° rotation of case 1/3 and case 4/6). However, the symmetry is broken by the solids passage of the vertical diameter in the upper and lower half of the drum (only triangle with contact to inner section walls or only circular outer wall is contacted, respectively). Therefore there is no symmetry along the horizontal diameter. This finally results in deviations in the periodicity and calculation of the cases.

The lengths of all interface lines are calculated for every 10° of rotation in the described manner using Geogebra for the bare drum and the investigated sectional internals (3, 4 & 6 sections). Additionally, two higher section numbers (8 and 12 respectively) have been computed. The calculations are done for three different filling degrees Φ=0.1/0.2/0.3.

Plotting the different modeled surface lines in the cross section against the angle of rotation shows a periodical oscillation of the surfaces, as presented exemplary in Figure III - 4.31.

The curve progression in Figure III - 4.31 reveals very high amplitude of the oscillation of interface lines. The s/wi and s/wo surfaces are disappearing completely in some cases, which means no contact of the solid bed to the inner or outer wall at all. This can be found in Figure III - 4.30 as well. The exemplary depicted state on the right side of Figure III - 4.31 presents one of these cases. The other way around, there are maximum values which cannot be exceeded, for example when the whole solid bed is lying on the outer wall while the section passes the lower vertical.

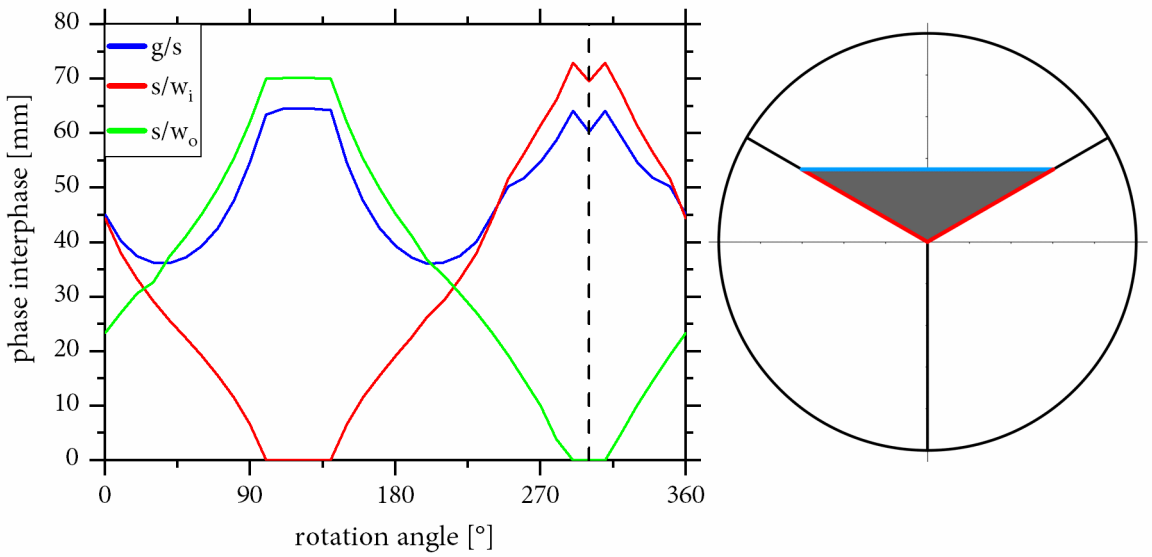

Figure III - 4.31: Left: modeled length of phase lines (one section) for each angle of rotation (DC5, Φ=0.2) with connection to example picture (dashed line); right: cross section of modeled state (adapted from [235])

4.3.1.2 Model validation

To validate the model data, the videos taken from the experiments are used and the derived pictures are compared for different angles of rotation (Figure III - 4.32).

Figure III - 4.32 shows the colored modeled surfaces in the left column for 3 sections and a filling degree of 0.2 (A1-4). These four pictures present the model rotated for 90 degrees clockwise with increasing picture number. Exemplary they visualize the change of the cross sectional shape of the solid bed. The second column (B1-4) shows shadowgraph-pictures taken from an experimental run with 3 sections (EC2) and a filling degree of 0.2 as in the model and a rotational speed of 3.8 1/min. The section positions in B1-4 are analogously to the model (A1-4). At the first glance, the shape of the solid bed cross section looks totally different to the modeled one because the model works with a horizontal surface of the solid bed. However, the solid bed will create a surface according to the angle of repose as can be seen in Figure III - 4.32, B1-4.

To prove the correctness of the model assumption, a third column of pictures is presented (C1-4). These pictures are taken from the same experimental run as the photos in B1-4. However, they are taken shortly after them, when the drum made an additional rotation around the dynamic angle of repose. Afterwards they are processed by rotating them backwards (anti clockwise) by the dynamic angle of repose, to show that the shape of the solid bed is exactly the same as in the model (A1-4).

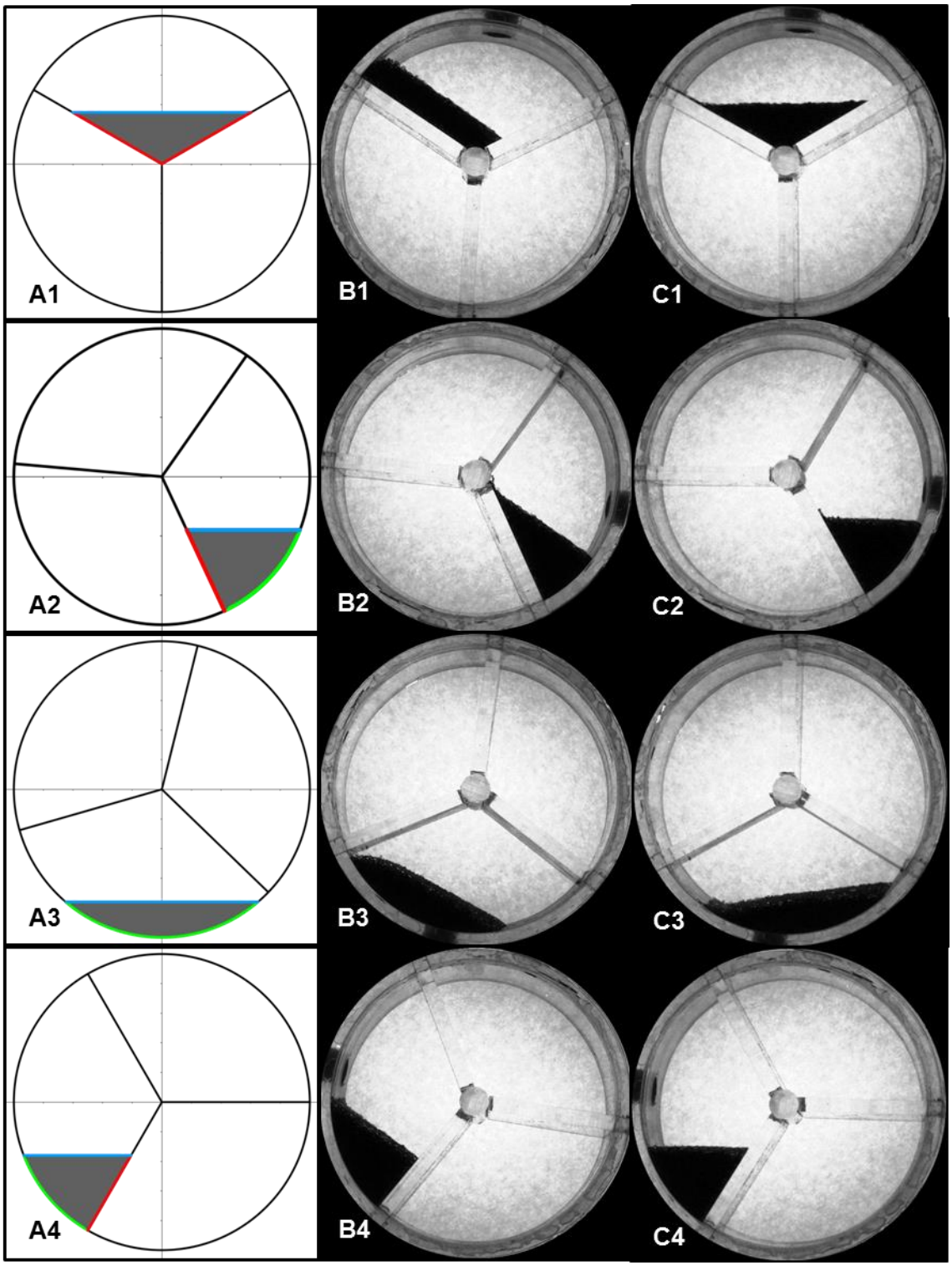

Figure III - 4.32: left: sketch of the model rotated for 90° in each picture (A1-4); middle: associated pictures from experiment (DC5, MC1; n=3.8; min-1; Φ=0.2) taken in the same rotation angle as the model pictures (B1-4); right: associated pictures from experiment as in the middle, but rotated anti clock wise for the solids angle of repose. Rotation direction left and middle pictures: clockwise (adapted from [235]).

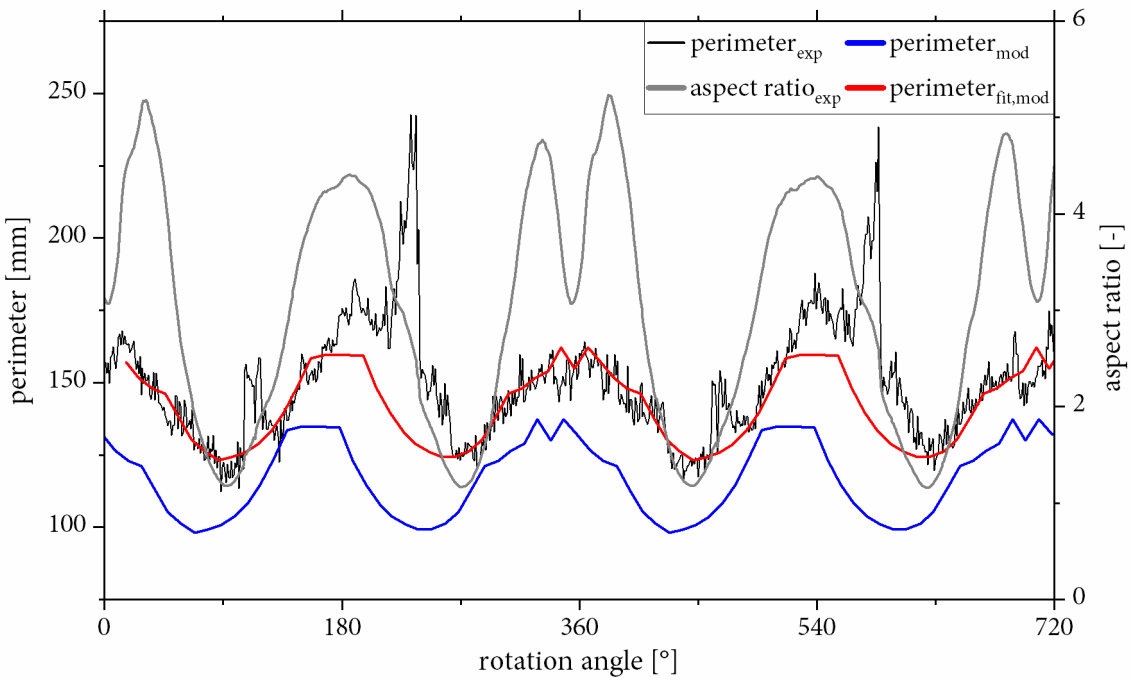

Figure III - 4.33: Diagram of solid-bed perimeter and aspect ratio from shadowgraph images (DC5; MC1; n=7.3; Φ=0.2) for 2 rotations and solid-bed perimeter from Geogebra® model (adapted from [235])

This is the proof that the model calculations are independent from the solids characteristics (angle of repose) because the surface oscillation is always phase shifted to the dynamic angle of repose. Additionally, this is shown by calculating the sum of the three surface lines g/s and s/w_i as well as s/w_o (modeled perimeter) and plotting it with the experimental perimeter (cf. Figure III - 4.23) as presented in Figure III - 4.33.

A good congruence of periodicity can be observed, but the range of values for the modeled perimeter is lower than the experimental perimeters. Furthermore, there is a deviation in the phase of periodicity. There are two reasons for the higher experimental perimeters: At first, there is a slight distortion in perspective due to the used normal, endocentric objective and the movement of the cross section in the observed area. This leads to a detection of a small amount of g/s surface in the third, axial dimension being detected as cross section in the shadowgraph picture. The second reason is the phase interface itself, which is no straight line but structured in the experiments due to the contours of the particles. The contours are evaluated as phase interface by ImageJ in the experimental procedure and therefore the perimeter increases. The shift in the oscillating phases is due to the use of a horizontal line as bulk surface in the model while in the experiment, the angle of repose can be observed as bulk surface (see Figure III - 4.32, B1-4).

With adding 25mm to all modeled perimeters and phase shifting the modeled values to the materials dynamic angle of repose, a corrected modeled perimeter is calculated and plotted in

Figure III - 4.33 (red). The corrected values are nearly congruent with the experiment. Even the decay in aspect ratio at about 360° and the connected change in shape and perimeter is represented by the model. It can also be found in the experimental perimeter. The experimental perimeter in Figure III - 4.33 shows peaks at about 110° and 220°. These peaks are created by artefacts in image analysis due to the shadow of the fill in plug (also visible in Figure III - 4.32, rows B and C).
Summarizing all these points, there is a good general congruence of model and experiment.

4.3.1.3 Derived impact on phase interfaces

In a rotary drum with sectional internals in operation all sections are filled in contrast to the model or the experimental setup, thus the overall phase interface line $PI_{sum,\varphi}$ as the sum of the phase interfaces of all N sections is calculated:

$$PI_{sum,\varphi} = \sum_{i=1}^{N} PI\left(\frac{360°}{i}\right) \tag{3.53}$$

The different phase interfaces of every section are phase shifted to the section angle which is defined by the total number of sections N. Due to the summation of the phase shifted sections the amplitudes of the periodic surface border oscillation (observable in Figure III - 4.31) are decreasing. The results for 3 sections (DC5) are shown in Figure III - 4.34.
In rotary drums without internals, the phase interfaces are not depending on the rotation angle of the drum (Figure III - 4.34, dashed lines). To describe the changes of phase interfaces in drums with sectional internals compared to the ones in the bare drum, the mean of the overall phase interface of the cross section is calculated.

$$\overline{PI} = \frac{1}{n} \cdot \sum_{i=0}^{n=360} PI_{sum,\varphi} \tag{3.54}$$

These mean values are a valid measure because of the lower oscillation as described before. All results are presented in Table III - 4.19. A fit a sine function to the data was not further investigated, since the process dependencies would consequently run in the coefficients. Due to the periodicity, the sine fluctuation is averaged in practice. Additionally, a comparison is made with the fix base value of the empty drum in the following.

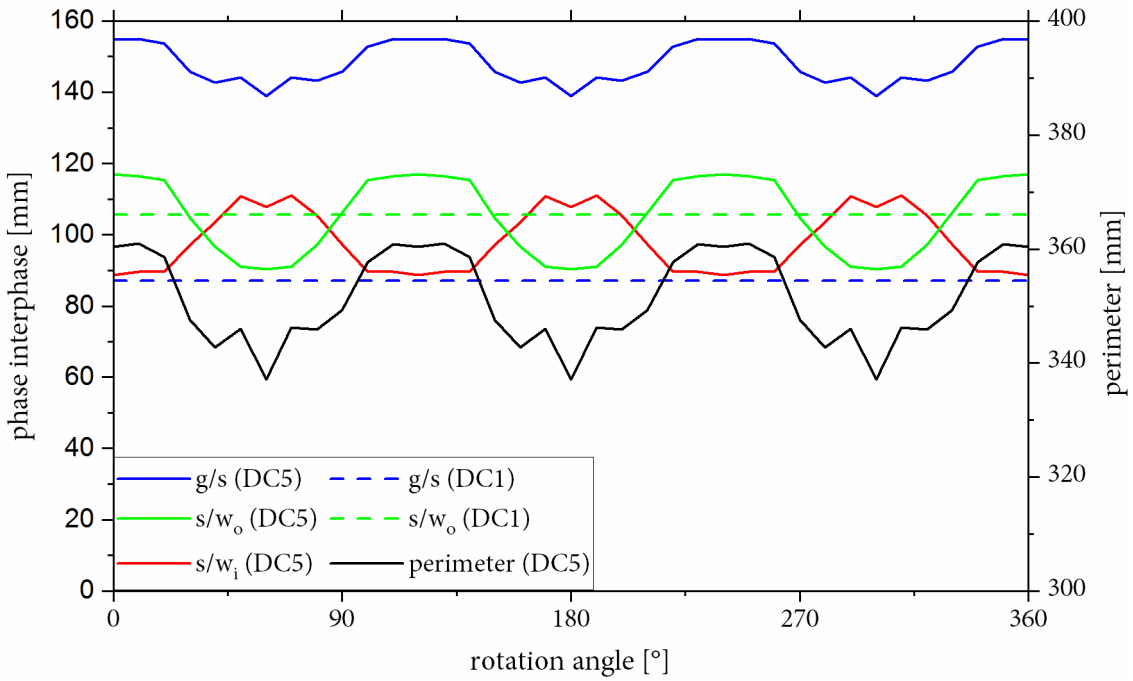

Figure III - 4.34: Modeled sum of length of phase lines (all sections) for each angle of rotation (DC5, Φ=0.2); Dashed lines show phase lines of bare drum in comparison (DC1, Φ=0.2); Modeled sum of all different interfaces is plotted as perimeter (adpated from [235]).

The relation of these mean values as best description for the phase interfaces in rotary drums with sectional internals is related to the surface borders of the bare drum in a surface-growth factor (SGF):

$$SGF = \frac{\overline{PI}(N)}{PI(bare)} \tag{3.55}$$

Using the model with different numbers of sections N and for different filling degrees, a pattern can be observed, which is shown in Figure III - 4.35 as the resulting diagram of all calculations.

Because of the missing s/wi interface in the bare drum the s/wi interface of the configurations with sectional internals is related to the s/wo interface of the bare drum.

Figure III - 4.35 shows the significant increase of the g/s phase compared to the bare drum when sectional internals are installed in general because SGF is much higher than 1. The SGF (and thus the increase in phase interface) is strongly correlating with the number of sections installed. The SGF is not rising linearly with the number of sections which are installed in general, but seems to converge to a constant value instead for 8 or more sections. In practice, section numbers higher than 12 are difficult to realize in construction anyway. Therefore, this description is assumed as satisfactory.

Table III - 4.19: Results of all modeled phase interface lengths as mean values [235]

g/s [mm]			
sections	**filling degree**		
	0.1	**0.2**	**0.3**
bare	72.8	87.1	94.7
3	122.2	148.1	160.9
4	140.8	171.8	188.2
6	161.8	207.0	230.9
8	208.1	236.2	252.5
12	217.0	274.3	311.5
s/w_o [mm]			
sections	**filling degree**		
	0.1	**0.2**	**0.3**
bare	81.5	105.6	124.5
3	80.8	105.1	123.2
4	77.9	101.0	118.4
6	79.3	106.4	121.8
8	97.5	110.0	119.3
12	91.4	114.2	130.2
s/w_i [mm]			
sections	**filling degree**		
	0.1	**0.2**	**0.3**
bare	0.0	0.0	0.0
3	73.1	98.1	118.6
4	102.9	137.9	164.7
6	147.4	198.9	241.8
8	217.2	261.1	292.6
12	276.4	382.0	468.8

In contrast to the section number, the filling degree does not lead to a further and significant gain of phase interface. There is no dependency concerning the filling degree although it leads to a higher variance of the values with increasing number of sections.

While the gas/solid-interface increase is rising with a higher number of sections, the solid/outer wall-interphase is keeping nearly constant values. Thus, there is no correlation of the number of sections and the s/wo phase interface. As already found for g/s interfaces the filling degree has no further influence on changes to the s/w_o interface. Compared to the increase in the g/s phase interface, the change in the s/w_o phase interface is therefore insignificant and can be neglected.

In Figure III - 4.35, the s/w_i phase interface SGF is calculated with the s/w_o interface of the bare drum. This is a good measure because of the independency of the s/w_o interface from the section number. As can be seen clearly, the inner wall surface is growing proportionally to the number of

sections. This can also be seen in the absolute values in Table III - 4.19. With roughly six or more sections, the surfaces of the inner wall are reaching values in the magnitude of the g/s interface.

The adapted SGF for the s/w_i surface is higher for roughly 10 or more sections. The overall heat exchange in rotary kilns is affected by the regenerative heat transfer from the walls as shown by Gorog et al. [244]. The walls heat up while passing the freeboard phase and the stored heat is transferred to the solid bed. This effect should be amplified by the inner walls and the s/w_i transfer will reach the same magnitude as the g/s transfer without heat loss through the outer wall.

Summarizing the findings that means heat loss in direct fired rotary kilns or driers due to conduction through the drum shell is not affected by sectional internals while heat flux to the solid bed can be improved significantly by higher solid-gas exchange surface and an additional surface to the inner walls. The other way around in indirect heated rotary drums sectional internals should not lead to improved process performance at all.

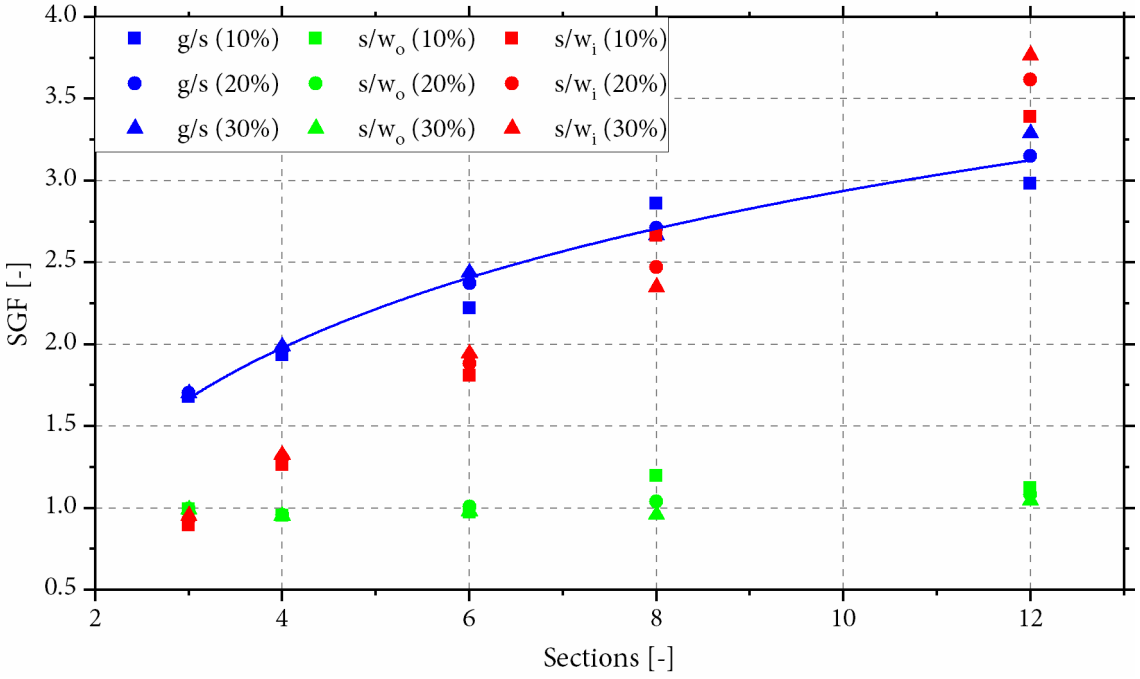

Figure III - 4.35: Values of SGF for different number of sections and different filling degrees (braced percentage) of the drum (adapted from [235])

4.3.2 Saeman-model with sectional internals

Linked to the transversal solid flow, the impact of sectional internals on the axial solid flow will be modeled in the following, since the influence could be clearly presented in the experimental investigation (chapters 4.1.1 & 4.1.2). The graphical comparison in chapter 4.1.2.6 (Figure III - 4.12) revealed that the solid bed pattern is similar to the profiles predicted by the Saeman-model (cf chapter 2.3.2). Therefore, a model approach based on the Saeman-model seems feasible and is elaborated in the following.

4.3.2.1 Modeling approach

To introduce the solid flow at the inlet end, a bare drum part is always needed. Thus, to implement the modeling, the drum is divided into two parts (see Figure III - 4.36) in axial direction.

Viewing from the outlet end, the first part of the drum (according to the calculation direction of the Saeman-model, from outlet to inlet end) is provided with sectional internals. The second part is considered as bare drum. The main issue in modeling the part with sectional internals is the fact that the height in the classic Saeman-model is valid for a circular cross section geometry, which no longer occurs when sectional internals are installed. The shape and therefore the height of the solid bed in one section is changing constantly due to the rotation of the drum, as presented in Figure III - 4.37 (cf. chapter 4.3.1 and [235]).

For a defined filling degree of a cross sectional slice at a defined axial position x_1 in the first part, the bed height is defined as $h_1(x_1)$. The bed height is dependent on the rotation angle/position of the section (c.f. Figure III - 4.37, Position I-III). Conversely, the filling degree would change while one rotation if a fixed defined height $h_1(x_1)$ (as the Saeman-Model provides) is assumed for the calculation.

According to the Saeman model, the height is defined orthogonal to the solid bed surface (see Figure III - 2.3). The bed surface is kept horizontal in modeling, since each state is repeated periodically due to rotation of the drum and the processes are only phase shifted by the dynamic repose angle (cf chapter 4.3.1.2). Thus, the height is assumed as the largest possible vertical perpendicular for the given solid bed shape (red lines, Figure III - 4.37).

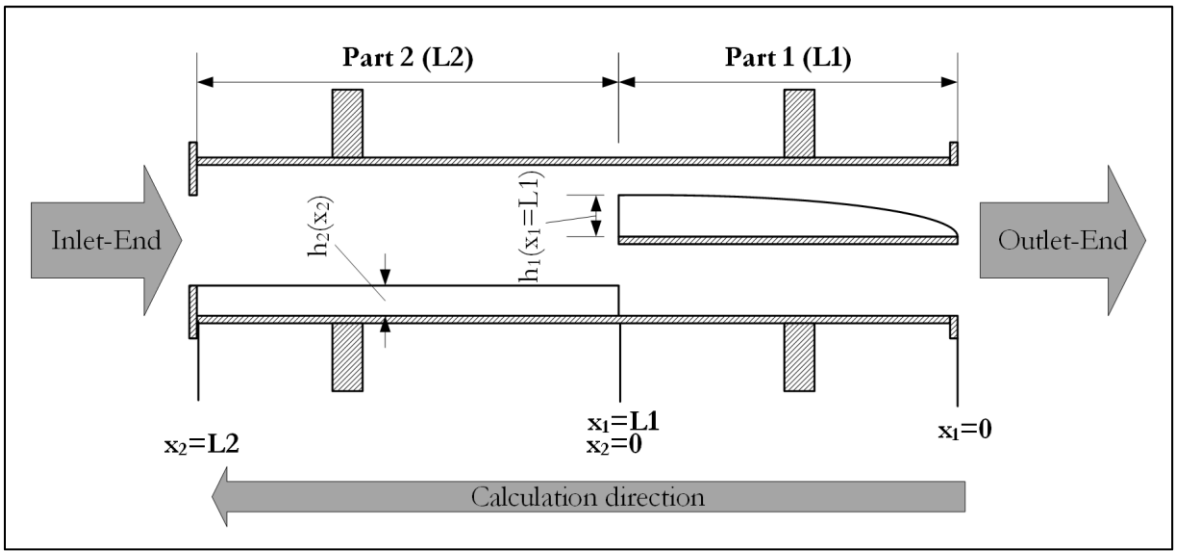

Figure III - 4.36: Sketch of basic assumptions and nomenclature in the modeling of axial solid transport with sectional internals

To model the solid bed, a suitable cross section shape or rotation position of the solid bed has to be assumed as a function of the Saeman height ($h_1(x)$). The cross section of the solid bed is therefore described as a function of the Saeman-height in part 1 $h_1(x_1)$ for different angle positions of the section (Figure III - 4.37):

$$A_{cross} = f\left(h_1(x_1)\right) \tag{3.56}$$

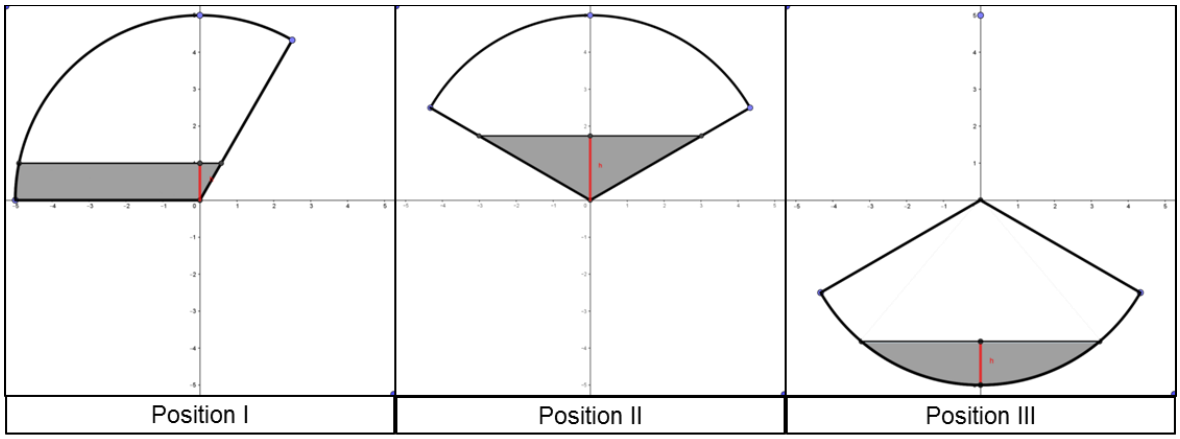

Figure III - 4.37: Exemplary sketch of the changing shape of the solid bed cross section area and thus the vertical height (h, red line) while one rotation of the drum for three exemplary positions. Calculations performed with GeoGebra. θ is constant to 0.3.

To calculate the area A_{cross} the angle of the sections γ is needed, which is defined by the number of sections N (in radians):

$$\gamma = \frac{2\pi}{N} \tag{3.57}$$

For the three tested rotation angles shown in Figure III - 4.37, the related equations to calculate the cross sectional occupancy by the solid bed (A_{cross}) are:

Position I:

$$A_{cross} = \frac{1}{2}\left[h_1^2 \cdot \tan\left(\gamma - \frac{\pi}{2}\right) + h_1^2 \cdot \tan\left(cos^{-1}\left(\frac{h_1}{r}\right)\right) + r^2 \cdot \left(\gamma - \frac{\pi}{2} - cos^{-1}\left(\frac{h_1}{r}\right)\right)\right] \tag{3.58}$$

Position II:

$$A_{cross} = h_1^2 \cdot \tan\left(\frac{\gamma}{2}\right) \tag{3.59}$$

Position III:

$$A_{cross} = \frac{r^2}{2} \cdot \left[2 \cdot \cos^{-1}\left(1 - \frac{h_1}{r}\right) - \sin\left(2\,cos^{-1}\left(1 - \frac{h_1}{r}\right)\right)\right] \tag{3.60}$$

Analogously to these 3 equations regarding 3 sections, geometric functions have been developed for the other configurations (4 sections: 4 test-equation; 6 sections: 5 test-equations).

The height of the solid bed is determined numerically in MatLab® by the Saeman ODE (equation (3.15)) using a Newton method with constant increment length. As drum length the length of the first drum part (cf. Figure III - 4.36) with sectional internals is used. The boundary condition is set to the particle diameter (100 µm). Furthermore, the parameter settings and the drum geometries from chapter 3.4.1 are used. The feed volume flow is calculated from the mass flow rate using the bulk density and corrected by the amount of back spillage. Assuming the ideal distribution of material in all section chambers, the volume flow is divided by the number of sections in the first part of the drum. The bed cross section area A_{cross} as a function of the height $h_1(x_1)$ is calculated for the different stated positions. Via numerical integration, the hold-up volume is computed for one section according to the bed height profile (Saeman) and afterwards multiplied with the number of sections to determine the total hold-up in part 1.

To calculate the second part of the drum a new boundary condition is needed. The end height ($h_1(L1)$), which results at the last calculation point in the first part of the drum is transformed into the corresponding cross sectional area.

As boundary condition for the second part of the drum (bare drum) the area equivalent value of the bed height in the bare drum is calculated. Using this condition ensures the law of mass conservation (with constant bulk density). In MatLab® this height is determined using the function "fminsearch" under variation of $h_2(x_2=0)$ to minimize the following squared difference:

$$\Delta A_{cross}^2 = \left(A_{cross}(h_2(x_2 = 0)) - N \cdot A_{cross}(h_1(L1))\right)^2 \tag{3.61}$$

The numerical calculation of $h_2(x_2=0)$ is necessary because the trigonometric expressions in area calculation cannot be rearranged to height. The starting height $h_{2,start}$ is used to continue the calculation in the second part of the drum according to the standard Saeman-procedure without internals.

The calculated hold-up results of both separate drum parts are added afterwards. The hold-up masses of the three different positions (and more with 4 or 6 sections) regarding the cross section areas in part 1 are compared to the experimental hold-up data in Figure III - 4.38.

It can be seen clearly, that the calculations with position I fit good to the experimental hold-up values. The best congruence *for all configurations and lengths of sectional internals* is reached for the similar position (a horizontal spoke with the solid bed upon it, Figure III - 4.37 - Position I). The selection of the correct model is therefore closely linked to the model validation. Further considerations are all done for the considered position.

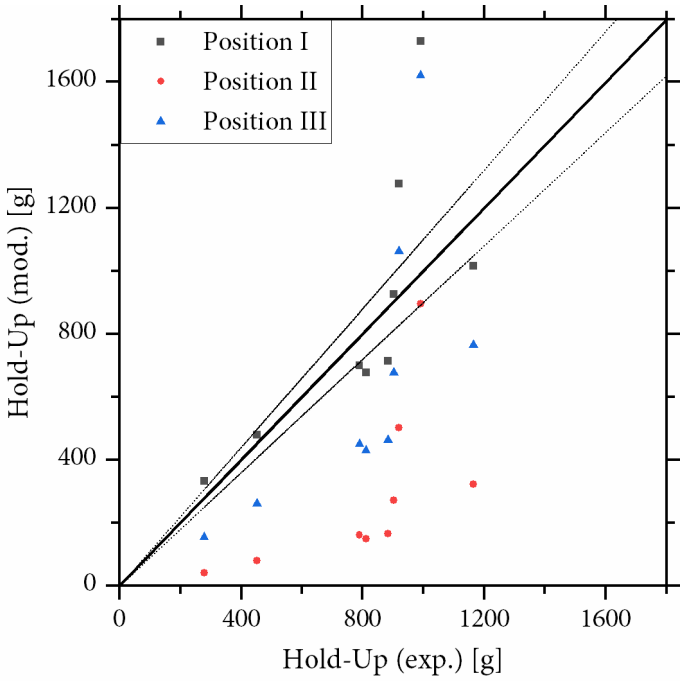

Figure III - 4.38: Diagram comparing the modeled and the experimental hold-up values for the example DC5L1 for the different analyzed section positions. Dotted lines symbolize ± 10% deviation.

4.3.2.2 Model validation

The validation of the model is performed as comparison of modeled hold-ups and experimental hold-ups (cf. chapter 4.1.2.3). The results of all experiments are presented in Figure III - 4.39. The modeled hold-up is based on calculations according to Figure III - 4.37, Position I as explained before.

Figure III - 4.39 shows 7 plots for the 7 investigated drum configurations, each diagonal indicates the ideal match, the dashed lines represent a range of ± 10% deviation from the ideal match.

Despite the bare drum diagram (DC1) all plots contain two data sets. At first, the data set “model” (black triangles) is considered. Figure III - 4.39 (a) is representing the bare drum and provides very good congruence of experimental values and the (standard) Saeman-model. The experimental methodology is therefore appropriate to fit literature models and the Saeman-model is proofed correct the other way around.

The other diagrams show the drum configurations with sectional internals from top to bottom with increasing number of sections (3, 4, 6). The left column displays the short versions (L1) the right column represents the longer versions of sectional internals (L2).

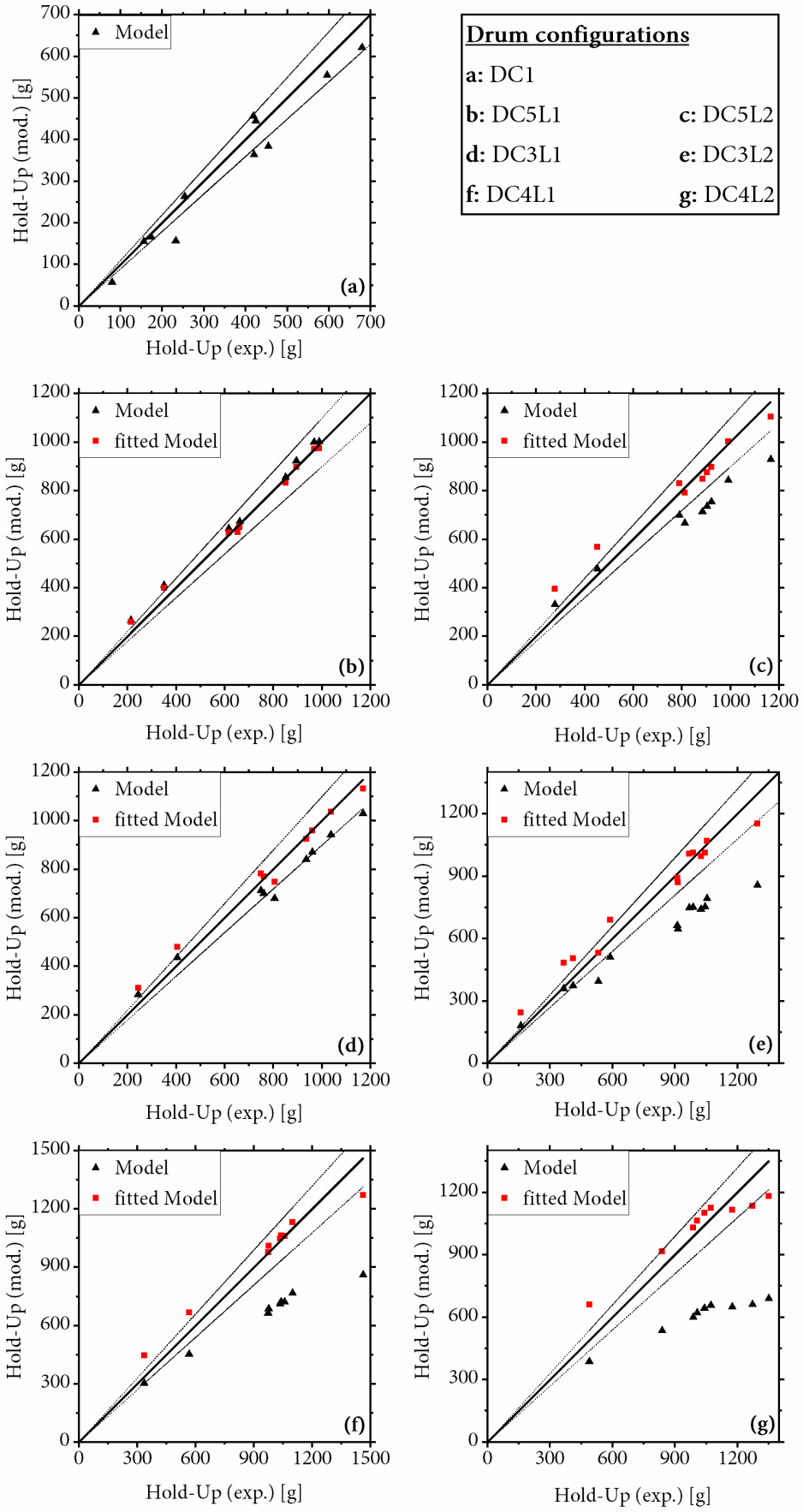

Figure III - 4.39: Diagrams comparing modeled and experimental hold-up values of all experiments for model validation. Affiliation to drum configurations for all seven diagrams in the upper right corner. Dotted lines symbolize ± 10% deviation.

The points representing the experiments with different operational parameters reveal a good correlation (straight line). This means the model is working perfectly qualitatively and no parameter is missing in the considerations. This can be seen in the regression coefficients (R^2, for model values) shown in Table III - 4.20, which are all well above 0.9.

However, it can be clearly noted that the agreement of experimental data and modeled values decreases with increasing number of sections (deviation from diagonal). The model is systematically underestimating the experimental hold-ups and the effect is increasing with higher section numbers. The slope of the imagined regression, which can be assumed as a factor in the modeling of the hold-up, needs correction. For this purpose the modeled hold-ups are multiplied with a fit-factor, which is adjusted to the experimental values via least squares method. This constant factor can be implemented in the modeling afterwards, since integration is not affected by a factor. Table III - 4.20 also shows the values of these fit factors for the described model.

Without sections (the bare drum, DC1) the factor is 1.00, corresponding to ideal congruence. Therefore, no further data set is needed for DC1 in Figure III - 4.39, as stated before. Additionally, this proves the good correlation of experimental methodology and Saeman-model providing a good mathematical model description.

Fitting all other configurations with sectional internals reveals fit factors differing from 1. The corrected modeled data (fit factors from Table III - 4.20) are also presented in Figure III - 4.39 as data sets with red squares and provide a good agreement (almost completely in the range of +/- 10% deviation) with experimental data.

It can be observed that the calculated fit factors depend on the length of sectional internals and on the number of sections installed. The trend of increasing fit-factor with increasing number of sections is the same for the short and the long internal version.

Table III - 4.20: Correlation coefficients between experimental and modeled hold-up for model validation regarding Figure III - 4.39 and fit factors to calculate the fitted model values. f(N) represents calculated values according to equation (3.62).

Sections	R^2		Fit-factor		
	L1	L2	L1	L2	f(N)
0		0.95		1.00	1.00
3	0.99	0.99	0.97	1.19	1.14
4	0.99	0.98	1.10	1.35	1.25
6	0.97	0.92	1.47	1.71	1.56

Therefore, the following function is developed, providing a good agreement with the fit factors determined from the comparison with the experimental values:

$$f(N) = 1 + \left(\frac{N}{8}\right)^2 \tag{3.62}$$

The fit factors estimated by this equation are also listed in Table III - 4.20 (right column). The progresses of the experimental fit factors as well as the factors estimated according to equation (3.62) are presented in Figure III - 4.40.

Possible reasons for the deviation of model and experimental values are the chosen assumptions in the calculation of the cross sectional area in part 1 of the drum. The calculated height values are not necessarily corresponding to the mean value of all rotation angles. This error is increasing with higher section numbers, which is a hint for the increasing fit factors depending on the section number.

In addition, the model does not take into account the negative slope of the solid bed in the transition region (between part 1 and part 2, cf. Figure III - 4.12. This effect is also accumulating with the section number.

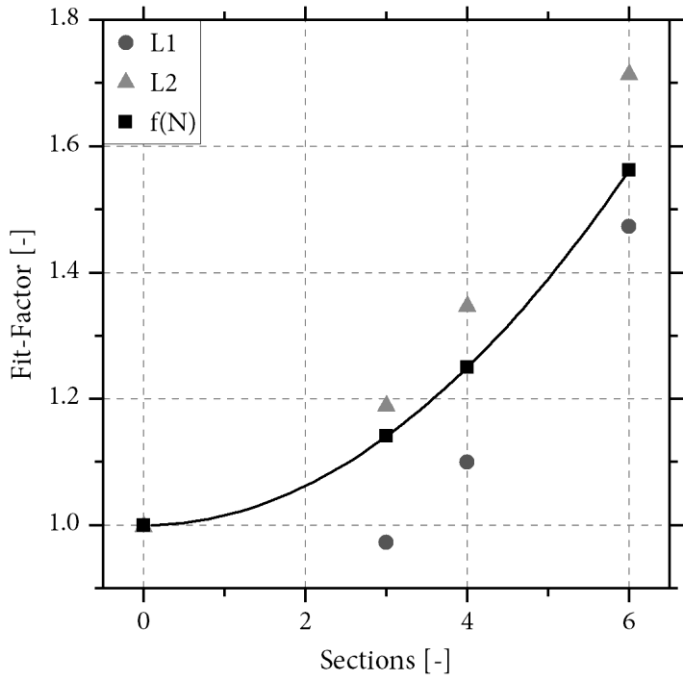

Figure III - 4.40: Diagram of the fit-factors depending on the number of sections. Visualization of data from Table III - 4.20 and equation (3.62).

4.3.3 Axially segmented lifters

A mathematical modelling (as already published in [237]) of the solid bed and the behavior of the single lifters is presented in the following to substantiate the experimental findings. It serves to generate a deeper understanding and to derive rules for dimensioning in practice.

4.3.3.1 Modeling approach

The model calculations are done for rectangular flights, since these are used in the experimental part of this study. An adaption is necessary for different flight designs. The sketch in Figure III - 4.41 serves as a basic description of the modelling approach.

All dimensions used and their nomenclature are shown in the sketch. L_L describes the axial length of the lifter as central component. The radial dimension of the flight is described with h_{Lr} (first element of the flight), the height of the overflow weir arranged orthogonally to the radial component (second flight element) is named h_L.

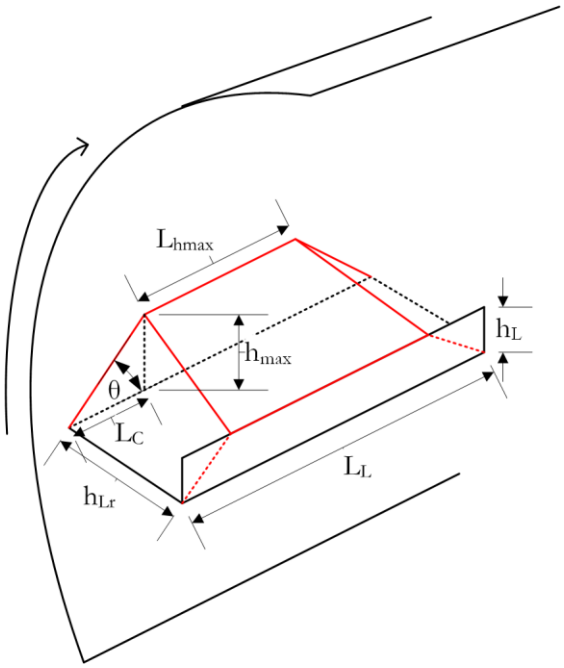

Figure III - 4.41: Sketch of the basic assumptions and values/dimensions included in the modelling calculations of the flights hold-up (adapted from [237]).

Furthermore, the modelling includes the following assumptions:

- The calculations are performed for the 9 o'clock position, where the radial part or bottom of the lifter is horizontal.
- The axial inclination (β) of the drum is neglected, as it is small compared to the angle of repose (θ). In the 9 o'clock position, the bottom of the lifter is therefore horizontal in the axial and radial dimensions.
- The dynamic angle of repose (θ) is assumed to occur in both directions (axial and radial), when the lifter emerges the solid bed and rises above it.
- For modelling purposes, the inner wall of the drum is assumed to be a flat plane in the region of the bed and the curvature is neglected. This assumption even fits better with increasing drum diameter for scale-up considerations.

The sketch in Figure III - 4.41 additionally shows the outline edges of the assumed bulk material filling (red lines) as it is formed for a finite axial length of the lifter. The maximum height h_{max} (orthogonal to the lifter bottom) created by the solid bed is always located at the outer wall. It is calculated with the help of geometric relations of the lifter in combination with the dynamic angle of repose:

$$h_{max} = h_L + d_P + h_{Lr} \cdot tan(\theta) \tag{3.63}$$

The axial length from the beginning of the lifter until h_{max} is reached on the drum wall is called L_C (cf. Figure III - 4.41). The calculation of L_C is performed with:

$$L_C = \frac{h_{max}}{\tan(\theta)} \tag{3.64}$$

The axial length at which h_{max} is reached and consequently the lifter is loaded to the theoretical maximum is denoted by L_{hmax}. Concluding, the following relationship can be established for all stated axial lengths:

$$L_L = L_{hmax} + 2 \cdot L_c \tag{3.65}$$

Consequently, the maximum height h_{max} (and thus a part of the lifter with optimum loading) is only achieved if the axial length of the lifter corresponds to at least 2*L_C. Otherwise, the lifter will not be filled to the capacity assumed in many models and considerations of the rotary drum cross-section (see introduction). Results for L_C as a function of different angles of repose and different geometries are exemplary presented in Figure III - 4.42.

L_C is strongly dependent on the material characteristics (angle of repose), which is plausible. Next to this, it is clearly observable that L_C depends on the geometric dimensions of the rectangular flight, namely the radial dimension (h_{Lr}) and the dimension of the orthogonal overflow dam (h_L). In addition to the ratio of the lengths of both lifter elements, the absolute dimensions are also decisive (cf. 10-5 and 20-10 in Figure III - 4.42). In any case, L_C is significantly larger than the dimensions of the two cross sectional lifter elements h_L and h_{Lr}.

Going back to the implications from equation (3.65), it can be derived that even if the maximum height h_{max} is reached, the optimum filling of the lifters is not achieved over the entire axial length. L_{hmax} should consequently occupy a large fraction of the lifter length L_L. This is equivalent to an overall axially longer lifter segment.

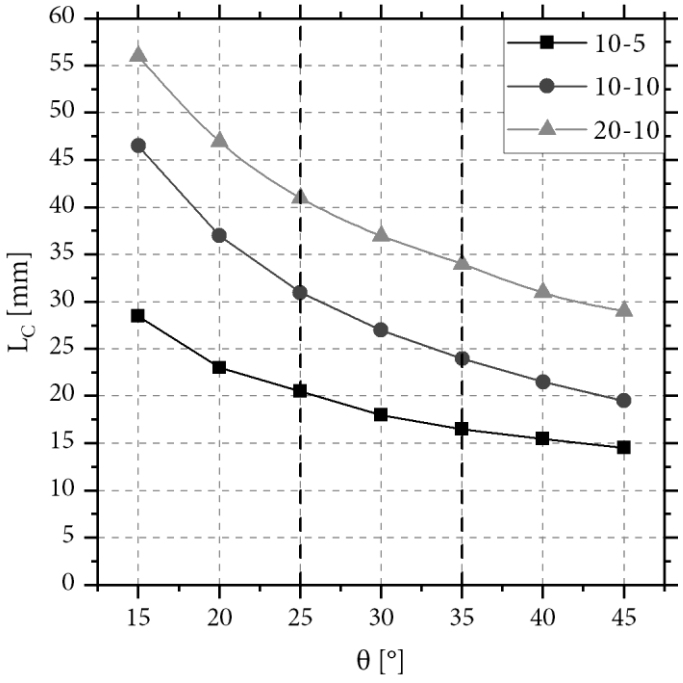

Figure III - 4.42: Length of the chord (L_C) dependent on the dynamic repose angle of solid material for different flight designs (legend meaning: h_{Lr}-h_L in mm). Adapted from [237].

In order to estimate the lifter performance, the hold-up volume of rectangular flights is calculated numerically according to Figure III - 4.41. The calculation is based on the symmetrical filling profile in the axial direction, due to the assumptions in modelling explained earlier. Thus, only one half of the lifter is calculated in the axial direction. For the numerical calculation purposes, the axial and radial direction of the lifter base is each divided into 100 equidistant sections. A height profile is calculated as a function of both directions (h_{hLr}, L_L), using the dynamic angle of repose. This profile is numerically integrated afterwards via summation to gain the hold-up volume (V_{hold}):

$$\frac{V_{hold}}{2} = \sum_{0}^{h_{Lr}} \sum_{0}^{\frac{L_L}{2}} h(h_{Lr}, L_L) \Delta L_L \Delta h_{Lr} \tag{3.66}$$

The calculation is carried out exemplarily for different angles of repose and for different geometries of the lifters. The determined hold-up volume is compared to a theoretical filling volume (V_∞) afterwards and subsequently used for the calculation of a filling ratio (used filling, UF). UF represents an axial efficiency factor regarding the filling of the lifters. The theoretical filling volume (V_∞) assumes the lifters as "infinitely" long in axial direction (without discharge in axial direction). UF is calculated as a ratio according to the following equation:

$$UF = \frac{V_{hold}}{V_\infty} \tag{3.67}$$

With UF, the calculations and models developed by many authors regarding the loading of lifters in the cross sectional view can be extended to include the effects of axial lifter length. It thus serves as a connection between cross sectional and axial lifter design. The results of exemplary calculations are presented in Figure III - 4.43.

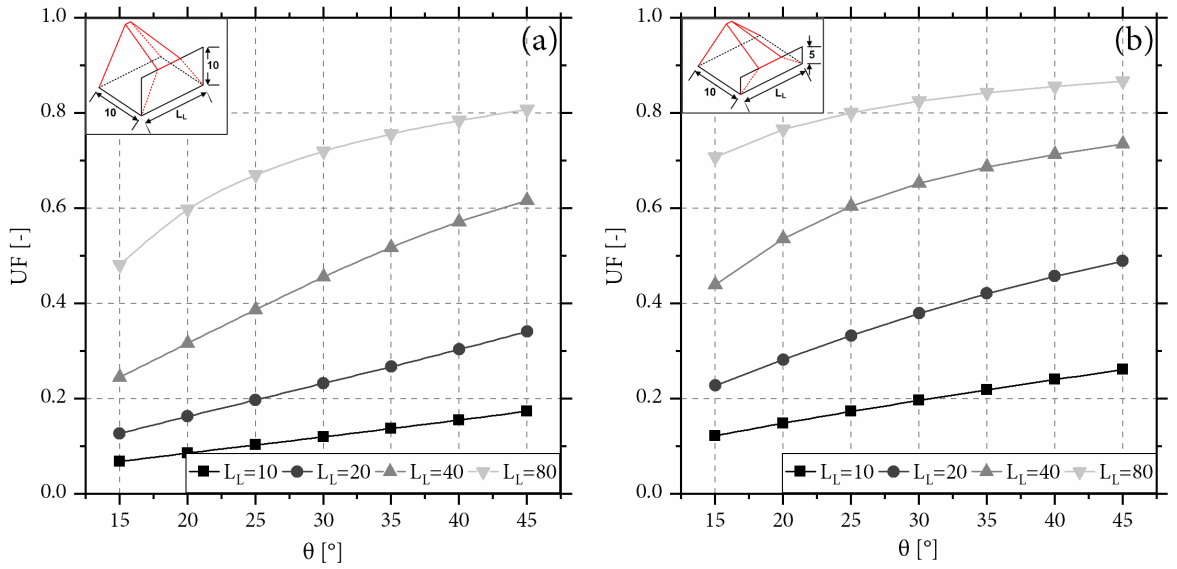

Figure III - 4.43: Used filling (UF) dependent on the dynamic angle of repose of material and the different designs of flights; a: h_{Lr}=10mm, h_L=10mm; b: h_{Lr}=10mm, h_L=5mm (adapted from [237]).

It can be seen very clearly that the actually utilized lifter's degree of filling (UF) depends significantly on the axial length. If all dimensions of the rectangular lifters are equal (Figure III - 4.43 a, black squares), the degree of utilization is only about 10% of the theoretically possible capacity. Material not lifted up does not participate in the advanced heat exchange with the gas-phase, as the major advantage of lifters (stated in the introduction). Consequently, the axial length L_L of the lifters should significantly exceed the length L_C in order to obtain reasonable utilization rates, when the lifters have open front ends. To the author's knowledge, this is the first time this axial effect is quantified (as already published in [237]). Therefore, from these findings the recommendation of $\mathbf{L_L > 5*h_{Lr}}$ for the lifter design in industrial practice is derived as a "rule of thumb". With this minimum axial length, reasonable filling degrees or UF-values of above 50% can be achieved for the lifters, assuming a mean angle of repose of 30°. Although the calculations were performed with rectangular lifters and exemplary dimensions, the general trend is transferable to other lifter types and shapes, as can also be seen in the cross sectional investigations in chapter 4.2.2.

4.3.3.2 Model validation

The calculations are indirectly validated by plausibility checks with the experimental data of this study. The LL-configuration (chapter 4.1.3) corresponds to the case of theoretically "infinitely long" lifters, which is contrasted with the SL-configuration with individual lifters of finite length. The dynamic angle of repose of the bulk material used in the experiments is about 30°. The dimensions

of the short lifters applied are h_{Lr}=10mm, h_L=5.5mm and L_L=10mm. In Figure III - 4.43 b, this geometry corresponds to the progression of the black squares and thus an UF-value of approx. 20% can be determined.

This value must be compared with the measured hold-ups. The evaluation of data in Table III - 4.12 reveals a mean hold-up increase factor of 1.47 for the L_L-configuration, while for the SL-configuration there is even a slight decrease in relation to the bare drum. This first of all confirms the trend of smaller axial lifter lengths influencing the hold-up negatively. The MRT-results in Table III - 4.12 also suggest this trend with mean increase factors of 1.06 for SL- and 1.75 for LL-configurations. A comparison of both factors reveals that the SL increment is only about 8.4% of the LL increment. This is in the order of magnitude of the UF value for this geometry, considering that mean values from measurements with experimental errors are used. However, the effects are additionally evoked by the superimposed "pseudo-backflow", as explained earlier. Thus a direct comparison of these values with the modelling is not possible. But combining the above considerations with the qualitative observation from the experimental part, a reasonable congruence is obtained with axial transport investigations and the modelling is plausible.

Besides the stated experimental data from chapter 4.1.3, the transversal investigations (chapter 4.2.2) can be used for validation. Comparing the L_{cont} and the L_{10mm} version of the L-type lifters, which are equal to the LL and SL-configuration in axial transport, reveals similar data. The DOE-means of mf_{OA} (occupied cross sectional area) lead to a used filling of roughly 25% (3.4/13.3) for the L_{10mm} version, which is nearly in perfect congruence to the calculated 20% from the model. This is a strong evidence for the validity of the model. Furhtermore, the data in chapter 4.2.2 shows the independence of the assumptions regarding the flight-type.

4.3.3.3 Effect of front side walls

In the modelling chapter, a rule of thumb was derived for dimensioning the axial length of lifters. In addition to this option of increasing the performance via the lifter length, there is the possibility of installing walls at the two facing ends of the lifter shovel or using dams, directly fixed to the lifters as an axial overflow weir. This option of construction also increases the mechanical stability of the lifters with regard to the occurring tilting moment when lifting up the solids due to the additional orthogonal reinforcement. In the case of dams, these could additionally be utilized as dams/overflow weirs through intelligent dimensioning.

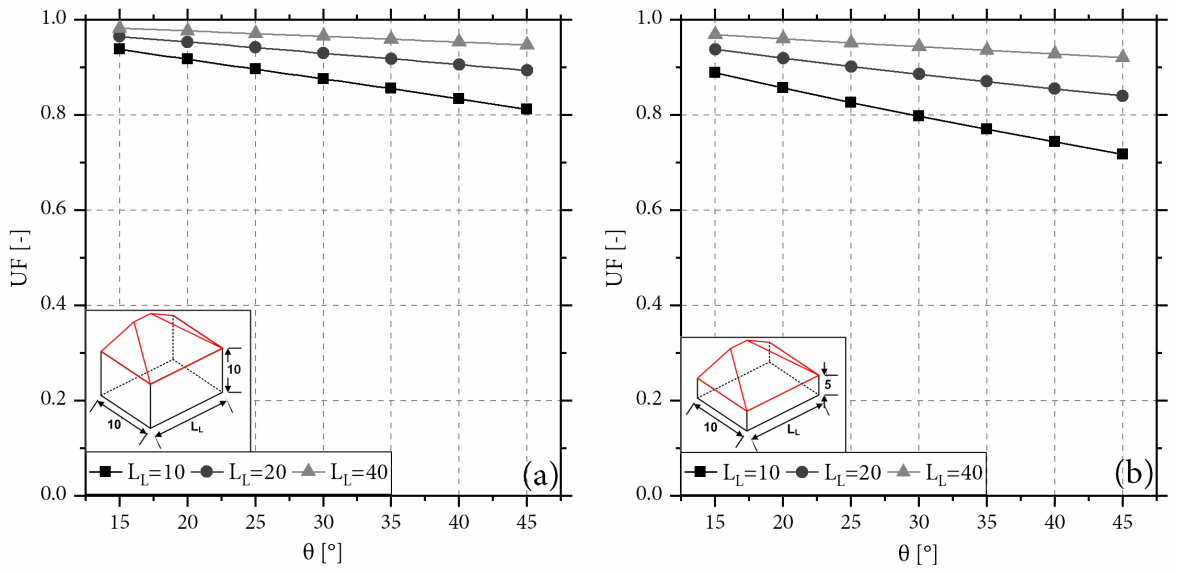

Figure III - 4.44: Used filling (UF) with front side walls dependent on the dynamic angle of repose of material and the different designs of flights; Side wall heights equal to hL; a: h_{Lr}=10mm, h_L=10mm; b: h_{Lr}=10mm, h_L=5mm (adapted from [237]).

For initial calculations, walls at the axially facing ends of the lifters are considered. The height of these walls is set equal to the height h_L of the second lifter element (the radial overflow weir). The exemplary results from these calculations are shown in Figure III - 4.44.

The situation is clearly different from the analogous calculations without front side walls (cf. Figure III - 4.43). The magnitude of UF is well above 80% in almost all cases. The influence of the axial lifter length L_L becomes almost negligible. In addition, the dependency on the bulk material properties (dynamic angle of repose) reverses. Large dynamic angles of repose now have a rather negative effect on the efficiency UF. However, the overall dependence from dynamic angles of repose (cf. slopes in Figure III - 4.44) is much smaller and almost negligible compared to axially open lifters.

Summarizing, the side walls represent an attractive alternative to higher lengths of the flights in enhancing the lifter performance for non-continuous lifters.

The calculations can be validated with the experimental data from chapter 4.2.2 considering the $L_{10mm,closed}$ version. The DOE means of measured mf_{OA} are even higher than the ones for the continious version. The reason is the doubling of lifters from the cross sectional view due to construction (angular shift of the single lifters). Therefore a strict comparability is not given, but the very positive impact of front side walls can be clearly seen in the experimental investigations as well.

5 Interim conclusion & Outlook

The analysis of solids transport in rotary kilns is the core part of this thesis. In the progress of the work, a new apparatus was developed which enables the above-mentioned analyses using optical and non invasive methods. This was mainly enabled by the transparent construction in PMMA. The development of the apparatus was focused on maximum flexibility with regard to dimensions and internals. Thus, transverse and axial solid transport can be analyzed with the apparatus both. In addition, the apparatus is capable of applying gas flows (countercurrent) and the related impact can be analyzed.

The applied experimental methods refer to a model solids system chosen and designed with focus on maximum recycling. The summarized results are presented below separately with regard to the internals.

5.1 Sectional internals

To the author's knowledge, the examinations regarding sectional internals (axial and transversal flow) are the first systematic investigations on this internal type. The analysis focuses on the number of sections and the length of the sectional internals. The following key findings regarding the effects of sectional internals can be summarized regarding the axial flow:

- In general, sectional internals have a significant impact on the axial solids transport in rotary drums.
- The dependencies regarding the process behavior are similar to bare drums concerning operational parameters as drum inclination, rotary speed and feed mass flow. However, the absolute values for MRT etc. and the differences of these values are larger with sectional internals resulting in a higher sensitivity of the system.
- The MRT as well as the rotary drum hold-up are increasing with the number of sections and for constant section numbers with their lengths up to a factor of 4 (for MRT). A model approach based on increase factors to describe this behavior has been provided (chapter 4.1.2.1).
- The capacity of the drum regarding mass flow decreases antiproportionally to the number of sectional internals and their lengths.
- If the capacity limit is reached, any further increase of the feed mass flow leads to an increase of back spillage and therefore reduces the effective mass flow passing the drum.

- The impact of sectional internals on the axial dispersion coefficient (D_{ax}) and therefore on axial mixing is negligible. A slight trend towards lower dispersion coefficients is observable. Values for D_{ax} are in the range of 10^{-4} to 10^{-7} m^2/s.
- The bed height profile proposed by the Saeman-model can be observed from the side, even when sectional internals are installed.

The findings on the process behavior of rotary drums with sectional internals can be used as a major step and improvement in process optimization and design of industrial rotary drums. The knowledge of increased sensitivity provides the use of sectional internals for the production of high tech materials, such as e.g. pigments or catalysts. These products need very precise adjustment in the production processes. In contrast to that, the decreasing capacity limits due to the found back-spillage have to be considered in designing rotary drums/ kilns with sectional internals.

Besides the axial flow, transversal flow investigations have been performed with the following main outcomes regarding mixing behavior and impact on exchange surfaces:

- The solid motion in the cross section with sectional internals is completely different from the bare drum. The solid bed shape depends on the angle of rotation and is not constant.
- Sectional internals are affecting the mixing kinetics and lead to higher specific mixing rates especially at lower rotational speeds and filling degrees.
- The behavior of particle systems with uniform particle size differs significantly from particle systems with a wider particle size distribution, which are more common in real industrial processes.
- Using bulk materials with a uniform particle size distribution, the sectional internals lead to slightly lower mixing indices compared to the bare drum.
- In segregating particle systems with different particle sizes, sectional internals lead to higher goodness of mixing compared to the bare drum.

The findings of this work can be utilized to improve the dimensioning of rotary drums with sectional internals or lead to a more (energy-) efficient operation of rotary drums or kilns. Furthermore, the impact of refurbishments of kilns with sectional internals can be estimated.

5.2 Lifters

Next to sectional internals also flighted rotary drums have been investigated regarding axial and transversal flow. The focus was on finding the impact of axial lifter length, since lifters in industrial flighted rotary drums are often designed non-continuously and thus the parameter was estimated

to have a high practical relevance. To the author's knowledge, this is the first time that the axial lifter length has been systematically analyzed. The findings and derived considerations for the axial flow are summarized to:

- The axial length of lifters has a massive influence on the solids transport and the process effect of the chosen lifters.
- The MRT is significantly increased compared to bare drums with long, continuous lifters, while short lifters have hardly any influence on the MRT, all other dimensions of the lifters being equal. Mathematical calculation approaches from literature were proved and modified.
- The axial dispersion coefficients are significantly larger for short lifters compared to the bare drum and to continuous lifters. Long lifters generate significantly smaller dispersion coefficients than in the bare drum. This can be explained by the "disturbance" of the cascading layer, which is normally responsible for axial mixing due to the internals. Literature calculations for estimating D_{ax} have been proved and modified for short lifters.
- By dropping solid material in the axial direction against the material flow, short lifters create a superimposed "pseudo-back-spillage" in the drum. Evidence for this approach is delivered by increased back-spillage at lower hold-ups and MRTs on the other hand. Moreover, the effect is undermined by the higher axial dispersion coefficients measured for short lifters.
- The solid density in the cross sectional airborne phase, which is necessary for heat exchange processes, is significantly worse for short lifters than for long lifters.
- As practical recommendation the axial length of lifters should not be less than a minimum length of 5 times the radial elongation without end walls.
- End walls have a major influence on the efficiency of short lifters and at the same time offer design advantages (reinforcement to prevent tangential side load).
- The pseudo backflow could be prevented or reduced if an overflow weir is installed on the lifter element in the inlet direction or an existing one is raised.

It can be clearly stated that it is very important to incorporate the axial length parameter in design and operation calculations for rotary drums with lifters. Besides the axial flow, impressive impact could also be found in the transversal investigation:

- For the investigated system, L-type lifters provided better results compared to EAD or EHD lifters.

- The cross sectional occupance of the gas phase with solids is affected massively by the axial lifter length. The axial length effect makes differences in the flight types negliglible.
- The shorter the lifter in axial direction, the worse is the cross sectional solid distribution in the gas phase.
- The installation of front side walls to axially segmented lifters massively improves the performance (compared to continious lifters).

The results regarding the cross sectional investigations are furthermore complementing the axial flow results qualitatively. The findings have been used to derive modeling considerations.

5.3 Modeling approaches

From the magnitude of experimental results, modeling approaches have been derived for the different internals. Regarding sectional internals the focus was on the calculation and quantification of the impact of the internals (section numbers and filling degrees) on the phase interfaces. The solid bed has been modeled with Geogebra® with a subsequent validation on experimental results.

The summarized results are:

- No linear but a logarithmic increase of the g/s-phase interface with the number of sections N was found.
- In contrast to the g/s-interface, the s/w_o interface stays roughly constant and the deviation from linearity is almost negligible in comparison.
- The s/w_i interface is increasing linearly with the number of sections.
- A novel surface growth factor (SGF) is proposed, which seems to reach a constant level asymptotically with a higher number of sections (8–12) for the g/s-phase interface.

Besides the transversal impact of sectional lifters, a calculation approach utilizing the widely known Saeman-model has been developed and applied in the modeling of the axial flow. The validation with experimental data (hold-ups) showed good congruence after the introduction of a fit factor, which again could be modeled with a simple function. Thus, the adapted model is capable of describing the axial solid flow. Summarizing, an extensive and full mathematical description of rotary drums with sectional internals is provided regarding the solid flow.

Regarding lifters from the experimental observation a geometric modeling approach was applied to calculate the impact of the axial lifter length for L-type lifters. The main outcomes from the calculations are (in congruence with experimental transversal flow findings for lifters):

- The validation with experimental data (axial flow and transversal flow) showed good agreement with the rather simple geometric model.
- The utilization of axially segmented lifters compared to continuous lifters (UF) is worse.
- The "rule of thumb" recommendation of $\mathbf{L_L > 5*h_{Lr}}$ for the lifter design regarding axial length in industrial practice is derived.
- The installation of front side walls is a good alternative to increase the performance of axially segmented lifters massively.

The intention in using a kind of efficiency factor (used filling, UF) in the modeling should enable the combination with existing modeling approaches regarding the transversal flow.

5.4 Outlook & further investigations

First of all, in additional elaborations the capabilities of the explained apparatus regarding furhter drum dimensions should be used to perform scaling considerations. In addition to the dimensions, the applied DOEs should be extended to explore further limits and to enable the application of non linear regression methods to the experimental data.

The presented apparatus and the experimental methods can be used and adapted to apply further methods. In first experiments, the material of transversal flow investigations with the bare drum has been used to apply particle image velocimetry (PIV). The integrated tool in ImageJ was used to calculate the velocity fields in the transversal granular flow. The results are plotted as vector plot in Figure III - 5.1. Although no calibration was performed and the velocity in the laminar wall addicted region is higher, the typically flow patterns of rolling motion can be observed clearly. This coincidental finding should be elaborated to enlarge the knowledge gained from this work. Further adjustments of the experimental procedure and data evaluation should lead to qualitatively better results.

The capability of the apparatus to apply gas flows (see description in chapter 3.1.2) should be used to analyze the impact of gas flows on the solid flow and rotary drum process behavior. In first experiments orienting analyses regarding the quantification of dust entrainment induced by the gas flow have been performed. Promising results were obtained, which show that the impact of process and operating parameters is measurable. Internals to affect the gas streams ("swirl generators") have been constructed (see Figure III - 5.2), that should be deeper analyzed regarding their impact in next steps.

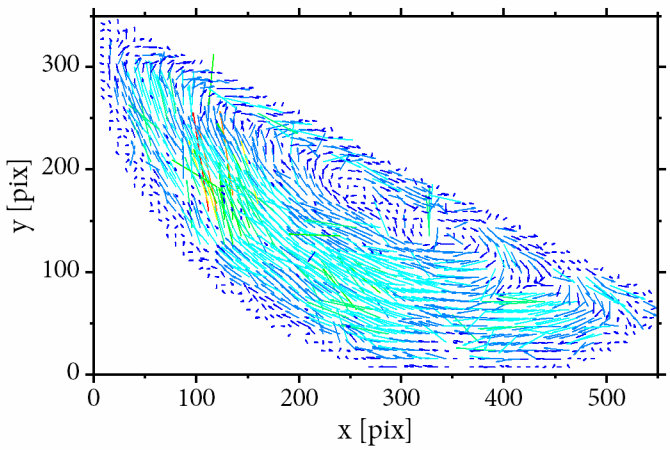

Figure III - 5.1: Vector plot of an exemplary PIV-analysis of video material from the transversal investigations with bare drums in this work.

The optical accessibility of the drum can be used to investigate the gas-stream in axial direction via PIV-measurements from the side of the drum. As shown exemplaryly in Figure III - 4.12, the solid bed profile can be observed from the side, which should be further analyzed quantitatively using ImageJ. First routines have been developed, which can be elaborated and extended.

Besides extending the experimental analyses, rigorous simulation approaches can be elaborated and applied. Simulations with DEM methods are frequently used in the investigation of solid transport processes and solid process equipment such as rotary drums. Furthermore, CFD simulation, e.g. with Fluent or OpenFOAM, is apparently also possible as Dissanayake et al. were able to show for the transverse flow in rotary drums [143]. The already existing experience with CFD modeling with OpenFOAM in the working group (in the field of stirring [245,246]) could be applied here.

Finally, parts of the results in solid flow investigations will be used in the progress of this work in the development of a full rotary kiln model.

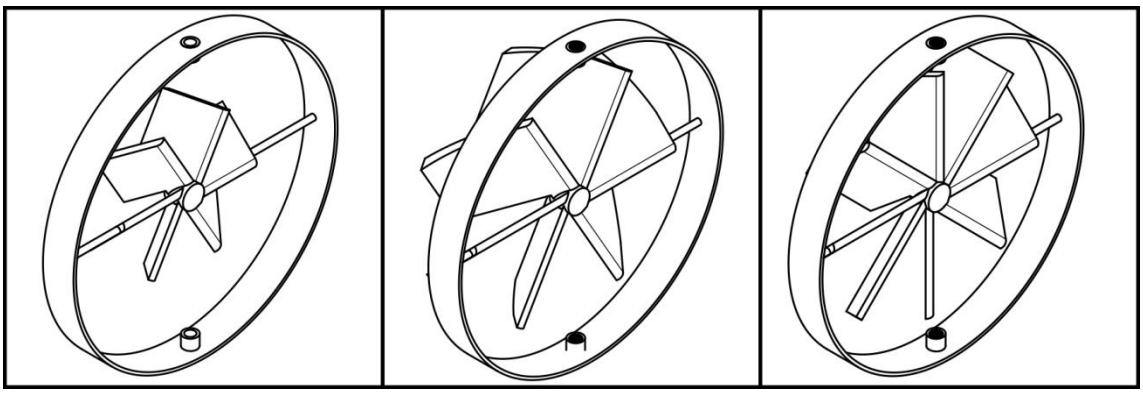

Figure III - 5.2: Exemplary representations of construced "swirl generators" with different blade numbers and blade sizes to affect the gas stream in the rotary drum.

Part IV Heat transport in rotary drums

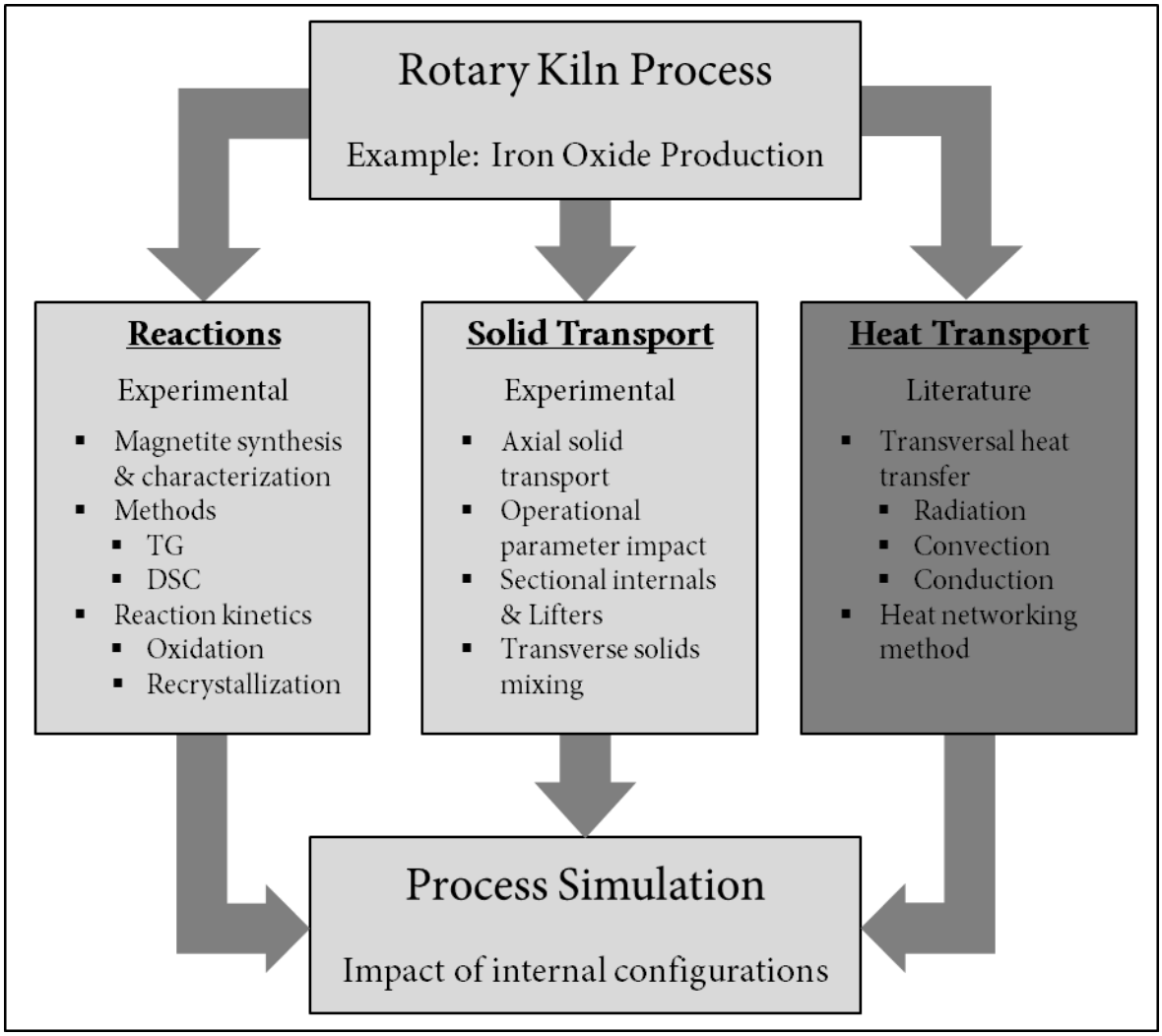

1 Introduction

In this part the heat transport processes occuring in rotary kilns are described. Since this topic has been investigated intensively by many authors, no additional experimental work is performed. In order to prepare for the final modeling of a rotary kiln process, the results and derived models of interest for this specific topic are adapted from literature. The literature provides studies of experimental investigations of heat transport processes in rotary drums and kilns. Furthermore, the modeling of the heat transport processes is provided with different investigations in literature. In this work the description is done with the derived model approaches published by different authors.

Basically, the heat transport processes in rotary kilns and their modeling is found on the general heat transport processes convection, conduction and radiation. The processes are considered as basic knowledge and only a brief introduction will be given. The specific derivation will not be provided, since the focus is on the application to rotary kilns.

Furthermore, as already explained in the overall introduction, the basic assumption is the cross section modeling. Thus, the transport processes are considered in the cross section of the rotary kiln, to prepare the final modeling in the last part of this thesis. In this work only steady state processes are considered, thus instationary descriptions are omitted.

2 Basic heat transport mechanisms

Heat transport is a basic transport process of (thermal) energy and similar to mass and impulse transport in its description. Every transport process can be reduced to the three fundamental processes *conduction, convection* and transfer. In addition, in the case of heat transport, the *radiation* mechanism is also important, especially at high temperatures [137]. In the following the basic mechanisms are introduced shortly.

2.1 Conduction

The transport of heat between neighboring molecules forming a substance, for example a wall is called conduction. Depending on the local temperature difference, the molecules collide with each other and transfer the heat within the material. If the material is a metal, the free electrons also transfer energy [247]. The following equation describes the heat flux orthogonally to a defined area (A) transferred via heat conduction (Fourier's law) [137,247]:

$$\dot{Q}_{cond} = -\lambda \cdot A \cdot \frac{\Delta T}{d} \tag{4.1}$$

The thermal conductivity (λ), the temperature difference (ΔT) and the distance or layer thickness (d) between the temperature potentials define the power transferred by the heat flux.
If the area is not a plane, e.g. a hollow cylinder or pipe and the area (A) is a function of the radius, the equation has to be transformed. With the axial length L, the circumference of the tube becomes an area. The integration according to r assuming a constant thermal conductivity yields the heat flux transferred by thermal conduction in a cylinder [247]:

$$\dot{Q}_{cond} = \lambda \cdot \frac{2\pi L}{\ln\left(\frac{r_2}{r_1}\right)} \cdot \Delta T \tag{4.2}$$

2.2 Convective heat transfer

In general, convection describes the heat transport in a flowing fluid due to the heat transported by the material itself. During heat transfer between a fluid and a solid wall, enthalpy transport from fluid to wall occurs due to flow of the fluid, which is called convective heat transfer. The magnitude of the transferred heat flux is defined by the heat transfer coefficient (α), the transfer area (A) and the temperature difference (ΔT) [247]:

$$\dot{Q}_{conv} = \alpha \cdot A \cdot \Delta T \tag{4.3}$$

To calculate the heat transfer coefficient, the (temperature dependent) characteristics of the fluid, flow parameters and the geometry of the wall are prerequisites [247]. Therefore, to calculate α, the principle of similarity is used. The dimensionless Nußelt number (Nu) is considered as a dimensionless heat transfer coefficient with [137,247]:

$$Nu = \frac{\alpha \cdot l}{\lambda} \tag{4.4}$$

Nu involves a charactersitic length (l), the heat transfer coefficient (α) and the thermal conductivity (λ) of the fluid. In order to describe forced convection (as usual in rotary kilns [130]), the Nusselt number is considered as a function of Reynolds number (Re) and Prandtl number (Pr):

$$Nu = f(Re, Pr) \tag{4.5}$$

Thus, the flow is described by the dimensionless Reynolds number, as it describes the ratio of inertial to frictional forces in the flow. It includes the flow velocity v, the density ρ, the kinematic (ν) or dynamic viscosity (η) of the fluid and a characteristic length l [137,247]:

$$Re = \frac{v \cdot l \cdot \rho}{\eta} \tag{4.6}$$

The third dimensionless parameter included, is the Prandtl number describing the material characteristics. Besides the kinematic or dynamic viscosity, it includes the thermal diffusivity (a) of the fluid, which is composed of the density, the thermal conductivity (λ) and specific heat capacity (c_p) of the fluid [137,247]:

$$Pr = \frac{\nu}{a} = \frac{\eta \cdot c_p}{\lambda} \tag{4.7}$$

2.3 Radiation

Thermal radiation is the phenomenon of matter emitting alternating electromagnetic fields (infrared spectrum) due to its own thermal motion [248]. Similarly matter can receive and absorb incoming thermal radiation. Thermal radiation is emitted and absorbed by all solid bodies. Thus, in addition to the convective heat transfer mechanism, the modeling of heat transfer by radiation is important in rotary kilns. To describe the emissivity of a body, the radiation is compared to that of an ideal black body, which is radiating perfectly (uniformly in all directions) with the intensity distribution as given by Planck. For real bodies however, the radiation may depend on various factors such as the temperature, the wavelength, the direction of radiation, and the location on the surface (unless it is homogeneous). Since the black body is by definition a perfect emitter, its emissivity is always ε=1. Real surfaces are colored and they follow a general emission law, where the

emission coefficient is depending on the wavelength, the radiating temperature and the solid angle. Moreover, a surface is called gray if its emission coefficient is independent of the wavelength. The emissivities of gray radiators are in the range of 0 to 1.

The heat flux is directly coupled to the temperature, independent of a transmitting medium (but dependent on the area). The heat flow including the emission of radiation emanating from a real body (gray radiator) is equal to (Stefan-Boltzmann law) [247]:

$$\dot{Q}_R = A \cdot \varepsilon \cdot \sigma \cdot T^4 \tag{4.8}$$

3 Heat transport in rotary kilns

In the cross-section of a directly heated rotary kiln, the heat transfer processes in the inner kiln take place between the gas phase (index G), the solid bed (index S) and wall (index W) as shown in Figure IV - 3.1. Furthermore, heat passes the kiln wall to the outer shell (index OS) and flows to the surrounding atmosphere (index A). In the case of the two dimensional cross section, the areas are considered as cross-sectional contact lines or lengths (cl), as the second dimension is the axial length.

As can be derived from the sketch, there are a total of five different heat transfers processes with the resulting heat fluxes [249,250]:

- Between gas and solid (index GS).
- Between hot gas and inner wall (index GW).
- Between wall and solid (index SW) in different mechanisms
- Through the wall to the outer shell (index WOS)
- From the outer wall to the surrounding atmosphere (OSA).

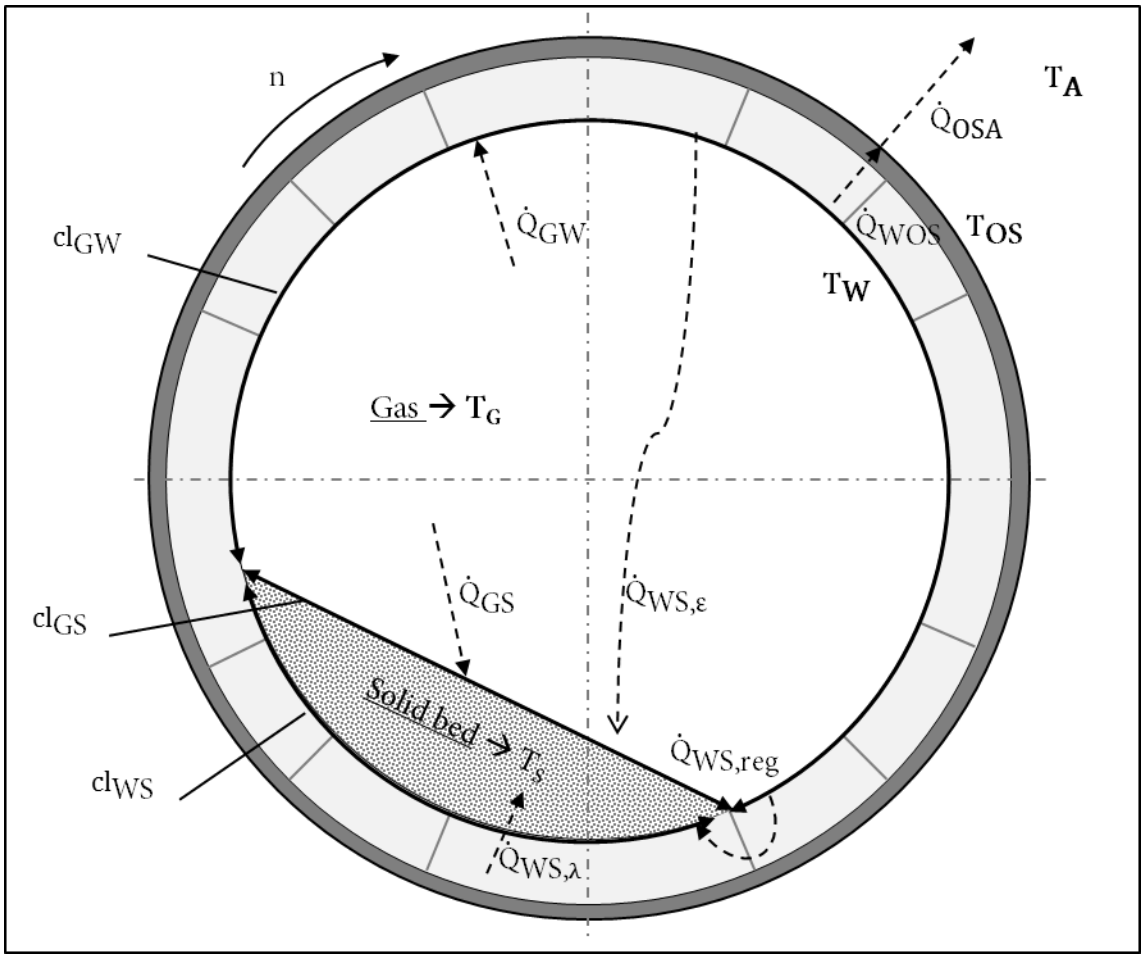

Figure IV - 3.1: Heat transport mechanisms in a directly fired rotary kiln

Due to the commonly high temperatures of the gas, it radiates onto the solid bed surface and the free inner wall surfaces. Superimposed on the dominant radiation mechanism is a convective heat transfer [249]. The additive linkage of the heat flux by radiation and convection results in the effective total heat fluxes between gas and solid ($\dot{Q}_{GS}$) as well as gas and wall ($\dot{Q}_{GW}$). The inner wall and the solid bed are connected via two different mechanisms. The inner wall surface absorbs heat and reflects it to the free surface of the solid bed via radiation, which results in the radiative heat flux ($\dot{Q}_{WS,\varepsilon}$). Additionally, the hot wall surface is transported beneath the solid bed surface due to the drum rotation. Heat is exchanged with the solid bed due to the direct connection (as the solid bed is not moving relatively to the wall, see rolling motion, Part III2.2.1) via conduction $\dot{Q}_{WS,\lambda}$. At least heat is lost through the kiln shell and dissipated to the surroundings (atmosphere). Assumptions are made in the depiction in Figure IV - 3.1, which lead to considerable simplifications:

- The steady-state approach allows the local temperatures of the single elements in the balance equations to be defined independently of time.

- High gas velocities can cause small particles to be dragged during the process and carried with the gas phase (dust entrainment). Such mixing processes of the gas and solids are excluded in the model. Both phases are always considered completely separated from each other.
- In industrial rotary kilns operated at low rotational frequencies and with solid material that has a uniform particle size distribution, full thermal homogenization of the active layer can be assumed [251].
- An ideally mixed gas phase is assumed, which can be attributed to the high Reynolds numbers (Re ~ 8000) and the high degree of turbulence in the gas phase [249]. Thus, the gas phase is considered as a homogeneous system in the cross section with an average temperature distributed over the cross section.
- The solid phase is ideally mixed in cross sectional direction [252].
- Axial mixing processes in the solid bed are neglected [249], which has also been shown experimentally in Part III.

In the following, the heat transport processes are described related to their basic mechanisms. The contact lengths (cl) are considered as exchange areas, since they result in an area in the subsequent integration of all equations with the axial length. Thus, all heat fluxes are derivatives to the axial direction (x).

3.1 Conductive heat transport (WOS)

The heat losses of industrial rotary kilns are based on the high temperatures inside the kiln and the large surfaces of the outer shell. Thermal insulation is only possible to a limited extent since the mechanical stability of the steel shell decreases with increasing temperature. Thus, the heat transport through the wall is an important parameter for the overall process. The higher the heat flux through the wall, the more energy must be supplied to the kiln to achieve the necessary process temperatures in the solid bed. The walls of a rotary kiln usually have a multi-layer structure, consisting of an inner layer of refractory material and the outer steel shell. Sometimes an air gap is situated between both layers provided by the brick construction. The refractory material is in contact with the hot gas phase and the solid, the air gap (if any) serves as additional thermal resistance. The steel shell provides the mechanical stability. Heat flow results from heat transfer through the kiln wall, which is a coupled mechanism of conduction through the wall and heat

removal by convection and radiation from the outer shell surface to the atmosphere. The following relationship results for heat conduction through the kiln wall:

$$\frac{d\dot{Q}_{WOS}}{dx} = k_{WOS} \cdot (T_W - T_{OS}) \tag{4.9}$$

The heat transport coefficient can be described as:

$$k_{WOS} = \frac{1}{2\pi} \cdot \sum_{j=1}^{n} \frac{1}{\lambda_{W,j}} \cdot \ln\left(\frac{r_i + s_{w,j}}{r_i}\right) \tag{4.10}$$

Herein, r_i is the inner radius, $\lambda_{W,j}$ is the thermal conductivity, and $s_{w,j}$ is the thickness of the respective wall layer. Table IV - 3.1 lists the relevant thermal conductivities of the rotary kiln wall materials.

Table IV - 3.1: Thermal conductivities of the wall materials of the rotary kiln at 800 °C [247]

Material	Therm. Conductivity λ_W [W/(m·K)]
Refractory	1.15
Air	0.07134
Steel	50

3.2 Convective heat transfers

The amount of heat transferred from a turbulent flowing gas to the solid bed surface and the inner wall of the drum is composed of the sum of the heat flows due to convection (index "C") and radiation (index "R") [244]. This results in the following relationships for the heat flows:

$$\dot{Q}_{GW} = \dot{Q}_{CGW} + \dot{Q}_{RGW} \tag{4.11}$$

$$\dot{Q}_{GS} = \dot{Q}_{CGS} + \dot{Q}_{RGS} \tag{4.12}$$

In this context, convective heat transfer can be considered as a coupled mechanism between heat conduction from the overflowed surface into the fluid and enthalpy transport with the flow [249].

3.2.1 Gas to wall (CGW)

The transported heat flux due to convection is described according to the Newtonian approach according to equation (4.3):

$$\frac{d\dot{Q}_{CGW}}{dx} = \alpha_{GW} \cdot cl_{GW} \cdot (T_G - T_W) \tag{4.13}$$

The contact length follows from the kiln geometry and solid transport. The main issue is to calculate the transport coefficient according to equation (4.4). The hydraulic diameter (d_h) is used instead of the drum diameter as the characteristic length, since a dimeter reduction is evoked by the solid bed height, according to the axial solids transport [253]. In the case of turbulent flows (Re > 2300), the Nußelt functions can only be determined empirically. Gnielinski gives a calculation equation supported by a large number of measured values and extended in the validity range of $10^4<Re_G<10^6$ and $0.6<Pr_G<1000$ [254,255]:

$$Nu = \frac{\left(\frac{\xi}{8}\right) \cdot Re_G \cdot Pr_G}{1 + 12.7 \cdot \sqrt{\frac{\xi}{8}} \cdot \left(Pr_G^{\frac{2}{3}} - 1\right)} \cdot \left[1 + \frac{1}{3} \cdot \left(\frac{d_h}{L}\right)^{\frac{2}{3}}\right] \tag{4.14}$$

L describes the drum length, the pressure drop occurring in the drum due to friction is represented with (ξ) as:

$$\xi = \left(1.8 \cdot log_{10}(Re_G - 1.5)\right)^{-2} \tag{4.15}$$

In the transition region between laminar and turbulent flow ($2300<Re_G<10^4$) equation (4.14) can be simplified for gasses ($0.5<Pr_G<1.5$) to:

$$Nu = 0.0214 \cdot \left(Re_G^{0.8} - 100\right) \cdot Pr_G^{0.4} \cdot \left[1 + \frac{1}{3} \cdot \left(\frac{d_h}{L}\right)^{\frac{2}{3}}\right] \tag{4.16}$$

The thermophysical properties in Re_G and Pr_G of the gas flow are described as a function of temperature using the power approach according to Müller [256] as shown in the appendix (chapter 6.1).

3.2.2 Gas to solid (CGS)

The process is similar to the transport described in the former chapter 3.2.1. The heat flow involves the solid bed surface area instead of wall surface and the respective temperature difference:

$$\frac{d\dot{Q}_{CGS}}{dx} = \alpha_{GS} \cdot cl_{GS} \cdot (T_G - T_S) \tag{4.17}$$

Furthermore, in the case of the solid in the casacing layer, the transport coefficient is assumed as a multiple of α_{CGW} according to Barr et al., where parameter f_{GS} is fitted to the process data in the range of 2-10 [249]:

$$\alpha_{CGS} = f_{GS} \cdot \alpha_{CGW} \tag{4.18}$$

3.2.3 Outer shell to atmosphere (COSA)

The heat flux dissipated from the outer shell surface to the environment by convection (index "COSA") is calculated with:

$$\frac{d\dot{Q}_{COSA}}{dx} = \alpha_{COSA} \cdot 2\pi \cdot (r_i + s_{w1} + s_{w2} + s_{w3}) \cdot (T_{OS} - T_A) \tag{4.19}$$

The convective heat transfer coefficient α_{COSA} corresponds to 10 W/(mK) in the present case [247]. Gnielinski describes the relationship for convective heat transfer at the outer shell surface of the rotary kiln from the superposition of free and forced convection. This approach can alternatively be used to calculate the convective heat transfer coefficient [247,257].

3.3 Radiative heat transfers (RGW, RGS, WS,$\boldsymbol{\varepsilon}$)

The heat flux transferred by radiation from the gas to the surface of the uncovered wall ($\dot{Q}_{RGW}$)and the free bed surface ($\dot{Q}_{RGS}$) results from the Stefan-Boltzmann law for gray radiators to [247]:

$$\frac{d\dot{Q}_{RGW}}{dx} = \varepsilon_{GW} \cdot \sigma \cdot cl_{GW} \cdot (T_G^4 - T_W^4) \tag{4.20}$$

$$\frac{d\dot{Q}_{RGS}}{dx} = \varepsilon_{GS} \cdot \sigma \cdot cl_{GS} \cdot (T_G^4 - T_S^4) \tag{4.21}$$

In addition, the radiative exchange between the solid bed surface and the uncovered inner wall surface must be taken into account:

$$\frac{d\dot{Q}_{WS,\varepsilon}}{dx} = \varepsilon_{WS} \cdot \sigma \cdot cl_{WS} \cdot (T_W^4 - T_S^4) \tag{4.22}$$

In this context ε_{GW}, ε_{GS} and ε_{WS} represent the effective emissivities, σ is the Stefan-Boltzmann constant with 5.67 10^{-8} W/(m^{2}K^4) and cl_{GW}, $cl_{GS}$and cl_{WS} the surfaces participating at the heat exchange.

To calculate the radiative exchange in industrial furnaces, a set of models was developed by Schupe using the net radiation method [258]. More precisely, it is a network method presented by Oppenheim for calculating the radiation exchange inside an industrial furnace. Here, the heat transfer is determined by a network of radiation resistances, analogously to electrical engineering.

Kirchhoff's law is applied in this context to calculate the individual radiation resistances, which are connected either in parallel or in series (cf. chapter 4) [259,260]. Assuming a flat solid bed surface and the fact that all radiation emitted by the solid bed and the wall is dissipated into the gas, the effective radiation exchange efficiencies are given by:

$$\varepsilon_{GW} = \frac{\varepsilon_G \cdot \varepsilon_W \cdot [1 + \varphi_{WS} \cdot (1 - \varepsilon_S) \cdot (1 - \varepsilon_G)]}{1 - K} \tag{4.23}$$

$$\varepsilon_{GS} = \frac{\varepsilon_G \cdot \varepsilon_S \cdot [1 + \varphi_{WS} \cdot (1 - \varepsilon_W) \cdot (1 - \varepsilon_G)]}{1 - K} \tag{4.24}$$

$$\varepsilon_{WS} = \frac{\varepsilon_W \cdot \varepsilon_S \cdot (1 - \varepsilon_G)}{1 - K} \tag{4.25}$$

With the view factor φ_{WS} and constant K described by [248]:

$$\varphi_{WS} = \frac{cl_{GS}}{cl_{GW}} \tag{4.26}$$

$$K = (1 - \varepsilon_G) \cdot (1 - \varepsilon_W) \cdot [\varphi_{WS} \cdot (1 - \varepsilon_S) \cdot (1 - \varepsilon_G) + (1 - \varphi_{WS})] \tag{4.27}$$

Consequently, for the calculation of the effective radiation exchange, the geometrical properties as well as the radiative character of the surfaces must be determined. The geometric properties can be derived from surface ratios between the uncovered inner wall of the rotary kiln and the solid bed surface. Whereas the radiation capacity results from the emissivity of the inner wall ε_W, the solid bed ε_S and the gas phase ε_G.

3.3.1 Radiation of solids

The emissivities of the wall surface have been determined in experimental measurements by Bauer et al., who studied the emissivity of some refractories for different temperature ranges [261]. They show, that at low temperatures or in the range of long wavelengths, the refractories exhibit emissivities between 0.85 and 1.0. In contrast, the average emissivity decreases with increasing temperature. Furthermore, the quantitative influence of temperature is mainly dependent on the refractory material. Chamotte is a refractory material of various compositions produced by firing caolitic raw materials (some of which are artificially enriched with Al_2O_3) and sintering them [247]. Consequently, a generally valid statement regarding the emissivity of the radiating inner wall surfaces cannot be made. For the process simulation, either such material-specific measurement

curves of the surface must be known or, in the case of a material with approximately constant emissivity, an averaged emissivity for the surface, which is constant over the length of the rotary kiln, must be approximated. For program use, the emissivity of the kiln lining in the temperature range between 400 and 1600 K is approximated with the following linear function [261]:

$$\varepsilon_W = -0.0003198 \cdot T_S + 1.043 \tag{4.28}$$

The emissivity curves of magnetite and hematite are shown in the appendix (chapter 6.2, Figure IV - 6.1) and exhibit a high emissivity level at values above 0.7 in the investigated spectrum. The emissivities increase with the wavelengths until their maximum values of roughly 1 at about 15 µm for magnetite and 14 µm for hematite, respectively. A weakly pronounced temperature dependence can only be observed in areas of very short as well as very long wavelengths [262].
Summarizing, an emissivity of 0.98, which is constant over the entire length of the rotary kiln or temperature range, can be assumed for the solid bed.

3.3.2 Radiation of Gases

Compared to solids (and surfaces), gases do not radiate continuously in the entire spectrum, but selectively in individual ranges. In order to apply the Stefan-Boltzmann law, the gray radiator model is also used to calculate the gas radiation. In this context, the emitted heat flux is integrated over the entire spectrum in order to subsequently use an averaged emissivity of the gas. Thus, the selective radiation range of the gas is overcome and the heat flux can be determined comparably to the radiation of solids. The gas radiation is based on the nuclear vibration of polyatomic molecules and depends primarily on the layer thickness, the partial pressure and the temperature. The layer thickness is used to describe the path length of the radiation in a gas layer, where an equivalent layer thickness s_{eq} is introduced for any geometry of the gas space. If the geometrical conditions are unknown, the equivalent layer thickness can be determined from the following approximation [247].

$$S_{eq} = 3.6 \cdot \frac{V_G}{A_G} \tag{4.29}$$

The optical density, which results from the product of the equivalent layer thickness and the partial pressure of the gas, is a fundamental parameter of gas radiation. In the appendix (Part IV, ch. 6.3, Figure IV - 6.2), the influence of the temperature and the variation of the optical density on the emissivities of H_2O and CO_2 is shown. It can be observed, that the increase in optical density results in a larger emissivity. This finding can be explained by the fact that with greater layer thickness, a greater number of radiating molecules are available within the gas phase. These molecules add more ranges to the overall spectrum and cause the individual bands to form higher and wider. The decrease of the emissivities with increasing temperature can be taken from the related emission spectrum. Thus, increasing temperatures lead to a shift of the intensity maxima to smaller wavelengths, where the capability of emission becomes lower.

In order to describe the progress of the emissivities below the gas temperatures of 1000K or 1300 K, the following correlation equation can be used according to Kostowski [263]:

$$\varepsilon_i = 1 - \exp\left[-G(T_G) \cdot \left(p_i \cdot S_{eq}\right)^k\right] \tag{4.30}$$

$$G(T_G) = b + c \cdot \frac{T_G}{1000°C} \tag{4.31}$$

The parameters k, b and c are listed as a function of temperature, partial pressure and layer thickness in the appendix (chapter 6.3). Only the components of the combustion gas CO_2 and H_2O are considered as technically relevant radiators. This conclusion results from the assumption that the elementary gases Nitrogen (N_2), Oxygen (O_2) and Argon (Ar) are transparent in the wavelength spectrum of thermal radiation. They practically do not absorb at low temperatures and pressures. However, other gases, for example, SO_2 and CO, have such pronounced absorption bands that their interaction with radiation cannot be neglected [264]. In the present case, it is assumed that these components are negligible in the calculation of heat transfer due to their low concentration in the gas phase [248]. Consequently, the gas phase in the rotary kiln has to be considered as a mixture of CO_2 and H_2O, which results in partial overlap of radiation ranges. Taking this effect into account, an approximation of the gas mixture averaged over the entire spectrum can be described as follows according to Hottel and Egbert [265]:

$$\varepsilon_G = \varepsilon_{CO_2} + \varepsilon_{H_2O} - \varepsilon_{CO_2} \cdot \varepsilon_{H_2O} \tag{4.32}$$

3.3.3 Outer shell to atmosphere (ROSA)

The heat flux dissipated from the outer mantle surface to the environment by radiation (index "ROSA") can be described with:

$$\frac{d\dot{Q}_{ROSA}}{dx} = \sigma \cdot \varepsilon_{ROSA} \cdot 2\pi \cdot (r_i + s_{w1} + s_{w2} + s_{w3}) \cdot (T_{OS}^4 - T_A^4) \tag{4.33}$$

To calculate the heat transfer through the wall, the convective and radiative heat transfer coefficients must be determined according to equation (4.19) and (4.33). Complementary to the convective heat transfer mechanism to the environment, the heat transfer by radiation from the outer shell surface to the environment is considered. Corresponding to the basic principle of radiative heat transfer, the radiative heat transfer coefficient is obtained for the external heat dissipation to the surroundings:

$$\varepsilon_{ROSA} = \varepsilon_{OSA} \tag{4.34}$$

Since the surrounding area is very large in relation to the outer shell surface, the relationship $\varepsilon_{OSA} = \varepsilon_{OS}$ can be established to estimate the radiation exchange efficiency. The emissivity of the outer shell material can be approximated over the entire length of the rotary kiln with ε_{OS}=0.9 [266].

3.4 Regenerative heat transport (WS,reg)

While the inner wall is uncovered from solids in the upper drum region, the wall absorbs heat by convection and radiation of the hot gas. As a result of the drum rotation the hot wall is transported beneath the solid phase, where the heat is released into the solid bed by conduction. This heat flux in radial direction is called regenerative heat transfer, is special for rotary kilns and has been studied by different authors. Gorog et al. [244] determined the refractory layer participating at the regenerative heat transfer to be roughly 15mm. Especially at lower temperatures they found this mechanism to be predominant together with convection. Herz et al. performed various experimental investigations of the rotary kiln wall temperature profile [252,267,268]. Agustini and Sonavane intensively studied the impact of the wall in rotary kiln heat transport [269,270] and

provide simplified modeling approaches. The regenerative heat transport can be described in general with:

$$\frac{d\dot{Q}_{WS,reg}}{dx} = \alpha_{WS,reg} \cdot cl_{WS} \cdot (T_W - T_S) \tag{4.35}$$

Agustini et al. propose a calculation basis for the regenerative heat transfer coefficient [271]:

$$\alpha_{WS,reg} = \frac{1}{\frac{1}{\alpha_{WS,\lambda} \cdot cl_{WS}} + \frac{1}{\alpha_{W,T} \cdot (cl_{WS} + cl_{GW})}} \cdot \frac{1}{cl_{WS}} \tag{4.36}$$

In equation (4.36), $\alpha_{W,T}$ is the heat transfer coefficient in the circumferential direction of the wall and $\alpha_{WS,\lambda}$ is the heat transfer coefficient describing the contact between wall and the solid bed. For this purpose, $cl_{WS}$and cl_{GW} represent the heat transfer areas between the solid covered wall and the lower solid bed border as well as between the gas phase and the uncovered wall. The heat transfer in the circumferential direction is independent of the kiln diameter and is described by the following relationship [271]:

$$\alpha_{W,T} = \pi \cdot \sqrt{\lambda_W \cdot \rho_W \cdot c_W \cdot n} \tag{4.37}$$

The thermophysical properties of the wall (refractory material: fireclay) are taken from the VDI heat atlas (λ_W = 1.05 W/mK, ρ_W = 2.15 g/cm^3 and c_W = 1.021 kJ/kgK) [247]. The heat accumulated in the wall is transferred to the solid bed in the lower drum part through contact to the solid bed. Tscheng and Watkinson provide an empirical correlation for the contact heat transfer coefficient [271,272]:

$$\alpha_{WS,\lambda} = 11.6 \cdot \left(\frac{n \cdot r^2 \cdot 2 \cdot \theta}{a_s}\right)^{0.3} \cdot \frac{\lambda_S}{cl_{WS}} \tag{4.38}$$

$$a_s = \frac{\lambda_S}{\rho_S \cdot c_{p,S}} \tag{4.39}$$

The contact heat transfer coefficient thus depends on the operating parameters filling degree Φ, rotational frequency n as well as on the material-specific parameters thermal conductivity λ_S, the specific heat capacity $c_{p,S}$ and the bulk density of the solid bed ρ_S.

4 Heat-networking

The heat transport processes explained earlier are combined in this chapter according to Figure IV - 3.1. The network method is used to calculate the individual heat flows. The application of this method is common in rotary kiln modeling [273]. Gorog et al. provide approaches with different complexity [274,275] also incorporating flames in rotary kilns. Li et al. used the method to set up a rotary kiln model [276].

Thermal network models are based on the relationship for thermal resistances, where all types of heat transfer processes can be incorporated. In this model, the temperatures of the solid, the gas, the inner and outer walls, and the atmosphere are considered as nodes and interconnected with thermal resistances. It is assumed that the heat transfer can be represented with the superposition of independent, one-dimensional heat transfers. According to Fourier's law, a heat flux ($\dot{Q}$) flows between two temperature potentials, which is proportional to the temperature difference ΔT. Analogously to Ohm's law, the thermal resistance can be determined with:

$$R_{th} = \frac{\Delta T}{\dot{Q}} \tag{4.40}$$

The electric or thermal conductivity represents the reciprocal of the ohmic resistance. The thermal resistances are connected according to Figure IV - 4.1 in series or in parallel, so that the heat flows can be balanced at the nodes. If n resistors are connected in series, they add up according to:

$$R = R_1 + R_2 + \cdots + R_n \tag{4.41}$$

If n resistors are connected in parallel, the conductivities or the reciprocal resistances are added to:

$$\frac{1}{R} = \frac{1}{R_1} + \frac{1}{R_2} + \cdots + \frac{1}{R_n} \tag{4.42}$$

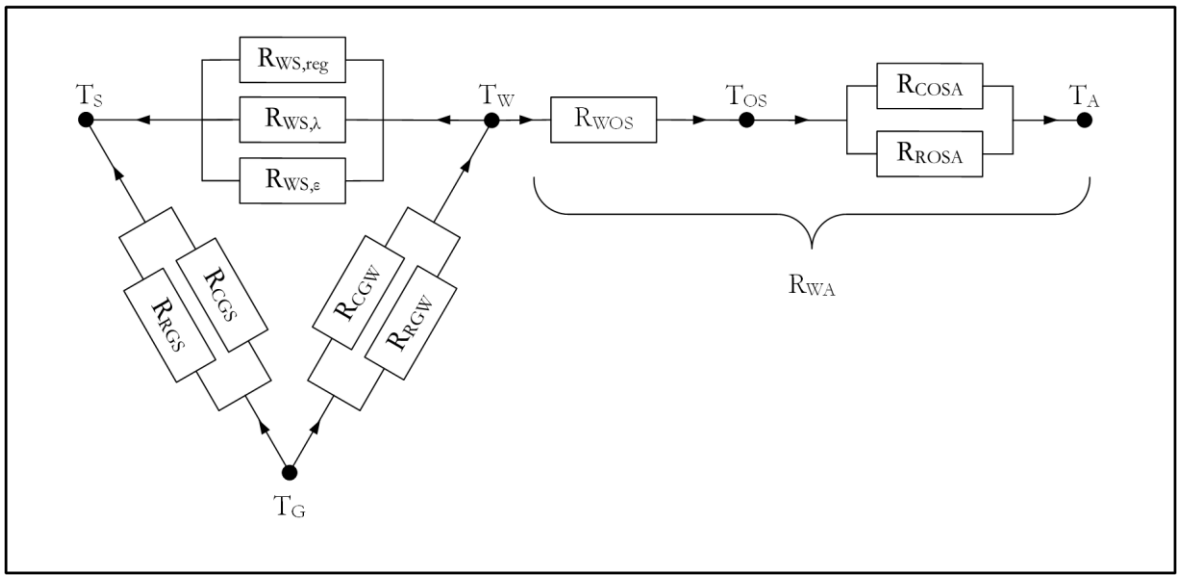

Figure IV - 4.1: Network of thermal resistances in the heat transport model of the rotary kiln

Boundary conditions for the temperatures are mandatory to solve the resulting systems of equations.

The direction of the heat flows is defined by the arrows presented in Figure IV - 4.1. The hot gas is considered with the highest temperature in the system. It transfers heat to the solid bed by radiation and convection, whereby the heat flow must overcome the thermal resistance R_{CGS} and R_{RGS} respectively. Similarly, the hot gas transfers heat to the inner wall. Furthermore, it is assumed that the inner wall has the second highest temperature in the system.

The net heat flux of the gas phase corresponds to the heat transferred from the gas to the solid and the wall. Since combustion was not considered in the present model, the heat of combustion is omitted and the gas phase balance results to (derivatives to axial direction are omitted due to clarity):

$$\dot{Q}_G = -\left(\dot{Q}_{RGW} + \dot{Q}_{CGW}\right) - \left(\dot{Q}_{RGS} + \dot{Q}_{CGS}\right) \tag{4.43}$$

The net heat flux of the solid phase results from the transferred heat from the gas to the wall as well as from the occurring reaction enthalpies of the solid phase $\dot{H}_R$:

$$\dot{Q}_S = \left(\dot{Q}_{RGS} + \dot{Q}_{CGS}\right) + \dot{Q}_{WS,\lambda} + \dot{Q}_{WS,\varepsilon} + \dot{H}_R \tag{4.44}$$

The balance of the inner wall results from the heat transfer from the hot gas to the inner wall, the heat transfer from the outer shell to the atmosphere, the regenerative heat flux, the contact heat transfer from the wall to the solid bed and the radiative heat flux from the wall to the solid bed according to the following equation:

$$\dot{Q}_{GW} = \dot{Q}_{WS,\lambda} + \dot{Q}_{WS,reg} + \dot{Q}_{WS,\varepsilon} + \dot{Q}_{WOS} + \dot{Q}_{OSA} \tag{4.45}$$

To calculate the temperature profile of the inner and outer wall, it is useful to apply the specific thermal conductivity (G) instead of the thermal resistance. The thermal conductivities around the inner wall are arranged in a star-connection (or Y-connection) according to Figure IV - 4.1, so that the inner wall temperature can be calculated as follows:

$$\begin{aligned}(G_{CGW} + G_{RGW}) \cdot (T_G - T_W) + \left(G_{WS,reg} + G_{RWS} + G_{WS,\lambda}\right) \cdot (T_W - T_S) \\ = G_{WA} \cdot (T_W - T_A)\end{aligned} \tag{4.46}$$

The resistance R_{WOS} (Figure IV - 4.1) combines the individual resistances R_{W1} (refractory), R_{W2} (air gap) and R_{W3} (steel shell). Between the inner wall and the atmosphere, all resistances are calculated according to Figure IV - 4.1 and summarized as heat loss conductance G_{WA}:

$$G_{WA} = \frac{1}{\left(\frac{1}{G_{W1}} + \frac{1}{G_{W2}} + \frac{1}{G_{W3}}\right) + \frac{1}{G_{COSA} + G_{ROSA}}} \tag{4.47}$$

The outer shell temperature depends on the incoming heat flows due to conduction through the wall and on the dissipated heat flows due to convection and radiation. Similarly to (4.46) the temperature of the outer wall is calculated as follows:

$$\left(\frac{1}{G_{W1}} + \frac{1}{G_{W2}} + \frac{1}{G_{W3}}\right) \cdot (T_W - T_{OS}) = (G_{COSA} + G_{ROSA}) \cdot (T_{OS} - T_A) \tag{4.48}$$

5 Interim conclusion

In this part of the work the heat transport processes taking place in a rotary kiln (without internals) are presented. Model equations for each mechanism and a modeling approach for the complete system are provided utilizing the network method. The single transport processes are explained in detail regarding the adaption to rotary kilns without any internals.

The gained knowledge will be used in the last part of this work to model a rotary kiln process. To finally do so, conservation equations are established for the gas and solid phases, which are valid within a defined balance volume. This results in the following separate differential equations based on the differential energy balances, which describe the changes in the temperatures over the length of the rotary drum [119]:

$$\frac{d\dot{H}_G}{dx} = \frac{d\dot{R}_F}{dx} + \frac{d\dot{Q}_{GS}(h, T_G, T_S)}{dx} + \frac{d\dot{Q}_{GW}(h, T_G, T_W)}{dx} \tag{4.49}$$

$$\frac{d\dot{H}_S}{dx} = \frac{d\dot{Q}_{GS}(h, T_G, T_S)}{dx} + \frac{d\dot{Q}_{WS,\lambda}(h, T_W, T_S)}{dx} + \frac{d\dot{Q}_{WS,\varepsilon}(h, T_W, T_S)}{dx} + \frac{d\dot{H}_R}{dx} \tag{4.50}$$

The change of the enthalpy flux of the gas phase $\dot{H}_G$ according to equation (4.49) corresponds to the heat flow $\dot{R}_F$, which is generated by the conversion of the fuel and not considered in this thesis. Therefore this expression equals to zero. In addition, the heat transferred from the gas to the solid and the wall is considered.

The change in enthalpy flow of the solid phase $\dot{H}_S$ is composed of the transferred heat of the gas and the wall and of occurring reaction enthalpy fluxes in the solid bed $d\dot{H}_R$. The equations are essentially coupled via the parameters listed in the heat flows:

- height of the bulk material (h)
- temperature of the gas phase (T_G)
- temperature of the solid bed (T_S)
- temperature of the inner wall (T_W)
- temperature of the outer wall/shell T_{OS}

Consequently, the overall model consists of intercoupled first-order ordinary differential equations, linked to a set of non-linear algebraic equations for the phenomenological description of heat transfer, fluid flow and thermodynamic characteristics.

Finally, the following advantages of the method can be summarized:

- The model is based on fundamental general knowledge regarding heat transport and thus easy to understand.
- The variables of state (temperatures) can be calculated considering their interdependencies.
- The netwok method is applicable and adaptable to various heat transfer problems.
- The model is capable of representing bare drum and sectional internals.
- The method enables easy extension regarding further material and mechanical components.

6 Appendix

6.1 Thermophysical properties

The thermophysical properties of the gas flow are described as a function of temperature using the power approach according to Müller [256]. The necessary exponents and material characteristics under standard conditions are listed in Table IV - 6.1. With the determined concentrations (molar fraction x_i) of the components in the gas phase, the weighted sum of the respective substance quantity in the gas flow is determined as follows.

$$\lambda_i(T_G) = \lambda_{i,n} \cdot \left(\frac{T_G}{T_{G,n}}\right)^{k_{\lambda,i}} \quad with \quad \lambda_G(T_G) = \sum x_i \cdot \lambda_i(T_G) \tag{4.51}$$

$$\nu_i(T_G) = \nu_{i,n} \cdot \left(\frac{T_G}{T_{G,n}}\right)^{k_{\nu,i}} \quad with \quad \nu_G(T_G) = \sum x_i \cdot \nu_i(T_G) \tag{4.52}$$

$$Pr_i(T_G) = Pr_{i,n} \cdot \left(\frac{T_G}{T_{G,n}}\right)^{k_{Pr,i}} \quad with \quad Pr_G(T_G) = \sum x_i \cdot Pr_i(T_G) \tag{4.53}$$

$$\rho_i(T_G) = \rho_{i,n} \cdot \left(\frac{T_G}{T_{G,n}}\right)^{k_{\lambda,i}} \quad with \quad \rho_G(T_G) = \sum x_i \cdot \rho_i(T_G) \tag{4.54}$$

Table IV - 6.1: Parameters of the temperature dependent characteristics of the gas phase at standard conditions at $T_{G,n}$=273.15 K [256]

Component	$k_{\lambda,i}$	$\lambda_{i,n}$	$k_{\nu,i}$	$\nu_{i,n}$	$k_{Pr,i}$	$Pr_{i,n}$	$\rho_{i,n}$
	[-]	[W/m·K]	[-]	x 10^{-5} [m^2/s]	[-]	[-]	[kg/m^3]
H_2O	1.42	0.016	2.13	1.074	-0.09	0.95	0.804
CO_2	1.04	0.017	1.77	0.727	0.03	0.73	1.964
N_2	0.76	0.024	1.67	1.333	0.02	0.7	1.250
O_2	0.80	0.025	1.67	1.368	0.02	0.7	1.428
Ar	0.69	0.017	1.69	1.194	0.00	0.67	1.784

6.2 Radiation of solids

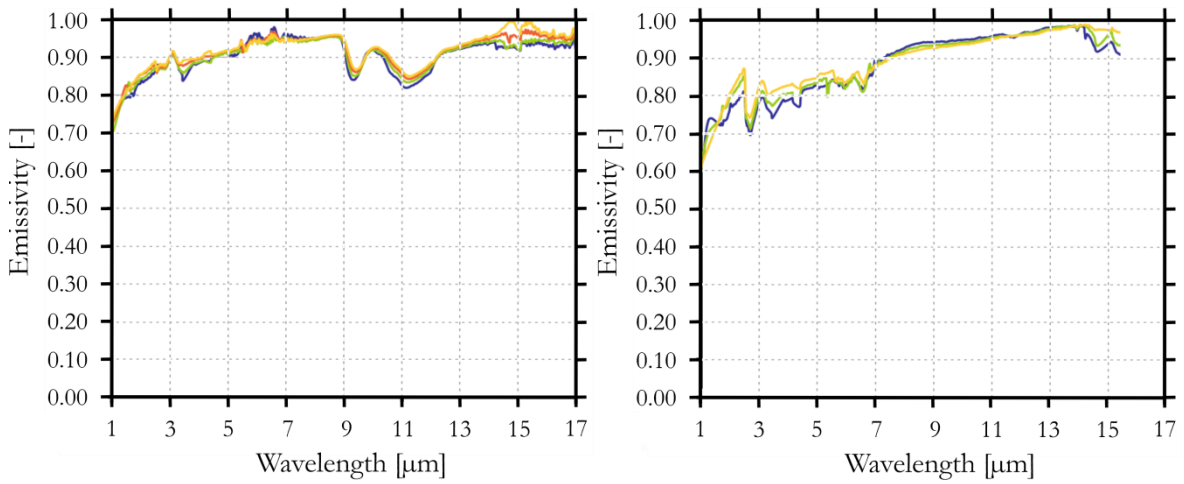

Figure IV - 6.1: Emissivities of magnetite Fe_3O_4 (left) and hematite Fe_2O_3 (right) [262]

6.3 Radiation parameters of gases

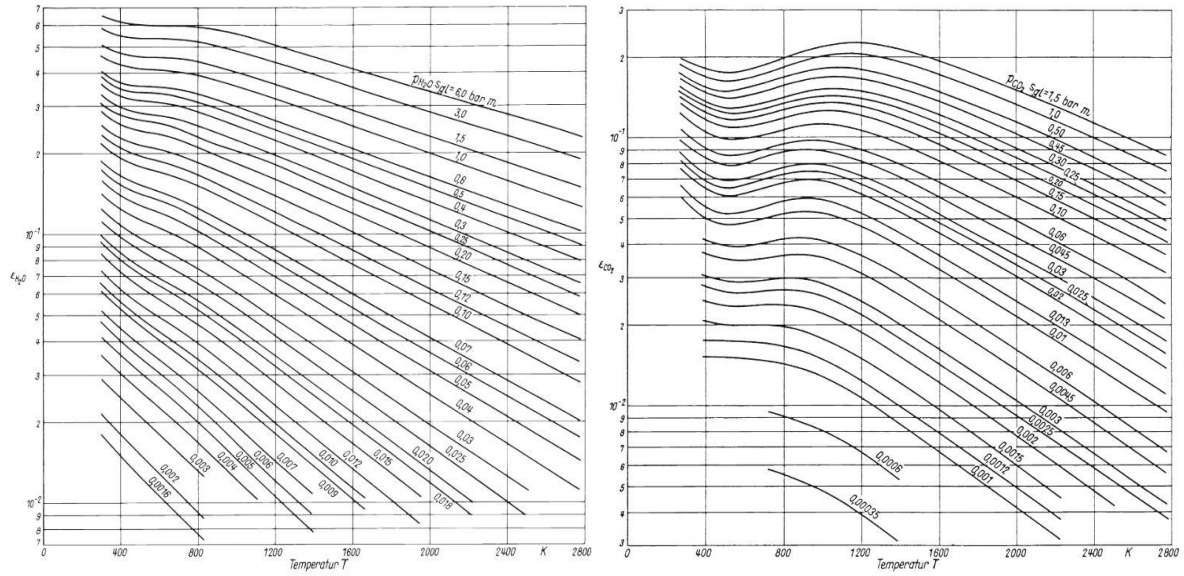

Figure IV - 6.2: Emissivities of steam (left) and carbon dioxide (right) at 1 bar total pressure in dependency of temperature and optical density [277]

The parameters k, b and c are listed as a function of temperature, partial pressure and layer thickness to be incorporated in the model according to Kostowski [263] in Table IV - 6.2.

Table IV - 6.2: Parameters in the radiation model for CO_2 and H_2O [263]

	CO_2			H_2O		
$p_i \cdot S_{eq}$ [bar m]	b	c	k	b	c	k
Temperature range: T = 200 ... 800°C						
70 ... 200	0.05070	0.03051	0.244	0.11039	-0.03959	0.367
10 ... 80	0.05000	0.02277	0.262	0.07526	-0.03358	0.470
4 ... 10	0.04608	0.01707	0.308	0.06151	-0.03602	0.580
0.93 ... 5	0.04596	0.01220	0.345	0.05772	-0.04022	0.372
0.093 ... 1	0.50320	-0.00168	0.527	0.06421	-0.05438	0.797
Temperature range T = 800 ... 1400°C						
70 ... 200	0.07350	-0.02081	0.310	0.09700	-0.03809	0.395
10 ... 80	0.07791	-0.02573	0.314	0.05729	-0.02375	0.530
4 ... 10	0.07613	-0.03038	0.374	0.04210	-0.01979	0.692
0.93 ... 5	0.07814	-0.03321	0.391	0.03892	-0.02027	0.814
0.1 ... 1	0.08697	-0.04108	0.614	0.04433	-0.025552	0.945

Part V Mathematical modeling

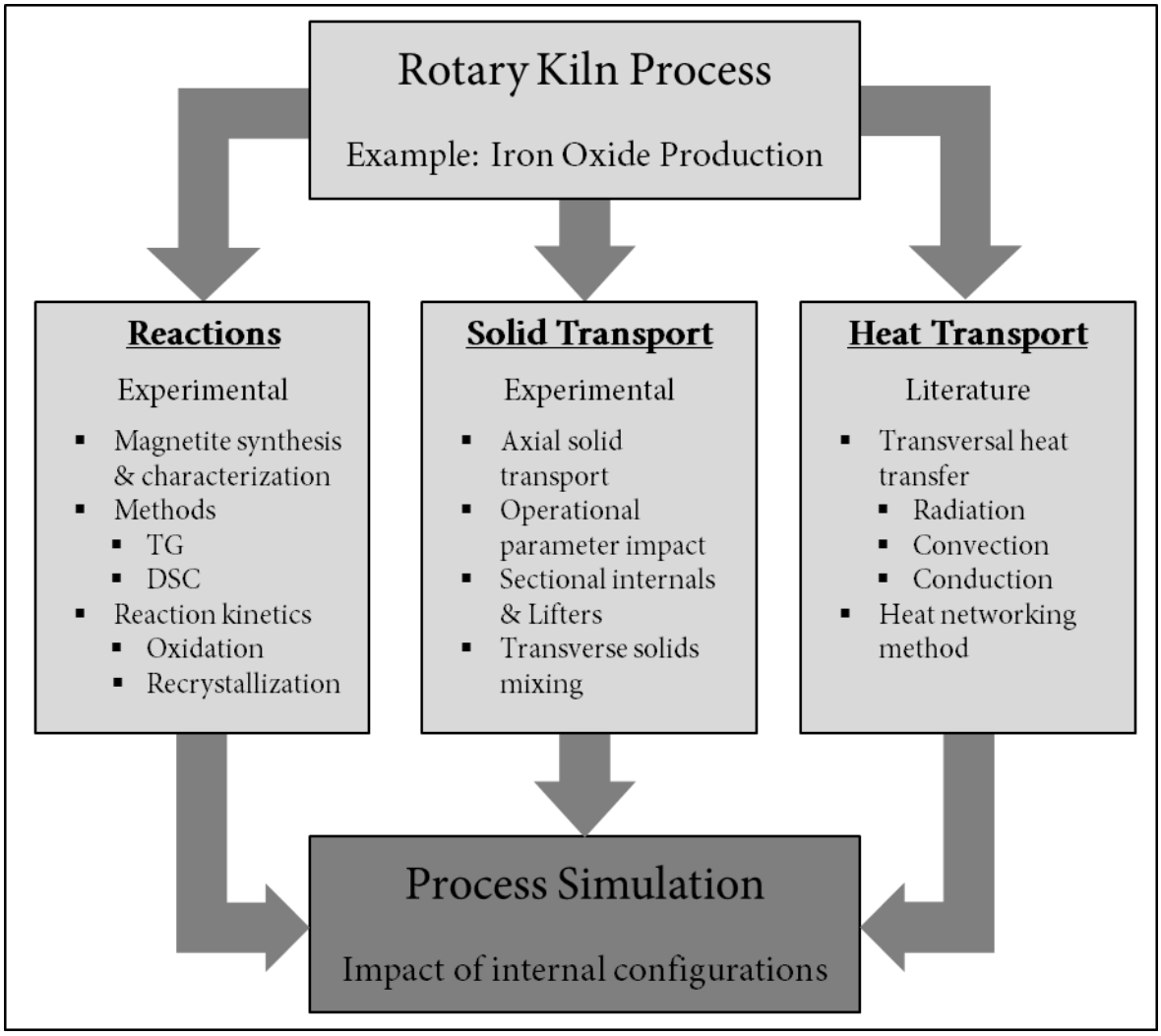

1 Introduction

In this final part of the thesis, the process modeling of rotary kiln process under investigation over the entire thesis is treated. In a stationary, one-dimensional (axial) mathematical model, the phenomenological relationships between the chemical reactions (Part II), the solids transport (Part III) and the heat transport (Part IV) are represented. The focus is on the estimation of the impact of sectional internals, as they have been intensively investigated in Part III with respect to solids transport, on the overall process.

The principle of cross-sectional modeling is introduced first and then adapted to the reference process. The presented and developed mathematical descriptions of the individual phenomena are adapted, complemented where necessary and then combined in the overall model.

The model is validated on the basis of the industrial reference process from iron oxide pigment production using the Laux process, and simulation results are presented for the bare kiln, as well as for the use of sectional internals. Finally, the model is utilized to perform a sensitivity analysis with regard to the important operating and design parameters.

2 Modeling rotary kilns

The modeling of rotary drums or rotary kilns in specific can be performed in different ways. The availability of computing performance enables the rigorous modeling with DEM or CFD methods, as utilized by various authors and research groups in the former past [143,144,150,241,278–281]. However, these methods are mostly adapted to single elementary issues and are not adapted to provide a full model of the kiln process incorporating all processes taking place in the kiln.

The method used to provide full process models is the one dimensional or axial modeling. A huge amount of publications is available regarding this kind of modeling especially for cement kilns. But further applications of rotary kilns have also been modeled, as presented in the following:

- Cement kilns [253,282,283]
- Limestone kilns [284,285]
- Alumina kilns [132]
- Iron oxide pellet production [61,62]

Since information on the total process behavior of the investigated kiln process is desired, the one dimensional modeling is applied in this work and will be explained in the further chapters.

2.1 One-dimensional axial modeling

The one dimensional axial modeling is based on slicing the kiln in axial direction into small cylinders of tiny height or axial length (dx), respectively. The process is sketched graphically in Figure V - 2.1

All processes can be calculated for this (in optimal case infinitesimal) axial slice or segment (i) assuming, that solid and gas phase are homogenous in constitution and temperature in this slice. This is valid if the residence time in the segment is higher than the mixing time. In order to describe the processes as well as resulting balances, these have to be considered as differential equations differentiated to the axial length (dx). Thus, the output of all incorporated variables in each segment (i) serve as input data for the calculations in the next segment (i+1). The first segment is calculated utilizing the given start values. In order to solve the system of equations, variables at one kiln end, such as the solid bed temperature the gas temperatures, are available. With the boundary conditions, the problem can be solved by applying a suitable numerical method in MatLab as will be described in chapter 2.2. The resulting algorithm and program structure will be explained briefly in chapter 2.3.

Beforehand, the last missing pieces of information are provided regarding the cross sectional modeling in the following.

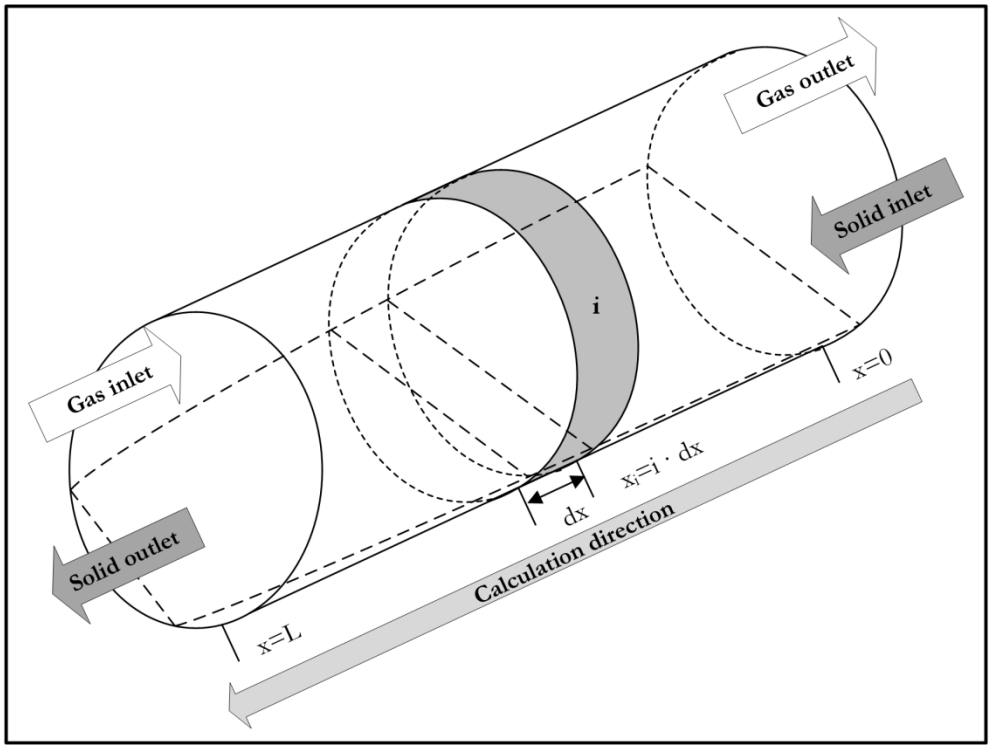

Figure V - 2.1: Sketch of the principle in one dimensional or axial modeling of rotary kilns or rotary drums.

2.1.1 Geometric modeling

The geometric relationships in the cross-section of the rotary kiln without sectional divisions are shown in Figure V - 2.2. Assuming a flat solid surface, the cross-sectional area of solid A_S (index "S") and gas A_G (index "G") can be calculated by including the inner kiln radius r_i and the central angle γ as follows:

$$A_S = \frac{r_i}{2} \cdot (\gamma - \sin(\gamma)) \tag{5.1}$$

$$A_G = \pi \cdot r_i^2 - A_S \tag{5.2}$$

For the contact lengths (cl) between the gas and solid bed (GS), the gas phase and the inner wall (GW), and the solid bed and the inner wall (SW), the following relationships result:

$$cl_{GS} = r_i \cdot 2 \cdot \sin\left(\frac{\gamma}{2}\right) \tag{5.3}$$

$$cl_{GW} = r_i \cdot (2\pi - \gamma) \tag{5.4}$$

$$cl_{SW} = r_i \cdot \gamma \tag{5.5}$$

The central angle (γ) is calculated taking into account the solid bed height (calculated according to the Saeman model):

$$\gamma = 2 \cdot \arccos\left(1 - \frac{h}{r_i}\right) \tag{5.6}$$

Since the cross-sectional area of the solid bed that is axially not constant, the hydraulic diameter (d_h) is used instead of the inner drum diameter as characteristic length for the convective heat transfer. This is calculated from the cross-sectional area of the gas and the circumference according to:

$$d_h = 4 \cdot \frac{A_G}{P_G} = 4 \cdot \frac{A_G}{cl_{GW} + cl_{GS}} \tag{5.7}$$

If sectional internals are installed, the calculation methods regarding the surface growth factors are applied as explained in Part III, chapter 4.3.1.

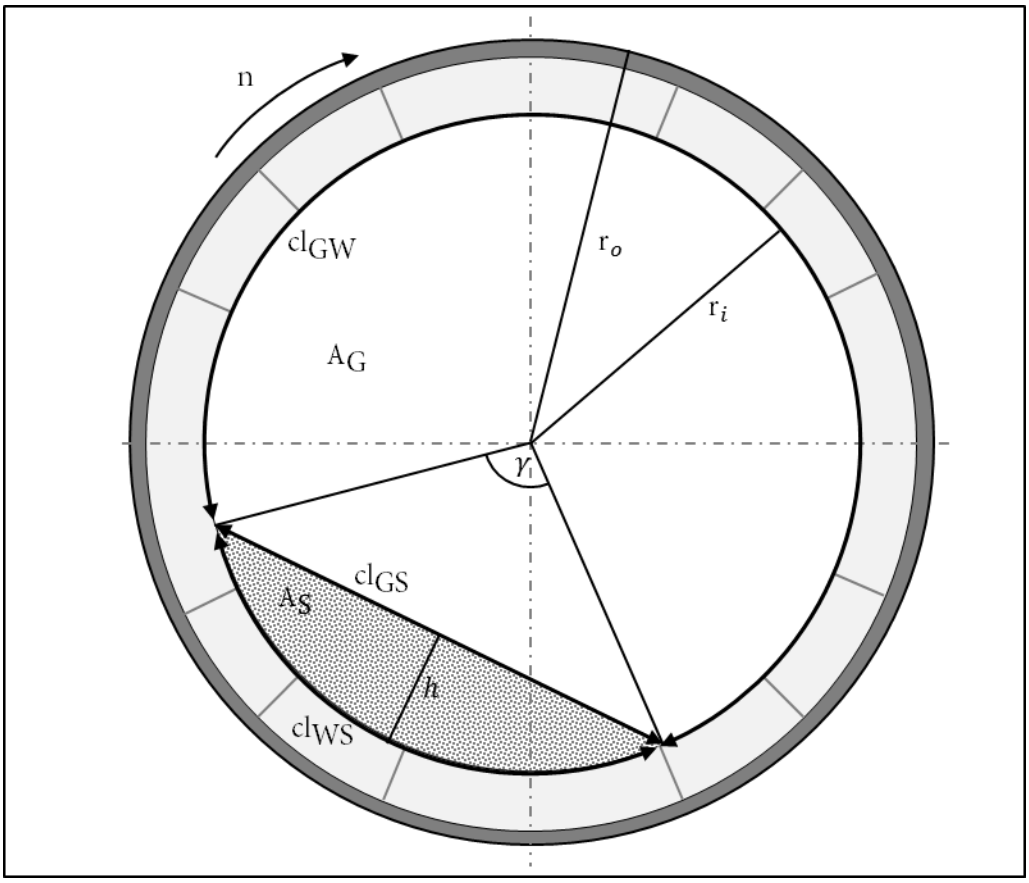

Figure V - 2.2: Geometric relationships in the cross section of a rotary drum without sectional internals

2.1.2 Heat transfer & heat balances

The heat transfer processes and the applied calculations are described in detail in Part IV of this work. The related contact lengths are determined as shown in the previous chapter.

To calculate the axial temperature profile of the gas phase, the change of the enthalpy or heat flux with the local mass flow and the specific heat capacity of the gas phase is required:

$$\frac{d\dot{H}_G}{dx} = \frac{d\dot{Q}}{dx} = \dot{m}_G \cdot c_{p,G}(T_G) \cdot \frac{dT_G}{dx} \tag{5.8}$$

For the calculation of the axial temperature profile of the solid bed with the local mass flow and the specific heat capacity of the solid bed follows in the same manner:

$$\frac{d\dot{H}_S}{dx} = \frac{d\dot{Q}_S}{dx} = \dot{m}_S \cdot c_{p,S}(T_S) \cdot \frac{dT_S}{dx} \tag{5.9}$$

The relationships in equations (5.8) and (5.9) contain temperature-dependent material characteristics and are therefore not linear.

2.1.3 Reaction modeling & mass balances

The reactions of the oxidization of mangetite to maghemite and the subsequent recrystallization to hematite have been described extensively in Part II of this work. The kinetic equations are given as ODE regarding the time and a transformation to ODEs regarding the axial length is required. The universal description of the conversion (X) regarding the time (t) is a function of the conversion, as shown in Part II:

$$\frac{dX}{dt} = f(X) \tag{5.10}$$

The equation can be extended with dx and rearranged subsequently, which leads to the introduction of the axial velocity of the solid or bulk material (v_S), as follows:

$$\frac{dX}{dx} \cdot \frac{dx}{dt} = f(X) \rightarrow \frac{dX}{dx} = \frac{f(X)}{v_S} \tag{5.11}$$

As functions regarding f(X) the models and data of Przepiera et al. for the oxidation and recrystallisation are used (AEG-A1 model) [47].

Additionally, the evaporation of water has to be taken into account as ‘pseudo-reaction’ (endothermic), since the feed material to the kiln includes a certain amount of moisture (~35%). The water evaporation is considered as a first order reaction [283]:

$$\frac{dc\left(H_2O(l)\right)}{dt} = -k_0 \cdot e^{-\frac{E_A}{RT}} \cdot c\left(H_2O(l)\right) \tag{5.12}$$

The activation energy is given with 42033.11 J/mol and the preexponential factor is 19666.67 s^{-1} [283] for an evaporation of free water. Potentially divergent drying kinetics would have to be investigated experimentally, since they are massively dependent on the material structure.

Summarizing, the following components change due to reactions (nomenclature and index in braces):

- Magnetite (M)
- Maghemite (Mh)
- Hematite (H)
- Oxygen (O2)
- Water (liquid: H2O; vapor: H2O_g)

The resulting mass balances regarding the species are calculated as molar balances and transformed to masses afterwards:

$$\frac{dn_M}{dx} = -\frac{dX_M}{dx} \cdot n_{M,start} \tag{5.13}$$

$$\frac{dn_{Mh}}{dx} = \frac{dn_M}{dx} \cdot \left(\frac{6}{-4}\right) - \frac{dX_{Mh}}{dx} \cdot n_{Mh} \tag{5.14}$$

$$\frac{dn_H}{dx} = \frac{dX_{Mh}}{dx} \cdot n_{Mh} \tag{5.15}$$

$$\frac{dn_{O_2}}{dx} = \frac{1}{4}\frac{dn_M}{dx} \tag{5.16}$$

$$\frac{dn_{H_2O}}{dx} = -\frac{k}{v_S} \cdot n_{H_2O} \tag{5.17}$$

2.2 Mathematical background

Different numeric methods can be applied in the solution of ODEs and ODE-systems. Runge-Kutta methods of different order are optimal in their accuracy with respect to the applied algorithm. The simplest method for the computation of initial value problems is the (forward) Euler method. This method is used during process modeling because of its simple adaptability (access to the functions for material data etc. in the algorithm is required) and will be briefly explained in the following. The task is to numerically solve an initial value problem in the interval $a \leq x \leq b$. Given is the (ordinary) differential equation (ODE) and the initial value (point $P_0(x_0;y_0)$) [286]:

$$y' = f(x, y) \tag{5.18}$$

The given interval is sliced into n small steps with the size δ [286]:

$$\delta = \frac{(b-a)}{n} \tag{5.19}$$

the approximate calculation of the function values of the solution curve "y = y(x)" is performed according to the following rule [286]:

$$y(x_i) \approx y_i = y_{i-1} + \delta \cdot f(x_{i-1}; y_{i-1}) \tag{5.20}$$

Starting from the given initial value $P_0(x_0;y_0)$, which is situated on the exact solution y = y(x), the solution in the first interval $x_0 \leq x \leq x_1$ is approximated by the tangent in point P_0.

The tangent's slope m_0 results from the differential equation $y' = f(x; y)$ by inserting the coordinates of the starting point P_0 as x and y values. The ordinate value at the point $x_1 = x_0 + \delta$ is calculated subsequently. The approximated calculation of the solution curve y = y(x) at the point x_2 is done analogously. The solution is then replaced in the interval $x_1 \leq x \leq x_2$ by a straight line passing through the point $P_1$and having the same slope as the tangent of the solution curve through P_1 at this point. The procedure is repeated in the described manner for the new starting point P_2, which is usually not situated on the exact solution. After a total of n calculation steps, the end point $P_n = (x_n; y_n)$ is reached. Figure V - 2.3 represents the procedure graphically.

The stepwise approximation of the exact solution y = y(x) by a straight line is a rough approximation, especially since the slope of the solution is considered at a single point, the left boundary position [286]. A sufficient accuracy of the approximation calculation is therefore only guaranteed for small step sizes. This is usually accompanied by a very high computational effort. In the present case, satisfactory results are obtained in an acceptable time period by using Euler's method and as a result, it is implemented in the process model.

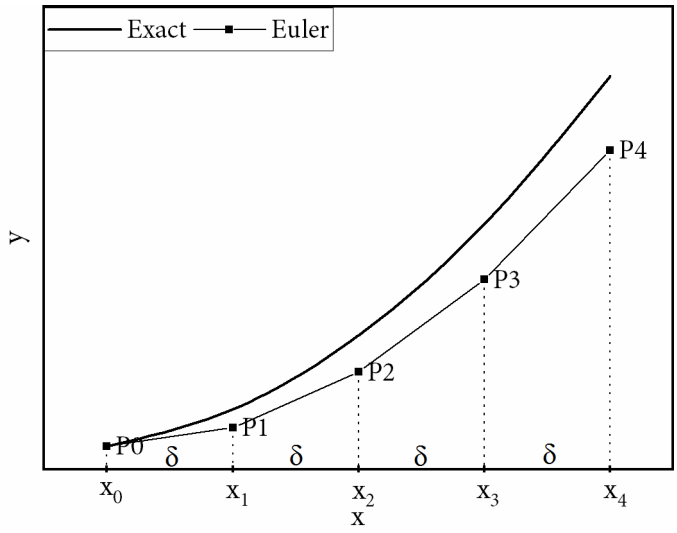

Figure V - 2.3: Exemplary sketch illustrating the Euler method. Adapted from [286]

2.3 Algorithm and programming

In the following, the structure of the developed algorithm to model the processes of the material and heat transport processes in a rotary kiln is described.

Figure V - 2.4 shows the flow chart of the modeling algorithm. In the first step, all relevant process parameters as well as the boundaries, geometries and initial conditions are defined. In this simulation, the solids volume flow is calculated according to the following empirical value:

$$\dot{V}_S = \frac{\dot{m}}{\rho_B} \cdot 1.4 \tag{5.21}$$

After the initiation the length is discretized and with the definition of the iteration parameter (step counter) i = 1 the first loop (Saeman loop) for the calculation of the axial fixed bed profile starts. This loop is solving the Saeman ODE utilizing the Euler method. Since there is no weir, setting the initial boundary condition (cf. Part III, ch. 2.3.2) for the bed height (h) to Bh(1) = 0.005 has proven to be effective. Additionally, the model is capable of the calculation of sectional internals according to the elaborations in Part III, ch. 4.3.2. The length of the sectioned part and the length of the bare drum part have to be provided in the program initiation as well as the number of applied sections.

Since the calculation direction of the Saeman equation is opposite to the motion direction of the solid, the calculated solid bed profile must be mirrored for further use in the model. Afterwards, the step counter (i) is reset to 1.

Analogously to the first (Saeman) loop, the second (balance) loop also realizes the Euler method to calculate the ODE-system provided by the considered processes. This first includes the calculation of the thermodynamic properties of the gas and the solids in each step (axial slice). Following, the determination of the cross-sectional areas, the contact length and the solid and gas velocities is performed. The reaction engineering calculations are performed according to the methods described in Part II (especially Part II, ch. 2.1.4.1 & 2.1.4.2). Afterwards, the mass balance (see chapter 2.1.3) as well as the mass transfer calculations are performed. In the next step the calculations of the heat transport processes (see Part IV) and the related heat balances (chapter 2.1.2) are calculated.

Finally, the results are printed or stored for further evaluation and visualization purposes.

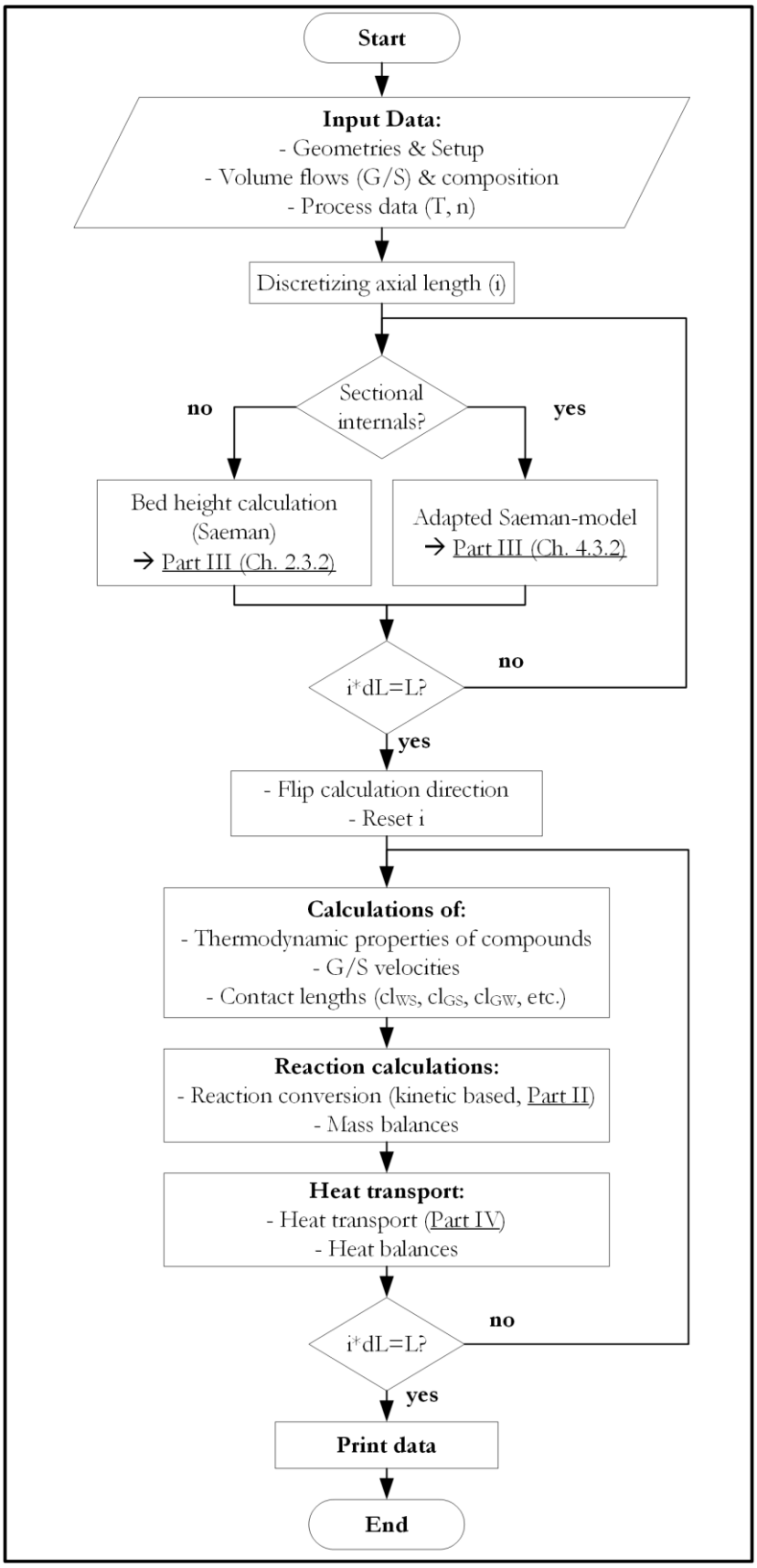

Figure V - 2.4: Flow chart of algorithm programmed in the process simulation

3 Results & Discussion

The results derived from the simulation runs with different parameter sets are presented in the following chapter.

3.1 Model validation

To check the process model against reality and validate it, measurements of the outer shell temperature (T_{OS}) were carried out at several axial points on the industrial reference kiln under operation. The results have been achieved with an IR-thermometer and are shown in Figure V - 3.1 compared to the results of the simulation. Since temperatures are fluctuating with the rotation of the kiln the minimum and maximum curve is indicated as grey area around the mean values. The kiln is operated in countercurrent flow of solids and gas, the solid flow direction is presented in Figure V - 3.1.

The initial boundary conditions specified in the simulation were matched to the real process regarding starting temperatures, operational parameters as feed mass flow and rotational speed and the geometries of the drum as diameter and length. The industrial kiln is divided in two parts in solid flow direction. The first part is equipped with lifters until a normalized length of 0.37, the second part is equipped with sectional internals. The transition is indicated as chain dotted line in Figure V - 3.1. Furthermore, the region of the drums tires (light grey) and the transmission sprocket (dark grey) are presented.

Up to the point where the internal structure changes (x/L=0.37), the shell temperature is rising continuously in simulation and measurements. For the industrial measurements, the maximum temperature is approx. 560 K at the transition point to sectional internals (x/L=0.37). The maximum shell temperature in the simulation is 550 K and slightly shifted into the sectional part (x/L=0.42). The operational measurements reveal a temperature drop afterwards, but settle in the range between 470 K and 510 K over subsequent kiln length. For the temperature curve of the simulation, a continuous drop to approx. 530 K can be observed after the temperature maximum. It is obvious, that for the industrial kiln the tires and the sprocket affect the shell temperature significantly, which is plausible.

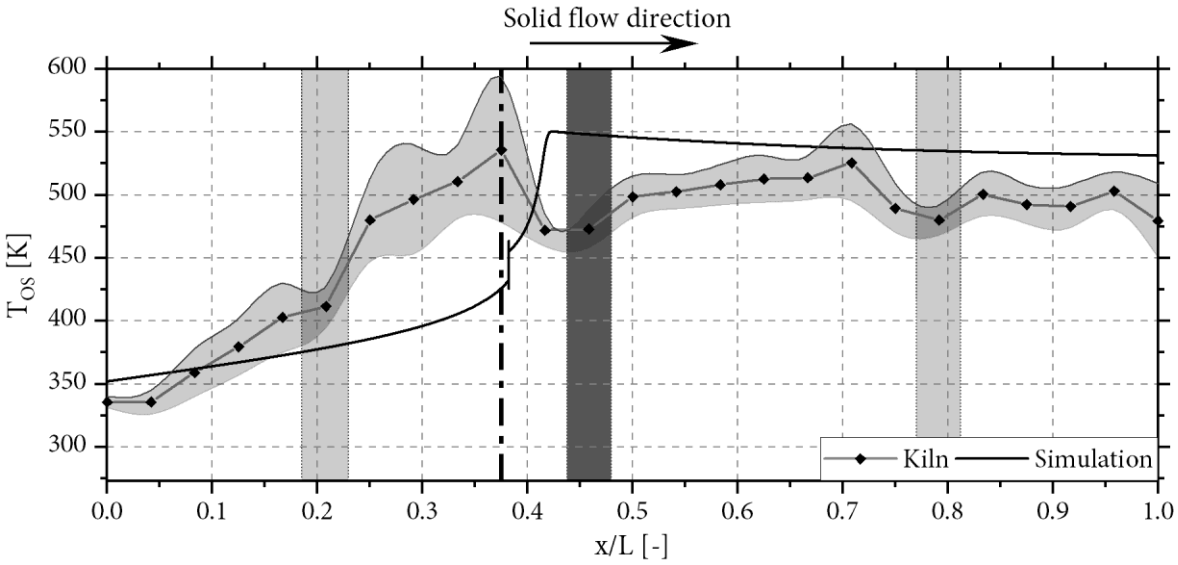

Figure V - 3.1: Measured and simulated axial temperature profile of the outer kiln shell. Vertical bars indicate kiln tires (light grey) and transmission sprocket (dark grey).

Although there are deviations from simulation to measured values the characteristic progress of the outer shell temperature is similar. Taking into account, that

- in the process model no lifters are considered in the first part,
- the reactions of trace elements (especially the highly exothermic oxidation of graphite) are not taken into account,
- the simulation excludes the tires and sprocket.

The congruence of simulation and industrial process is considered as reasonable. Although the potential of model improvements is given, the capability of the investigation of the impact of operational parameters is given.

3.2 Impact of operational parameters

A simulation for the (imaginary) bare drum configuration serves as basis for the sensitivity analysis, to compare the influence of the sectional internals in the further investigations.

The upper part of Figure V - 3.2 shows the axial progress of the solid bed height in the bare rotary kiln. A solid bed height of approx. 0.13 m can be found at the solid inlet end. Due to the axial movement of the bulk material outlet direction (x/L = 1), the solid bed height initially remains constant up to a standardized kiln length of approx. 0.7. Towards the outlet end, the solid material is discharged from the kiln and the initial boundary condition of the Saeman calculation

(h=0.005m) is observed. For the average residence time of the bulk material, a value of τ = 27 min is obtained over the entire length of the kiln.

In the middle part of Figure V - 3.2, the axial development of the gas, solid bed, inner wall and outer wall temperatures are shown. The gas-flow is countercurrent to the solids. The solids and the inner wall are heated up to a normalized kiln length of approx. 0.55. At the beginning of the furnace, the rise of the inner wall temperature is higher than the solids one. This is due to the larger surface area of the kiln wall in relation to the solid. The gas heats up from 1025 K (gas inlet side) to a maximum temperature of $T_{G,max}$= 1130 K. Heat is transferred to the free solids surface and the kiln lining and the temperature decreases to 523 K at the gas outlet side (initial boundary condition in the simulation). Magnetite is added to the rotary kiln with a starting temperature of 323 K (solid inlet). After the moisture in the solid is evaporated, the oxidation of magnetite begins and the released reaction enthalpy heats the solids rapidly to a maximum temperature of $T_{S,max}$ = 1240 K. In this process, the temperature of the solids exceed that of the inner wall. In the further progress to the outlet end, the solid bed releases heat to the gas as well as to the inner wall. This reduces the temperature of the solid to an outlet temperature of 1060 K. The outer wall temperature follows the inner wall temperature, but is at a lower temperature level due to the thermal insulation of kiln lining and shell.

The lower part of Figure V - 3.2 shows the axial progress of the reaction based on the mass fractions of the solid and the reactive gas components. The initial moisture is almost completely evaporated up to a normalized furnace length of approx. 0.45.

Oxidation of the magnetite starts at a length of about x/L=0.3 and the conversion to the intermediate maghemite proceeds very rapidly (up to about x/L=0.45). With complete conversion to maghemite, the transformation to hematite begins. The complete conversion is reached at a length of x/L=0.6. As a result of the oxidation, the mass fraction of oxygen in the gas phase decreases towards the inlet opening.

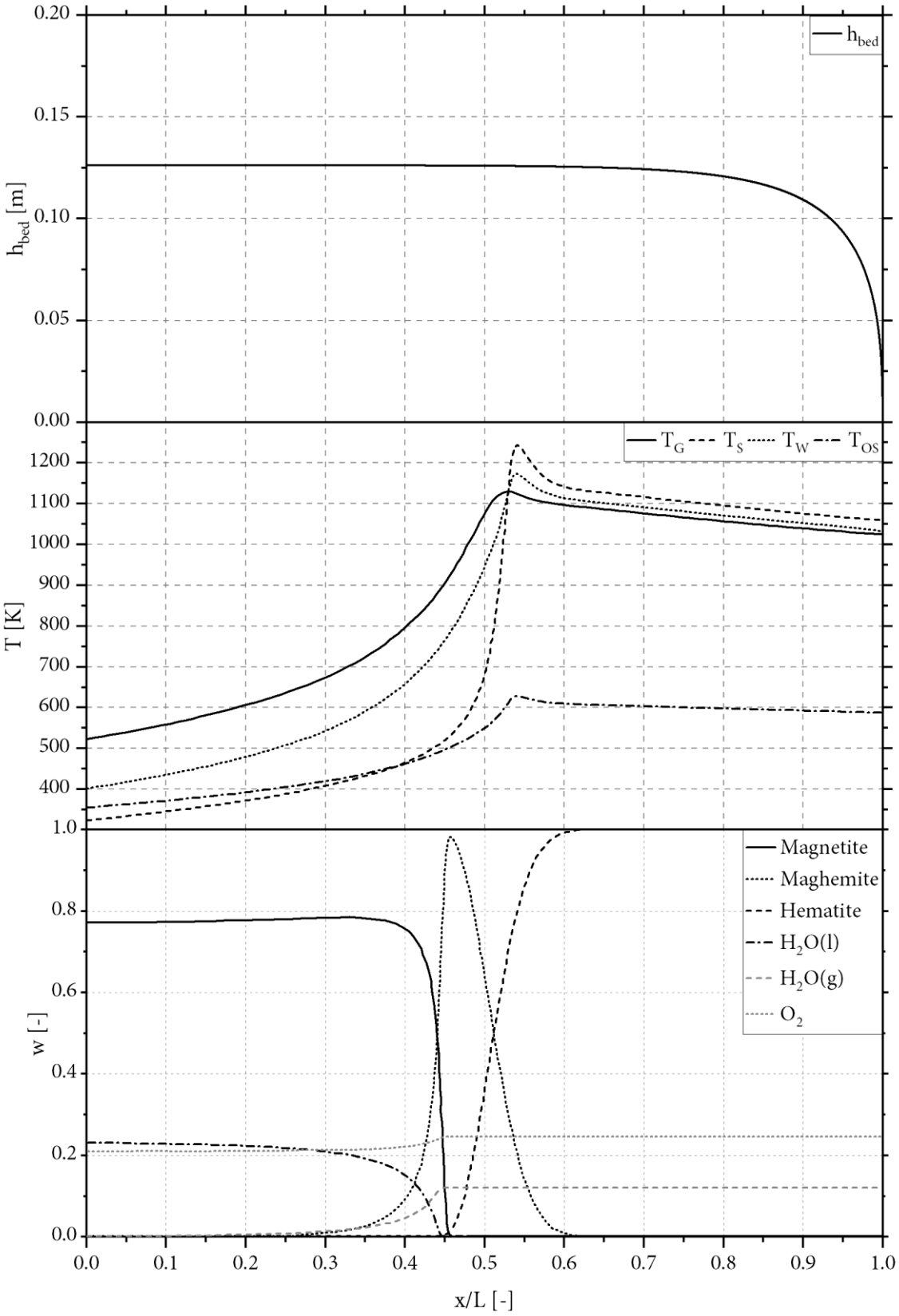

Figure V - 3.2: Axial progress of solid bed height (top), relevant temperatures (middle) and composition of solid and gas phase for a bare drum simulation.

3.2.1 Sensitivity regarding rotational speed (bare drum)

For the sensitivity analysis, the operating parameter rotational frequency (n) is first varied and the associated effects on the process are analyzed. Apart from the rotational frequency, all other process parameters were kept constant in accordance with the simulation in chapter 3.2. The upper part of Figure V - 3.3 presents the progresses of the axial solid bed height profile for a rotational frequency variation from n = 1 to n = 5 min^{-1}. The reduction of the rotational frequency leads to the increase of the axial solid bed height to about h = 0.21 m at the inlet end. Consequently, the GS-heat transfer surface becomes larger with lower rotational frequency and the average residence time increases to τ = 54 min at the same time. The highest setting of the rotational frequency to n = 5 min^{-1} results in a solid bed height of approx. h = 0.07 m and the integrated residence time is calculated to τ = 11 min. It can be seen in the lower part of Figure V - 3.3 that the maghemite conversion shifts toward the outlet end as the rotational frequency is increased. However, complete maghemite conversion is observed for all settings. For n= 1 min^{-1}, complete conversion is achieved at approx. x/L= 0.5. In contrast, for n = 5 min^{-1}, complete conversion is reached at approx. x/L=0.8. The characteristic progresses and slopes of the conversion curves are similar.

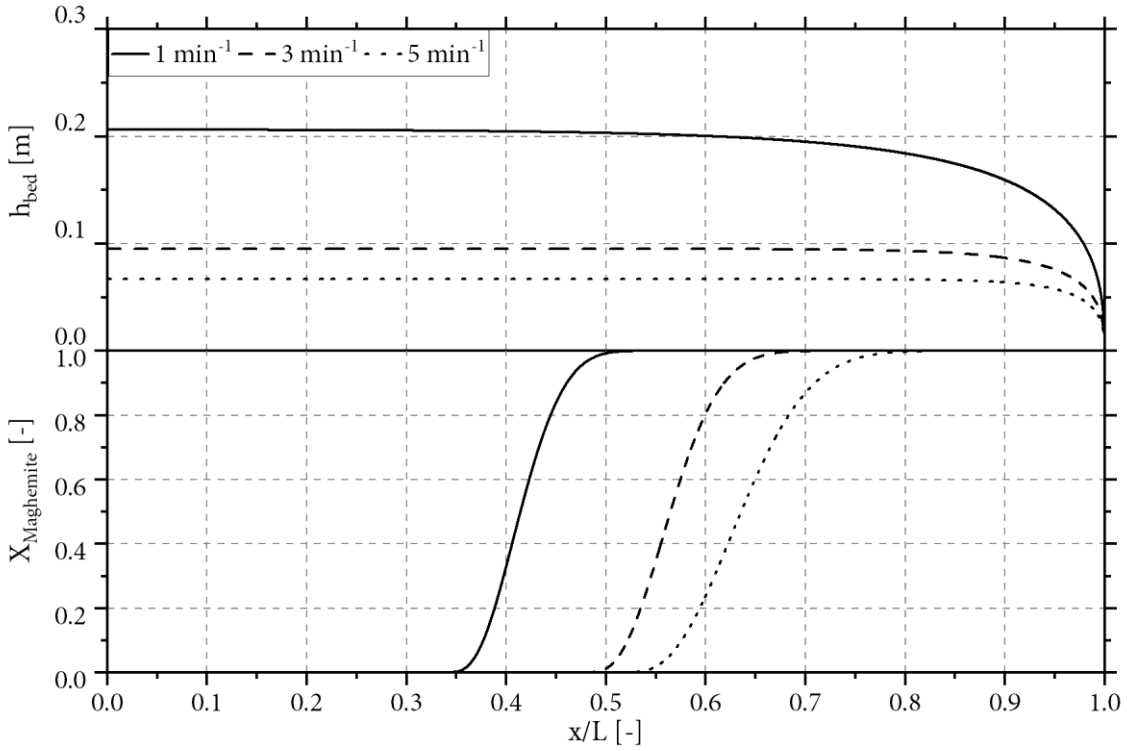

Figure V - 3.3: Sensitivity analysis regarding the rotational speed on the axial solid bed height profile and the axial conversion progress of maghemite in the kiln without sectional internals

3.2.2 Sensitivity regarding kiln inclination (bare drum)

In the second step, the axial kiln inclination (β) is varied (design parameter) as part of the sensitivity analysis and in order to analyze the associated effects on the process. Except for the inclination angle, all other parameters were kept constant, in accordance with the simulation in chapter 3.2. The upper part of Figure V - 3.4 presents the progresses of the axial solid bed height with variations of the inclination angle from β = 1° to β = 5°. Reducing the inclination angle to β = 1° results in a maximum solid bed height of about h = 0.2 m at the inlet end. With the solid bed height, the cumulated mean residence time also increases to τ = 47 min. Increasing the kiln inclination to β = 5° leads to a solid bed height of h = 0.06 m and the residence time with this setting is calculated to be τ = 11 min.

Comparably in the lower part of Figure V - 3.4 it can be seen that the maghemite conversion shifts toward the outlet as the inclination angle is increased. Complete maghemite conversion is observed for all settings. However, for high inclinations the conversion is just reached (x/L=1). The characteristic progresses and slopes of the conversion curves are also approximately similar here. In contrast to the rotational speed, the sensitivity of changes is higher regarding changes of the kiln inclination (cf. maghemite conversion).

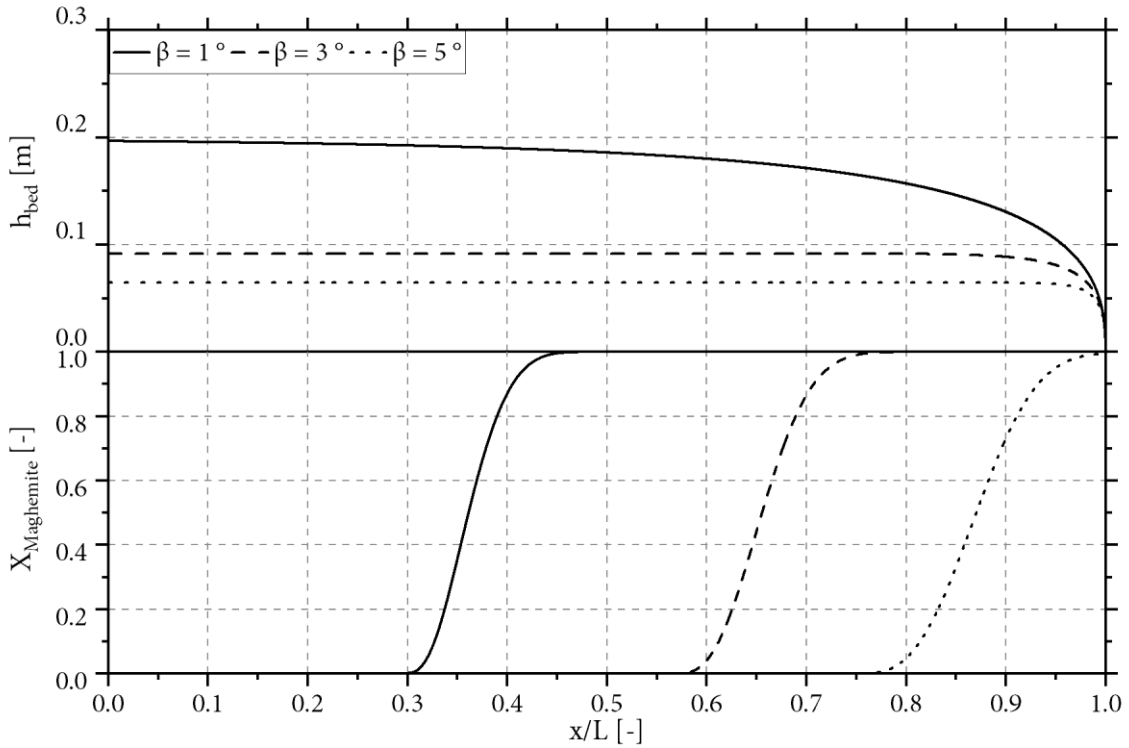

Figure V - 3.4: Sensitivity analysis regarding the axial kiln inclination on the axial solid bed height profile and the axial conversion progress of maghemite in the kiln without sectional internals

3.3 Impact of sectional internals

Figure V - 3.5 shows the simulation results for a rotary kiln with 12 sections, with other conditions equal to the bare drum simulation (Figure V - 3.2). The kiln is assumed to be equal to the process example for validation, in which the sections start at x/L=0.37 (vertical dashed line).

From the upper part of Figure V - 3.5 it can be seen that in the first part without internals (approximately up to x/L=0.37), a solid bed height of h=0.15 m is reached. The solids accumulate up to the transition to the second part with sections. The part with sections is characterized by a strong decrease of the solid bed height, since the solids are distributed to the single sections. In the second part, the solid bed height remains constant until almost the kiln outlet. Towards the outlet, the solids are discharged from the kiln analogously to the bare drum at the specified boundary condition of h 0.005m. The overall average residence time of the bulk material is calculated to τ = 94 min over the entire kiln length.

In the middle part of Figure V - 3.5, the axial temperature progresses are shown. The gas is also fed in countercurrent to the solid. Magnetite enters the rotary kiln at a temperature of 323 K at the solid inlet end. Up to a length of about x/L=0.37, the solid inner and outer wall temperatures increase moderately. The inner wall temperature has the highest system temperature in the area of the solid inlet and reaches a maximum temperature of approx. $T_{W,max}$ = 910 K. In the transition region from the bare drum to the sectional part, an increase of the inner and outer wall temperatures can be observed. This can be addressed to the discontinuity in the simulation calculation and the underlying equations at this point.

The solid heats up to a maximum temperature of approx. $T_{S,max}$ = 950 K due to the released reaction enthalpy after the oxidation of the magnetite and thus exceeds the inner wall temperature. In the further progress, the solid releases the heat to the gas as well as to the inner wall up to the solid outlet end. This reduces the solid temperature at the outlet end to 870 K. The outer wall temperature follows the inner wall temperature at a lower temperature level, as in the bare kiln.

The gas enters the kiln in countercurrent flow at a temperature of about 850 K and heats to a maximum temperature of about $T_{G,max}$ = 880 K. The heat transfer to the free surface of the bulk material and the kiln lining leads to the lowering of the gas temperature to 523 K (initial boundary condition), in accordance with the simulation of the bare drum.

The lower part of Figure V - 3.5 presents the axial reaction progress based on the mass fractions of the solid and the reactive components in the gas phase. The moisture in the solid is almost completely evaporated up to about x/L=0.425. Oxidation of the magnetite starts at approx. x/L=0.3.

Magnetite is completely converted to maghemite within to approx. x/L=0.43. With complete conversion to maghemite, conversion to hematite begins and is finished at approx. x/L=0.475. As a result of oxidation, the mass fraction of oxygen in the gas phase also decreases toward the inlet port. Compared to the bare drum, the sectional internals thus lead to a shift of the reaction zone towards the solid inlet of the kiln. The reaction takes place in the transition region from the bare drum part to the sectional part. Another striking feature is the overall lower temperature level compared to the bare kiln simulation (roughly 200K), which is due to the improved heat transfer surfaces. Thus, the thermal efficiency increases by the use of sectional internals.

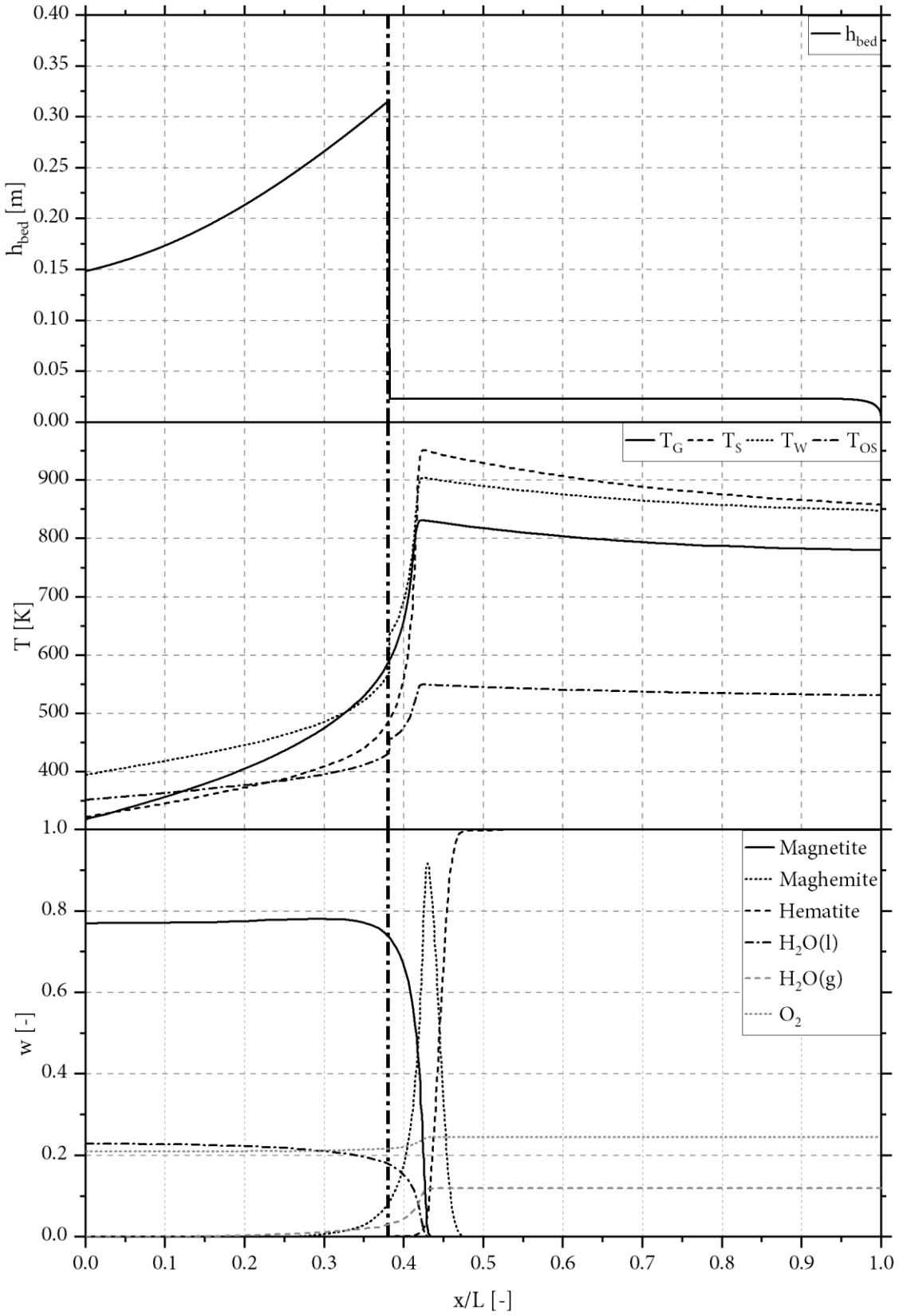

Figure V - 3.5: Axial progress of solid bed height (top), relevant temperatures (middle) and composition of solid and gas phase for a simulation of a rotary kiln with 12 sections. Sectional internals start at x/L=0.37 (indicated with vertical line).

3.3.1 Sensitivity regarding rotational speed (with sections)

For this sensitivity analysis, the operating parameter rotational frequency (n) is varied analogously to chapter 3.2.1 in order to analyze the associated process impact. Except the rotational frequency, all other process parameters were kept constant in accordance with the simulation in chapter 3.3.

The upper part of Figure V - 3.6 shows the progresses of the axial solid bed. It can be seen that the reduction in rotational frequency to n= 1 min^{-1} leads to an increase in the axial solid bed height to approx. h = 0.27 m at the inlet end of the kiln. At the same time, the cumulated mean residence time increases to τ = 156 min. The highest rotational frequency (n = 5 min^{-1}) results in a solid bed height of approx. h = 0.07 m, and the residence time is calculated to τ = 48 min.

It can be seen in the lower part of Figure V - 3.6, that the conversion of maghemite shifts toward the outlet end as the rotational frequency is increased. Equivalent to the bare drum simulation, full maghemite conversion is also observed for all settings. The progresses and slopes of the conversion curves are approximately similar. For n=1 min^{-1}, complete conversion is achieved at x/L =0.4 and thus earlier than without sectional internals. For the highest setting (n=5 min^{-1}), full conversion is reached at x/L=0.55.

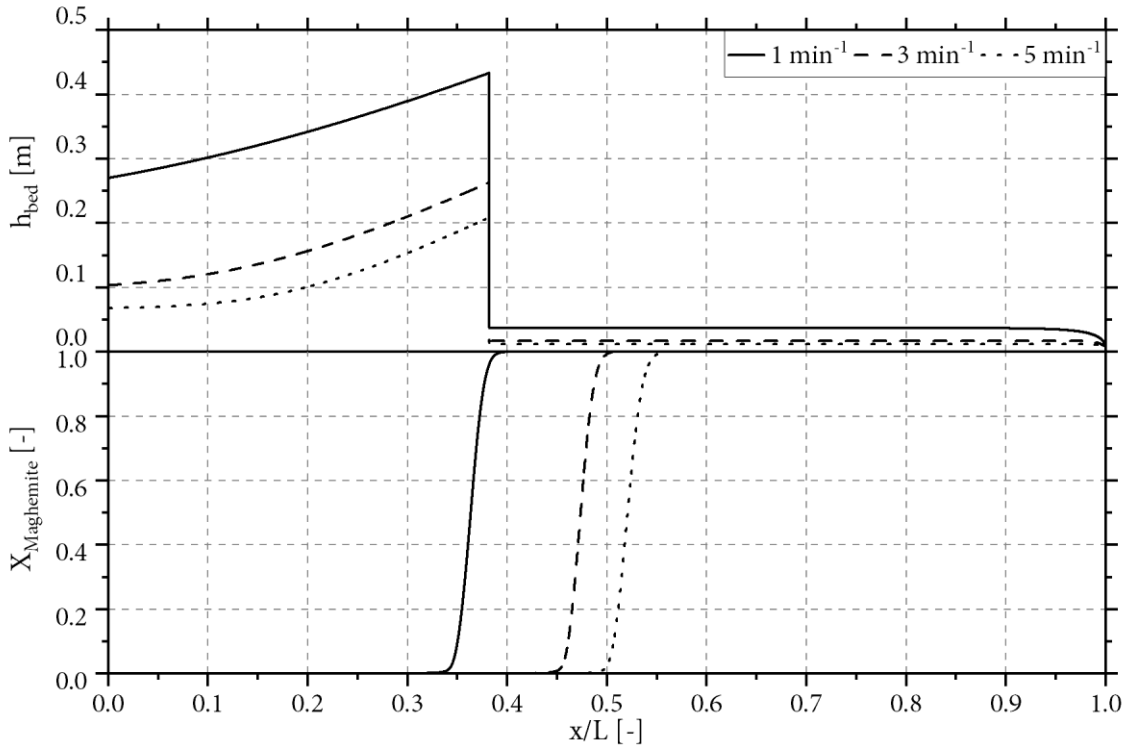

Figure V - 3.6: Sensitivity analysis regarding the rotational speed on the axial solid bed height profile and the axial conversion progress of maghemite in the kiln with sectional internals

3.3.2 Sensitivity regarding kiln inclination (with sections)

Equivalent to chapter 3.2.2, in the following the inclination angle (β) is varied as a design parameter in order to analyze the associated process impact. Again, all other parameters were kept constant in accordance with the simulation in chapter 3.3.

Figure V - 3.7 (upper part) shows, that the kiln inclination of β = 1° results in a maximum solid bed height of h = 0.33 m at the inlet end of the kiln. The mean residence time is τ = 156 min in this circumstances. Increasing the inclination angle to β = 5° results in a solid bed height of h = 0.06 m and the residence time reduces to τ = 43 min under this setting.

In analogy to Figure V - 3.4, the lower part of Figure V - 3.7 reveals that the maghemite conversion shifts towards the outlet kiln end as the inclination angle is increased. Complete maghemite conversion is also found for all settings. The lowest setting (β = 1°) results in full conversion at x/L= 0.33. In contrast, complete conversion is achieved at x/L=0.75 with β = 5°. The shapes of the conversion curves are also similar once more.

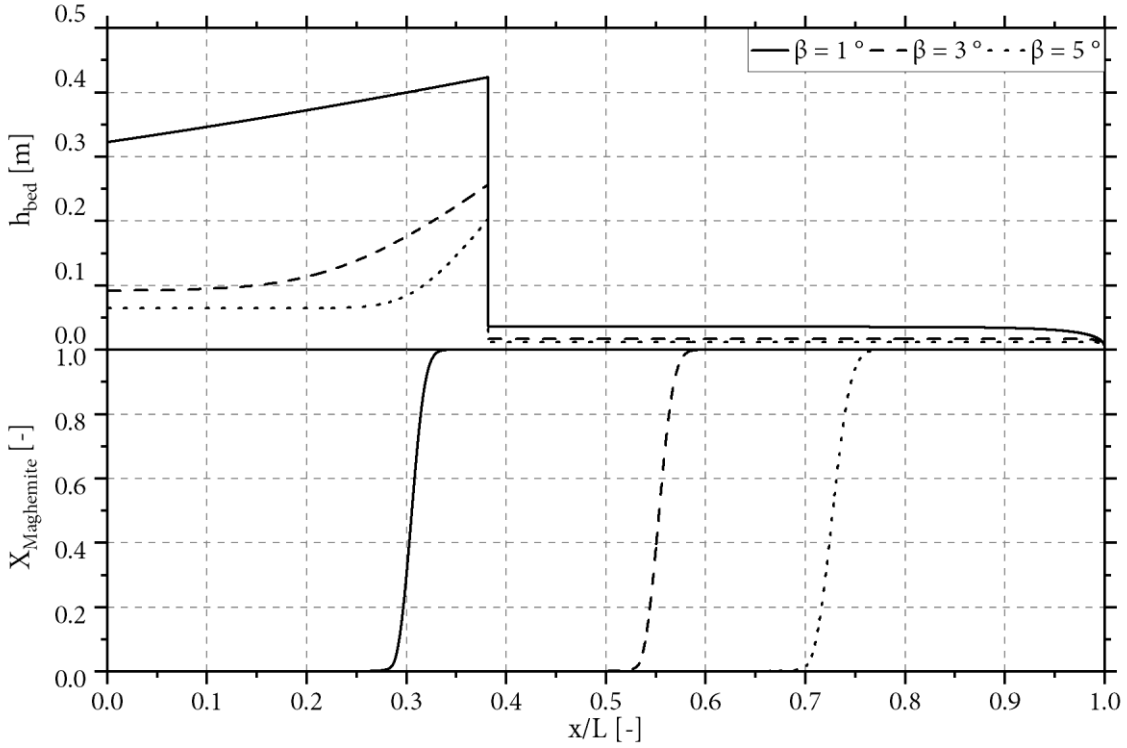

Figure V - 3.7: Sensitivity analysis regarding the rotary kiln inclination on the axial solid bed height profile and the axial conversion progress of maghemite in the kiln with sectional internals

3.3.3 Sensitivity regarding section number (with sections)

Finally, the number of sections is varied as a design parameter, with all other parameters kept constant according to the simulation in chapter 3.3.

Figure V - 3.8 (lower part) shows the maghemite conversion curves, when the number of sections is varied from N = 1 to N = 12. In this context, N = 1 indicates the bare rotary kiln without sections (cf. simulation in chapter 3.2). It is shown, that the increase in section number causes a shift of the maghemite conversion towards the kilns inlet end. The full maghemite conversion can be observed for all section numbers. The conversion curve of the bare kiln (N = 1) reveals a different characteristic progress compared to the conversion in kilns with sectional internals. The full maghemite conversion is reached at x/L=0.65 in the case of the bare kiln. In contrast, complete conversion is reached at x/L=0.45 with 12 sections. The characteristic progress of conversion is similar for all section numbers (except the bare drum).

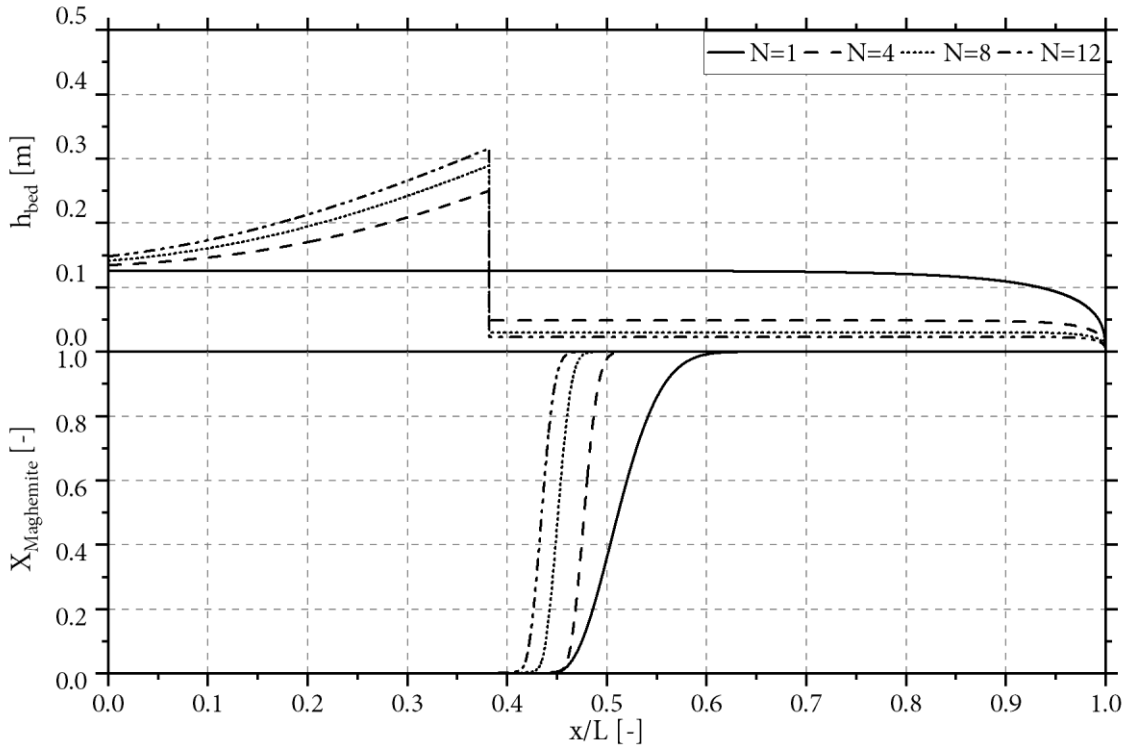

Figure V - 3.8: Sensitivity analysis regarding the number of sections (N) on the axial solid bed height profile and the axial conversion progress of maghemite in the kiln with sectional internals

4 Interim conclusion

In this part of the thesis, the industrial reference process (rotary kiln) was modeled using theoretical solution approaches. In this context, a mathematical model, which includes the phenomenology of chemical reaction, heat transfer and solid material transport inside a rotary kiln, was successfully developed.

The basis for the simulation of the overall process was initially the modeling of the axial solids transport inside the kiln. To do so, the gained knowledge of the experimental investigations in Part III of this thesis was incorporated. Thus, to the author's knowledge, for the first time a process model of a rotary kiln with sectional internals has been simulated in this work. The extent, to which these sectional internals contribute and impact to the kiln process have been calculated and visualized. With the material and energy balancing of infinitesimal axial kiln segments, the axial temperature profiles of the gas phase, the solid bed, the inner and outer walls, the conversion curves of the components as well as the axial solid bed height profile in the rotary kiln with and without sections were calculated.

In order to validate the process model, operational measurements of the outer shell temperature over the entire axial length were carried out on an industrial reference kiln. The comparison of the simulation results and measured data provides characteristically reasonable agreement for the axial temperature progress. Differences are assumed to be evoked by the missing lifter simulation in the process model and the missing carbon oxidation reaction.

Sensitivity analyses were performed for both process models (bare kiln & kiln with sections) to describe the influence of the design parameter (inclination angle) and the operating parameter (rotational frequency). It is known that both parameters have a rather indirect influence on the heat transport processes inside the rotary kiln. Both parameters are incorporated in the calculation of the axial height profile, which is followed by the calculation of the cross-sectional area of the solids and finally, with the inclusion of the solids volume flow, the determination of the solid velocity. The latter has a decisive impact on the residence times and consequently on the conversion progress. In both process models, it was shown that a low inclination angle and a low rotational frequency lead to an increase in the residence time. Accordingly, the high residence times are accompanied by a shift of the maghemite conversion towards the solid inlet end. Thus, a shorter kiln would be required for complete conversion. The influence of the number of sections on the process behavior becomes particularly clear when looking at the maghemite conversion curves in chapter 3.3.3. As

the number of sections increases, the conversion curves shift in the direction of the solid inlet end. This confirms the assumption that internals improve mass and heat transfer.

5 Outlook

As part of further work, the improvement and extension of the process model should be focussed. Further kiln internals and especially lifters should be incorporated in the model (improve comparability to industrial reference process). The influence of these lifters on the heat transport processes in the furnace should be described in future extensions of the process model.

Furthermore, the secondary reactions, including carbon combustion, were also not considered in the presented model. Since the combustion of even small amounts of carbon causes a high release of energy, the model should be enhanced in this respect. In order for this process model to be used in an industrial context, the model should be extended to include a flame model. Corresponding to the mass balances of the individual gas components, this model then results in further differential equations for describing the stoichiometric combustion of the fuel and local temperature differences.

By using the Avrami-Erofeev A3 kinetics model, good results were obtained in this work. However, the kinetics models and further influencing variables (especially Fe^{2+}/Fe^{3+}-ratio) investigated in Part II of this thesis are not incorporated yet. The implementation of these models should be the beginning of further work. Additionally, the implementation of other numerical solving methods (e.g. Runge-Kutta algorithms) should be pursued to avoid numerical instabilities and reduce calculation times.

Part VI Final conclusion

1 Summary

This thesis deals with the oxidation and calcination process in the rotary kiln during iron oxide pigment production according to the Laux process. The rotary kiln process is considered in its entirety, but particular attention is paid to the special design of the kiln/reactor with various internals and their effects. The findings based on the experimental work are universally valid and thus improve the general knowledge on rotary kilns with internals.

The overall approach is based on the decomposition of the kiln process into its individual phenomena and the subsequent combination of the findings in a mathematical model. To comply with the chosen approach and subsequent structure of the work the results have been summarized in the related parts of the work, to which reference is made here. The following is a condensed extract of these interim conclusions.

In Part II of the thesis ("Reactions in iron oxide conversion") a detailed literature review on the reactions from magnetite to maghemite to hematite is presented, elaborating the complexity of the reactions by the dependencies on the characteristics of the magnetite educt. Therefore, for a more detailed analysis, in an experimental part magnetite is prepared on laboratory scale with the precipitation process and the oxidation and subsequent recrystallization are studied by TG and DSC measurements. The focus is on the investigation on the reaction kinetics and it could be elaborated, that

- in the technically relevant range (>10 vol.% O_2) of the oxygen concentration there are no effects on the oxidation kinetics.
- no significant (kinetic) effects with respect to heating rates up to 20 K/min are observable.
- different activation energies (reaction behavior) are linked to the preparation of magnetites from different iron salts.
- industrial Laux magnetites reveal a significant difference to samples prepared by the precipitation method in the transformation temperatures from maghemite to hematite (about 150K higher).

The results further indicate the high influence of the Fe^{2+}/Fe^{3+}-ratio of the magnetite educt, especially on the heat balance of the reaction (enthalpy of oxidation).

The core part of the thesis (Part III) "Solid transport in rotary drums" focuses on the solid transport processes in rotary drums. In a literature review, the state of the art is elaborated, from which the

gap and thus the further need for investigations in the field of rotary drums with sectional internals emerged. In addition, questions are also raised in the area of rotary drums with lifters and in particular (axially) non-continuous lifters. For the subsequent experimental investigation of the solids transport, an apparatus was developed, which is highly modular and flexible regarding analyzing techniques (axial/transversal), applicable types of internals and their dimensions and further extensions as e.g. applications of gas flow analysis. Due to the construction in PMMA, visual insights into the rotary drum model are possible, which enables the analysis in the axial and transverse direction utilizing optical methods.

Concerning the axial solids transport, the effects of sectional internals, their length and also the number of sections are investigated. The main results can be summed up to:

- Sectional internals increase residence time.
- Sectional internals decrease the capacity.
- Sectional internals do not affect the axial dispersion.
- Sectional internals do not impact on the general dependencies on operational parameters.
- The Saeman-model could be adapted to describe sectional internals.

While the axial mixing (axial dispersion coefficients in the range 10^{-4} to 10^{-7} m^2/s) is comparable to the bare drum, the residence times increase significantly with sectional internals. This increase depends on the length and number of sections, which was quantified in an empirical equation on the basis of the measured data. In the opposite direction to the residence time, the capacity of the rotary kiln decreases due to sectional internals. The dependencies with respect to the operating parameters rotary speed, solids mass flow/throughput and the design parameter inclination angle are comparable to the bare drum. Visually, an analogy to the axial solid bed height profile for bare drums, which can be calculated according to Saeman, was observed for sectional internals. For the first time, the Saeman model was adapted for sectional internals and the validation of the developed method with the experimental data showed a very good agreement.

In the transverse direction, fundamentally different motion patterns could be observed compared to the bare drum. Regarding transversal transport the main results are:

- Sectional internals improve mixing kinetics
- Sectional internals improve mixing goodness for segregating particle systems
- Sectional internals increase exchange surfaces

The kinetics of the transverse solids mixing is faster (mixing rates k up to 7.9 1/rev) than in the bare drum, which could be attributed to the different mixing mechanism due to the periodic change of

the cross-sectional shape of the solid bed. For the same reason, an advantage of sectional internals could be found in terms of mixing goodness, especially for inhomogeneous bulk materials. The cross-section analysis also provided insights into the differences of exchange areas between gas, wall and solid bed when using sectional internals. These were also quantified as a function of section number using experimentally validated calculations and an empirical equation was established for calculation.

The analysis of axially discontinuous designed lifters showed a massive influence on the axial solids transport compared to continuous lifters. The axial dispersion increases up to one magnitude in direct comparison. Due to the influence of the (axial) design on the hold-up, the residence times are also affected significantly. These are in the range of the bare drum for axially segmented lifters, but are significantly increased for axially continuous lifters. Qualitative observations of the experimental analysis showed that the hold-up of axially segmented lifters is significantly worse, which was confirmed in transverse flow measurements. The solid sprinkling in the gas phase density is significantly lower and a clear relation to the axial length could be established. This phenomenon was further confirmed in model calculations, which are consistent with the experimental results. The effective loading for short lifters can be only <10% of the theoretical loading (continuous lifters) from which $\mathbf{L_L > 5 * L_r}$ (L_L=axial length; L_r=radial extent) was derived as a reasonable rule of thumb for the lifter design.

Part IV of the thesis deals with "Heat transport in rotary drums" and the processes occurring in a rotary kiln are described. For this purpose, approaches from literature were researched and adapted. A mathematical model containing all superimposed heat transport mechanisms is set up using the network method. The material-specific characteristics for the rotary kiln process and their temperature-dependent calculation methods are presented.

In Part V of the thesis ("Mathematical modeling"), all results from the previous parts are combined in an overall mathematical model of the rotary kiln process. For this purpose, the method of "cross-section modeling" is applied and the individual phenomena in the cross-section are described by means of differential equations according to the axial direction. The equations are solved using the newton method and the axial profile of temperatures and concentrations in the rotary kiln is determined. A validation with the industrial reference process shows reasonable agreement for the assumed general conditions. A sensitivity analysis of the operating and design parameters was

performed with the model. In particular, the influence of sectional internals, which was analyzed for the first time, has to be highlighted as a unique feature. It was possible to show how the processes determined in the solids transport analysis affect the shift of the reaction zones towards the solids input end. The use of sectional internals also reduces the temperature level in the kiln by approx. 200K due to the changed exchange surfaces for this process.

The main and superior objectives of this theses and the dedicated investigative work have been stated in the introduction in Part I. The main goals

- Gain information on the process and develop a deeper understanding of the rotary kiln process
- Investigate the impact of the used kiln internal structure and sectional internals in particular
- Develop a tool to predict the rotary kiln behavior and investigate the impact of different internal types
- Optimize the rotary kiln process if possible with the stated information

have been fully accomplished during the work, as the presented condensed results show.
Finally, this thesis provides an extensive insight into rotary drums with internals and the internal impact on the overall process. Finally, many different options and ideas to optimize the internals and the kiln process have been provided during the work, which leads to the outlook.

2 Outlook

Analogously to the previous summary, topic-related outlooks have been provided in the respective parts of the work and refernce is made to these specific outlooks.

Regarding Part II, the application of furhter analysing techniques (e.g. XRD) should be applied to elaborate the understanding of the reaction mechanisms and subsequently the reaction kinetics. In doing so, the quantifications of the magnetite characteristics on their kinetic behavior should be possible.

In the field of solids transport in rotary drums (Part III), experiments in different scales should be performed to validate and generalize the findings of this work. Additionally, more than the introduced internals (e.g. chains, guided flights etc.) are thinkable to investigate. Furthermore, the analysis of the gas flow should be taken into focus. First approaches to influence the gas flow have already been made in the work. With the developed apparatus and prerequisites, further experimental research is obvious. Promising potential in the optimization of the overall kiln process is estimated, especially if dedusting is also taken into account.

A main future goal related to the overall work should be the improvement of the presented process model (Part IV & Part V). Promising potential is estimated in the incorporation of influencing variables and effects in the process model to improve the accuracy. Especially the introduction of the Fe^{2+}/Fe^{3+}-ratio and the inclusion of further side reactions as carbon combustion should be pursued. Since pigment production is the incentive of the industrial reference process, the incorporation of color data will be a next big goal. However, the complexity of color measurements and derivation of predictions especially in combination with the known complexity of material properties requires extensive research work here.

Besides the model improvement further investigation of kiln processes in genereal should be pursued. Finally, due to the necessity of CO_2-reduction in the future, adaptions of the model to alternative heating concepts are thinkable. The chosen modular structure of the work enables the tracking of topic related next steps as well as the further elaboration of the overall process model in the future.

3 Symbols & Abbreviations

In the following the symbols and abbreviations are explained. Where possible, the general consensus of symbols was used. The indices are not introduced since they are self explanatory in the regarding consensus.

3.1 Latin

Symbol	Description	Unit
a	Temperature conductivity	$m^2 \cdot s^{-1}$
A	Area	m^2
c	Concentration	$mol \cdot L$
c_p	Heat capacity	$J \cdot (kg \cdot K)^{-1}$
C	Conductivity	$S \cdot m^{-1}$
C	Concentration (dimensionless)	-
cl	Contact length	m
d	Layer thickness	m
d_h	Hydraulic diameter	m
d_P	Particle diameter	m
D	Diffusion coefficient	$m^2 \cdot s^{-1}$
D	Diameter	m
E	Density distribution	various
E_A	Activation Energy	$J \cdot mol^{-1}$
f	Fraction	-
$f(x)$	Function	
F	Cumulative distribution	-
g	Gravitation constant (earth)	$m \cdot s^{-2}$
$g(x)$	Integrated rate law	-
G	(Thermal) conductivity	$W \cdot m^{-1}$
h	Height	m
H	Enthalpy	J
$\dot{H}$	Enthalpy flux	$J \cdot s^{-1}$
H_B	DSC-signal (baseline)	
H_S	DSC-signal	
k	Mass transfer coefficient	$m \cdot s^{-1}$
k	Heat transfer coefficient	$W \cdot (m \cdot K)^{-1}$
k	Rate constant	s^{-1}
k_0	Preexponential factor	s^{-1}
$k(x)$	Arrhenius function	-
l	Length	m
L	Length (drum)	m
m	Mass	kg
$\dot{m}$	Mass flow	$kg \cdot s^{-1}$
M	Molar mass	$kg \cdot mol^{-1}$
M	Lacey mixing index	-

Symbol	Description	Unit
mf	Mean fraction	-
n	Amount of substance	mol
n	Dispersion parameter (PSD)	-
n	Number / counter	-
n	Rotational speed/frequency	s^{-1}
N	Number / counter	-
$p(x)$	Temperature integral	-
$\dot{Q}$	Heat flux	$J \cdot s^{-1}$
$Q_0(x)$	Summarized PSD	-
r_C	Reaction core radius	m
R	Fe^{2+}/Fe^{3+}-ratio	-
R	Radius	m
R	(Thermal) resistance	$K \cdot W^{-1}$
R	Universal gas constant	$J \cdot (mol\ K)^{-1}$
$\dot{R}_F$	Heat flux fuel	$J \cdot s^{-1}$
s	Standad deviation (experimental)	various
s	Layer thickness	m
S	Surface	m^2
t	Time	s
$\bar{t}$	Mean residence time	s
T	Temperature	K
v	Velocity	$m \cdot s^{-1}$
V	Volume	m^3
$\dot{V}$	Volume flow	$m^3 \cdot s^{-1}$
x'	Location parameter (PSD)	m
X	Conversion	-

3.2 Greek

Symbol	Description	Unit
α	Heat transfer coefficient	$W \cdot (m^2 \cdot K)^{-1}$
β	Heating rate	$K \cdot s^{-1}$
β	Drum inclination	°
δ	Stoichiometry deviation	-
$\Delta_f H^0$	Standard heat of formation	$J \cdot mol^{-1}$
$\Delta_R H$	Reaction enthalpy	$J \cdot mol^{-1}$
Δm_{rel}	Specific/relative mass change	-
ρ	Density	$kg \cdot m^3$
ν	Stoichiometric coefficient	-
Φ	Filling degree	-
ω	Angular velocity	s^{-1}
σ	Standard deviation (theory)	Various
σ	Stefan Boltzmann constant	$W \cdot m^{-2} \cdot K^{-4}$
θ	Angle of repose	°
θ	Residence time (dimensionless)	-

Symbol	Description	Unit
τ_{hyd}	Hydrodynamic residence time	s
Δ	Difference (in combination)	-
λ	Length (dimensionless)	-
γ	Section angle	°
η	Dynamic viscosity	$Pa \cdot s$
λ	Thermal conductivity	$W \cdot (m \cdot K)^{-1}$
ϵ	Emissivity	-
φ	Rotation angle	°
φ	View factor	-
ν	Kinematic viscosity	$J \cdot s \cdot kg^{-1}$
γ	Central angle	°

3.3 Abbreviations

Abbreviation	Description
AEG	Avrami-Erofeev
AFC	Axial flow configuration
BET	Brunauer, Emmet, Teller (surface)
BS	Back spillage
BSR	Back spillage ratio
CFD	Computational fluid dynamics
CSS	Cross sectional shrinkage
DC	Drum configuration
DEM	Discrete element method
DOE	Design of experiments
DSC	Differential scanning calorimetry
DTA	Differential thermal analysis
EAD	Equal angular distribution
EHD	Equal horizontal distribution
Exp	Experiment
fcc	Face centered cubic
g	Gas
HU	Hold-up
IF	Increase factor
IR	Infrared
LED	Light emitting diode
LL	Long lifter
MC	Material combination
MGV	Mean grey value
MIF	Mean increase factor
MRT	Mean residence time
NL	No lifter
ODE	Ordinary differential equation
PI	Phase interface
PIV	Particle image velocimetry

Abbreviation	Description
R	Reaction
PMMA	Polymethylmetacrylate
PSD	Particle size distribution
rel	Relative
RRSB	Rosin, Rammler, Sperling, Bennet (PSD)
RTD	Residence time distribution
s	Solid
SEM	Scanning electron microscopy
SGF	Surface growth factor
SL	Short lifter
Std	Standard deviation
TEM	Transmission electron microscopy
TG	Thermogravimetry
TGA	Thermogravimetric analysis
UF	Used filling
w	Wall
XRD	X-ray diffraction
XRF	X-ray fluorescence

4 List of Publications

Peer-reviewed publications:

1. J. Priessen, T. Kawka, M. Behrens, H.J. Schultz, Cross-section-phenomena in rotary drums with sectional internals, Powder Technology 381 (2020) 229-244, DOI: 10.1016/j.powtec.2020.11.048
2. J. Priessen, T. Kreutzer, G. Irgat, M. Behrens, H.J. Schultz, Solid Flow in Rotary Drums with Sectional Internals: An Experimental Investigation, Chemical Engineering Technology 44 (2021) 300-309, DOI: 10.1002/ceat.202000148
3. J. Priessen, T. Kawka, J. Alisic, M. Behrens, H.J. Schultz, Rotary drums with sectional internals: Experimental investigation on the influence of section number and section length, Powder Technology 386 (2021) 262-274, DOI: 10.1016/j.powtec.2021.03.031
4. J. Priessen, F. Barths, M. Behrens, H.J. Schultz, The length of axially segmented lifters in flighted rotary drums: influence on solid transport, Drying Technology (accepted article), DOI: 10.1080/07373937.2021.1995408

Conference Proceedings:

1. J. Prießen, H.J. Schultz, Untersuchung und Optimierung eines industriellen Drehrohrofenprozesses zur Pigmentherstellung, Chemie Ingenieur Technik 90 (2018) 1175, DOI: 10.1002/cite.201855096
2. J. Prießen, K. Graf, M. Behrens, H.J. Schultz, Changes of phase interfaces in rotary drums with sectional internals, Chemie Ingenieur Technik 92 (2020) 1313, DOI: 10.1002/cite.202055134
3. J. Prießen, M. Behrens, H.J. Schultz, Solid transport in rotary drums with different internals, Chemie Ingenieur Technik 92 (2020) 1302, DOI: 10.1002/cite.202055139
4. J. Prießen, M. Behrens, H.J. Schultz, Mixing and segregation in rotary drums with sectional internals, Chemie Ingenieur Technik 92 (2020) 1313-1314, DOI: 10.1002/cite.202055135

Presentations / Talks:

1. 03/2019: Annual symposium ProcessNet Subject Division „Mischvorgänge", Essen, "Analyse von Feststofftransport- und Mischprozessen in Drehrohren"
2. 05/2019: „Masterseminar" Hochschule Niederrhein – Fachbereich Chemie, Krefeld, „Analyse von Feststofftransportprozessen in Drehrohen"
3. 03/2020: Annual symposium ProcessNet Subject Division „Mischvorgänge", Würzburg, "Untersuchung der axialen Vermischung in Drehrohren mit verschiedenen Einbauten"
4. 03/2020: Annual symposium ProcessNet Subject Division „Drying Technology", Frankfurt, "Analyse von Feststofftransportprozessen in Drehrohren mit verschiedenen Einbauten"
5. 03/2021: Annual symposium ProcessNet Subject Division „Mischvorgänge", Online, "Einfluss von Sektionaleinbauten auf das Mischungsverhalten im Querschnitt von Drehrohren"

In addition to the public presentations, 8 internal presentations/talks at University of Duisburg-Essen, Niederrhein University of Applied Sciences and Lanxess Deutschland GmbH have been given.

Posters:

1. 09/2018: Annual ProcessNet conference und 33rd annual DECHEMA Biotechnology conference, Aachen, „Untersuchung und Optimierung eines industriellen Drehrohrofenprozesses zur Pigmentherstellung"
2. 03/2019: 6th Promovendentag Niederrhein University of Applied Sciences, Mönchengladbach, "Determination of residence times in rotary tube equipment with different internals"
3. 03/2020: Annual symposium ProcessNet Subject Division „Mischvorgänge", Würzburg, "Untersuchung des Mischungsverhaltens im Querschnitt von Drehrohren mit verschiedenen Sektionaleinbauten"
4. 03/2020: Annual symposium ProcessNet Subject Division „Drying Technology", Frankfurt, "Mathematische und experimentelle Querschnittsanalyse von Drehrohren mit verschiedenen Sektionaleinbauten"
5. 09/2020: Annual ProcessNet conference und 34th annual DECHEMA Biotechnology conference, Online, "Mischung und Segregation in Drehrohren mit verschiedenen Sektionaleinbauten"

6. 09/2020: Annual ProcessNet conference und 34th annual DECHEMA Biotechnology conference, Online, “Veränderung der Phasengrenzfläche in Drehrohren durch Einsatz von Sektionaleinbauten“
7. 09/2020: Annual ProcessNet conference und 34th annual DECHEMA Biotechnology conference, Online, “Feststofftransport in Drehrohren mit unterschiedlichen Einbauten“
8. 03/2021: : Annual symposium ProcessNet Subject Division „Mischvorgänge”, Online, “Axialvermischung in Drehrohren mit Sektional- und Hubschaufeleinbauten“

5 References

[1] J. Laux, 8/2/1928, Verfahren zur Herstellung aromatischer Amine. (DE463773 (C)). DE.

[2] J. Laux, 12.01.1931, Verfahren zur Herstellung aromatischer Amine. (DE515758 (C)). Deutsches Reich.

[3] J. Laux, 20.08.1928, Verfahren zur Herstellung aromatischer Amine. (DE464561 (C)). Deutsches Reich.

[4] J. Laux, 29.01.1931, Verfahren zur Herstellung aromatischer Amine. (DE516999 (C)). Deutsches Reich.

[5] J. Laux, 21.02.1931, Verfahren zur Herstellung aromatischer Amine. (DE518929 (C)). Deutsches Reich.

[6] R.M. Cornell, U. Schwertmann, The iron oxides: Structure, properties, reactions, occurences and uses, 2nd ed., Wiley-VCH, Weinheim, 2003.

[7] G. Buxbaum (Ed.), Industrial inorganic pigments, 3rd ed., Wiley-VCH, Weinheim, 2005.

[8] H. Endriß (Ed.), Aktuelle anorganische Bunt-Pigmente, Vincentz, Hannover, 1997.

[9] E. Wiberg, N. Wiberg, G. Fischer, Lehrbuch der anorganischen Chemie, 102nd ed., Walter de Gruyter, Berlin, New York, 2007.

[10] F. Lagroix, S.K. Banerjee, M.J. Jackson, Geological Occurrences and Relevance of Iron Oxides, in: D. Faivre (Ed.), Iron Oxides, Wiley, 2016, pp. 7–30.

[11] R.E. Rosensweig, Magnetic Fluids, Annu. Rev. Fluid Mech. 19 (1987) 437–461.

[12] R. Lawaczeck, M. Menzel, H. Pietsch, Superparamagnetic iron oxide particles: contrast media for magnetic resonance imaging, Appl. Organometal. Chem. 18 (2004) 506–513.

[13] S. Bagheri, N.M. Julkapli, Modified iron oxide nanomaterials: Functionalization and application, Journal of Magnetism and Magnetic Materials 416 (2016) 117–133.

[14] K. Raj, R. Moskowitz, Commercial applications of ferrofluids, Journal of Magnetism and Magnetic Materials 85 (1990) 233–245.

[15] E. Riedel, Anorganische Chemie, 6th ed., de Gruyter, Berlin, 2004.

[16] R. Schrader, A. Simon, G. Ackermann, Untersuchungen an Magnettontrgern. I. Zur Kenntnis des Zusammenhanges der Struktur ferromagnetischer Eisenoxyde mit Dynamik und Kopiereffekt von Magnetophonbndern, Z. Anorg. Allg. Chem. 273 (1953) 65–83.

[17] T.W. Swaddle, P. Oltmann, Kinetics of the magnetite–maghemite–hematite transformation, with special reference to hydrothermal systems, Canadian Journal of Chemistry 58 (1980) 1763-1772.

[18] P.S. Sidhu, R.J. Gilkes, A.M. Posner, Mechanism of the low temperature oxidation of synthetic magnetites, Journal of Inorganic and Nuclear Chemistry 39 (1977) 1953–1958.

[19] L.S. Darken, R.W. Gurry, The System Iron—Oxygen. II. Equilibrium and Thermodynamics of Liquid Oxide and Other Phases, J. Am. Chem. Soc. 68 (1946) 798–816.

[20] L.S. Darken, R.W. Gurry, The System Iron-Oxygen. I. The Wüstite Field and Related Equilibria, J. Am. Chem. Soc. 67 (1945) 1398–1412.

[21] I.I. Diakonov, Thermodynamic properties of iron oxides and hydroxides. II. Estimation of the surface and bulk thermodynamic properties of ordered and disordered maghemite (γ-Fe203), ejm 10 (1998) 17–30.

[22] R.A. Robie, Hemingway Bruce S., Thermodynamic Properties of Minerals and Related Substances at 298.15 K and 1 Bar (10^5 Pascals) Pressure and at Higher Temperatures. U. S. Geological survey bulletin 2131, United States Government Printing Office, Washington, 1995.

[23] P.W. Atkins, J. de Paula, Physikalische Chemie, 5th ed., Wiley-VCH Verlag GmbH & Co. KGaA, Weinheim, 2013.

[24] Hemingway Bruce S., Thermodynamic properties for bunsenite, NiO, magnetite, Fe3O4 and hematite, Fe2O3, with comments on selected oxygen buffer reactions, American Mineralogist 75 (1990) 781–790.

[25] P. Kampeis, Chemische und verfahrenstechnische Untersuchungen zur Erzeugung ferrithaltiger Suspensionen im Hinblick auf einen Einsatz als Zusatzstoff für die Magnetseparation, Karlsruhe, 1998.

[26] M.E. Fleet, The structure of magnetite, Acta Crystallogr B Struct Crystallogr Cryst Chem 37 (1981) 917–920.

[27] J. Huber, Zur Natur von gamma-Fe2O3. Dissertation, Gießen, 2004.

[28] G.A. SAWATZKY, J.M.D. Coey, A.H. MORRISH, Mössbauer Study of Electron Hopping in the Octahedral Sites of Fe3O4, Journal of Applied Physics 40 (1969) 1402–1403.

[29] E.J.W. VERWEY, Electronic Conduction of Magnetite (Fe3O4) and its Transition Point at Low Temperatures, Nature 144 (1939) 327–328.

[30] E. Verwey, P.W. Haayman, Electronic conductivity and transition point of magnetite (“Fe3O4”), Physica 8 (1941) 979–987.

[31] A. Nielsen, Magnetit - ein Material für die Spinelektronik. Dissertation, München, 2009.

[32] K. Starke, Zur Struktur künstlicher Magnetite, Zeitschrift für Physikalische Chemie 42B (1939).

[33] C.-G. Nestler, A. Faust, B. Kämpfe, D. Lange, K. Hübner, Röntgenographische und chemische Untersuchungen zum Fehlordnungsgrad und zur Stöchiometrie von Magnetit, Krist. Techn. 9 (1974) K57-K60.

[34] M.E. Fleet, The structure of magnetite: defect structure II, Acta Crystallogr B Struct Crystallogr Cryst Chem 38 (1982) 1718–1723.

[35] R. Schrader, G. Büttner, Untersuchungen über y-Eisen(III)-oxid, Z. Anorg. Allg. Chem. 320 (1963) 205–219.

[36] C. Greaves, A powder neutron diffraction investigation of vacancy ordering and covalence in γ-Fe2O3, Journal of Solid State Chemistry 49 (1983) 325–333.

[37] I. David, J.E. Welch, The Oxidation of Magnetite and related spinels, Transactions of the Faraday Society (1956) 1642–1650.

[38] U. Colombo, G. Fagherazzi, F. Gazzarrini, G. Lanzavecchia, G. Sironi, Mechanisms in the First Stage of Oxidation of Magnetites, Nature 202 (1964) 175–176.

[39] W. Feitknecht, K.J. Gallagher, Mechanisms for the oxidation of Fe3O4, Nature (1970) 548–549.

[40] W. Feitknecht, H.W. Lehmann, Über die Oxydation von Magnetit zu y-Fe2O3, Helv. Chim. Acta 42 (1959) 2035–2039.

[41] U. Colombo, G. Fagherazzi, F. Gazzarrini, G. Lanzavecchia, G. Sironi, Mechanism of Low Temperature Oxidation of Magnetites, Nature 219 (1968) 1036–1037.

[42] W. Feitknecht, U. Mannweiler, Der Mechanismus der Umwandlung von y- zu a-Eisensesquioxid, Helvetica Chimica Acta 50 (1967) 570-581.

[43] K. Egger, Zur Oxydation natürlicher Magnetite : differenzthermoanalytische und röntgenographische Verfolgung des Reaktionsverlaufes (1963).

[44] K. Egger, W. Feitknecht, Über die Oxydation von Fe3O4 zu y- und a-Fe2O3: Die differenzthermoanalytische (DTA) und thermogravimetrische (TG) Verfolgung des Reaktionsablaufes an künstlichen Formen von Fe3O4, Helv. Chim. Acta 45 (1962) 2042–2057.

[45] K.J. Gallagher, W. Feitknecht, U. Mannweiler, Mechanism of oxidation of magnetite to y-Fe2O3, Nature (1968) 1118–1121.

[46] B. Gillot, A. Rousset, G. Dupre, Influence of Crystallite Size on the Oxidation Kinetics of Magnetite, Journal of Solid State Chemistry 25 (1978) 263–271.

[47] K. Przepiera, A. Przepiera, Kinetics of thermal transformations of precipitated magnetite and goethite, Journal of Thermal Analysis and Calorimetry (2001) 497–503.

[48] P.K. Gallagher, E.M. Gyorgy, H.E. Bair, An anomaly in the oxidation rate of magnetite at its Curie temperature, The Journal of Chemical Physics 71 (1979) 830–835.

[49] J.P. Sanders, P.K. Gallagher, Kinetics of the oxidation of magnetite using simultaneous TG/DSC, J Therm Anal Calorim 72 (2003) 777–789.

[50] E.R. Monazam, R.W. Breault, R. Siriwardane, Kinetics of Magnetite (Fe 3 O 4) Oxidation to Hematite (Fe 2 O 3) in Air for Chemical Looping Combustion, Ind. Eng. Chem. Res. 53 (2014) 13320–13328.

[51] M. Klepka, K. Lawniczak-Jablonska, M. Jablonski, A. Wolska, R. Minikayev, W. Paszkowicz, A. Przepiera, Z. Spolnik, R. van Grieken, Combined XRD, EPMA and X-ray absorption study of mineral ilmenite used in pigments production, Journal of Alloys and Compounds 401 (2005) 281–288.

[52] G. Schimanke, M. Martin, In situ XRD study of the phase transition of nanocrystalline maghemite (y-Fe2O3) to hematite (a-Fe2O3), Solid State Ionics (2000) 1235–1240.

[53] J. Adnan, W. O'Reilly, The transformation of y-Fe2O3 to a-Fe2O3: thermal activation and the effect of elevated pressure, Physics of the Earth and Planetary Interiors 110 (1999) 43–50.

[54] W. Feitknecht, Einfluss der Teilchengrösse auf den Mechanismus von Festkörperreaktionen, Pure and Applied Chemistry 9 (1964) 423–440.

[55] G.T. Schimanke, Zur kinetischen Stabilität von nanokristallinem Maghemit. Dissertation, Darmstadt, 2001.

[56] S. Grimm, T. Stelzner, J. Leuthäußer, S. Barth, K. Heide, Particle size effects on the thermal behaviour of maghemite synthesised by flame pyrolysis, Thermochimica Acta 300 (1997) 141–148.

[57] H.J. Cho, M. Tang, P.C. Pistorius, Magnetite Particle Size Distribution and Pellet Oxidation, Metall and Materi Trans B 45 (2014) 1213–1220.

[58] D. Papanastassiou, G. Bitsianes, Mechanisms and kinetics underlying the oxidation of magnetite in the induration of iron ore pellets, MT 4 (1973) 487–496.

[59] Ru-quan LIANG, Shuo YANG, Fu-sheng YAN, Ji-cheng HE, Kinetics of Oxidation Reaction for Magnetite Pellets, Journal of Iron and Steel Research 9 (2013) 16–20.

[60] O. Levenspiel, Chemical reaction engineering, 3rd ed., Wiley, Hoboken, NJ, 1999.

[61] R.A. Davis, Mathematical model of magnetite oxidation in a rotary kiln furnace, Can. J. Chem. Eng. 74 (1996) 1004–1009.

[62] R.A. Davis, D.J. Englund, Model and Simulation of a Ported Kiln for Iron Oxide Pellet Induration, Can. J. Chem. Eng. 81 (2003) 86–93.

[63] M. Tang, H.J. Cho, P.C. Pistorius, Early Gaseous Oxygen Enrichment to Enhance Magnetite Pellet Oxidation, Metall and Materi Trans B 45 (2014) 1304–1314.

[64] T.K. Sandeep Kumar, N.N. Viswanathan, H.M. Ahmed, C. Andersson, B. Björkman, Estimation of Sintering Kinetics of Oxidized Magnetite Pellet Using Optical Dilatometer, Metall and Materi Trans B 46 (2015) 635–643.

[65] J.D. Menczel, R.B. Prime (Eds.), Thermal analysis of polymers: Fundamentals and applications, Wiley, Hoboken, NJ, 2009.

[66] D.A. Skoog, J.J. Leary, Instrumentelle Analytik: Grundlagen - Geräte - Anwendungen, Springer, Berlin, Heidelberg, 1996.

[67] Thermische Analyse (TA) - Begriffe; Text Deutsch und Englisch, 2019th ed., Beuth, 2019.

[68] P.K. Gallagher, Thermomagnetometry, Journal of Thermal Analysis 49 (1997) 33–44.

[69] W. Smykatz-Kloss, S.J. St. Warne (Eds.), Thermal analysis in the geosciences, Springer, Berlin, 1991.

[70] Netzsch GmbH, Manual TG209 F1 Libra.

[71] Netzsch GmbH, Manual TG209 cell with TASC 414/3-Controller.

[72] G.W.H. Höhne, W.F. Hemminger, H.-J. Flammersheim, Differential Scanning Calorimetry, 2nd ed., Springer, Berlin, Heidelberg, 2003.

[73] Netzsch GmbH, Manual DSC 204 Phoenix.

[74] B. Wunderlich, Thermal analysis of polymeric materials, Springer, Berlin, 2005.

[75] A. Frick, C. Stern, DSC-Prüfung in der Anwendung, Hanser, München, 2006.

[76] Kunststoffe – Dynamische Differenz-Thermoanalyse (DSC): Teil 5: Bestimmung von charakteristischen Reaktionstemperaturen und -zeiten, Enthalpie und Umsatz, Beuth, 2014.

[77] A. Khawam, D.R. Flanagan, Basics and applications of solid-state kinetics: a pharmaceutical perspective, Journal of pharmaceutical sciences 95 (2006) 472–498.

[78] L. Papula, Mathematische Formelsammlung für Ingenieure und Naturwissenschaftler: Mit zahlreichen Rechenbeispielen und einer ausführlichen Integraltafel, 9th ed., Vieweg, Wiesbaden, 2006.

[79] G.H. Vogel, Lehrbuch Chemische Technologie: Grundlagen verfahrenstechnischer Anlagen, Wiley-VCH, Weinheim, 2004.

[80] A. Khawam, D.R. Flanagan, Solid-state kinetic models: Basics and mathematical fundamentals, The journal of physical chemistry. B 110 (2006) 17315–17328.

[81] Y. Han, Theoretical study of thermal analysis kinetics. Dissertation, Kentucky, 2014.

[82] V. Georgieva, L. Vlaev, K. Gyurova, Non-Isothermal Degradation Kinetics of CaCO 3 from Different Origin, Journal of Chemistry 2013 (2013) 1–12.

[83] S. Vyazovkin, C.A. Wight, Isothermal and Nonisothermal Reaction Kinetics in Solids: In Search of Ways toward Consensus, J. Phys. Chem. A 101 (1997) 8279–8284.

[84] S. Vyazovkin, C.A. Wight, Isothermal and non-isothermal kinetics of thermally stimulated reactions of solids, International Reviews in Physical Chemistry 17 (1998) 407–433.

[85] R. Gomez-Villacieros, L. Hernan, J. Morales, A. Ortega, J.L. Tirado, Limitations in the formal kinetic analysis of isothermal and thermogravimetric data, Thermochimica Acta 85 (1985) 287–290.

[86] P.D. Garn, S.F. Hulber, Kinetic Investigations by Techniques of Thermal Analysis, C R C Critical Reviews in Analytical Chemistry 3 (1972) 65–111.

[87] N. Liu, H. Chen, L. Shu, M. Statheropoulos, Error evaluation of integral methods by consideration on the approximation of temperature integral, J Therm Anal Calorim 81 (2005) 99–105.

[88] C.D. Doyle, Kinetic analysis of thermogravimetric data, J. Appl. Polym. Sci. 5 (1961) 285–292.

[89] C.D. Doyle, Estimating isothermal life from thermogravimetric data, J. Appl. Polym. Sci. 6 (1962) 639–642.

[90] C.D. DOYLE, Series Approximations to the Equation of Thermogravimetric Data, Nature 207 (1965) 290–291.

[91] G.I. Senum, R.T. Yang, Rational approximations of the integral of the Arrhenius function, Journal of Thermal Analysis 11 (1977) 445–447.

[92] V.M. Gorbachev, Linear and hyperbolic temperature programming in non-isothermal kinetics, Journal of Thermal Analysis 10 (1976) 191–194.

[93] J. Cai, L. Bi, Precision of the Coats and Redfern Method for the Determination of the Activation Energy without Neglecting the Low-Temperature End of the Temperature Integral, Energy Fuels 22 (2008) 2172–2174.

[94] A.W. Coats, J.P. Redfern, Kinetic Parameters from Thermogravimetric Data, Nature 201 (1964) 68–69.

[95] A.W. Coats, J.P. Redfern, Kinetic parameters from thermogravimetric data. II., Journal of Polymer Science Part B: Polymer Letters 3 (1965) 917–920.

[96] R. Ebrahimi-Kahrizsangi, M.H. Abbasi, Evaluation of reliability of Coats-Redfern method for kinetic analysis of non-isothermal TGA, Transactions of Nonferrous Metals Society of China 18 (2008) 217–221.

[97] J.J.M. Órfão, Review and evaluation of the approximations to the temperature integral, AIChE J. 53 (2007) 2905–2915.

[98] R. Robl, Über ferromagnetische Eisenoxyde, Angew. Chem. 70 (1958) 367–371.

[99] M.K. Shahid, S. Phearom, Y.-G. Choi, Synthesis of magnetite from raw mill scale and its application for arsenate adsorption from contaminated water, Chemosphere 203 (2018) 90–95.

[100] P. Tipsawat, U. Wongpratat, S. Phumying, N. Chanlek, K. Chokprasombat, S. Maensiri, Magnetite (Fe3O4) nanoparticles: Synthesis, characterization and electrochemical properties, Applied Surface Science 446 (2018) 287–292.

[101] V.P. Ponomar, Synthesis and magnetic properties of magnetite prepared by chemical reduction from hematite of various particle sizes, Journal of Alloys and Compounds 741 (2018) 28–34.

[102] A. Simon, G. Ackermann, Untersuchungen am Magnetogrammträger. III. Zur Kenntnis des Zusammenhanges zwischen Darstellungbedingungen von Magnetiten und y-Eisen(III)-oxyden und deren magnetischen Eigenschaften, Z. Anorg. Allg. Chem. 285 (1956) 309–321.

[103] U. Schwertmann, Über die Synthese definierter Eisenoxyde unter verschiedenen Bedingungen, Z. Anorg. Allg. Chem. 298 (1959) 337–348.

[104] Christina K. Vogt, Herstellung und Anwendung von Aggregaten aus oberflächenaktiven Nanopartikeln und Magnetit für den Einsatz in der Magnetseparation. Dissertation, Karlsruhe, 2006.

[105] A. Simon, H.-H. Emons, Untersuchungen am Magnetogrammträger. IX. Die Oxydation von Eisen(II)-hydroxyden und die Bildung von Magnetiten in Pufferlösungen, J. Prakt. Chem. 13 (1961) 163–176.

[106] A. Simon, H.-H. Emons, Untersuchungen am Magnetogrammträger. VIII. Die Bildung von Magnetiten aus a- und y-Eisen(III)-hydroxyden und Eisen(II)-hydroxyden, J. Prakt. Chem. 13 (1961) 106–116.

[107] S. Brunauer, P.H. Emmett, E. Teller, Adsorption of Gases in Multimolecular Layers, J. Am. Chem. Soc. 60 (1938) 309–319.

[108] Bestimmung der spezifischen Oberfläche von Feststoffen durch Gasadsorption nach Brunauer, Emmett und Teller (BET), Beuth, 1993.

[109] I.E. Dubois, S. Holgersson, S. Allard, M.E. Malmström, Dependency of BET surface area on particle size for some granitic minerals, Proceedings in Radiochemistry 1 (2011) 75–82.

[110] M. Stieß, Mechanische Verfahrenstechnik 1, 2nd ed., Springer, Berlin, Heidelberg, New York, 2005.

[111] A. Weibel, R. Bouchet, F. Boulc', P. Knauth, The Big Problem of Small Particles: A Comparison of Methods for Determination of Particle Size in Nanocrystalline Anatase Powders, Chem. Mater. 17 (2005) 2378–2385.

[112] Darstellung von Korn-(Teilchen-)größenverteilungen: RRSB, Beuth, 1976.

[113] K. Leschonski, W. Alex, B. Koglin, Teilchengrößenanalyse. 1. Darstellung und Auswertung von Teilchengrößenverteilungen (Fortsetzung), Chemie Ingenieur Technik 46 (1974) 101–106.

[114] G. Jander, K.F. Jahr, G. Schulze, J. Simon, R. Martens-Menzel, Maßanalyse: Titrationen mit chemischen und physikalischen Indikationen, 19th ed., de Gruyter, Berlin, Boston, 2017.

[115] U.R. Kunze, G. Schwedt, Grundlagen der qualitativen und quantitativen Analyse: 25 Tabellen, 5th ed., Wiley-VCH, Weinheim, 2002.

[116] P.K. Gallagher, Applications of thermoanalytical methods to the study of thin films, Journal of Thermal Analysis 38 (1992) 17–26.

[117] F. Hund, Inorganic Pigments: Bases for Colored, Uncolored, and Transparent Products, Angew. Chem. Int. Ed. Engl. 20 (1981) 723–730.

[118] Frederick Ransome, 20.04.1886, Manufacturing Cement. (340357). United States of America.

[119] A.A. Boateng, Rotary kilns: Transport phenomena and transport processes, Elsevier/Butterworth-Heinemann, Amsterdam, 2008.

[120] W.H. Duda, Cement-data-book, 3rd ed., Bauverl., Wiesbaden, 1985.

[121] H. Helmrich, K. Schügerl, Drehrohrreaktoren in der Chemietechnik, Chemie Ingenieur Technik 51 (1979) 771–778.

[122] N. Narçin, S. Aydln, K. Şeşen, F. Dikeç, Reduction of iron ore pellets with domestic lignite coal in a rotary tube furnace, International Journal of Mineral Processing 43 (1995) 49–59.

[123] G. Vogt, Verfahrenstechnische Entwicklungen des Röstens im Drehrohrofen, Chemie Ingenieur Technik 35 (1963) 48–54.

[124] S. Kuhnke, K. Peters, Hochtemperaturtechnik, Chemie Ingenieur Technik 64 (1992) 964–967.

[125] W. Kaminsky, H. Sinn, J. Janning, Technische Prototypen für die Altreifen-und Kunststoff-Pyrolyse, Chemie Ingenieur Technik 51 (1979) 419–429.

[126] J. Otschik, T. Jentsch, H. Bätz, Modellierung und Messung des Feststofftransportes in Drehrohren zur Pyrolyse von Hausmüll, Chemie Ingenieur Technik 69 (1997) 1293–1294.

[127] H.-J. Gehrmann, Mathematische Modellierung und experimentelle Untersuchungen zur Pyrolyse von Abfällen in Drehrohrsystemen. Dissertation, Weimar, 2005.

[128] J. Mellmann, L. Hoyer, T. Rensch, Mathematisches Modell und experimentelle Untersuchungen zur thermischen Bodenreinigung in Drehrohröfen, Chemie Ingenieur Technik 65 (1993) 1102–1103.

[129] J. Scholz, B.G. Müller, J. Schwedes, W.-D. Deckwer, Einsatz eines Drehtrommelreaktors mit Mahlkugeln zur mikrobiologischen Bodensanierung, Chemie Ingenieur Technik 70 (1998) 431–435.

[130] T. Ginsberg, Dynamische Modellierung von Drehrohröfen. Dissertation, Aachen, 2010.

[131] J. Prießen, H.J. Schultz, Untersuchung und Optimierung eines industriellen Drehrohrofenprozesses zur Pigmentherstellung, Chemie Ingenieur Technik 90 (2018) 1175.

[132] Z. Yi, H. Xiao, J. Song, G. Ma, J. Zhou, Mathematic simulation of heat transfer and operating optimization in alumina rotary kiln, J. Cent. South Univ. 20 (2013) 2775–2780.

[133] E. Specht, F.H. Becker, Drehrohröfen, in: K.-H. Grote, J. Feldhusen (Eds.), Dubbel, Springer Berlin Heidelberg, Berlin, Heidelberg, 2014, pp. 690–699.

[134] J.D. Sullivan, C.G. Maier, O.C. Ralston, Passage of solid particles through rotary cylindrical kilns, U.S. Bur. Mines, Tech. Paper 384 (1927) 1–42.

[135] H. Henein, J.K. Brimacombe, A.P. Watkinson, Experimental study of transverse bed motion in rotary kilns, Metall and Materi Trans B (1983) 191–205.

[136] H. Henein, J.K. Brimacombe, A.P. Watkinson, The modeling of transverse solids motion in rotary kilns, Metallurgical Transactions B (1983) 207–220.

[137] W.R.A. Vauck, H.A. Müller, Grundoperationen chemischer Verfahrenstechnik, 11th ed., Dt. Verl. für Grundstoffindustrie, Stuttgart, 2000.

[138] J. Mellmann, The transverse motion of solids in rotating cylinders - forms of motion and transition behavior, Powder Technology 118 (2001) 251–270.

[139] M. Stieß, Mechanische Verfahrenstechnik 2, Springer, Berlin, 1994.

[140] J. Mellmann, E. Specht, X. Liu, Prediction of rolling bed motion in rotating cylinders, AIChE J. 50 (2004) 2783–2793.

[141] J. Perron, R.T. Bui, Rotary cylinders: Transverse bed motion prediction by rheological analysis, Can. J. Chem. Eng. 70 (1992) 223–231.

[142] A.A. Boateng, Boundary layer modeling of granular flow in the transverse plane of a partially filled rotating cylinder, International Journal of Multiphase Flow 24 (1998) 499–521.

[143] S. Dissanayake, S. Karunarathne, J. Lundberg, L.-A. Tokheim, CFD Study of Particle Flow Patterns in a Rotating Cylinder Applying OpenFOAM and Fluent, in: Linköping Electronic Conference Proceedings, Proceedings of the 58th Conference on Simulation and Modelling (SIMS 58) Reykjavik, Iceland, September 25th – 27th, 2017. CFD study of Particle Flow Patterns in a Rotating Cylinder Applying OpenFOAM and Fluent, Linköping University Electronic Press, 2017, pp. 137–143.

[144] D.A. Santos, M.A. Barrozo, C.R. Duarte, F. Weigler, J. Mellmann, Investigation of particle dynamics in a rotary drum by means of experiments and numerical simulations using DEM, Advanced Powder Technology 27 (2016) 692–703.

[145] H. V, Mathematical Modelling of the Dynamics of Granular Materials in a Rotating Cylinder. PhD-Thesis, Thiruvananthapuram, 2003.

[146] A.A. Boateng, P.V. Barr, Modeling of particle mixing and segregation in the transverse plane of a rotary kiln, Chemical Engineering Science 51 (1996) 4167–4181.

[147] R. Hogg, Mixing and Segregation in Powders: Evaluation, Mechanisms and Processes, KONA 27 (2009) 3–17.

[148] pne (Ed.), MHBD080-21[57-140] qxd.

[149] J.M. Ottino, D.V. Khakhar, Mixing and Segregation of Granular Materials, Annu. Rev. Fluid Mech. (2000) 55–91.

[150] R.J. Brandao, R.M. Lima, R.L. Santos, C.R. Duarte, M.A. Barrozo, Experimental study and DEM analysis of granular segregation in a rotating drum, Powder Technology 364 (2020) 1–12.

[151] A.I. Nafsun, F. Herz, E. Specht, H. Komossa, S. Wirtz, V. Scherer, X. Liu, Thermal bed mixing in rotary drums for different operational parameters, Chemical Engineering Science 160 (2017) 346–353.

[152] I.A. Resende, M.V.C. Machado, C.R. Duarte, M.A.S. Barrozo, An experimental analysis of coffee beans dynamics in a rotary drum, Can. J. Chem. Eng. 95 (2017) 2239–2248.

[153] X. Liu, C. Zhang, J. Zhan, Quantitative comparison of image analysis methods for particle mixing in rotary drums, Powder Technology 282 (2015) 32–36.

[154] D.V. Khakhar, J.J. McCarthy, T. Shinbrot, J.M. Ottino, Transverse flow and mixing of granular materials in a rotating cylinder, Physics of Fluids 9 (1997) 31–43.

[155] G.J. Finnie, N.P. Kruyt, M. Ye, C. Zeilstra, J. Kuipers, Longitudinal and transverse mixing in rotary kilns: A discrete element method approach, Chemical Engineering Science 60 (2005) 4083–4091.

[156] T. Haeldermans, M.A. Lataf, G. Vanroelen, P. Samyn, D. Vandamme, A. Cuypers, K. Vanreppelen, S. Schreurs, Numerical prediction of the mean residence time of solid materials in a pilot-scale rotary kiln, Powder Technology 354 (2019) 392–401.

[157] A. Chatterjee, A.V. Sathe, M.P. Srivastava, P.K. Mukhopadhyay, Flow of materials in rotary kilns used for sponge iron manufacture: Part I. Effect of some operational variables, MTB 14 (1983) 375–381.

[158] A. Chatterjee, A.V. Sathe, P.K. Mukhopadhyay, Flow of materials in rotary kilns used for sponge iron manufacture: Part II. Effect of kiln geometry, MTB 14 (1983) 383–392.

[159] A. Chatterjee, P.K. Mukhopadhyay, Flow of materials in rotary kilns used for sponge iron manufacture: Part III. Effect of ring formation within the kiln, MTB 14 (1983) 393–399.

[160] W.C. Saeman, Passage of solids through rotary kilns: factors affecting time passage., Chemical Engineering Progress 47 (1951) 508–514.

[161] X.Y. Liu, E. Specht, Mean residence time and hold-up of solids in rotary kilns, Chemical Engineering Science 61 (2006) 5176–5181.

[162] H. Kramers, P. Croockewit, The passage of granular solids through inclined rotary kilns, Chemical Engineering Science 1 (1952) 259–265.

[163] L. Vàhl, W.G. Kingma, Transport of solids through horizontal rotary cylinders, Chemical Engineering Science 1 (1952) 253–258.

[164] X.Y. Liu, J. Zhang, E. Specht, Y.C. Shi, F. Herz, Analytical solution for the axial solid transport in rotary kilns, Chemical Engineering Science 64 (2009) 428–431.

[165] S. Ngako, R. Mouangue, S. Caillat, A. Kuitche, E. Saragba, Numerical investigation of bed depth height, axial velocity and mean residence time of inert particles in steady state industrial cement rotary kiln: Case of Figuil Plant in Cameroon, Powder Technology 271 (2015) 221–227.

[166] M. Danish, S. Kumar, S. Kumar, Exact analytical solution for the bed depth profile of solids flowing in a rotary kiln, Powder Technology 230 (2012) 29–35.

[167] E. Specht, Y.-C. Shi, H. Woche, J. Knabbe, U. Sprinz, Experimental investigation of solid bed depth at the discharge end of rotary kilns, Powder Technology 197 (2010) 17–24.

[168] H.-J. Bartsch, Taschenbuch mathematischer Formeln für Ingenieure und Naturwissenschaftler: Für Studium und Beruf, 23rd ed., Fachbuchverl. Leipzig im Hanser-Verl., München, 2014.

[169] N. Descoins, J.-L. Dirion, T. Howes, Solid transport in a pyrolysis pilot-scale rotary kiln: Preliminary results—stationary and dynamic results, Chemical Engineering and Processing: Process Intensification 44 (2005) 315–321.

[170] L.G. Ndiaye, S. Caillat, A. Chinnayya, D. Gambier, B. Baudoin, Application of the dynamic model of Saeman to an industrial rotary kiln incinerator: Numerical and experimental results, Waste management (New York, N.Y.) 30 (2010) 1188–1195.

[171] D.M. Scott, J.F. Davidson, S.-Y. Lim, R.J. Spurling, Flow of granular material through an inclined, rotating cylinder fitted with a dam, Powder Technology 182 (2008) 466–473.

[172] P.V. Danckwerts, Continuous flow systems, Chemical Engineering Science 2 (1953) 1–13.

[173] E.B. Nauman, Residence Time Theory, Ind. Eng. Chem. Res. 47 (2008) 3752–3766.

[174] R.G. Sherritt, J. Chaouki, A.K. Mehrotra, L.A. Behie, Axial dispersion in the three-dimensional mixing of particles in a rotating drum reactor, Chemical Engineering Science 58 (2003) 401–415.

[175] Y. Gao, F.J. Muzzio, M.G. Ierapetritou, A review of the Residence Time Distribution (RTD) applications in solid unit operations, Powder Technology 228 (2012) 416–423.

[176] O. Levenspiel, W.K. Smith, Notes on the diffusion-type model for the longitudinal mixing of fluids in flow, Chemical Engineering Science 6 (1957) 227–235.

[177] R. Rutgers, Longitudinal mixing of granular material flowing through a rotating cylinder - Part I: Descriptive and theoretical, Chemical Engineering Science 20 (1965) 1079–1087.

[178] A.-Z. Abouzeid, T.S. Mika, K.V. Sastry, D.W. Fuerstenau, The influence of operating variables on the residence time distribution for material transport in a continuous rotary drum, Powder Technology 10 (1974) 273–288.

[179] R. Rutgers, Longitudinal mixing of granular material flowing through a rotating cylinder - Part II: Experimental, Chemical Engineering Science 20 (1965) 1089–1100.

[180] A.-Z. Abouzeid, D.W. Fuerstenau, K.V. Sastry, Transport behavior of particulate solids in rotary drums: Scale-up of residence time distribution using the axial dispersion model, Powder Technology 27 (1980) 241–250.

[181] D. Revol, C. Briens, J. Chabagno, The design of flights in rotary dryers, Powder Technology 121 (2001) 230–238.

[182] M. Krokida, D. Marinos-Kouris, A.S. Mujumdar, Rotary Drying, in: A.S. Mujumdar (Ed.), Handbook of Industrial Drying, CRC Press, 2006.

[183] W. Blumberg, E.-U. Schlünder, Transversale Schüttgutbewegung und konvektiver Stoffübergang in Drehrohren. Teil 2: Mit Hubschaufeln, Chemical Engineering and Processing: Process Intensification 35 (1996) 405–411.

[184] C. Baker, The design of flights in cascading rotary dryers, Drying Technology 6 (1988) 631–653.

[185] O.O. Ajayi, M.E. Sheehan, Application of image analysis to determine design loading in flighted rotary dryers, Powder Technology 223 (2012) 123–130.

[186] O.O. Ajayi, M.E. Sheehan, Design loading of free flowing and cohesive solids in flighted rotary dryers, Chemical Engineering Science 73 (2012) 400–411.

[187] N.J. Fernandes, C.H. Ataide, M.A.S. Barrozo, Modeling and experimental study of hydrodynamic and drying characteristics fo an industrial rotary dryer, Brazilian Journal of Chemical Engineering (2009) 331–341.

[188] H. Lee, S. Choi, Lifter design for enhanced heat transfer in a rotary kiln reactor, J Mech Sci Technol 27 (2013) 3191–3197.

[189] K.S. Hatzilyberis, G.P. Androutsopoulos, An RTD study for the flow of lignite particles through a pilot rotary dryer part II: flighted drum case, Drying Technology 17 (1999) 759–774.

[190] R.G. Sherritt, R. Caple, L.A. Behie, A.K. Mehrotra, The movement of solids through flighted rotating drums. Part II solids-gas interaction and model validation, Can. J. Chem. Eng. 72 (1994) 240–248.

[191] J. Kelly, Flight design in rotary dryers, Drying Technology 10 (1992) 979–993.

[192] M.A. Karali, Analysis study of the axial transport and heat transfer of a flighted rotary drum operated at optimum loading. Dissertation, Magdeburg, 2015.

[193] M.A. Karali, F. Herz, E. Specht, J. Mallmann, Comparison of image analysis methods to determine the optimum loading of flighted rotary drums, Powder Technology 291 (2016) 147–153.

[194] M.A. Karali, E. Specht, F. Herz, J. Mellmann, Different camera and light positions to facilitate image analysis processing in rotary drums studies, Powder Technology 306 (2017) 55–60.

[195] M.A. Karali, E. Specht, F. Herz, J. Mellmann, H.A. Refaey, Unloading characteristics of flights in a flighted rotary drum operated at optimum loading. Powder Technology, 333, 347-352 (2018).

[196] M.A. Karali, K.R. Sunkara, F. Herz, E. Specht, Experimental analysis of a flighted rotary drum to assess the optimum loading, Chemical Engineering Science 138 (2015) 772–779.

[197] K. Cronin, M. Catak, J. Bour, A. Collins, J. Smee, Stochastic modelling of particle motion along a rotary drum, Powder Technology 213 (2011) 79–91.

[198] A. Afacan, J.H. Masliyah, Solids hold-up in rotary drums, Powder Technology 61 (1990) 179–184.

[199] A.S. Bongo Njeng, S. Vitu, M. Clausse, J.-L. Dirion, M. Debacq, Effect of lifter shape and operating parameters on the flow of materials in a pilot rotary kiln: Part I. Experimental RTD and axial dispersion study, Powder Technology 269 (2015) 554–565.

[200] A.S. Bongo Njeng, S. Vitu, M. Clausse, J.-L. Dirion, M. Debacq, Effect of lifter shape and operating parameters on the flow of materials in a pilot rotary kiln: Part II. Experimental hold-up and mean residence time modeling, Powder Technology 269 (2015) 566–576.

[201] J.-P. Pan, T.-J. Wang, J.-J. Yao, Y. Jin, Granule transport and mean residence time in horizontal drum with inclined flights, Powder Technology 162 (2006) 50–58.

[202] C. Baker, Air-solids drag in cascading rotary dryers, Drying Technology 10 (1992) 365–393.

[203] M. Renaud, J. Thibault, A. Trusiak, Solids transportation model of an industrail rotary dryer, Drying Technology 18 (2000) 843–865.

[204] M.A. Karali, E. Specht, J. Mellmann, H.A. Refaey, M.R. Salem, A.Y. Elbanhawy, Granular transport through flighted rotary drums operated at optimum-loading: Mathematical model, Drying Technology 38 (2020) 495–505.

[205] J. Thibault, P.I. Alvarez, R. Blasco, R. Vega, Modeling the Mean Residence Time in a Rotary Dryer for Various Types of Solids, Drying Technology 28 (2010) 1136–1141.

[206] R. Dietze, 21.03.1939, Heat exchange apparatus. (2151087). United States of America.

[207] V.J. Azbe, 29.09.1953, Kiln. (2653809). United States of America.

[208] V.J. Azbe, 24.03.1959, Method of and apparatus for treating calcareous materials. (2879052). United States of America.

[209] N.E. Andersen, 29.05.1962, Rotary kiln with built-in heat exchanger. (US3036822). United States of America.

[210] C. Rochelsberg, 02.01.1964, Drehrohrofen mit Zelleneinbauten. (DE000001085089). Bundesrepublik Deutschland.

[211] J. Thibault, J.J. Stephansky, J.N. Snyder, 10.02.2004, Rotary kiln heat exchanger and method of assembling same. (US6688884). United States of America.

[212] J. Thibault, J.J. Stephansky, J.N. Snyder, J. Smaroff, 03.02.2015, Rotary kiln heat exchanger and method of assembling same. (USRE45360). United States of America.

[213] O.M. Wicken, L.L. Gill, 17.04.1962, Rotary kiln with heat exchanger. (US3030091). United States of America.

[214] G.E. Ransom, 19.07.1994, Trefoil construction for rotary kilns. (5330351). United States of America.

[215] L.R. Whaley, A.L. Renkey, 07.06.2007, Heat exchanger for rotary kilns. (US20070128566A1). United States of America.

[216] P. Dussossoy, 08.10.1962, Échangeur de chaleur. (FR000001309321A). Frankreich.

[217] P. Dussossoy, 17.08.1965, Heat Exchange structure for a rotary kiln. (US3201100). United States of America.

[218] W.A. Reayney, D.W. Reaney, 02.06.1959, Preheater for rotary kiln. (US2889143). United States of America.

[219] R. Bucchi, 28.07.1970, Heat recuperator structure in a rotary cement kiln. (US3521867). United States of America.

[220] J. Xu, Y. Ma, Simulation Analysis of Gas-solid Two-phase Flow for Heating Catalyst in Rotary Multi-cavity Kiln, IOP Conf. Ser.: Mater. Sci. Eng. 398 (2018) 12010.

[221] P. Wainwright, D. Cresswell, Synthetic aggregates from combustion ashes using an innovative rotary kiln, Waste management (New York, N.Y.) 21 (2001) 241–246.

[222] K.S. Venkataraman, D.W. Fuerstenau, Effect of lifter shape and configuration on material transport part I: In rotating drums, Powder Technology 46 (1986) 23–32.

[223] E.B. Arruda, J. Façanha, L.N. Pires, A.J. Assis, M. Barrozo, Conventional and modified rotary dryer: Comparison of performance in fertilizer drying, Chemical Engineering and Processing: Process Intensification 48 (2009) 1414–1418.

[224] B.C. Silvério, E.B. Arruda, C.R. Duarte, M. Barrozo, A novel rotary dryer for drying fertilizer: Comparison of performance with conventional configurations, Powder Technology 270 (2015) 135–140.

[225] W. Walbrecker, 26.03.1953, Drehrohrofen. (DE000000876156B). Bundesrepublik Deutschland.

[226] K. Sattler, Thermische Trennverfahren: Grundlagen, Auslegung, Apparate, 3rd ed., Wiley-VCH, Weinheim, 2001.

[227] K. Kröll, Trocknungstechnik: Zweiter Band Trockner und Trocknungsverfahren, Springer Berlin Heidelberg, Berlin, Heidelberg, 1978.

[228] B. Luczak, R. Müller, M. Ulbricht, H.J. Schultz, Experimental analysis of the flow conditions in spiral jet mills via non-invasive optical methods, Powder Technology 325 (2018) 161–166.

[229] B. Luczak, R. Müller, C. Kessel, M. Ulbricht, H.J. Schultz, Visualization of flow conditions inside spiral jet mills with different nozzle numbers– Analysis of unloaded and loaded mills and correlation with grinding performance, Powder Technology 342 (2019) 108–117.

[230] B. Luczak, Flow conditions inside spiral jet mills and impact on grinding performance, Universitätsbibliothek Duisburg-Essen, Duisburg, Essen, 2018.

[231] B. Lewandowski, Investigation of complex multiphase flows by advanced optical methods at the example of the flotation process of fluorite, 2019.

[232] J. Prießen, M. Behrens, H.J. Schultz, Solid transport in rotary drums with different internals, Chemie Ingenieur Technik 92 (2020) 1302.

[233] J. Priessen, T. Kreutzer, G. Irgat, M. Behrens, H.J. Schultz, Solid Flow in Rotary Drums with Sectional Internals: An Experimental Investigation, Chem. Eng. Technol. 44 (2021) 300–309.

[234] J. Priessen, T. Kawka, J. Alisic, M. Behrens, H.J. Schultz, Rotary drums with sectional internals: Experimental investigation on the influence of section number and section length, Powder Technology 386 (2021) 262–274.

[235] J. Priessen, T. Kawka, M. Behrens, H.J. Schultz, Cross-section-phenomena in rotary drums with sectional internals, Powder Technology (2020) 229–244.

[236] J. Hagen, Chemiereaktoren: Auslegung und Simulation, Wiley-VCH, Weinheim, 2004.

[237] J. Priessen, F. Barths, M. Behrens, H.J. Schultz, The length of axially segmented lifters in flighted rotary drums: influence on solid transport, Drying Technology (2021) 1–18.

[238] P.S.T. Sai, G.D. Surender, A.D. Damodaran, V. Suresh, Z.G. Philip, K. Sankaran, Residence time distribution and material flow studies in a rotary kiln, MTB 21 (1990) 1005–1011.

[239] J. Prießen, M. Behrens, H.J. Schultz, Mixing and segregation in rotary drums with sectional internals, Chemie Ingenieur Technik 92 (2020) 1313–1314.

[240] D.V. Khakhar, J.J. McCarthy, J.M. Ottino, Radial segregation of granular mixtures in rotating cylinders, Physics of Fluids 9 (1997) 3600–3614.

[241] D.A. Santos, C.R. Duarte, M. Barrozo, Segregation phenomenon in a rotary drum: Experimental study and CFD simulation, Powder Technology 294 (2016) 1–10.

[242] Y.L. Ding, R. Forster, J. Seville, D.J. Parker, Segregation of granular flow in the transverse plane of a rolling mode rotating drum, International Journal of Multiphase Flow 28 (2002) 635–663.

[243] J. Prießen, K. Graf, M. Behrens, H.J. Schultz, Changes of phase interfaces in rotary drums with sectional internals, Chemie Ingenieur Technik 92 (2020) 1313.

[244] J.P. Gorog, T.N. Adams, J.K. Brimacombe, Regenerative heat transfer in rotary kilns, MTB 13 (1982) 153–163.

[245] A. Stefan, S. Hindges, H.J. Schultz, Simulation of Heat Exchange in Vessels with Helical Coils and Influence of Stirrer Position, Chemie Ingenieur Technik 89 (2017) 470–474.

[246] A. Stefan, Enhancement of energy efficiency in stirred tank reactors by use of computational fluid dynamics, 2019.

[247] VDI-Wärmeatlas: Mit 320 Tabellen, 11th ed., Springer Vieweg, Berlin, Heidelberg, 2013.

[248] R. Jeschar, E. Kostowski, R. Alt, Wärmestrahlung in Industrieöfen, 1st ed., Papierflieger-Verl., Clausthal-Zellerfeld, 2004.

[249] P.V. Barr, J.K. Brimacombe, A.P. Watkinson, A heat-transfer model for the rotary kiln: Part I. pilot kiln trials, MTB 20 (1989) 391–402.

[250] P.V. Barr, J.K. Brimacombe, A.P. Watkinson, A heat-transfer model for the rotary kiln: Part II. Development of the cross-section model, MTB 20 (1989) 403–419.

[251] M. Kwapinska, G. Saage, E. Tsotsas, Continuous versus discrete modelling of heat transfer to agitated beds, Powder Technology 181 (2008) 331–342.

[252] F. Herz, I. Mitov, E. Specht, R. Stanev, Influence of the Motion Behavior on the Contact Heat Transfer Between the Covered Wall and Solid Bed in Rotary Kilns, Experimental Heat Transfer 28 (2015) 174–188.

[253] C. Csernyei, A.G. Straatman, Numerical modeling of a rotary cement kiln with improvements to shell cooling, International Journal of Heat and Mass Transfer 102 (2016) 610–621.

[254] V. Gnielinski, Neue Gleichungen für den Wärme- und den Stoffübergang in turbulent durchströmten Rohren und Kanälen, Forsch Ing-Wes 41 (1975) 8–16.

[255] V. Gnielinski, Ein neues Berechnungsverfahren für die Wärmeübertragung im Übergangsbereich zwischen laminarer und turbulenter Rohrströmung, Forsch Ing-Wes 61 (1995) 240–248.

[256] R. Müller, Die Annäherung der Temperaturabhängigkeit der Transportkoeffizienten von Gasen durch einen Potenzansatz, Chemie Ingenieur Technik 40 (1968) 344–349.

[257] Volker Gnielinski, Neue Gleichungen für den Wärme- und den Stoffübergang in turbulent durchströmten Rohren und Kanälen, Forsch. ing.-Wes 41 (1975) 8–16.

[258] W. Schupe, Vereinfachte Berechnung des Strahlungswärmeübergangs in Industrieöfen und Vergleich mit Messungen in einer Versuchsbrennkammer. Dissertation, Clausthal-Zellerfeld, 1974.

[259] A.K. Oppenheim, The Engineering Radiation Problem - an example of the interaction between engineering and mathematics // The Engineering Radiation Problem - an example of the interaction between engineering and mathematics, Z. angew. Math. Mech. 36 (1956) 81–93.

[260] A.K. Oppenheim, Radiation analysis by network method, Trans ASME 65 (1956) 725–735.

[261] W. Bauer, R. Steinhardt, Emissionsgrade feuerfester Baustoffe, Gas, Wärme international 39 (1990) 388–391.

[262] S. Bohnes, S. Wirtz, V. Scherer, Einfluss von Belägen in Hochtemperaturprozessen: Simultane Messung der Wärmeleitfähigkeit und der spektralen Emissionskoeffizienten in Abhängigkeit der stofflichen Eigenschaften, 2008.

[263] E. Kostowski, Analytische Bestimmung des Emissionsgrades von Abgasen, Gaswärme International (1991) 529–534.

[264] T. Redemann, Entwicklung innovativer Tunnelofenkonzepte zum Brennen von keramischem Gut anhand eines mathematischen Prozessmodells. Dissertation, Magdeburg, 2019.

[265] H.C. Hottel, R.B. Egbert, The radiation of furnace gases, Trans ASME 63 (1941) 297.

[266] H.O. Gardeik, H. Ludwig, Berechnung des Wandwärmeverlustes von Drehöfen und Mühlen. Teil I: Grundlagen. (Heft 2), 1980,, Zement-Kalk-Gibs International 33 (1980) S. 53-62.

[267] F. Herz, I. Mitov, E. Specht, R. Stanev, Experimental study of the contact heat transfer coefficient between the covered wall and solid bed in rotary drums, Chemical Engineering Science 82 (2012) 312–318.

[268] F. Herz, I. Mitov, E. Specht, R. Stanev, Influence of operational parameters and material properties on the contact heat transfer in rotary kilns, International Journal of Heat and Mass Transfer 55 (2012) 7941–7948.

[269] S.S. Agustini, Regenerative Action of the Wall on the Heat Transfer for Directly and Indirectly Heated Rotary Kilns. Dissertation, Magdeburg, 2006.

[270] Y. Sonavane, Influence of the Wall on the Heat Transfer Process in Rotary Kiln. Dissertation, Magdeburg, 2010.

[271] S.S. Agustini, A. Queck, E. Specht, Modeling of the Regenerative Heat Flow of the Wall in Direct Fired Rotary Kilns, Heat Transfer Engineering 29 (2008) 57–66.

[272] S.H. Tscheng, A.P. Watkinson, Convective heat transfer in a rotary kiln, Can. J. Chem. Eng. 57 (1979) 433–443.

[273] E. Specht, Heat and mass transfer in thermoprocessing: Fundamentals, calculations, processes, 1st ed., Vulkan Verlag, Essen, 2017.

[274] J.P. Gorog, T.N. Adams, J.K. Brimacombe, Heat transfer from flames in a rotary kiln, MTB 14 (1983) 411–424.

[275] J.P. Gorog, J.K. Brimacombe, T.N. Adams, Radiative heat transfer in rotary kilns, MTB 12 (1981) 55–70.

[276] S.-Q. Li, L.-B. Ma, W. Wan, Q. Yao, A Mathematical Model of Heat Transfer in a Rotary Kiln Thermo-Reactor, Chem. Eng. Technol. 28 (2005) 1480–1489.

[277] H.C. Hottel, R.B. Egbert, Radiant heat transmission from water vapor, Transactions of the American Institute of Chemical Engineers 38 (1942) 531–568.

[278] H. Liu, H. Yin, M. Zhang, M. Xie, X. Xi, Numerical simulation of particle motion and heat transfer in a rotary kiln, Powder Technology 287 (2016) 239–247.

[279] M.A. Delele, F. Weigler, G. Franke, J. Mellmann, Studying the solids and fluid flow behavior in rotary drums based on a multiphase CFD model, Powder Technology 292 (2016) 260–271.

[280] M. Gürtürk, H.F. Oztop, N.A. Pambudi, CFD analysis of a rotary kiln using for plaster production and discussion of the effects of flue gas recirculation application, Heat Mass Transfer 54 (2018) 2935–2950.

[281] L. Zhang, Z. Jiang, F. Weigler, F. Herz, J. Mellmann, E. Tsotsas, PTV measurement and DEM simulation of the particle motion in a flighted rotating drum, Powder Technology 363 (2020) 23–37.

[282] K.S. Mujumdar, V.V. Ranade, Simulation of Rotary Cement Kilns Using a One-Dimensional Model, Chemical Engineering Research and Design 84 (2006) 165–177.

[283] H.A. Spang, A dynamic model of a cement kiln, Automatica 8 (1972) 309–323.

[284] M. Lee, S. Lee, A mathematical model of calcination of limestone in rotary kiln, Steel Research 70 (1999) 15–21.

[285] H. Shahin, S. Hassanpour, A. Saboonchi, Thermal energy analysis of a lime production process: Rotary kiln, preheater and cooler, Energy Conversion and Management 114 (2016) 110–121.

[286] L. Papula, Mathematik für Ingenieure und Naturwissenschaftler: Ein Lehr- und Arbeitsbuch für das Grundstudium, 12th ed., Vieweg + Teubner, Wiesbaden, 2009.